

**STRUCTURAL STUDIES OF SILICALITE AND
METALLOSILICATE MOLECULAR SIEVES OF MFI
TYPE USING NON-AMBIENT POWDER X-RAY
DIFFRACTION TECHNIQUE**

**A THESIS
SUBMITTED TO THE
UNIVERSITY OF PUNE
FOR THE DEGREE OF
DOCTOR OF PHILOSOPHY
(IN CHEMISTRY)**

**BY
Mr. DEU SOUDAGAR BHANGE
CATALYSIS DIVISION
NATIONAL CHEMICAL LABORATORY
PUNE 411008, INDIA**

**Dr. (Mrs.) VEDA RAMASWAMY
(RESEARCH GUIDE)**

APRIL 2008

CERTIFICATE

Certified that the work incorporated in the thesis entitled, **“Structural studies of silicalite and metallosilicate molecular sieves of MFI type using non-ambient powder X-ray diffraction technique”** submitted by **Mr. Deu Soudagar Bhange**, for the degree of **Doctor of Philosophy**, was carried out by the candidate under my supervision in the Catalysis Division, National Chemical Laboratory, Pune, India. Materials obtained from other sources have been duly acknowledged in the thesis.

Dr. (Mrs.) Veda Ramaswamy

Research Guide

DECLARATION

I hereby declare that the thesis entitled “**Structural studies of silicalite and metallosilicate molecular sieves of MFI type using non-ambient powder X-ray diffraction technique**”, submitted for the Degree of Doctor of Philosophy to the University of Pune, has been carried out by me at the National Chemical Laboratory, Pune under the supervision of my research guide Dr. (Mrs.) Veda Ramaswamy. The work is original and has not been submitted in part or full by me for any other degree or diploma to this or any other University.

(Deu S. Bhange)

DEDICATED
TO
MY BELOVED PARENTS

Acknowledgements

I take this opportunity to express my deepest sense of gratitude towards my research supervisor, Dr. (Mrs.) Veda Ramaswamy for her invaluable guidance, numerous discussions and constructive suggestions throughout the course of this work. It is extremely difficult for me to express in words my gratitude towards her, who stood by me throughout my research work, guided me not only towards becoming an able researcher but also a good human being. Without her persuasion and interest, it would not have been possible for me to gain the confidence that I have today. I would like to express my profound gratitude to Dr. A.V. Ramaswamy, Dr. S. Sivasankar and Dr. Rajiv Kumar, former Heads of Catalysis Division, NCL, for their help and co-operation. I also wish to thank Dr. Michaël Deschamps [Orleans, France] for his help and discussions for NMR spectroscopic data during my research work. I am grateful to Dr. Karoly Lazar [Hungary] for Mössbauer spectroscopic data. I am thankful to Dr. A. B. Mandal, Director, Central Leather research Institute, Chennai for giving permission to work with my guide during the writing of the thesis.

I owe my special thanks to Dr. C. V. V. Satyanarayana, Dr. P. N. Joshi, Dr. C.S. Gopinath, Dr. K. Selvaraj, Mr. R. K. Jha, Mr. A.B. Gaikwad, Mr. Tejas, Mr. Niphadkar and Mr. Purushottam for their help and support. I would like to thank all my teachers in various classes for the love and encouragement that I received from them and who taught me science and the value of education.

It gives me great pleasure to thank my labmates Pallavi, Nisha, Mahesh, Muru, Vaneet and Preeti for their constant help, encouragement and the nice time I had with them. I would like to thank my friends Ganesh, Sachin, Balu, Lakshi, Prashant, Rohit, Koteswara Rao, Richa, Surekha, Maitri, Kalaivani, Jayashree, Damodiran and my friends in NCL for their co-operation, encouragement, invaluable help and moral support rendered by them.

Words are not enough to express my love and gratitude to my family members. It gives me great pleasure to thank my parents, my brothers Dattatraya and Shahu, vahini and my nephew Vaibhav and Dhanashree for their love, unfailing support, tremendous patience, trust and encouragement that they have shown to me. I am very much indebted to them. I also thank my family friends Uday, Santosh and Tanaji for their affection and support.

I am grateful to director of NCL, Dr. S. Sivaram for allowing me to use the laboratory facilities. I also thank UGC, New Delhi, India, for the financial support in the form of junior and senior research fellowships. Above all, I thank God for his blessings, for forgiving my mistakes, for leading me in the right path and for being there whenever I needed.

Contents

Chapter 1:	Introduction and literature survey	1
1.1	Introduction	
1.2	Structure of zeolites	1
1.2.1	Mobil Five (MFI) type silicalite and metallosilicate molecular sieves	3
1.2.2	The Unit cell of MFI Framework	4
1.3	Modification of Zeolites	5
1.3.1	Isomorphous substitution by hydrothermal method	5
1.3.2	Modification of zeolites by post synthesis methods	6
1.3.2.1	Cation exchange	6
1.3.2.2	Solid state reactions	6
1.3.2.3	Metal impregnation	7
1.3.2.4	Silylation	7
1.4	Powder X-ray Diffraction	7
1.4.1	Strengths and Limitations of Powder XRD	11
1.4.2	Applications of powder X-ray diffraction	11
1.4.2.1	Phase identification (Qualitative analysis)	11
1.4.2.2	Quantitative Phase analysis	12
1.4.2.3	Determination of crystallinity	13
1.4.2.4	Crystallite Size	13
1.4.2.5	Strain analysis	14
1.4.2.6	Lattice parameters or unit cell dimensions	15
1.4.2.7	Structure solution using powder X-ray diffraction	17
1.5	Rietveld Refinement	19
1.5.1	General Structure Analysis System (GSAS)	21
1.6	Powder X-ray diffraction in zeolite materials	22
1.6.1	Isomorphous substitution of ‘T’ atoms by heteroatoms	23
1.6.2	Location of the isomorphously substituted hetero atoms (T sites) in the framework	24
1.6.3	Location/orientation of organic molecules in the zeolite channel	25

1.7	Non-ambient <i>in-situ</i> X-ray diffraction analysis	25
1.7.1	High Temperature X-ray Diffraction	26
1.7.1.1	Reaction Kinetics	28
1.7.1.2	Phase Transition	28
1.7.1.3	Thermal Expansion Coefficients of materials	29
1.7.2	Low temperature X-ray diffraction	30
1.7.2.1	Study of materials, which are liquids or gases at room temperature	32
1.7.2.2	Charge density analyses	33
1.7.2.3	Phase transitions and thermal expansion coefficients	33
1.8	High/Low temperature XRD of zeolites/molecular sieve materials	34
1.9	Other analytical tools used for the characterization of metallosilicate molecular sieves	35
1.9.1	Thermal Analysis (TG/DTA)	35
1.9.2	Diffuse reflectance UV-visible spectroscopy	35
1.9.3	Fourier transform Infra-red (FTIR) spectroscopy	36
1.9.4	Nuclear Magnetic Resonance (NMR) Spectroscopy	37
1.10	Scope of the thesis	37
1.11	Objectives of the present investigation	38
1.12	Outline of the thesis	39
1.13	References	40
Chapter 2: Synthesis and Characterizations of Silicalite and Metallosilicate Molecular Sieves		
2.1	Introduction	48
2.2	Hydrothermal synthesis of metallosilicate (MFI) molecular sieves	48
2.2.1	Iron-silicalite-1 (FeS-1)	48
2.2.2	Titanium silicalite-1 (TS-1)	48
2.2.3	Zirconium silicalite-1 (ZrS-1)	49
2.3	Characterization	53
2.3.1	Powder X-ray diffraction	53
2.3.2	Rietveld refinement	54
2.3.3	Diffuse reflectance UV-visible spectroscopy	54
2.3.4	Fourier transform infra-red spectroscopy	54

2.3.5	Scanning electron microscopy (SEM) and Energy Dispersive Analysis of X-rays (EDAX)	55
2.3.6	Thermal analysis	55
2.3.7	²⁹ Si MAS NMR spectroscopy	55
2.3.8	Fe Mössbauer Spectroscopy	55
2.4	Results and discussions	56
2.4.1	Powder X-ray diffraction	56
2.4.2	Diffuse reflectance UV-visible spectroscopy	64
2.4.3	FTIR spectroscopy	67
2.4.4	Scanning electron microscopy	69
2.4.5	Thermal analysis	70
2.4.6	²⁹ Si MAS NMR spectroscopy	71
2.4.7	Mössbauer Spectroscopy	74
2.5	Conclusions	76
2.6	References	76
Chapter 3: Thermal Expansion Behavior of Silicalite and Metallosilicate Molecular Sieves		
3.1	Introduction	79
3.2	Experimental	81
3.2.1	Collection of XRD patterns for thermal stability studies	81
3.2.2	Data collection for negative thermal expansion studies	82
3.2.3	Rietveld Refinement	83
3.3	Results and discussion	84
3.3.1	Thermal Stability Analysis	84
3.3.2	Detailed structural analysis of silicalite-1 for negative thermal expansion (NTE) studies	91
3.3.3	NTE behavior of metal incorporated molecular sieves	104
3.4	Conclusions	116
3.5	References	117
Chapter 4: Non-isothermal Kinetic Studies Of The Template Decomposition From The Silicalite-1 Framework		
4.1	Introduction	119
4.1.1	Kinetics of reactions	119

4.1.2	Theoretical background	120
4.1.3	New Method of analysis	121
4.1.4	Template decomposition in as synthesized MFI type molecular sieves	123
4.2	Experimental	124
4.2.1	Data collection for kinetic analysis using HTXRD and TG	124
4.2.2	Kinetic studies	125
4.3	Results and Discussion	127
4.3.1	Kinetic studies using HTXRD technique	127
4.3.2	Kinetic studies using TG analysis	135
4.3.3	Structural changes in the silicalite-1 as function of template removal	139
4.4	Conclusions	141
4.5	References	141
Chapter 5: Low Temperature XRD (LTXRD) Studies		
5.1	Introduction	144
5.2	Experimental	149
5.2.1	Data collection for LTXRD studies	149
5.2.2	Rietveld Refinement	149
5.3	Results and Discussion	150
5.3.1	Phase transition in TS-1	150
5.3.2	An attempt to locate Ti in the MFI framework by low temperature XRD	157
5.3.3	Phase Transition in FeS-1	161
5.3.4	An attempt to locate Fe in the MFI framework by low temperature XRD	168
5.4	Conclusions	171
5.5	References	172
Chapter 6: Summary and conclusions		175

ABBREVIATIONS

AAS	Atomic absorption spectroscopy
A	Frequency factor
AlPO ₄	Aluminophosphates
covEPE	Covalent elastic polarizable environment method
SBU	Secondary building units
DIFFaX	Diffracted Intensities From Faulted Crystals
DTA	Differential thermal analysis
DTG	Differential thermogravimetry
E_a	Apparent activation energy
FTIR	Fourier transform infra-red
$g(\alpha)$	Integral of the kinetic model function $f(\alpha)$
F_{hkl}	Structure factor
GUI	Graphical user interface
GSAS	General Structure Analysis System
HTXRD	High temperature powder X-ray diffraction
hkl	Miller indices
ICDD	International center for diffraction data
ICSD	Inorganic crystal structure database
k	Rate constant
LDA	Local density approximation;
L_{hkl}	Lorentz polarization factor, ,
LTXRD	Low temperature X-ray diffraction
MAS-NMR	Magic angle spinning - Nuclear magnetic resonance
M_{hkl}	Reflection multiplicity
MFI	Mobil FIVE
MEL	Mobil ELEven
MC	Monte Carlo method
MD	Molecular Dynamics
MM	Molecular Mechanics
NPD	Neutron Powder Diffraction
N_j	Site occupancy multiplier

NTE	Negative thermal expansion
ONIOM	N-layer integrated molecular orbitals and molecular mechanics method
QM-pot	Hybrid quantum mechanics/potential function method
PDF	Powder diffraction files
P_{hkl}	Preferred orientation correction function
PTE	Positive thermal expansion
R	Molar gas constant
R_{wp}	Weighted profile R -value
R_{exp}	Statistically expected R -value
RIETAN	Rietveld Analysis
RUM	Rigid unit modes
s	Scale factor
TDS	Thermal diffuse scattering
T_p	Temperature at which the reaction rate is maximum
TPA ⁺	Tetrapropylammonium cations
E_a	Apparent activation energy
TS-1	Titanosilicate-1
T_f	Phase transition temperature
TR-PXRD	Time resolved powder X-ray diffraction
TPABr	Tetra-propylammonium bromide
TPAOH	Tetrapropylammonium hydroxide
UCV	Unit cell volume
WT	Wall thickness
XRD	X-ray diffraction
XRPD	X-ray powder diffraction
XRS-82	X-ray Rietveld System
ZSM-5	Zeolite Socony Mobile-5

Chapter **1**



Introduction And Literature Survey



1.1 Introduction

Zeolites/molecular sieves are crystalline microporous materials, which have become extremely successful as catalysts for oil refining, gas separation, petrochemicals and organic synthesis in the production of fine and speciality chemicals. Zeolites are microporous crystalline aluminosilicates with three-dimensional framework structures and have attracted particular attention due to the following specific features of these materials: (1) They have very high surface area and adsorption capacity, (2) Active sites, such as acid sites for instance, can be generated in the framework and their strength and concentration can be tailored for a particular application, (3) Their intricate channel structure allows the zeolites to present different types of shape selectivity, *i.e.*, product, reactant, and transition state, which can be used to direct a given catalytic reaction toward the desired product avoiding undesired side reactions. The widespread use of these catalysts is due to the enhanced selectivity for the desired products, easy work up and recovery from the reaction mixture, regeneration once it is deactivated and a lower tendency to form by-products. All of these properties of zeolites, which are of paramount importance in catalysis and make them attractive choices for the above processes, are ultimately dependent on the thermal and hydrothermal stability of these materials. Structurally, these are framework aluminosilicates, which are based on an infinitely extending three-dimensional network of AlO_4 and SiO_4 tetrahedra linked to each other by sharing of oxygens.

Zeolites are technologically an important class of materials utilized in a wide variety of industrial applications, including catalysis [1-3], ion exchange [4, 5], back fill material for nuclear waste disposal [6] and chemical sensing [7]. The catalytic properties of zeolites are in large part determined by the framework composition of the zeolite [8]. Alteration of the Si/Al ratio or other modifications such as extra-framework cation exchange, isomorphous substitution, pore blockage, elimination of external sites can lead to quite dramatic variations in the catalytic activity and in the stability of the zeolite framework [9].

1.2 Structure of zeolites

A general understanding of the basic building units is rather important in order to relate the large number of complex structures of the zeolite and related materials as suggested by Szostak [10]. There are primary building units and secondary building

units. The primary building units of a zeolite material are the individual tetrahedral (TO_4) units where T is Si and Al. The tetrahedra share all corners to generate 3-dimensional network. The primary building units condense and form various polymeric units known as secondary building units (SBU) [11, 12], comprising single or double ring structures as represented in Figure 1.1 a and b. These Secondary building units may be assembled in many ways to give a large number of different zeolite structure types. The network of interconnected tetrahedra constitutes the zeolite framework (Figure 1.2 a and b). The individual pentasil units combine to form long chains as shown in Figure 1.2 a. These SBU linked chains join together to form a layer (Figure 1.2 b), which comprises the framework structure of ZSM-5 as shown in Figure 1.2 c.

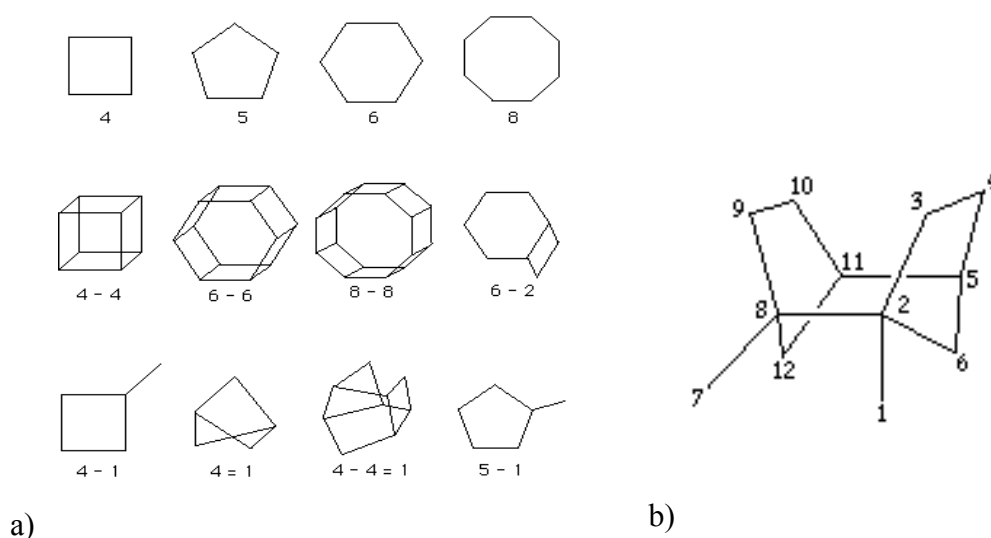


Fig. 1.1 (a) and (b) Secondary Building Unit (SBU) in pentasil zeolites.

ZSM-5 and ZSM-11 are end members of a series of zeolites (aluminosilicates) called pentasils. These zeolites have structures, which may be generated by the appropriate stacking of layers. In ZSM-11, neighboring layers are related by reflection operator (σ) and in ZSM-5 by inversion operator (I). Other possible arrangements lead to intermediate structures or inter-growths of ZSM-5 and ZSM-11. The pore systems in pentasils are of particular interest in catalytic studies. The channel system is different in these two zeolites: MFI (pore size $5.3 \times 5.6 \text{ \AA}$ and $5.1 \times 5.5 \text{ \AA}$) consists of both straight and sinusoidal channels, whereas in MEL (pore size $5.3 \times 5.4 \text{ \AA}$), both the intersecting channels are straight. Unlike other zeolites, MFI and MEL have pores of uniform dimensions and do not have large supercages. The differences in pore size

and type between zeolites of different framework structure have important consequences in the sorption and catalytic properties of zeolites. Even relatively minor structural differences between ZSM-5 and ZSM-11 result in detectable differences in catalytic properties. Silica polymorphs of MFI (ZSM-5) and MEL (ZSM-11) families are designated as silicalite-1 [13] and silicalite-2 [14], respectively which are prepared with $\text{Si/Al} = \infty$.

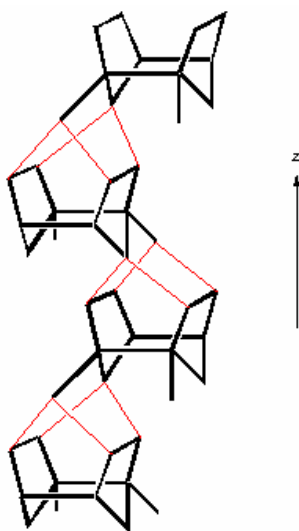


Fig. 1.2 a) SBU linked chains.

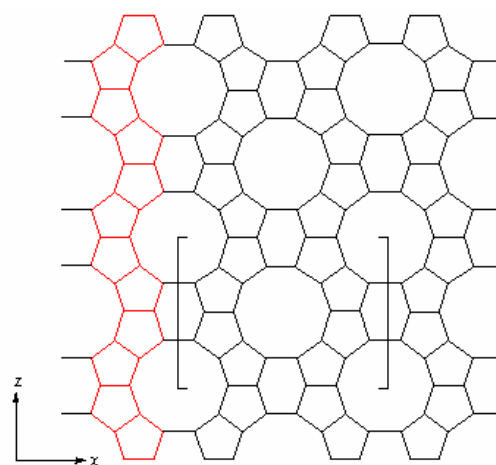


Fig. 1.2 b) Layer formed from linked chains in ZSM-5 structure.

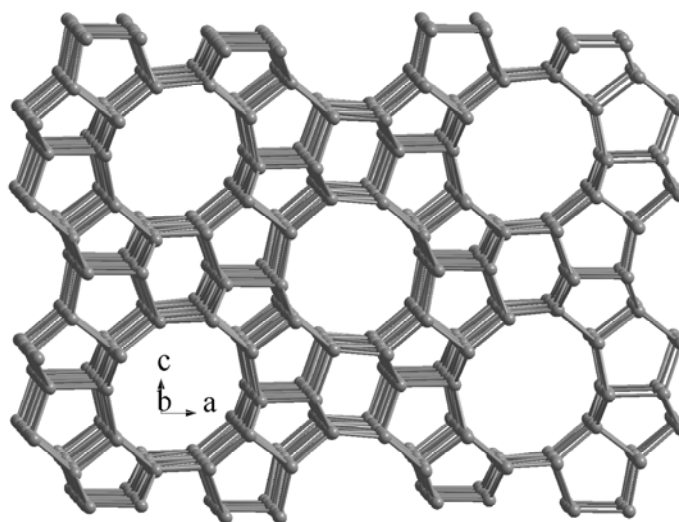


Fig. 1.2 c) MFI framework viewed along 'b' direction i.e. 010 view.

1.2.1 Mobil Five (MFI) type silicate and metallosilicate molecular sieves

Zeolite Socony Mobil-5 (ZSM-5) is composed from the five membered ring structures and is a pentasil zeolite and is designated by a three-letter code MFI (Mobil

Five). The MFI framework [15] shows a two-dimensional pore system consisting of two intersecting sets of tubular channels, [16, 17] a linear one parallel to the 'b' direction, with an opening of approximately 5.3 x 5.6 Å, and a sinusoidal one parallel to the 'a' direction, with an opening of 5.1x5.5 Å. Both channels are defined by 10-member rings of SiO₄ tetrahedra. MFI-type zeolites (zeotype) materials are among the most important microporous solids because of their large use in the field of catalysis and fine chemistry. The most used MFI material is ZSM-5 zeolite, first synthesized in the Mobil laboratories in the late 1970s.

1.2.2 The unit cell of MFI framework

MFI type materials have two crystal phase symmetries, orthorhombic (space group *Pnma* 62) and monoclinic (space group *P2₁/n*) [18]. While as-synthesized ZSM-5 has the orthorhombic symmetry, the calcined form of ZSM-5 is monoclinic at room temperature and shows orthorhombic symmetry at 75 °C [19]. The silica polymorphs of ZSM-5 (silicalite-1) also have orthorhombic and monoclinic symmetry at room temperature in as synthesized and calcined forms respectively. The symmetry of calcined forms, other than silica polymorphs depends on the framework composition and the temperature. Isomorphously substituted metallosilicate molecular sieves *viz.*, TS-1, FeS-1 etc., have orthorhombic symmetry in both as synthesized and calcined form at higher metal concentration ($\text{Si/M} \leq 150$). At very low concentration of metal ($\text{Si/M} \geq 150$) the phase is in monoclinic symmetry.

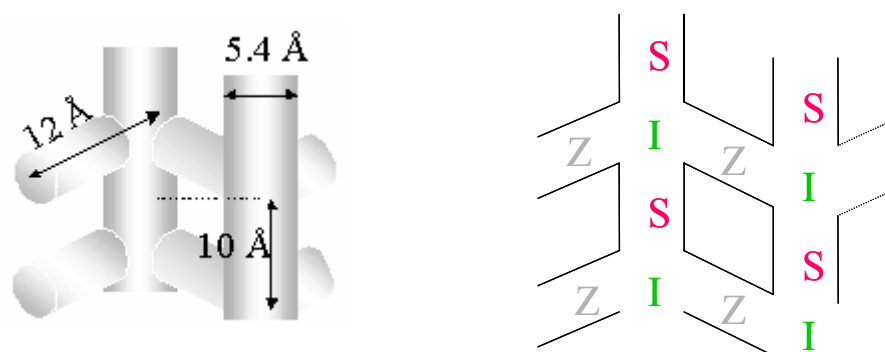


Fig. 1.3 Schematic presentation of Channel system in MFI unit cell (S = straight, Z = zigzag or sinusoidal and I = intersection point).

One unit cell in orthorhombic symmetry contains 8 asymmetric units and one asymmetric unit contains 12 T atoms. Hence one unit cell contains 96 T atoms. While

in monoclinic symmetry one unit cell has 4 asymmetric units and one asymmetric unit contains 24 T atoms [18]. The channel system of the silicalite-1 showing straight and sinusoidal channel are shown in Figure 1.3. Length of the zigzag *i.e.* sinusoidal chain is 12 Å for one unit cell while length of straight channel is 10 Å. There are 4 straight channels, 4 sinusoidal channels and 4 intersections in one unit cell of silicalite-1 ($\text{Si}_{96}\text{O}_{192}$). The diameter of the straight channel is 5.4 Å.

1.3 Modification of zeolites/molecular sieves

The catalytic properties of zeolites have been enhanced by modifying their structure. There are different ways of zeolite modification by direct hydrothermal synthesis or by post synthesis methods. Isomorphous substitution, cation exchange, metal impregnation, chemical vapor deposition and solid-state reactions are the ways of zeolite structure modification.

1.3.1 Isomorphous substitution by hydrothermal method

Many researchers have demonstrated that isomorphously substituted zeolites can be prepared by direct synthesis or post-treatment methods. Goldsmith [20] was the very first to report isomorphous substitution of silicon by germanium in the lattice. This was followed by isomorphous substitution of Si^{4+} or Al^{3+} by elements such as B^{3+} [21-25], Fe^{3+} [22, 23], Ga^{3+} [22, 24], Ti^{4+} [26], V^{5+} [27], etc. It has been reported [28] that isomorphous substitution of Si and Al by Ge, P, B, Ga and Al modify the acid strength and hence catalytic properties of various zeolites. The isomorphous substitution of Si by other tetrahedrally coordinated heteroatoms (different from Al^{III}) such as Ti^{IV} , Zr^{IV} or Fe^{III} in small amounts (up to 2-3% in weight) provides new materials, named as titanium silicalite-1 [26], zirconium silicalite-1 [29] and Fe-silicalite-1 [22, 23], respectively (designated as TS-1, ZrS-1 and FeS-1), showing specific catalytic properties in oxidation and hydroxylation reactions, depending on the coordination state of the heteroatom.

Due to the differences in ionic radii and T-O bond distances, the unit cell parameters and consequently the unit cell volume (UCV) changes gradually with the degree of metal substitution in the zeolite framework. The incorporation of heteroatoms in the zeolites increase/decrease the unit cell volume depending on the higher/lower ionic radii of the heteroatom with respect to silicon. Substitution of other T atoms in the framework may have an impact on diffusion characteristic of zeolites

either as (a) a change in the pore size due to the shortening or lengthening of the M-O-Si bond length and ultimately of M-O-Si bond angle or (b) a change in the affinity of the diffusing molecule for the substituted T-atom. The ionic radii [30] and T-O bond distances of different isomorphously substitutable cations are shown in Table 1.1. The differences in pore size and type between zeolites of different framework structure have important consequences in the sorption and catalytic properties of zeolites. Even relatively minor structural differences result in detectable differences in catalytic properties.

Table 1.1 Ionic radii and T-O bond distances of isomorphously substitutable cations.

Cation	Ionic radii, Å	T-O bond distance, Å
Si ⁴⁺	0.26	1.61
V ⁵⁺	0.36	1.71
Al ³⁺	0.39	1.74
Ti ⁴⁺	0.42	1.77
Sn ⁴⁺	0.55	1.90
Zr ⁴⁺	0.59	1.94
Fe ³⁺	0.49	1.84

1.3.2 Modification of zeolites by post synthesis methods

1.3.2.1 Cation exchange: Majority of the zeolites synthesized are in their cationic forms, wherein positively charged cations neutralize the charge created by the aluminium tetrahedra in the framework. These extraframework cations are exchangeable and the degree of cation exchange depends on the factors such as cation nature, size and its charge etc. To produce the protonic or hydrogen form of zeolite, the ammonium exchange is carried out in aqueous solutions and is calcined to convert the ammonium form of zeolite into the hydrogen form. Another cationic forms of the zeolites such as Ca²⁺, K⁺ and Cs⁺ etc., can be synthesized by this method.

1.3.2.2 Solid state reactions: A common method of ion exchange with an aqueous solution of the corresponding metal salts, for bringing metal cations onto extraframework positions of zeolite fails sometime due to bulky hydration shell of cation to be exchanged, *e.g.* Ga³⁺ [31]. The method then applied is solid-state reaction, prerequisite of this is to prepare an intimate mixture of two components, *i.e.* the

microporous solid and the compound, which contains the in-going cation. Recently Hagen *et al.* [32, 33] applied the solid state reaction to various kinds of proton containing supports (H-ZSM-5, zeolite Y, silica and γ -alumina) and low-melting (non-noble) metals such as Zn, Mg, Mn, Fe and Ga.

1.3.2.3 Metal impregnation: The molecular sieve material is brought in contact with a solution containing the components to be deposited on the zeolite surface. The even distribution of adsorbed active species is quite difficult to attain and sometimes pore blockage may occur in impregnated zeolites. Highly dispersed distribution of active species is achieved by impregnation by soaking or with an excess solution [34].

1.3.2.4 Silylation: To passivate the external acid sites/surface hydroxyl groups of zeolites, the organic volatile compound such as $\text{Si}(\text{OCH}_3)_4$, $\text{Si}(\text{OC}_2\text{H}_5)_4$ are deposited by chemical vapor deposition methods. The ability to control the constriction of the pore mouth precisely can contribute to enhanced shape selectivity by changing the relative diffusivity of molecules [35].

1.4 Powder X-ray Diffraction

Powder diffraction is the phenomenon of diffraction of any electromagnetic waves or particles on polycrystalline (powdered, bulk or thin film) materials, which is used in wide variety experimental settings. Powder X-ray diffraction is a versatile technique employed for structural characterization of solids. The powder X-ray diffraction method was devised and developed during the First World War (1916) by a Dutch/Swiss team, Peter Debye and Paul Scherrer, in Gottingen, Germany and independently, marginally later, by an American, Albert W. Hull. Diffraction from microcrystalline and amorphous powder can be studied by the powder XRD technique. Powder X-ray diffraction (PXRD) pattern contains a wealth of useful information provided one can exploit and extract the same, with patience in synthesizing good materials and healthy scientific aptitude to apply modern computational facilities. However, in comparison with the information obtained by single crystal intensity data, the PXRD profiles yield far poorer information mainly due to equivalent and overlapping reflections. Compared to the three dimensional location of each reflection in a single crystal diffraction experiment, the powder diffraction pattern can give only one dimensional data due to the rotational projection of the randomly oriented reciprocal lattices. PXRD is a long-range technique sensitive to the basic periodic structure of a solid sample.

The diffraction principle developed by W.L. Bragg is the most general and powerful diffraction theory. A simplified mathematical expression was established for the diffraction conditions. Bragg's Law is derived by considering the conditions necessary to make the phases of the beams coincide when the incident angle equals and reflecting angle [36].

$$\text{Bragg's law: } n\lambda = 2d \sin \theta \quad (1.1)$$

The rays of the incident beam are always in phase and parallel up to the point at which the top beam strikes the top layer at atom z (Figure 1.4).

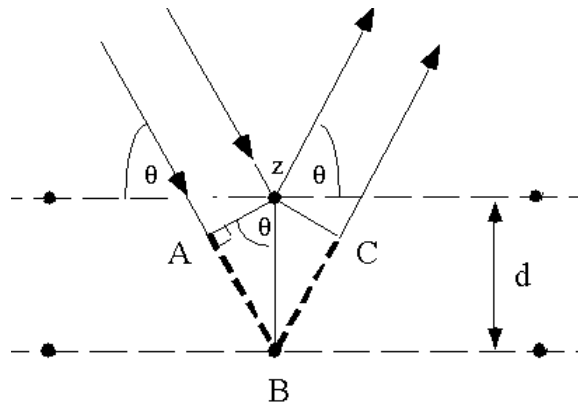


Fig. 1.4 Derivation of Bragg's Law using the reflection geometry and applying trigonometry. The lower beam must travel the extra distance ($AB + BC$) to continue traveling parallel and adjacent to the top beam.

The second beam continues to the next layer where it is scattered by atom B . The second beam must travel the extra distance $AB + BC$ if the two beams are to continue traveling adjacent and parallel. This extra distance must be an integral (n) multiple of the wavelength (λ) for the phases of the two beams to be the same:

$$n\lambda = AB + BC \quad (1.2)$$

Recognizing d as the hypotenuse of the right triangle ABz , we can use trigonometry to relate d and θ to the distance ($AB + BC$). The distance AB is opposite θ so,

$$AB = d \sin \theta \quad (1.3)$$

Because $AB = BC$ equation (1.2) becomes,

$$n\lambda = 2AB \quad (1.4)$$

Substituting equation (1.3) in equation (1.4) we have:

$$n\lambda = 2d \sin \theta \quad (1.1)$$

This is the expression for X-ray diffraction given by Bragg.

Bragg law was derived on the basis of single crystal X-ray diffraction.

The structures of various compounds such as NaCl, KCl, KBr, diamond etc. were the first complete structures determined at that time using Bragg's law of X-ray diffraction [37]. This discovery has attracted the attention of the researcher worldwide. But the applications were limited to the single crystals only. In 1916 Debye-Scherrer developed a technique called as Debye-Scherrer technique, which is considered to be the basis of powder diffraction [38]. Structure of LiF was the first structure, which has been solved by the powder diffraction technique. After these discoveries, the technique of powder diffraction method has become popular amongst the researcher in industries and academia due to its outstanding applications in identification of the compounds in single phase as well as in mixtures [39]. In the later part of 20th century powder XRD has been widely practiced as an analytical tool in the industries. The conventional analytical powder diffractometer has been continued as a workhorse for many researchers, both experts as well as beginners.

Powder diffraction is the one-dimensional representation of the three dimensional reciprocal space of individual crystallites. This causes severe overlapping of the Bragg's reflections, and this overlapping is more serious in crystals having lower symmetry. Another problem is associated with the preferred orientation of the particles in the specimen mounted for analysis. If more number of particles are oriented along one specific crystallographic direction, the resultant diffraction pattern will show the enhanced intensities for the reflections due to the crystallographic planes along that direction. If the particles are of needle, plate or cubic shapes this preferred orientation (PO) effect should be taken into consideration. One of the solutions for this PO problem is to rotate (spin) the sample holder during the data collection, which can minimize this orientational effect.

Usually the two types of geometries used for powder diffraction are Bragg-Brentano (reflection) or Debye-Scherrer (transmission) geometry [40], depending upon the need of experiments and nature of the sample.

- i) In the Debye-Scherrer geometry, a capillary loaded with the sample is made to rotate about its axis to get a better powder average. This method is very useful when the sample is hydrophilic and more sensitive to moisture. When the sample in capillary absorbs more X-rays and it is difficult to penetrate the X-rays through the full diameter of the sample, the Debye-Scherrer method fails.

- ii) In this case the Bragg-Brentano geometry plays an important role and produce enough intense pattern for solving the structure. Different types detectors are used for the detection of diffracted X-rays such as, position sensitive detector (PSD), ionization chambers and area detectors depending on the experimental requirements. The Bragg-Brentano and Debye-Scherrer geometries are shown in the Figure 1.5 a) and b) respectively.

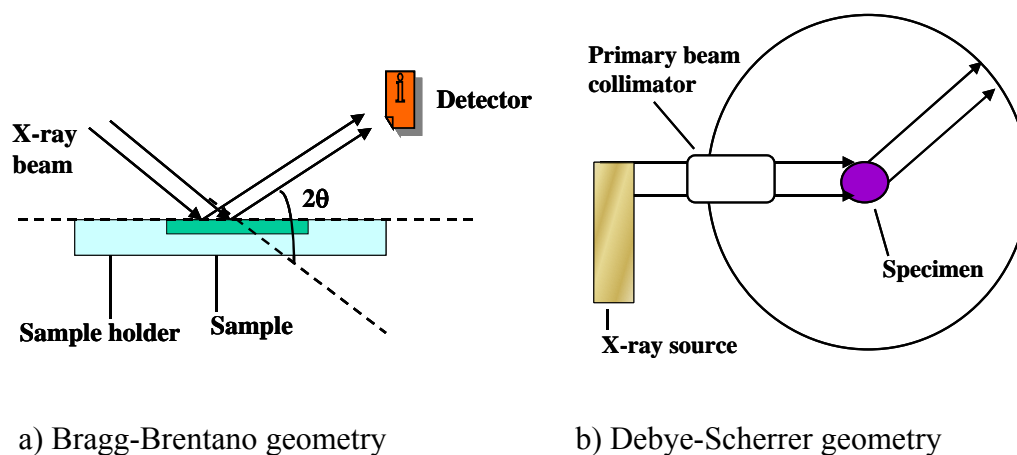


Fig. 1.5 Commonly used geometries for powder diffraction.

- iii) In Debye-Scherrer method, sample is filled in a sealed capillary, mounted on a rotating sample holder, whose axis of rotation is concentric with the capillary. Collimated parallel beams of X-rays enter the camera in radial direction and bathes the sample in capillary. In conventional laboratory this method is not having the wide applications due to the weak luminosity of reflection and low angle resolution. Due to this reason this method is used more and more often in diffractometers with bright synchrotron source. If there is preferred orientation in the sample the Debye-Scherrer geometry is used to gain the reliable intensities in comparison with the Bragg-Brentano geometry.
- iv) In Bragg-Brentano method of powder diffraction a specimen is loaded on a flat sample stage made up of glass, quartz or alumina. This method is widely used in the laboratory scale. Some of the instruments have the accessories where these plates can be spin horizontally; this some time helps to make the equal orientation of particles in all directions.

Powder X-ray diffraction is essentially very simple: crystal scatters a collimated, monochromatic beam of X-rays and the scattered beams diffracted by the sample are then measured. Processing information about the position and intensity of these diffracted X-ray beams (or reflections) yields information about the atomic arrangement within the crystalline material. However, modern crystallography is not only about knowing the positions of the atoms and corresponding bond distances, angles and related features within a material. The far more important and interesting aspect of this technique is the correlation of structural features with physical properties. This can include optical, magnetic and conductive effects as well as the structural behavior under external stimulus or in different chemical environments.

1.4.1 Strengths and limitations of powder X-ray diffraction

Like any other techniques powder X-ray diffraction also has some limitations and difficulties.

Strengths:

- 1) Powerful and rapid (< 20 min) technique for identification of an unknown material.
- 2) In most cases, it provides an unambiguous material determination.
- 3) Sample preparation is easy and fast. Sample is nondestructive.
- 4) XRD instruments are widely available in most of the laboratories.
- 5) Data interpretation is relatively straightforward.

Limitations:

- 1) Only homogeneous and single-phase materials are suited for identification of an unknown.
- 2) Standard reference files of inorganic compounds (*d*-spacings, *hkl*s) are required.
- 3) The detection limit is > 2%.
- 4) Overlapping of peaks (reflections) is severe and their decomposition is difficult.

1.4.2 Applications of powder X-ray diffraction

1.4.2.1 Phase identification (Qualitative analysis)

Each powder diffraction pattern is characterized by the unique distribution of the intensities of Bragg reflections and their positions (*d*'-spacing). In powder diffraction patterns the peak positions are defined by unit cell parameters and the intensities are defined by the distributions of atoms in the unit cells. Thus every

individual compound has its own “fingerprint” XRD pattern. This feature is used in the identification of the phases using powder diffraction data. The collection of diffraction patterns for large number of compounds, allows identification of unknown by recording its diffraction pattern and then exactly matching it with the diffraction pattern collected for known substances. For the matching of powder pattern one should have the data sets for ‘ d ’ or 2θ values and relative intensities of the reflections. Digital databases are available for the comparison *viz.*, powder diffraction files (PDF) from international center for diffraction data (ICDD), inorganic crystal structure database (ICSD). One can match their digital patterns with the standards available by using the different softwares available.

For the phase analysis of unknown substance the powder pattern is recorded by taking care that the sample should be in the form of fine grains (~ 325 mesh) and preferred orientation should be avoided. After collection of diffraction pattern the ‘ d ’ values can be calculated by Bragg’s law using ‘ 2θ ’ values and the intensities can be converted into relative intensities by the formula $I/I_{max} \times 100$, where I_{max} is intensity of the strongest reflection in the pattern. After having the data for unknown phase one can proceed to match the ‘ d ’ value of the strongest reflection in the experimental pattern available in the database. After proper matching of the first ‘ d ’ value of the most intense peak, the second and third intense reflections are matched to the closest ‘ d ’ values. After good agreement in these matching the proper PDF card number is located and the ‘ d ’ values and relative intensities of the remaining reflection are matched. After getting the full agreement, identification of the compound is completed.

1.4.2.2 Quantitative phase analysis

Quantitative phase analysis is used to determine the concentration of different phases that are present in a mixture. Before carrying out the quantitative analysis of various phases present in the mixture, it is important to know qualitatively the phases that are present in the mixture (qualitative phase analysis). The intensity of characteristic diffraction peak of a phase is proportional to its weight fraction in a multicomponent mixture [41]. This forms the basis for quantitative phase analyses of crystalline components in mixture of different phases. The relation between intensity and concentration is not linear in many cases. This is because of the absorption

coefficient of mixture; preferred orientation and extinction effect (back scattering of the diffracted rays in the crystal) varies. There are many methods, which can be used for the quantitative analysis of the different phases in the mixture *viz.*, internal standard or external standard, etc [42]. Rietveld refinement of the XRD pattern is also done for the quantification of the phases that requires the knowledge of the crystal structure of all the phases present in the mixture.

1.4.2.3 Determination of crystallinity

The powder XRD pattern of the crystalline materials shows the sharp reflections. Powder pattern of amorphous materials shows the broad background signal. Especially many polymers show semicrystalline behavior *i.e.* part of the material forms ordered crystallite by folding of the molecule. One and the same molecule may well be folded into two different crystallites and thus form a tie between the two. This part is prevented from the crystallization and hence the crystallinity of the material never reaches to 100%. Powder X-ray diffraction technique is used to determine the crystallinity of these materials by comparing the integrated intensity of the background pattern to that of the sharp peaks. The crystallinity of the materials can be calculated from the following formula:

$$\%Crystallinity = \frac{A(\text{reflection})}{A(\text{reflection} + \text{background})} \times 100$$

Where, A (reflection) is area under all the reflections and A (reflection + background) is nothing but the gross/bulk area *i.e.* area under reflections plus background area. One can compare the crystallinity that with the standard materials. The relative crystallinity of the material is calculated when the structure of material under study is disturbed by doping with other elements partially or fully. The higher crystalline material is considered as 100% crystalline and the relative crystallinity of the other materials is calculated for examining the effect of doping on crystallinity of the materials.

1.4.2.4 Crystallite size

For a polycrystalline sample consisting of sufficiently large size and strain free crystallite, X-ray diffraction should yield sharp lines. In principle, an appropriate analysis of the diffraction profile should yield such information as the mean crystalline dimension or the size of coherent crystalline domains, distribution of

crystallites sizes and the nature and extent of lattice imperfections. Crystallite size causes the peak to broaden as the size become smaller than $\sim 2000 \text{ \AA}$.

Crystallite size L (\AA) can be determined from the corrected line broadening (β) in the sample using Scherrer equation [43]:

$$L = \frac{k\lambda}{\beta \cos \theta}$$

where θ and λ have their usual meanings, L is the mean dimension of the crystallites composing the powder sample or the thickness of the crystal in a direction perpendicular to the diffracting planes, K is a constant approximately equals to 0.9 – 1.0 and related both to crystallite shape and to the way in which β and L are related. The sample is ground to 325 mesh and packed firmly into a rectangular sample holder. Instrumental broadening is determined using a highly crystalline silicon standard ($d = 3.1345 \text{ \AA}$, 111 line) assuming a Gaussian profile and β is the line width on the 2θ scale in radians corrected for instrumental broadening.

1.4.2.5 Strain analysis

Dislocations and subgrains in the crystals behave as a defect, which have the impact on powder X-ray diffraction pattern [44]. The density of the dislocations is not uniform; they tend to group themselves into walls (sub-grain boundaries) and producing strain in crystal. If there is uniform tensile strain on the grains of the crystal at right angles, their spacing becomes larger than d_0 and the position of corresponding reflection is shifted to lower 2θ region in the diffraction pattern. This shift in line position is used for calculations of macrostress. For the grain where there is non-uniform strain is present, for one portion the plane spacing exceeds the d_0 , while for the other portion the plane spacing is less than d_0 and somewhere in between it equals to d_0 . Hence it is thought that the grain is composed of a number of small regions in each of which the plane spacing is substantially constant but different from the spacing in adjoining regions. These regions cause the various sharp diffraction lines. The sum of these lines is nothing but the broadened peak, which is experimentally observed. The following relation between the broadening and the non-uniformity of the strain is established after differentiating the Bragg's law:

$$b = \Delta 2\theta = -2 \frac{\Delta d}{d} \tan \theta$$

where, b is the extra broadening, over and above the instrumental breadth of the line, due to a fractional change in Bragg plane spacing $\Delta d/d$. Hence, using above equation and from the observed broadening one can calculate the variation in strain. This value of $\Delta d/d$ includes both tensile and compressive microstrain. The value of tensile or compressive strain alone is obtained by dividing two to the strain $\Delta d/d$.

1.4.2.6 Lattice parameters or unit cell dimensions

The unit cell is the basic building block of a crystal, repeated infinitely in three dimensions. It is characterised by three vectors (a , b , c) that form the edges of a parallelepiped and the angles between the vectors (α , the angle between b and c ; β , the angle between a and c ; γ , the angle between a and b). The lengths are measured from one corner of the cell, which is taken as origin. These lengths and angles are called as the lattice parameters of the unit cell. These lattice parameters are used to calculate the unit cell volume of the system. The formulae for calculation of unit cell volumes for different systems are given in Table 1.2.

Table 1.2 Formulae for calculation of unit cell volumes.

System	d_{hkl}
Cubic	$V = a^3$
Tetragonal	$V = a^2 c$
Orthorhombic	$V = abc$
Hexagonal	$V = \frac{\sqrt{3}a^2 c}{2} = 0.866a^2 c$
Monoclinic	$V = abc \sin \beta$
Triclinic	$V = abc \sqrt{1 - \cos^2 \alpha - \cos^2 \beta - \cos^2 \gamma + 2 \cos \alpha \cos \beta \cos \gamma}$

The unit cell parameters of a polycrystalline powder are determined from a powder XRD scan for both known and unknown structures [41]. For known structures, the peak positions of the sample are matched with the reflections of known structure and a least square fitting of the peak positions is done using the respective formula for calculation of a , b and c (Table 1.3). The d values measured from the experimental sample profile are corrected with respect to internal silicon standard and the corrected d values are used for unit cell dimension calculations.

Table 1.3 Formulas for calculating interplanar spacings, d_{hkl} [41].

System	$a : b : c$	$\alpha : \beta : \gamma$	d_{hkl}
Cubic	$a=b=c$	$\alpha=\beta=\gamma=90^\circ$	$\frac{a_0}{\sqrt{h^2 + k^2 + l^2}}$
Tetragonal	$a=b \neq c$	$\alpha=\beta=\gamma=90^\circ$	$\frac{a_0}{\sqrt{h^2 + k^2 + (l/c)^2}}$
Orthorhombic	$a \neq b \neq c$	$\alpha=\beta=\gamma=90^\circ$	$\frac{b_0}{\sqrt{(h/a)^2 + k^2 + (l/c)^2}}$
Hexagonal	$a=b \neq c$	$\alpha=\beta=90^\circ,$ $\gamma=120^\circ$	$\frac{a_n}{\sqrt{(h^2 + hk + k^2) + (l/c)^2}}$
Monoclinic	$a \neq b \neq c$	$\alpha=\gamma=90^\circ,$ $\beta \neq 90^\circ$	$\frac{b_0}{\sqrt{\frac{(h/a)^2 + (l/c)^2 - \frac{2hl}{ac} \cos \beta}{\sin^2 \beta} + k^2}}$
Triclinic	$a \neq b \neq c$	$\alpha \neq \beta \neq \gamma \neq 90^\circ$	$\frac{b_n}{\sqrt{\begin{vmatrix} h/a & \cos \gamma & \cos \beta \\ k & 1 & \cos \alpha \\ l/c & \cos \alpha & 1 \end{vmatrix} + k \begin{vmatrix} 1 & h/a & \cos \beta \\ \cos \gamma & k & \cos \alpha \\ \cos \beta & l/c & 1 \end{vmatrix} + l \begin{vmatrix} 1 & \cos \gamma & \cos \beta \\ \cos \gamma & 1 & k \\ \cos \beta & \cos \alpha & l/c \end{vmatrix}}}$

The unit cell parameters are not constant and are changing with the temperature and pressure. The isomorphous substitution or doping can decrease/increase the values of the unit cell parameters depending on the ionic radii of the dopant. Precise and accurate unit cell parameters even for materials having complex diffraction patterns with severe peak overlap can be obtained by Rietveld technique.

For unknown structures, indexing of the reflections or peak positions from the XRD profile is to be done using one of the many softwares available. There are many softwares available but all of them use different algorithms and the final solutions from different indexing softwares have to be compared and suitable repeated solution is taken to identify the space group from the indexed reflections. When unit cell parameters are known it is fairly easy to index the powder pattern. But it becomes trickier and time consuming if one has to index a new, unknown and never indexed phase. The different equations used for calculation of unit cell parameters (a , b and c) from the ' d ' spacing depending upon the symmetry of the material under study are given in Table 1.3 [41].

1.4.2.7 Structure solution using powder X-ray diffraction

Crystal structure determination of the materials ranging from high temperature superconductor and fullerenes to zeolites is achieved by using powder X-ray diffraction data. The single crystal X-ray diffraction method is conventional method for structure solution. But many industrially important materials ranging from ceramics to catalysts to pharmaceuticals are in powder form and cannot be grown as single crystals. Hence the powder diffraction method of structure analysis is the only choice to gain/obtain the structural information that is the fundamental for the understanding of the properties (which are strongly depends on structures) of these materials. Lots of information is available on the structure solution from powder diffraction data, in the form of web sources including tutorials and mailing groups (sdpd) and textbooks [45].

- a) The first step, which is very important in structure determination from powder diffraction data, is the producing of high-quality polycrystalline sample (high purity and crystallinity). After that a choice of radiation is important and neutron, synchrotron and laboratory X-rays can be used as source for data

collection. Once the source of choice is selected the next step is data collection.

- b) In the data collection step one should collect the data of high-resolution by optimizing the step size, counting times and data range. The next step is indexing of diffraction pattern; care should be taken at this step because many times some programs fails to give the correct unit cell.
- c) There are many autoindexing programs available such as TREOR90 [46], DICVOL91 [47], ITO [48], etc. The full list of indexing programs is available on the Internet at <http://www.ccp14.ac.uk/solution/indexing/>. For the sake of accuracy it is important to check the results obtained by using particular software are reproducing with the other software or not and sometime it is difficult to achieve the successful results by using the particular program.
- d) After determination of the accurate unit cell, the associated space group must be determined. This is a critical task to assign a space group and it is rare to assign a space group that is correct. In many cases several space groups need to be investigated and a further reduction in the symmetry can be achieved with trial and error method. After determination of unit cell parameter and selection of space group, the reflection positions in the powder pattern can be calculated.
- e) The diffracted intensity associated with these reflections then determined by using whole-pattern-fitting technique similar as used in Rietveld refinement and this procedure is known as intensity extraction.
- f) The intensity extraction can be performed using least-square method of Pawley [49] or an iterative method of Le Bail [50]. These integrated intensities are not used in further steps but this procedure is used to establish the appropriate profile parameters for whole-profile applications.
- g) When there is strong overlapping of reflections and it is difficult to consider them independently, the method of equipartitioning (taking peak-shape function in consideration) is applied. If whole-profile fitting is applied the method of equipartition can be bypassed but when the Patterson and Direct methods applied, it is necessary to apply the equipartition method to determine the intensities of overlapping reflections.

- h) After this step whatever information we have, is nothing but the pseudo-single-crystal dataset that is list of hkl and I_{hkl} . After these steps the actual process of structure determination starts and the different methods are used.
- i) The i) adaptations of single crystal techniques, ii) direct-space methods, which uses prior chemical knowledge, and iii) hybrid approaches are the three categories of the methods applied.
- j) The final step is the completion of structure that involves finding of any missing atom by the use of Fourier mapping, resolving disorder problems.

1.5 Rietveld Refinement

In a single crystal structure refinement, the differences between the intensities measured in a diffraction experiment and those calculated from an approximate model are minimized by adjusting the atomic parameters. Since the intensities of individual reflections in a powder pattern are often obscured by overlap in 2θ , this method cannot be applied satisfactorily to powder data. In 1969, however, Hugo Rietveld developed a new whole profile fitting method for the refinement of crystal structures using neutron powder diffraction data [51, 52], and thereby revolutionized the scope of powder diffraction. He minimized the difference between the observed powder diffraction pattern and the pattern calculated from model. By refining the fit of the powder pattern rather than that of the individual reflection intensities (which would first have to be extracted from the powder pattern), he was able to circumvent the overlap problem. In the late 70's the method was adapted to accommodate the more complex peak shape inherent to X-ray powder patterns, and has since become the standard refinement method for all powder data.

In a Rietveld refinement procedure, initially a powder pattern is calculated from an approximate structural model using estimated peak shape and approximate unit cell parameters. This is compared with the experimental data and the difference between the two is calculated. This difference is then minimized by refining the profile parameters (width and asymmetry of the peaks, 2θ zero point, unit cell dimensions) and structural parameters (atomic coordinates and thermal parameters). The refinement is continued with progressively better profile and structural parameters until the difference plot approaches the statistical scatter of the data.

The fit of the observed and calculated patterns is usually quantified in terms of reliability factors (*R*-values). The weighted profile *R*-value, R_{wp} that is used as a guide to follow the Rietveld refinement, is defined as:

$$R_{wp} = \left\{ \frac{\sum w_i (y_i(obs) - y_i(calc))^2}{\sum w_i (y_i(obs))^2} \right\}^{1/2}$$

where $y_i(obs)$ is the observed intensity at step i , $y_i(calc)$ the calculated intensity, and w_i the weight. The expression in the numerator is the value that is minimized during the refinement. The final R_{wp} should approach the statistically expected *R*-value, R_{exp} , which reflects the quality of the data and is defined as

$$R_{exp} = [(N - P) / \sum w_i y_i(obs)^2]^{1/2}$$

where, N is the number of steps measured, P the number of refinable parameters (*i.e.* the number of structural parameters and the number of profile parameters), w_i the statistical weight ($w_i = 1 / y_i(obs)$) and $y_i(obs)$ the observed count rate at step i . An *R*-value based on the agreement between the individual structure factors, *F_{hkl}*, similar to that reported for single crystal refinements can also be calculated by distributing the intensities of overlapping reflections according to the model.

And the goodness of fit is given by:

$$\chi^2 = R_{wp} / R_{exp}$$

which should approach unity.

The Rietveld or the whole pattern refinement method has become recently the standard structure refinement technique for all powder data.

The following steps are involved in a structure refinement with powder data:

- 1) Collection of the powder diffraction data
- 2) Determination of the peak shape function
- 3) Evaluation of the starting values for the profile parameters
- 4) Selection of the space group/indexing of the pattern
- 5) Refinement of the profile parameters
- 6) Addition of geometric restraints
- 7) Generation of a difference electron density map
- 8) Interpretation of a difference electron density map
- 9) Repetition of steps 7 and 8 until the structure model is complete
- 10) Rietveld refinement of the structural and profile parameters.

Some sources of systematic errors in Rietveld refinement are as preferred orientation, background, profile shapes, absorption, specimen displacement, specimen transparency, 2θ zero error and instrument beam instability, etc. Generally used softwares for Rietveld refinement of the diffraction data are General Structure Analysis System (GSAS) [53], FullProf [54], X-ray Rietveld System (XRS-82) [55], Rietveld Analysis (RIETAN) [56], DBWS [57], etc. In our studies we have used GSAS for Rietveld analysis extensively, X'Pert Plus (Rietveld refinement package provided by Panalytical) is also used in some cases.

1.5.1 General Structure Analysis System (GSAS)

GSAS is a comprehensive system for the refinement of structural models to both X-ray and neutron diffraction data and it is one of the best programs available. Allen C. Larson and Robert B. Von Dreele of Los Alamos National Laboratory have created GSAS. Executable versions of GSAS are distributed more-or-less freely. It can handle powder diffraction data from a mixture of phases refining structural parameters for each phase. Up to 99 different sets of data can be modeled using mixtures of up to 9 different phases. It is a set of programs for the processing and analysis of both single crystal and powder diffraction data obtained with X-rays or neutrons. GSAS is designed to be easy to use and features a menu driven editor (EXPEDT) equipped with help listings and error trapping features. EXPEDT is used to prepare all input for the main calculation programs in GSAS. EXPGUI [58] is a graphical user interface for the Los Alamos GSAS package. EXPGUI does two things: it can be used to directly modify the GSAS experiment file with a graphical user interface (GUI) and it can be used to invoke the programs inside the GSAS package such as EXPEDT, GENLES, FOURIER. These programs can be run from a menu or in many cases by pressing buttons. GSAS provides several useful information such as, Fourier maps, difference Fourier maps, Patterson maps, difference Patterson maps, h,k,l , reflection list files, etc. GSAS offers restraints that can be included in a model. So-called "hard constraints" reduce the actual number of parameters in a model, by grouping parameters so that a single shift (possibly scaled) is applied to each parameter in the group. The reduced χ^2 or "goodness of fit" is defined in GSAS by the minimization function as:

$$\chi^2 = \frac{M}{(N_{obs} - N_{var})}$$

where, M is the minimization function, N_{obs} is the total number of observations in all histograms and N_{var} is the number of variables in the least squares refinement.

1.6 Powder X-ray diffraction in zeolite and molecular sieves

Zeolites provide a good example of the fruitful symbiosis between mineralogists, structural crystallographers, inorganic chemists and materials scientists [59-62]. Aluminosilicate continue to play an increasingly important technological role in the petroleum and petrochemical industries [63]. The properties of zeolites that are exploited in their use as catalysts, as sorbents or as ion-exchangers each reflect particular structural characteristics [64]. A detailed knowledge of structure is therefore a prerequisite for understanding zeolite performance. Zeolite structural characterization, however, is hampered by the complexity of zeolite structures, by their relatively unfavorable X-ray scattering characteristics and by their general unavailability as suitably large single crystals. In addition, problems of phase purity, homogeneity, intergrowths or stacking disorder are relatively common, preventing the application of traditional methods for structure elucidation. In such cases, a combination of techniques, such as powder X-ray diffraction, electron microscopy, high-resolution solid state NMR, computer simulation and model building is commonly used to obtain structural information [65-67]. The crystal structures of a number of zeolitic materials have been solved and refined directly from powder diffraction data, leading to structural knowledge of several new materials and new zeolite structure types [68].

Information about the location of the catalytically active centers (T sites) and their distribution over different possible crystallographic positions has a great importance in understanding the catalytic processes deeper. Detail information about the system at the microscopic level can be obtained from Rietveld analysis method. Comparison of the structural results with the experimental data permits the verification of the structural model, and if the model appears to be valid, an interpretation of the experimental data can be provided. Availability of large number of softwares made the powder XRD an important technique in the zeolite field. DIFFaX (Diffracted Intensities From Faulted Crystals) [69] code is used to quantify the phases in the disordered materials such as zeolite- β , Faujasite and MEL/MFI intergrowths and then matching with the observed powder pattern [70]. In many cases it is very difficult to grow single crystal of suitable size for structure determination,

where powder XRD provides valuable information about the structures of these materials. McCusker *et al.* [71] have solved numerous structures of zeolitic materials with the help of powder X-ray diffraction data and Rietveld refinement technique. Orientation of organic molecules in the zeolitic channels is studied with the help of PXRD and Rietveld refinement, which provides valuable information about the interaction of these molecules with the zeolitic frameworks [72]. Rietveld refinement of the PXRD data has been used to locate the heteroatoms in metallosilicate molecular sieve [73, 74]. Powder XRD studies of the zeolitic materials carried out at non-ambient conditions has yielded the wealth information regarding their structures at high temperature. Phase transition of the zeolitic materials and their thermal expansion/contraction has been studied using high temperature as well as low temperature XRD technique.

1.6.1 Isomorphous substitution of 'T' atoms by heteroatoms

Isomorphous substitution of T element in a silicalite molecular sieve leads to the modification of its acidic or redox properties and hence to tailoring of its catalytic and shape selective properties. Powder X-ray profiles of silicalite-1 (all silica polymorph) prepared by various research workers, during their preparation of molecular sieves by isomorphously substituting the T element by tin, zirconium, vanadium, chromium, molybdenum, differ in their crystallinity (80-95%) and their unit cell volume values [43]. Whenever a metal ion is being substituted, a metal free all silica polymorph should also be prepared for deciphering the unit cell expansion/contraction. Increase or decrease in the unit cell volume of the substituted structures with respect to the corresponding silica polymorph is a clear indication of the presence of metal atom in the framework. The extent of this change in unit cell volume depends on the size (ionic radii) of the incorporated metal (T) atom and the corresponding T-O bond distance. Depending on the ionic radii of the substituting atom, the unit cell expands (ionic radii > Si) or contracts (ionic radii < Si) than silicon. The 2θ position of the reflections in the XRD pattern shifts to the higher angle when there is contraction and to the lower angle when there is expansion of unit cell. The maximum concentration of titanium that can be incorporated at the framework position of TS-1 for example is only 2.4 Ti atoms per unit cell [75]. The higher concentration of titanium incorporation by other workers [76] may leads to the

presence of extra-framework metal atoms in the structure. As the ionic radii of the metal atom increases, the concentration of the substituted metal atom in the framework decreases. The variations in the unit cell volume obtained by various workers is an indication to the inherent problems in synthesizing zeolites and molecular sieves with repeatable metal substitution in the framework.

Notari [77] has derived an equation to calculate the changes in the unit cell volume on isomorphous substitution of Si^{4+} with bigger Ti^{4+} ions, with respect to pure silicalite which is given below.

The equation is:

$$V_x = V_{\text{Si}} - V_{\text{Si}} (1 - d_M^3 / d_{\text{Si}}^3) x$$

Where V_{Si} is the unit cell volume of pure silicalite, d_M^3 and d_{Si}^3 are the tetrahedral T-O bond distances for the substituted tetravalent metal and silicon atoms, mostly reported in the crystal chemistry of these elements and $x = M/(\text{Si}+M)$, output atomic ratios of the sample obtained by chemical analysis (AAS/ICP).

1.6.2 Location of the isomorphously substituted heteroatoms (T sites) in the framework

The substitution of Si by heteroatoms (Ti, Fe, Zr, etc.,) modifies the acidic properties of the molecular sieves and hence the location of the substituted atom in the framework is important to correlate the changes that are seen in the catalytic data by the modification. Numerous efforts have been made for location of hetero T atoms in the framework by using molecular dynamic studies and synchrotron or laboratory powder X-ray diffraction. By the computational methods Oumi *et al.* [78] reported T8 as preferential substitution tetrahedral sites for Ti, whereas Njo *et al.* [79] reported T2 and T12, which are different. The quantum mechanical calculations of Jentys and Catlow [80] and Millini *et al.* [74], supports the experimental results from the PXRD data at room temperature reported by Lamberti *et al.* [73] that Ti is homogeneously distributed on the MFI framework or may be slightly partitioned on different sites in different samples.

The location of heteroatoms in the framework is carried out with the help of Rietveld refinement of powder X-ray diffraction pattern. Different strategies are used in the refinement of the occupancies of the heteroatoms M and Si in the 12 T sites of the framework. These strategies employed in literature [73] are a) occupancy of both

M and Si are equally distributed (0.5 Si and 0.5 M) in all tetrahedral sites, b) simultaneous refinement of the T and Si proportion ($T + Si = 1.0$) in all tetrahedral sites, with the total T content of the sample constrained to the value measured by chemical analysis and c) refinement of T and Si content ($T + Si = 1.0$) of individual T sites one at the time, with no chemical constraints. The test performed in literature [74], clearly indicate that the refinement strategy does not substantially influence the final results.

1.6.3 Location/orientation of organic molecules in the zeolite channel

The location of adsorbed molecules within the pore systems of zeolites is of importance in understanding sorbate-sorbate and sorbate-zeolite interactions that ultimately influence the catalytic, adsorptive and transport properties of the system. Because of the general difficulty in obtaining single crystals of zeolites, powder diffraction techniques are frequently used to locate sorbate molecules in zeolite frameworks. The locations of adsorbed organic molecules as well as metal ions can be obtained from Rietveld refinement of powder diffraction data. Furthermore, information about structural changes in the zeolite framework as a function of the adsorption characteristics can also be obtained. Successful studies on location of adsorbed organic molecules such as benzene, cyclohexane and xylene isomers within high-symmetry zeolite frameworks such as faujasite, [72, 81] as well as more complex frameworks such as ZSM-5 [82, 83] are reported in literature. Nair *et al.* [84] have reported the location of ortho- and meta-Xylene in silicalite-1 framework using powder X-ray diffraction recently.

1.7 Non-ambient *in-situ* X-ray diffraction analysis

The far more important and interesting aspect of the XRD technique is the correlation of structural features with physical properties. This can include optical, magnetic and conductive effects as well as the structural behavior under external stimulus or in different chemical environments. The resulting knowledge increases our understanding of the complex, underlying processes, ultimately aiding the design of new materials in which the desired chemical or physical properties are enhanced. From this point of view, the control of the external environment of the sample during data collection is important and one of the most basic environmental variables that can be tuned to the user's requirements is the temperature of material under study.

Altering the temperature of a material will change its behavior and therefore, its chemical and physical properties in a number of ways. The study of the structure–property relationship in the solid state is a preliminary step in the design of new materials with physical properties that fulfill industrial requirements.

In this regard, the high/low temperature and high/low pressure studies of powder sample are relatively faster since the time of exposure required for data collection is very small. The kinetics of the reactions [85], phase transformations [86], can be studied very easily and routinely due to the very small time required for data collection. X-ray diffraction (XRD) at non-ambient conditions can be used for a variety of applications that needed to be investigated *in-situ*. Examples of such processes are the reactions involving the solid-state phase transitions, crystallite growth, thermal expansion, etc. High temperature X-ray diffraction technique can be used as a complementary technique to thermogravimetry (TG) and differential scanning calorimetry (DSC), in calculating the activation energy and know the kinetics of the reaction.

1.7.1 High temperature X-ray diffraction (HTXRD)

High temperature X-ray diffraction is the technique where sample temperature is maintained to the desired value and diffraction pattern is collected at that temperature. Time resolved and/or temperature resolved changes in structure could be gained by this technique. Isothermal and non-isothermal kinetics of the process can be studied by using this technique. Different types of heating chambers are available in high temperature XRD instruments. Platinum plate, heating furnace and hot air gun are the three ways of heating the sample in HTXRD technique. The high temperature X-ray diffraction technique is widely used in materials science, geosciences, thin film technology and catalysis to study the kinetics of synthesis, phase transition, desorption and decomposition reactions. Some of the applications of HTXRD in general are discussed below.

HTK 16 High-Temperature Camera

The HTK 16 high-temperature chamber is used for X-ray studies with direct sample heating. Temperature range one can study is from ambient to 1600 °C (HTK 16). The temperature of the heating filament is controlled by the TCU 2000 Temperature Control Unit. Investigations can be carried out in vacuum or various

gases depending on the experiment and the used heating filament (Pt, Ta, W, C or others on request). The thermal elongation of the metal heating filaments is compensated by a precise linear stage, which guarantees a high position stability of the filament over the whole temperature range. Integrated alignment slits allow exact positioning even at high temperatures. Two thermocouples are available for temperature control and sample temperature measurement. The new graphite-heating filament with inert sample support platelets offers the advantages of better temperature homogeneity in the sample and a higher chemical resistance. The front cover of the chamber has a bayonet catch and can be quickly removed for sample exchange. Prior to applying any sample, a soft cloth and a suitable solvent, were used, if required to remove residues of previous samples. The sample is applied by the use of a spatula to press the powder into the groove of the sample holder. The powder's surface is subsequently smoothed by means of a glass platelet. If it is needed the powder is mixed with a small quantity of diluted Zapon lacquer solution to avoid the sample from falling off of the groove. The design of the Anton-Parr HTK 16 high-temperature chamber is shown in the Figure 1.6 The HTK 16 is a well-proven instrument for many applications such as structure analysis, mineralogical studies, and investigations of chemical reactions.

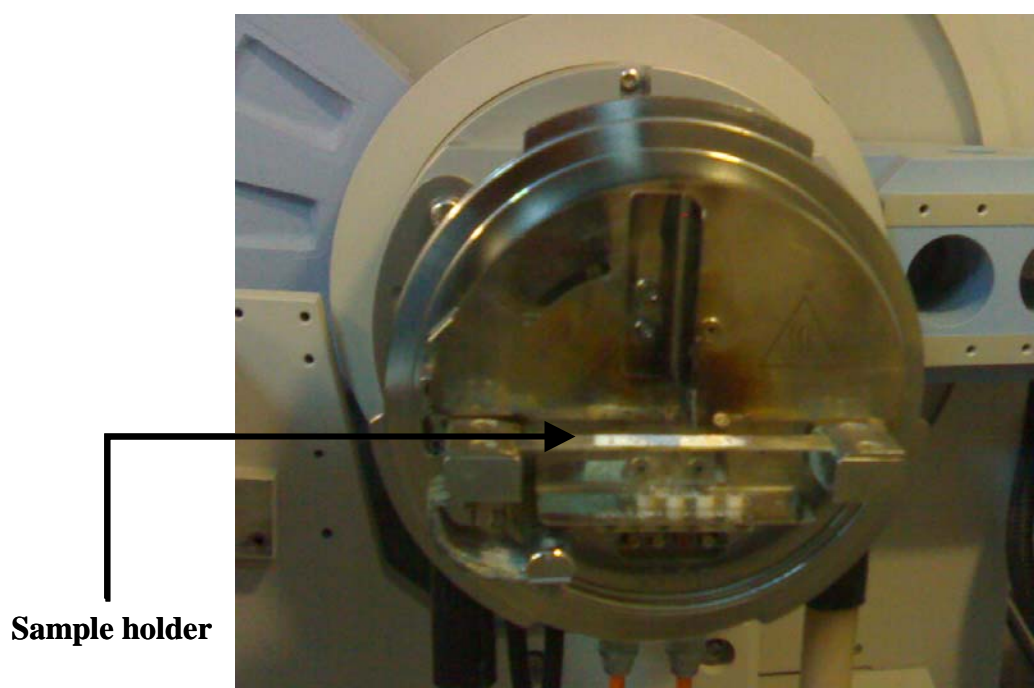


Fig. 1.6 The Anton-Parr HTK 16 high-temperature chamber.

1.7.1.1 Reaction Kinetics

Time-resolved, *in-situ* powder diffraction experiments can provide unique insights regarding the mechanisms and kinetics of the chemical synthesis. The technique eliminates the need for quenching and work-up, during which the sample may undergo significant and indeterminable structural changes. Secondly, it allows the direct observation of crystalline intermediate phases and their subsequent transformation into the product phase. Finally, *in-situ* experiments provide an easy method for determining the effect of changing reaction variables and allow one to monitor the interconversion of different phases as conditions are varied. Number of important solid state reactions including intercalation, molten flux, and hydrothermal syntheses have been described in literature by the use of *in-situ* X-ray diffraction data collected using energy dispersive powder diffraction techniques. A real-time *in-situ* energy dispersive X-ray powder diffraction technique is reported to monitor the intercalation of a guest species into a solid host and the time dependence of the extent of reaction [87]. *In-situ* X-ray diffraction allows the observation of the growth and decay of individual phases in complex reactions as demonstrated by Gross *et al.* [88] for a deeper understanding of the hydrogen desorption behavior of hydrogen rich materials. *In-situ* high temperature X-ray diffraction can help to study the reaction kinetics for the formation of thin films from a stacked bilayer precursor [89]. The mass fractions of the reacting phases were determined by comparing the integrated intensities of selected reflections collected for the minimum possible time during the reaction with that of the end of the reaction. In these studies the phase abundances were quantified via Rietveld refinement of the powder XRD data collected at room temperature taken after the completion of the reactions [90].

1.7.1.2 Phase Transition

A process by which a systems changes from one state to another state with different properties, as a result of changes in temperature or pressure is called as phase transition. High temperature XRD is used widely in the phase transition studies. The monoclinic to orthorhombic phase transition in zeolite ZSM-5 is studied with the help of HTXRD technique [19]. The phase transitions studies are very important where the technologically important properties of the materials are totally dependent on the structures of those materials *viz.*, conductive and magnetic properties.

1.7.1.3 Thermal Expansion Coefficients of materials

During heat transfer, the energy that is stored in the intermolecular bonds between atoms changes. When the stored energy increases, the length of the molecular bond also increases. As a result, solids typically expand in response to heating and contract on cooling; this response to temperature change is expressed as its coefficient of thermal expansion (α):

$$\alpha = \frac{dl}{l \times dT}$$

where, ' l ' is length at initial temperature and ' dl ' is the difference between initial length and the length at final temperature and ' dT ' is the temperature difference. The linear thermal expansion coefficient relates to the change in temperature with the change in the linear dimension of the material. It is the fractional change in length per degree of temperature change. It is a necessary parameter for solving many materials science problems and is critical for understanding the nature of residual stress in materials. Thermal expansion has been related to other thermodynamic parameters through Grüneisen rules [91]. It is a factor in the equations describing many important properties of solids. The expansion and contraction of material must be considered when designing large structures, when using tape or chain to measure distances for land surveys, when designing molds for casting hot material, and in other engineering applications when large changes in dimension due to temperature are expected.

Thermal expansion is also used in mechanical applications to fit parts over one another, e.g. a bushing can be fitted over a shaft by making its inner diameter slightly smaller than the diameter of the shaft, then heating it until it fits over the shaft, and allowing it to cool after it has been pushed over the shaft, thus achieving a 'shrink fit'. There exist some alloys with very small coefficients of thermal expansion (CTE), used in applications that demand very small changes in physical dimension over a range of temperatures. One of these is Invar 36 (FeNi alloy having Ni 36%), with a coefficient in the 0.6×10^{-6} range. These alloys are useful in aerospace applications where wide temperature swings may occur. The thermal expansion coefficient is also important in studying the materials, which are contracting on heating. Research on these materials will help to make the materials with zero thermal expansion (ZTE), which are having wide range of applications.

1.7.2 Low temperature X-ray diffraction

In low temperature XRD instruments, liquid nitrogen is passed in a controlled manner through the sample holder to provide the cooling atmosphere. The Pirani gauge head at the front measures the pressure. Samples may be examined from ca. 723 K to 80 K under vacuum, or in a controlled relative humidity atmosphere. Low temperature XRD is employed to follow changes in the unit cell dimensions at low temperature, and observe structural changes occurring at phase transition as a function of temperature and also the relative humidity changes. The low temperature XRD helps in the determination of accurate structure by freezing the thermal motion of the atom in structure thereby allowing the proper refinement of the structural coordinates (especially thermal parameters). The availability of low temperature XRD facilities has increased recently as a result of a great number of varieties of currently marketed cooling devices. It is generally accepted that the structural information obtained by the low temperature XRD is of better quality than that obtained at room temperature because of the control of the thermal motion.

The correlations between structure and properties are well demonstrated by a wide variety of applications of low temperature XRD. Lowering the temperature of the experiment (298-80 K) enables the collection of more valuable data by increasing the intensity of reflections. Thus the peak intensity to background ratio is also improved. The atomic electron densities are better located in Fourier maps, because of the presence of higher order data and because they are confined to a smaller volume due to the reduction in the thermal motion. In this way, estimated standard deviations of the atomic coordinates will be lowered and more accurate bond lengths and angles can be derived. It is also evident that less thermal motion leads to less smearing of the electron density, lowering the temperature will improve the chances of locating and properly characterizing smaller features of the electron density. For example, it will increase the chances of locating and refining the positions of hydrogen atoms, which have only one electron contributing to the scattering of X-rays. Moreover, as a consequence of the increase in intensity, lowering the temperature of the XRD experiment will also allow the study of samples that at room temperature do not diffract X-rays strongly enough to be measured. In this way, reliable atomic positions can be obtained from samples that diffract too weakly, due to crystal size or dynamic disorder. Some of the studies which one can carry out with these techniques are discussed below.

TTK 450 Low-Temperature Camera

The TTK 450 Low-Temperature Camera (Figure 1.7), mounted on goniometer, permits temperature studies to be made by X-ray methods at temperatures from approximately -193 to 450°C. To ensure reliable operation of the TTK 450, the following accessory parts are required: TCU 100 Temperature Control Unit, Flow Controller, Vacuum Equipment, Appropriate adapter for the goniometer, with or without alignment stage as shown in Figure 1.8. For low-temperature operation, the accessory parts required are: Liquid Nitrogen Controller (LNC), Low-Temperature Equipment and liquid nitrogen (LN₂) Dewar. The TTK 450 allows one to run measurements under various atmospheric conditions (air, vacuum, inert gas) at different temperatures (full temperature range is from -193°C to 450°C). The camera is always operated with the cooling-water cycle on. This is absolutely necessary to avoid the effect of working temperature to the goniometer, freezing of camera and goniometer axis, and freezing of residual water contained in the bottom, which may cause damage of the camera. To ensure uniform temperature distribution within the camera, the TTK 450 cover is used with the vacuum flange closed also when working under normal atmosphere.

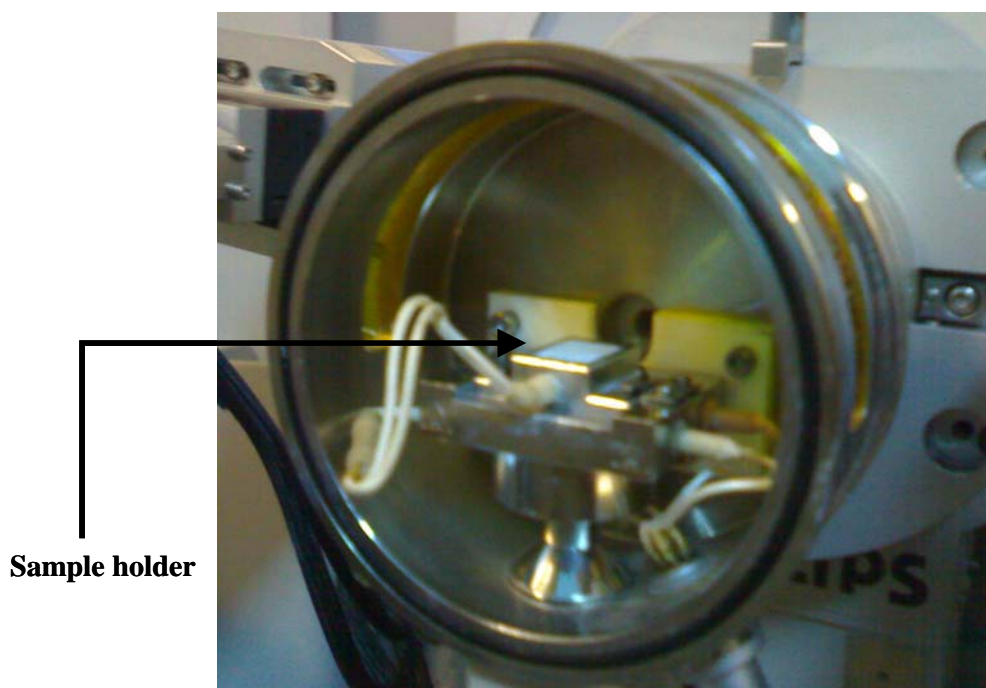


Fig. 1.7 The Anton-Parr TTK 450 high-temperature chamber.

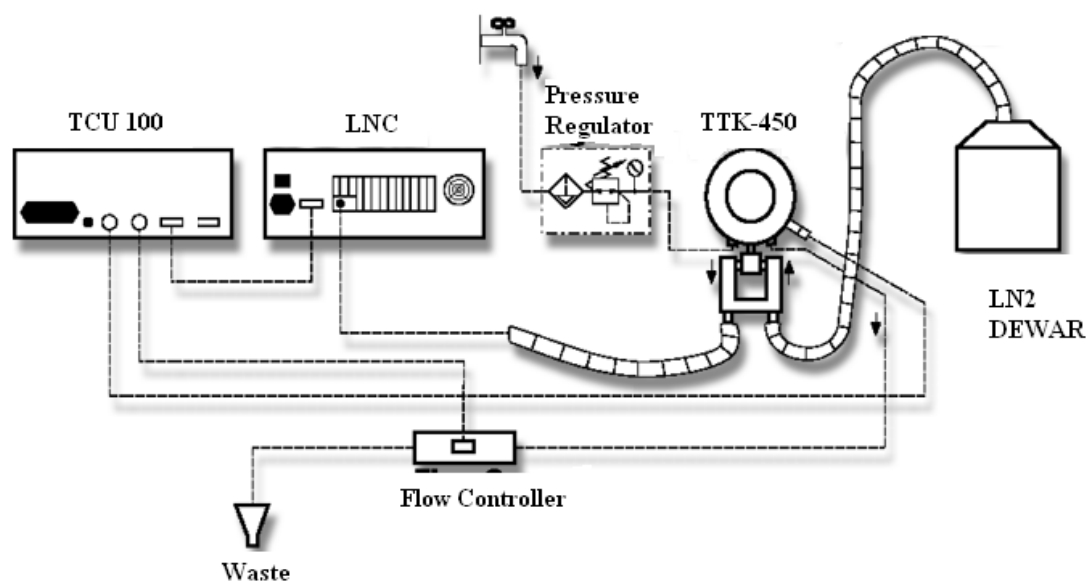


Fig. 1.8 Schematic view of the configuration of low temperature X-ray diffraction.

1.7.2.1 Study of materials, which are liquids or gases at room temperature

It is obvious that low temperature is needed in order to study materials in the crystalline state, which are either liquids or gases at room temperature. The need for structural information on these types of materials has stimulated the development of specific methods for growing crystals ‘*in-situ*’, *e.g.* in the diffraction apparatus which will be used to perform these studies [92]. The basis of the technique involves cooling a liquid or a gas inside a capillary until they solidify. This will usually produce a polycrystalline sample. Warming up slowly will eventually melt these crystallites, although not all of them will melt together. The aim is to melt all but one crystallite, which will then become the seed of a crystal of the appropriate size for the diffraction experiment. This will be obtained by slow cooling of the sample, allowing the seed to grow and avoiding sudden precipitation of multiple crystallites. However, crystallization by cooling often produces polycrystalline samples because nucleation occurs at lower temperatures than the melting point of the sample or the saturation point of the solution. In this respect, an important advance has been the use of an infrared laser for localized heating and melting of the sample in the capillary, which also avoids interference with the cold stream of gas from the low temperature device [92]. One of the advantages of growing a crystal on the diffractometer is the possibility of observing the crystallization process by diffraction.

1.7.2.2 Charge density analyses

The use and progressive improvement in the applications of low temperature XRD have been linked traditionally to experiments performed to study the distribution of electrons in a material. The aim of a typical XRD experiment is to find all atomic positions corresponding to the atoms forming a certain material, but these are obtained by considering atoms as spherical clouds of electrons. The positions of the atoms are then obtained by calculating the centroid of these electron clouds, as X-rays interact mainly with the electrons in atoms and not with nuclei. It is natural therefore, if X-rays interact with electrons, that X-ray diffraction can be used to study the distribution of electrons within a material. However, this means that a diffraction experiment carried out with this purpose must look for finer details in a structure, *i.e.* the location of individual electrons and not just the atom as positioned in the center of an electron cloud. As such, the experiment and the data thus obtained have to be of enhanced quality.

Lowering the temperature of the experiment, improves the quality of the data by reducing thermal diffuse scattering (TDS) and anharmonicity and by increasing the intensity of the reflections, thus charge density experiments are best carried out at low temperatures. The reduction of thermal motion and as a consequence the reduction in the smearing of the electron density, not only permits the identification of small features of the electron density like hydrogen atoms, but also subtle features like the presence and location of lone pairs, the electron density participating in bonding, the electron density participating in intermolecular interactions, charge transfer between molecules and many more. The high resolution XRD data collected at low temperature is least influenced by the valence electrons and contains mainly information on the core electrons and hence atomic positions and thermal displacement parameters thus obtained are more correct and are very similar to those obtained from neutron diffraction studies [93-95].

1.7.2.3 Phase transitions and thermal expansion coefficients

Low temperature crystallographic studies are essential in order to understand the reasons that a given material presents a particular chemical or physical property. Moreover, determining the crystal and molecular structures of a compound above and below a phase transition aids the understanding of the mechanisms controlling certain

phase transitions and enables the correlation of structures with chemical and physical properties. Furthermore, following the changes in the values of unit cell parameters with temperature can lead to the detection of even very subtle phase transitions associated with changes in a materials properties, *e.g.* magnetic, optical, electric and so on. Low and temperature controlled experiments enable the identification of the key elements that account for a given property, which is the first step towards the design of new materials showing enhanced properties.

Another area in which this information proves very useful is in the study of materials those expand on lowering the temperature [96]. There are a number of potential applications for this kind of material related to the possibility of producing composites that display a net zero coefficient of expansion over a wide range of temperatures, *e.g.* optical mirrors, fiber optics, cookware and also of manufacturing materials with tailored expansion coefficients that match with those of another material, of importance in electronic and biomedical applications.

1.8 High/Low temperature XRD of zeolites/molecular sieve materials

Non-ambient powder X-ray diffraction has been employed to study the thermal expansion behavior of zeolites and molecular sieves both at low temperatures as well as high temperature. Tschaufeser and Parker [97] have reported the prediction of thermal expansion behavior of zeolites and molecular sieves by computational methods. Most of them are showing negative thermal expansion *i.e.* the lattice contract on heating. Gale [98] and Couvest *et al.* [99] also reported similar prediction as the result of computational studies. These predictions made the study of thermal expansion behavior of zeolitic materials very crucial, as these materials can find applications in making the material of zero thermal expansion. Powder X-ray diffraction is a very important technique to extract the lattice parameters accurately as compared to the single crystal X-ray diffraction method, where the mounting of the crystal is more susceptible to changes as a function of temperature, because of the changes occurring in the mounting position during orientation of crystal. Bull *et al.* [100] observed that the lattice parameters by single crystal XRD was inferior as compared to powder XRD data.

The powder X-ray diffraction involves use of internal standards, and is therefore a much more reliable measurement. Hence the use of high temperature powder X-ray diffraction plays an important role in determining accurately the

changes in lattice parameters as a function of temperature. Thermal expansion behavior of pure silica zeolites ITQ-1, ITQ-3 and SSZ-23 [101], ITQ-4 [102], faujasite [103], ZSM-5 [104-106], $\text{AlPO}_4\text{-5}$ [104] and AlPO-17 [107] is studied by using temperature variable powder X-ray diffraction technique. Rietveld refinement of the powder pattern collected at elevated temperature helps in refining the positional coordinates and the thermal parameters.

1.9 Other analytical tools used for the characterization of metallosilicate molecular sieves

Physico-chemical characterization techniques *viz.*, X-ray diffraction (XRD), Infrared (IR) and diffuse reflectance Ultraviolet-visible (DRUV-vis) spectroscopic techniques and magic angle spinning-nuclear magnetic resonance (MAS-NMR) spectroscopy are used to ascertain the isomorphous substitution of the metal atoms which are modifying the acidity of the molecular sieves. In addition to these above said techniques, Mossbauer spectroscopy also have been used to obtain the structural information of the zeolites and molecular sieves. Thermogravimetric analysis (TG, DTG) techniques are used to study the thermal behavior *viz.*, template decomposition and dehydration of zeolites and molecular sieves.

1.9.1 Thermal Analysis (TG/DTA)

Thermal analysis provides information on the dehydration of the as-synthesized materials and decomposition temperatures of organic additive/template molecules entrapped or occluded into the channels of zeolites and molecular sieves structure. Thermo analytical data obtained from TGA, DTA and DTG studies are useful in evaluating the thermal properties of zeolites and molecular sieves [108]. The shape and splitting of endotherms (low temperature) helps to identify location of water molecules and also helps in studying kinetics of dehydration of water molecules. TG studies are used to study the thermal stability of the zeolites and molecular sieves and effect of the increasing silica to alumina ratio on the thermal stability [109, 110].

1.9.2 Diffuse reflectance UV-visible spectroscopy (DRUV-vis)

The diffuse reflectance UV-visible spectroscopy is known to be a very sensitive and useful technique for the identification of the electronic state of the metal

atom as well as ligand geometry in intrazeolite complexes. It gives information about the d-orbital splitting through d-d transitions and the ligand-metal interaction through the ligand to metal charge transfer transitions. UV-vis spectroscopy is useful in confirming the presence of metal ions in the framework structure of metallosilicates, such as titanosilicates (TS-1) and iron silicalites (FeS-1). For example, the diffuse reflectance spectrum of TS-1 showed a strong transition around 212 nm, whereas the silicalite-1 did not show any such signal [111] and pure TiO₂ (anatase) absorbs at 312 nm [112], confirming Ti in tetrahedral coordination in TS-1. Boccuti *et al.* [113] have also observed a transition around 208 nm in TS-1 and assigned to an electronic transition having charge transfer character involving Ti (IV) sites. The charge transfer probably occurs from the excitation of an oxygen 2p electron in the valence band to the empty d orbitals of titanium ions. Isomorphously substituted transition metals for Si *viz.*, Fe [22], V [27], Zr [29], Cr [114], etc. in zeolites and molecular sieves are also studied by this technique for their coordination in these structures.

1.9.3 Fourier transform Infra-red (FTIR) spectroscopy

In a FTIR instrument, the polychromatic source is modulated into an interferogram that contains the entire frequency region of the source and hence the entire IR frequency region is measured simultaneously.

IR spectroscopy technique has provided useful information regarding the structural details of zeolites. It has been used to confirm isomorphous substitution [115], crystal purity [116] and acid sites [117]. The assignments of IR region where different types of bending and stretching modes in zeolites and molecular sieves give signals are given in Table 1.4.

Table 1.4 Zeolite infrared assignments.

Internal tetrahedra:	Wavenumber, cm ⁻¹	External linkages	Wavenumber, cm ⁻¹
Asymmetric stretching	1250-950	Double ring	650-500
Symmetric stretching	720-650	Pore opening	300-420
T-O bending	420-500	Sym. stretching	750-820
		Asym. stretching	1050-1150 (sh)

Mid-infrared spectroscopy has been employed to further identify framework incorporation of other elements. The shifts in band positions of the symmetric and asymmetric vibration modes have been observed with successful incorporation of gallium, iron, boron [22] and titanium [26] into the silicate/aluminosilicate structures.

1.9.4 Nuclear magnetic resonance (NMR) spectroscopy

High-resolution solid-state NMR spectroscopy has emerged as a complementary technique to diffraction measurements for the investigation of solid-state structures, the former probing local environments and the latter long-range periodicities and orderings. Information from NMR studies has been particularly valuable for the structure determination of zeolites and molecular sieves [118, 119]. The following structural information regarding zeolites/molecular sieves we can extract from NMR spectroscopy.

- (i) Silicon and aluminium ordering.
- (ii) $n_{\text{Si}}/n_{\text{Al}}$ ratio of the zeolite.
- (iii) Identification of framework and non-framework aluminium.
- (iv) Incorporation of metal into zeolites frameworks.
- (v) Determination of acidity of hydroxyl group.

²⁹Si Magic angle spinning NMR

²⁹Si NMR spectra is useful in the direct determination of Si/Al ratio of the lattice. Also, the method has the advantage that it detects the ‘M’ atoms (isomorphously substituted heteroatoms) directly from their effect on the Si atoms in the frameworks and thus detects only the framework heteroatoms and the Si/M ratio for the framework. Silica polymorphs of the zeolite are mainly having Si(O-Si)₄ groupings and are extremely narrow. Because of the excellent resolution, these spectra can be exploited in a number of ways to obtain subtle information regarding zeolite structures not easily obtainable by other techniques. The ²⁹Si NMR is used in the phase transitions and thermal expansion behavior and crystal structural solution studies [100, 120-121].

1.10 Scope of the thesis

Powder X-ray diffraction technique at non-ambient temperature is a useful tool to follow the changes occurring in the unit cell parameters as a function of

temperature. The kinetics of the reaction can also be studied at isothermal or non-isothermal conditions using this technique. Thermal stability of the material can be checked *in-situ* using HTXRD technique. The technique of variable temperature XRD is helpful in phase transition studies. The zeolitic materials are predicted as the materials which contracts on heating hence it is important to study these materials using high temperature XRD technique.

In recent years the study of negative thermal expansion behavior has become a topic of interest, as these materials can be used to make the materials of desired thermal expansion. Zeolites and molecular sieves show negative thermal expansion on heating. The synthesis of zeolite molecules is assisted with the help of structure directing agent called as template. It is essential to remove the template for accessing the pores of zeolites for the desired catalytic applications. It is done generally by heating the material at high temperatures called as calcinations. The isomorphous substitution of heteroatoms in the framework structure of the silica polymorph of zeolites modify the catalytic properties of these materials. Location of the heteroatom in the framework is essential to study the mechanism of catalytic reactions. Changes in temperature also alter the phase of the MFI type materials. Hence the MFI types of materials are chosen for the non-ambient powder X-ray diffraction studies.

1.11 Objectives of the present investigation

- 1) To study the thermal stability of MFI type molecular sieves *viz.*, silicalite-1, iron silicalite-1 (FeS-1), titanium silicalite-1 (TS-1) and zirconium silicalite-1 (ZrS-1) using HTXRD technique.
- 2) To study the thermal expansion behavior of silicalite-1 and to compare the observed behavior of the silicalite-1 with that of the metallosilicate molecular sieves by using HTXRD technique.
- 3) To propose the possible mechanism of negative thermal expansion in the MFI type of molecular sieves by using the Rietveld refinement procedure for determination the changes in the bond distances and bond angles.
- 4) To study the reaction kinetics of template decomposition in as synthesized silicalite-1 using two different techniques *in-situ* HTXRD and TG.
- 5) To study the phase transition in TS-1 and FeS-1 metallosilicate molecular sieves and to locate the heteroatom in the MFI framework using *in-situ* LTXRD technique and Rietveld refinement procedure.

1.12 Outline of the thesis

The thesis is divided into six chapters with proper references at the end of each chapter. The thesis describes hydrothermal synthesis of silicalite-1 and metallosilicate molecular sieves, various physicochemical characterization and powder XRD at non-ambient conditions (HTXRD and LTXRD). The thesis includes new investigations on different structural properties of the silicalite-1 and metallosilicate molecular sieves such as negative thermal expansion, kinetics of the template decomposition reaction, phase transition and location of the Fe and Ti atoms in respective silicalite samples.

Chapter 1 presents general introduction to the zeolites and MFI type molecular sieves. It also gives the details about powder X-ray diffraction technique and its application for various property studies such as determination of crystallinity, crystallite size, phase analysis, determination of unit cell parameters and structure determination are outlined briefly. Rietveld refinement technique is outlined in this chapter with its principle and various parameters that can be monitored during the Rietveld analysis and also the information about GSAS (General Structure Analysis System) software used for Rietveld refinement is described briefly. This chapter also describes the applications of powder X-ray diffraction technique for the characterization of zeolite molecular sieves and summarizes the available literature on it. The *in-situ* powder X-ray diffraction technique at high temperature and low temperature is discussed with its applications. Other analytical tools used for the characterization of metallosilicate molecular sieves such as UV-vis, FTIR and MAS-NMR spectroscopy are described in brief.

Chapter 2 describes the hydrothermal synthesis of metallosilicate molecular sieves with different Si/M (M=Fe, Ti and Zr) ratio in synthesis gel. Detailed experimental procedures on various physical and spectroscopic techniques, *viz.*, powder XRD, SEM, EDAX, FTIR, UV-vis, TGA and NMR involved in the characterization of the metallosilicate molecular sieves are illustrated in this chapter. Results of the Rietveld refinement of powder patterns are presented in this chapter, which show the expansion in unit cell parameters as a result of isomorphous substitution of Si by Fe, Ti and Zr.

Chapter 3 describes an *in-situ* HTXRD studies on silicalite-1 and metallosilicate molecular sieves (FeS-1, TS-1 and ZrS-1) with MFI structure (Si/M = 50) to study the thermal stability and thermal expansion behavior as a function of temperature. The results of the thermal stabilities are discussed and compared with the

theoretical studies in literature. We have made an attempt to study the structural changes that occur in silicalite-1 as a function of temperature. The chapter also describes the HTXRD studies carried out on the metallosilicate molecular sieves TS-1, Fe-silicalite-1 and ZrS-1 of different Si/M ratio.

Chapter 4 describes the non-isothermal kinetic studies of the decomposition of the tetrapropylammonium cations (TPA^+) intercalated in silicalite-1 framework using HTXRD technique and the results are correlated with the thermogravimetric studies. The kinetic analysis is carried out using the plots of conversion factors (α) versus temperature. Apparent activation energy of template decomposition is measured without any prior knowledge of the reaction mechanism using Kissinger and Flynn-Wall-Ozawa methods. The reaction order determined using the new method of Kennedy and Clark and possible explanations for the reaction kinetics are discussed.

Chapter 5 describes the investigation of the phase transition temperature for various TS-1 and FeS-1 samples to determine the effect of Si/M ratio on the phase transition (from orthorhombic to monoclinic) temperature. These metallosilicate molecular sieves show orthorhombic phase in $Pnma$ space group at room temperature whereas at low temperature the structure is transformed to monoclinic symmetry (space group $P2_1/n$). Attempts have been made to locate the heteroatoms in the silicalite framework for TS-1 and FeS-1 samples at low temperature (below room temperature and above the temperature of phase transition) by using the Rietveld refinement technique. The results of the location of heteroatoms are also discussed and compared with the results in literature.

Chapter 6 gives general summary of all the work done on the non-ambient powder XRD studies of MFI type of metallosilicate molecular sieves and describes the major findings of these studies.

1.13 References

1. B. Smit, Theo L.M. Maesen, *Nature*, 451 (2008) 671.
2. A. Corma, *Chem. Rev.*, 95 (1995) 559.
3. A. Corma, *Chem. Rev.*, 97 (1997) 2373.
4. M. J. Stephenson, S. M. Holmes, R. A. W. Dryfe, *Angew. Chem., Int. Ed.*, 44 (2005) 3075.

5. F. Ramoa Ribeiro "Proceedings of the NATO Advanced Study Institute on Zeolites: Science and Technology", Alcabideche, Portugal, 1983 p.591.
6. H. Faghihian, M. G. Maragheh A. Malikpour, *J. of Radioanal., and Nuclear Chemistry*, 254 (2002) 545.
7. H. Xiao, J. Zhang, J. Dong, M. Luo, R. Lee, V. Romero, *Opt. Lett.*, 30 (2005) 1270.
8. D. W. Breck, *J. Chem. Edn.*, 41 (1969) 41.
9. W. Lowenstein, *Am. Minerals*, 39 (1954) 92.
10. R. Szostak, *Molecular Sieves: Principles of Synthesis and Identification* (Van Nostrand Reinhold, New York, 1989) p. 3.
11. F. Liebau, *Structural Chemistry of Silicates: Structure, Bonding and Classification*, (Springer-Verlag Series, Berlin 1985).
12. C. R. A. Catlow, *Modelling of Structure and Reactivity in Zeolites* (Academic Press Limited, London, 1992).
13. E.M. Flanigen, J. M. Bennett, R. W. Grose, J. P. Cohen, R. L. M. Patton, R. Kirchner, J. V. Smith, *Nature*, 272 (1978) 512.
14. D. M. Bibby, N. B. Milestone, L. P. Aldridge, *Nature*, 280 (1979) 664.
15. www.iza-structure.org/databases/
16. G. T. Kokotailo, S. L. Lawton, G. T. Olson, W. M. Meier, *Nature*, 272 (1978) 437.
17. G.T. Olson, G.T. Kokotailo, S.L. Lawton, W.M. Meier, *J. Phys. Chem.*, 85 (1981) 2238.
18. Available from website of *International Zeolite Association* <http://www.iza-structure.org/databases/>.
19. D. G. Hay, H. Jaeger, *J. Chem. Soc., Chem. Commun.*, (1984) 1433.
20. T. R. Goldsmith, *Min. Mag.*, 29 (1952) 952.
21. K. Becker, H. John, K. Steinburg, M. Weber, K. Nestler, *Catalysis on Zeolites* (D. Kallo and Kh. M. Minachev, Eds.), *Akademia Kiado*, Budapest (1988) 515.
22. C. Naccache, Y. Ben Tarrit, *Zeolite Science and Technology*, F. R. Riberio, A. E. Rodrigues, L. D. Rollmann and E. Naccache, Eds.) *Martinus Nijhoff*, The Haque (1984) 373.
23. R. Szostak, T. L. Thomas, *J. Catal.*, 100 (1986) 555.

24. G. N. Rao, V. P. Shiralkar, A. N. Kotasthane, P. Ratnasamy, *Molecular Sieves; Synthesis of Microporous Materials*, Vol. 1, (1992) Ed. M. L. Occelli and H. E. Robson, Van Nostrand Reinhold-New York.
25. Kh. M. Minachev, V. V. Khariamov, V. I. Garanin, *Catalysis on Zeolites* (D. Kallo and Kh. M. Minachev, Eds.), *Akademia Kiado*, Budapest (1988) 489.
26. G. Perego, G. Bellusi, C. Corono, M. Taramasso, F. Buonomo, *Stud. Surf. Sci. Catal.*, 28 (1986) 129.
27. M. Taramasso, G. Perego, B. Notari, U.S. Patent No. 4,410,501, 1983.
28. M. Tielens, M. Geelen, P. A. Jacobs, *J. Catal.*, 91 (1985) 352.
29. B. Rakshe, Veda Ramaswamy, S. G. Hegde, R. Vetrivel, A. V. Ramaswamy, *Catal. Lett.*, 45 (1997) 41.
30. R. D. Shannon, *Acta. Cryst.*, A 32 (1976) 751.
31. R. Fricke, H. Kosslick, G. Lischke, M. Richter, *Chem. Rev.*, 100 (2000) 2303.
32. A. Hagen, E. Schneider, A. Kleinert, F. Roessner, *J. Catal.*, 222 (2004) 227.
33. A. Hagen, E. Schneider, M. Bentner, A. Krogh, A. Kleinert, F. Roessner, *J. Catal.*, 226 (2004) 171.
34. J. P. Brunelle, *Preparation of Catalysts, II*. (B. Delmon, P. Grange, P.A. Jacobs, G. Poncelet) (Elsevier, Amsterdam, 1979) p. 211.
35. I. Wang, C. L. Ay, B. J. Lee, M. H. Chen, *Proc. Of 9th Inter. Congr. Catal.* (Eds. Chem. Inst., Canada, 1988) p. 324.
36. W. L. Bragg, '*Proceedings of the Cambridge Philosophical Society*', 17 (1914) 43.
37. P. P. Ewald, ed. '*Fifty years of X-Ray Diffraction*', (Utrecht: International Union of Crystallography, 1962) see pp. 31-56 and 293-294 for accounts of the Von Laue experiments.
38. P. Debye, P. Scherrer, *Z. Phys.*, 17 (1916) 277.
39. F. H. Chung, D. K. Smith, '*Industrial Applications of X-ray Diffraction*' CRC Press, 2000.
40. V. K. Pecharsky, P. Y. Zavalij '*Fundamentals of powder diffraction and structural characterization of materials*' (2003) Kluwer academic publishers.
41. H. P. Klug, L. E. Alexander, *X-Ray Diffraction Procedures: For*

- Polycrystalline and Amorphous Materials*, (1974) p. 618 John Wiley and Sons, New York.
42. D. L. Bish, J. E. Post (Eds.) *Modern Powder Diffraction*, Mineralogical Society of America, Washington, 1989.
 43. Veda Ramaswamy, *Catalysis; Principles and Applications*, (2002) pp.95, Ed., B. Viswanathan, S. Sivasanker, A. V. Ramaswamy, Narosa Publishing house, New Delhi.
 44. B. D. Cullity, S. R. Stock, '*Elements of X-ray Diffraction*' (2001) third edition, Prentice Hall.
 45. W. I. F. David, K. Shankland, L. B. McCusker, C. Baerlocher '*Structure Determination From Powder Diffraction Data*' 2002 p.49, Oxford science publications.
 46. P. E. Werner, L. Eriksson, M. Westdahl, *J. Appl. Cryst.*, 18 (1985) 367.
 47. A. Boultif, D. Louer, *J. Appl. Cryst.*, 24 (1991) 987.
 48. J. Visser, *J. Appl. Cryst.*, 2 (1969) 89.
 49. G. S. Pawley, *J. Appl. Cryst.*, 14 (1981) 357.
 50. A. Le Bail, H. Duroy and J.L. Fourquet, *Mater. Res. Bull.* 23 (1988) 447.
 51. H. M. Rietveld, *Acta. Crystallogr.*, 22 (1967) 151.
 52. H. M. Rietveld, *J. Appl. Cryst.*, 2 (1969) 65.
 53. A. C. Larson, R. B. Von Dreele, "*General Structure Analysis System (GSAS)*", Los Alamos National Laboratory Report LAUR 86-748 (2000).
 54. J. Rodriguez-Carvajal, *Commission on Powder Diffraction (IUCr). Newsletter*, 26 (2001) 12.
 55. Ch. Baerlocher, (in collaboration with A. Hepp and L.B. McCusker), *The X-ray Rietveld System (XRS-82)*, a set of computer programs for the Rietveld refinement of X-ray powder data, Institut für Kristallographie, ETH, Zürich, 1982.
 56. F. Izumi, T. Ikeda, *J. Crystallogr. Soc. Jpn.*, 42 (2000) 516.
 57. L. Bleicher, J. M. Sasaki, C. O. P. Santos, *J. Appl. Cryst.*, 33 (2000) 1189.
 58. B. H. Toby, *EXPGUI*, a graphical user interface for *GSAS*, *J. Appl. Cryst.*, 34, (2001) 210.
 59. D. L. Bish, D. W. Ming, *Natural Zeolites: Occurrence, Properties, Applications*, Vol. 45. 2001.

60. Ch. Baerlocher, *Zeolites*, 6 (1986) 325.
61. S. Inagaki, T. Yokoi, Y. Kubota, T. Tatsumi, *Chem. Commun.*, (2007) DOI: 10.1039/b713466e.
62. I. Diaz, M. Hernandez-velez, R. J. Martin Palma, H. V. Garcia, J. P. Pariente, J. M. Martinez-Duart, *Applied Physics A*, 79 (2004) 565.
63. D. J. O'Rear, J. F. Mayer, U.S. Patent, 4171257.
64. J. Dwyer, A. Dyer, *Zeolites for Industry*, Papers presented at a symposium organized by the Solvent Extraction and Ion Exchange Group of the SCI and the British Zeolites Association, held in Manchester from 3-5 April 1984.
65. J. M. Thomas, D. E. W. Vaughan, *J. Phys. Chem. Solids*, 50 (1989) 449.
66. Z. A. Kaszkur, R. H. Jones, D. Waller, C. R. A. Catlow, J. M. Thomas, *J. Phys. Chem.*, 97 (1993) 426.
67. L. B. McCusker, *Stud. Surf. Sci. Catal.*, 84 (1994) 341.
68. W. M. Meier, D. H. Olson, C. Baerlocher, *Atlas of Zeolite Structure Types*, 4. Aufl., Elsevier, New York, 1996.
69. J. M. Newsam, M. M. J. Treacy, W. T. Koetsier, C. B. De Gruyter, *Proc. Royal Soc. London A*420 (1988) 375.
70. M. M. J. Treacy, *Manual of DIFFaX*, (2000).
71. L. B. McCusker, "The art of zeolite structure analysis" in Proc. 14th Intl. Zeolite Conf., E. van Steen, L. H. Callanan, M. Claeys (eds), Document Transformation Technologies, Cape Town, South Africa, 2004, pp. 42-52, and (2004) *Stud. Surf. Sci. Catal.*, 154, 41.
72. N. P. Østbo, R. Goyal, H. Jobic, A. N. Fitch, *Micropor. Mesopor. Mater.*, 30 (1999) 255.
73. C. Lamberti, S. Bordiga, A. Zecchina, A. Carati, A.N. Fitch, G. Artioli, G. Petrini, M. Salvalaggio, G.L. Marra, *J. Catal.*, 183 (1999) 222.
74. R. Millini, G. Perego, K. Seiti, *Stud. Surf. Sci. Catal.*, 84 (1994) 2123.
75. R. Millini, E. Previde Massara, G. Perego, G. Bellusi, *Zeolites*, 12 (1992) 943.
76. A. Thangaraj, M. J. Eapen, S. Sivasanker, P. Ratnasamy, *J. Catal.*, 130 (1991) 1.
77. B. Notari, *Catal. Today*, 18 (1993) 163.
78. Y. Oumi, K. Matsuba, M. Kubo, T. Inui, A. Miyamoto, *Micropor. Mater.*, 4

- (1995) 53.
79. S. L. Njo, H. van Koningsveld, B. van de Graaf, *J. Phys. Chem. B* 101 (1997) 10065.
80. A. Jentys, C. R. A. Catlow, *Catal. Lett.* 22 (1993) 251.
81. M. Czjzek, T. Vogt, H. Fuess, *Angew. Chem., Int. Ed. Engl.* 28 (1989) 770.
82. B.F. Mentzen, *J. Appl. Crystallogr.*, 21 (1988) 266.
83. H. van Koningsveld, F. Tuinstra, H. van Bekkum, J. C. Jansen, *Acta Crystallogr., B* 45 (1989) 423.
84. S. Nair, M. Tsapatsis, *J. Phys. Chem. B*, 104 (2000) 8982.
85. H. Ricardo Z. Sandim, B. V. Morante, P. A. Suzuki, *Materials Research*, 8 (2005) 293.
86. N. A. Sennova, R. S. Bubnova, S. K. Filatov, P. Paufler, D. C. Meyer, A. A. Levin, I. G. Polyakova, *Cryst. Res. Technol.*, 40 (2005) 563.
87. S. M. Clark, J. S. O. Evans, D. O'Hare, C. J. Nuttall, H. Wong, *J. Chem. Soc., Chem. Commun.*, (1994) 809.
88. K.J. Gross, S. Guthrie, S. Takara, G. Thomas, *Journal of Alloys and Compounds*, 297 (2000) 270.
89. S. Kim, W. K. Kim, R. M. Kaczynski, R. D. Acher, S. Yoon, T. J. Anderson, O. D. Crisalle, E. A. Payzant, S. S. Li, *Journal of Vacuum Science and Technology A: Vacuum, Surfaces and Films* 23 (2005) 310.
90. K.M. Forster, J.P. Formica, J.T. Richardson, D. Luss, *Journal of Solid State Chemistry*, 108 (1994) 152.
91. G.B. Mitra, S.K. Mitra, *Nature*, 179 (1957) 1295.
92. R. Boese, M. Nussbaumer, *In situ Crystallization Techniques, in Correlations, Transformations and Interactions in Organic Crystal Chemistry, IUCr Crystallographic Symposia*, ed. D. W. Jones and A. Katrusiak, Oxford University Press, Oxford, England, 1994, vol. 7, p. 20–37
93. B. N. Figgis, B. B. Iversen, F. K. Larsen, P. A. Reynolds, *Acta Crystallogr., Sect. B*, 49 (1993) 794.
94. B. B. Iversen, F. K. Larsen, B. N. Figgis, P. A. Reynolds, A. J. Schultz, *Acta Crystallogr. Sect. B*, 52 (1996) 923.
95. P. Coppens, A. Vos, *Acta Crystallogr., Sect. B*, 27 (1971) 146.
96. J. S. O. Evans, *J. Chem. Soc., Dalton Trans.*, (1999) 3317.

97. P. Tschaufeser, S. C. Parker, *J. Phys. Chem.*, 99 (1995) 10609.
98. J. D. Gale, *J. Phys. Chem. B*, 102 (1998) 5423.
99. J. W. Couvest, R. H. Jones, S. C. Parker, P. Tschaufeser, C. R. A. Catlow, *J. Phys. Condens. Matter*, 5 (1993) L329.
100. I. Bull, P. Lightfoot, L. A. Villaescusa, L. M. Bull, R. K. B. Gover, J. S. O. Evans, R. E. Morris, *J. Am. Chem. Soc.*, 125 (2003) 4342.
101. D. A. Woodcock, P. Lightfoot, P. A. Wright, L. A. Villaescusa, M.J. Díaz-Cabañas, M. A. Cambor, *J. Mater. Chem.*, 9 (1999) 349.
102. D. A. Woodcock, P. Lightfoot, L. A. Villaescusa, M.J. Díaz-Cabañas M. A. Cambor, D. Engberg, *Chem. Mater.*, 11 (1999) 2508.
103. M. P. Attfield, A. W. Sleight, *J.C.S., Chem. Commun.*, 5 (1998) 601.
104. S.H. Park, R.W. Grosse Kunstleve, H. Graetsch, H. Gies, *Stud. Surf. Sci. Catal.*, 105 (1997) 1989.
105. B. A. Marinkovic, P. M. Jardim, A. Saavedra, L. Y. Lau, C. Baehtz, R. R. de Avillez, F. Rizzo, *Micropor. Mesopor. Mater.*, 71 (2004) 117.
106. P. M. Jardim, B. A. Marinkovic, A. Saavedra, L. Y. Lau, C. Baehtz, F. Rizzo, *Micropor. Mesopor. Mater.*, 76 (2004) 23.
107. M. P. Attfield, A. W. Sleight, *Chem. Mater.*, 1 (1998) 2013.
108. R. M. Barrer, D. A. Langley, *J. Chem. Soc.*, (1958) 3804.
109. J. A. Rabo, *Zeolite Chemistry and Catalysis*, Eds. Beringer, F. M., Am. Chem. Soc. Washington D.C., (1976) p. 285.
110. H. Bremer, W. Marke, R. Schodel, F. Vogt, *Adv. Chem. Ser.*, 121 (1973) 249.
111. A. Thangaraj, R. Kumar, S. P. Mirajkar, P. Ratnasamy, *J. Catal.*, 130 (1991) 1.
112. R. J. H. Clark, "Chemistry of Titanium and Vanadium", Elsevier, Amsterdam, (1968) 272.
113. M. R. Boccuti, K. M. Rao, A. Zecchina, G. Leofanti, G. Petrini, "Structure and Reactivity of Surfaces", *Stud. Surf. Sci. Catal.*, 48 (1989) 133.
114. T. Selvam, M. P. Vinod, *Appl. Catal. A: General*, 134 (1996) L197.
115. H. Kosslick, V. A. Tuan, R. Fricke, Ch. Penker, W. Pilz, W. J. Storek, *Phys. Chem.*, 97 (1993) 5678.
116. P. A. Jacobs, H. K. Beyer, J. Valyon, *Zeolites*, 1 (1981) 161.

-
117. H. Karge, *Stud. Surf. Sci. Catal.*, 65 (1991) 133.
 118. A.T. Bell and A. Pines, “*NMR Techniques in Catalysis*” Heinemann eds., MarcelDekker, New York, 1994.
 119. C. A. Fyfe, H. Gies, Y. Feng, G. T. Kokotailo, *Nature*, 341 (1989) 223
 120. L. A. Villaescusa, P. Lightfoot, S. J. Teat, R. E. Morris, *J. Am. Chem. Soc.*, 123 (2001) 5453.
 121. D.H. Brouwer, P.E. Kristiansen, C.A. Fyfe, M.H. Levitt, *J. Am. Chem. Soc.*, 127 (2005) 542.

Chapter **2**

Synthesis And Characterization Of Silicalite And Metallosilicate Molecular Sieves

2.1 Introduction

In order to study the powder X-ray diffraction at non-ambient temperature for the MFI type molecular sieves, iron silicalite-1 (FeS-1), titanium silicalite-1 (TS-1) and zirconium silicalite-1 (ZrS-1) were synthesized hydrothermally and calcined at 773 K. Physicochemical characterization of these molecular sieves were done using powder XRD, IR, UV, MAS NMR, SEM-EDAX and Mössbauer spectroscopic techniques.

2.2 Hydrothermal synthesis of metallosilicate (MFI) molecular sieves

2.2.1 Iron silicalite-1 (FeS-1)

FeS-1 samples of different Si/Fe ratios (24, 36, 50, 72, 75, 100 and infinity *i.e.* silica polymorph of MFI) were synthesized by modified hydrothermal synthesis method reported elsewhere [1]. The typical synthesis of FeS-1 is outlined in Figure 2.1. In a typical synthesis of FeS-1 sample with Si/Fe=50, 50g of sodium silicate (28% SiO₂) was dissolved in 50g demineralized (DM) water (beaker-1). In a another beaker-2, 1.885g Fe(NO₃)₃.9H₂O was dissolved in a mixture 5g of DM water and 4.5g H₂SO₄. Content of beaker-2 were added to the beaker-1 slowly with continuous stirring and after complete addition, the mixture was stirred for 30 min. 6g TPAOH in 10 ml of water was added finally to the stirred mixture and resulting mixture was further stirred for 30 min. The gel so formed was allowed to crystallize in a Teflon lined autoclave for 3 days at 433 K. The solid obtained was separated, washed, dried and calcined at 823 K. The calcination was carried out for 8 h under controlled condition with a heating rate of 1K/min. (The silica polymorph of MFI structure was prepared by the same procedure without addition of iron salt.) While the as synthesized samples are designated, as SFS-24, SFS-36, SFS-50, SFS-72, SFS-75, SFS-100 and SFS-∞, corresponding calcined samples are designated as CFS-24, CFS-36, CFS-50, CFS-72, CFS-75, CFS-100 and CFS-∞. The integer shows the Si/Fe ratio of the synthesis gel.

2.2.2 Titanium silicalite-1 (TS-1)

TS-1 samples of different Si/Ti ratios (30, 50, 60, 75, 80, 100 and infinity *i.e.* silica polymorph) were synthesized by the hydrothermal synthesis method reported elsewhere [2]. A typical hydrothermal synthesis of titanium silicalite-1 with MFI structure (TS-1) was carried out using the following molar composition of the gel: 1.0

SiO_2 : x TiO_2 : 0.18 TPAOH: 17 H_2O , where $x = 0.033, 0.02, 0.0166, 0.013, 0.0125$ and 0.01 and TPAOH = tetrapropylammonium hydroxide. The typical synthesis of TS-1 is outlined in Figure 2.2. In a typical synthesis of TS-1 sample with Si/Ti=50, 25g of ethyl silicate (40% SiO_2) was taken and to this 4.2g of titaniumbutoxide was added with continuous stirring. 30.45g of TPAOH (20%) was added to this solution drop wise under stirring and stirring was further continued for 30 min. The required quantity (26.64g) of water was added at last. The gel so formed was allowed to crystallize in a Teflon lined autoclave at 433 K for 24 h. The solid obtained was separated by centrifugation, dried and calcined at 823 K. The calcination was carried out for 8h with heating rate 1K/min. (The silica polymorph of MFI structure was prepared by the same procedure without addition of titanium tetrabutoxide.) The as synthesized samples are designated, as STS-30, STS-50, STS-60, STS-75, STS-80, STS-100 and STS- ∞ and the samples designated as CTS-30, CTS-50, CTS-60, CTS-75, CTS-80, CTS-100 and CTS- ∞ are the corresponding calcined samples. The integer denotes the Si/Ti ratio in synthesis gel.

2.2.3 Zirconium silicalite-1 (ZrS-1)

Zirconium containing, Al-free medium pore molecular sieves (Si/Zr molar ratios = 50, 75 and 100) with MFI structure were synthesized in alkaline medium as per the procedure described by Rakshe *et al.* [3]. The hydrothermal synthesis of zirconium-silicates with MFI structure (ZrS-1) was carried out using the following molar composition of the gel: 1.0 SiO_2 : x ZrO_2 : 0.5 TPAOH: 30 H_2O , where $x = 0.01, 0.013$ and 0.02 and TPAOH = tetrapropylammonium hydroxide. The typical synthesis of ZrS-1 with Si/Zr = 50 is outlined in Figure 2.3. In a typical synthesis, 0.466 g of zirconium tetrachloride, ZrCl_4 (Merck, 99%) in 5 g of distilled water was added to 21.25 g of tetraethyl orthosilicate, $\text{Si}(\text{OC}_2\text{H}_5)_4$ (Aldrich, 98%) under slow stirring. After 15-20 min. of stirring, 50.84 g of tetrapropylammonium hydroxide (Aldrich, 20% aqueous) was added drop-wise. The stirring was continued for 1h. The remaining volume (8.0 g) of water was added and the resulting mixture was stirred for further 30 min. to get a homogenous clear gel (pH = 12.25) and was transferred to a stainless steel autoclave. The crystallization was conducted at 433 K for 48 h, under static condition. After the crystallization, the solid product was filtered, washed with deionized water, dried at 383 K and calcined in air at 823 K for 8 h (The silica polymorph of MFI structure was prepared by the same procedure without addition of

zirconium salt). The as synthesized samples are designated as SZS-50, SZS-75, SZS-100 and SZS- ∞ and the samples designated as CZS-50, CZS-75, CZS-100 and CZS- ∞ are the corresponding calcined samples. The integer denotes the Si/Zr ratio in synthesis gel. Samples with Si/M = ∞ (M= Fe, Ti and Zr) were prepared for each set of samples since the source of silicon was different for the three metal incorporated synthesis.

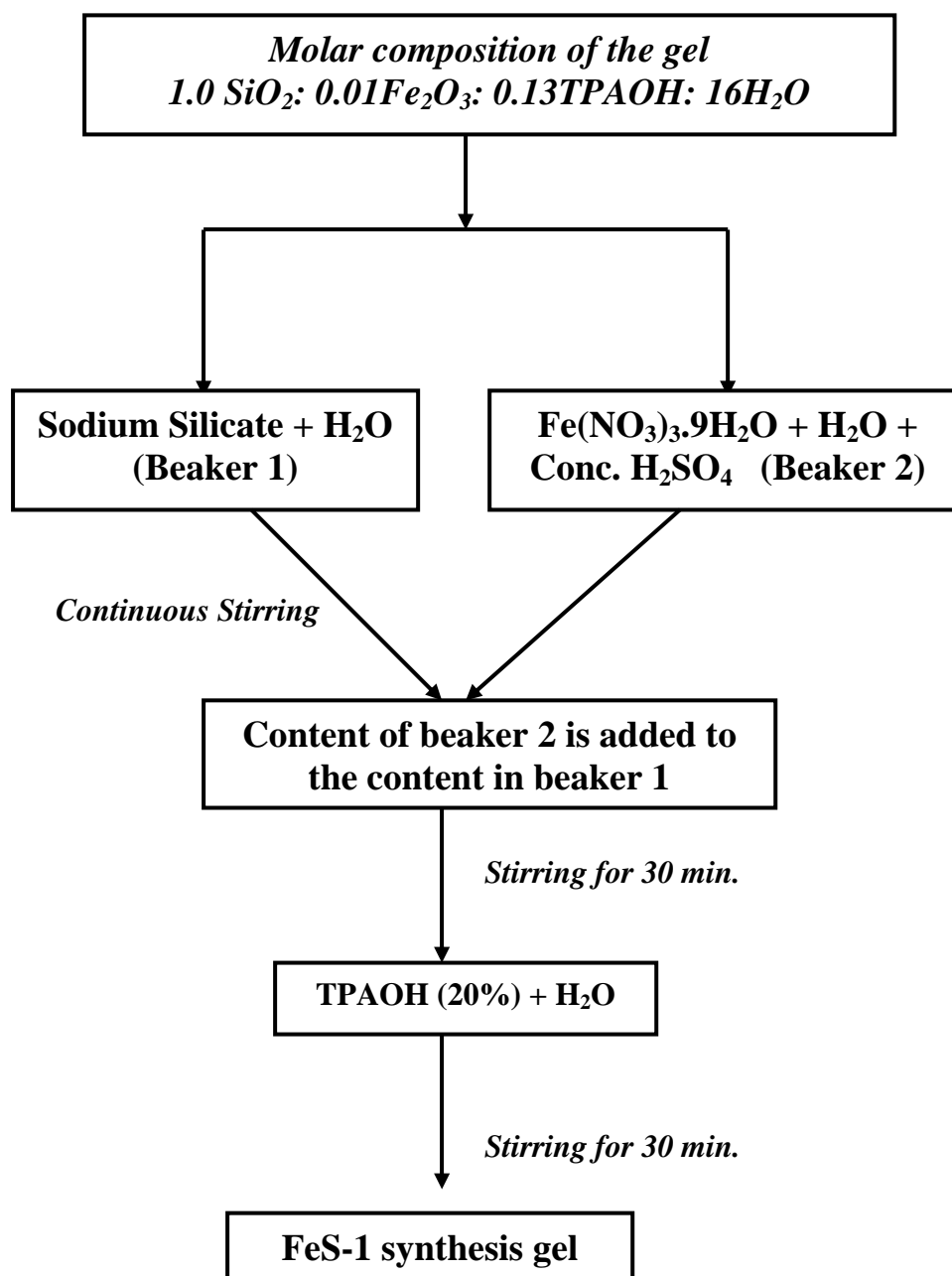


Fig. 2.1 Outline of the procedure used for synthesis gel preparation of FeS-1 (Si/Fe=50).

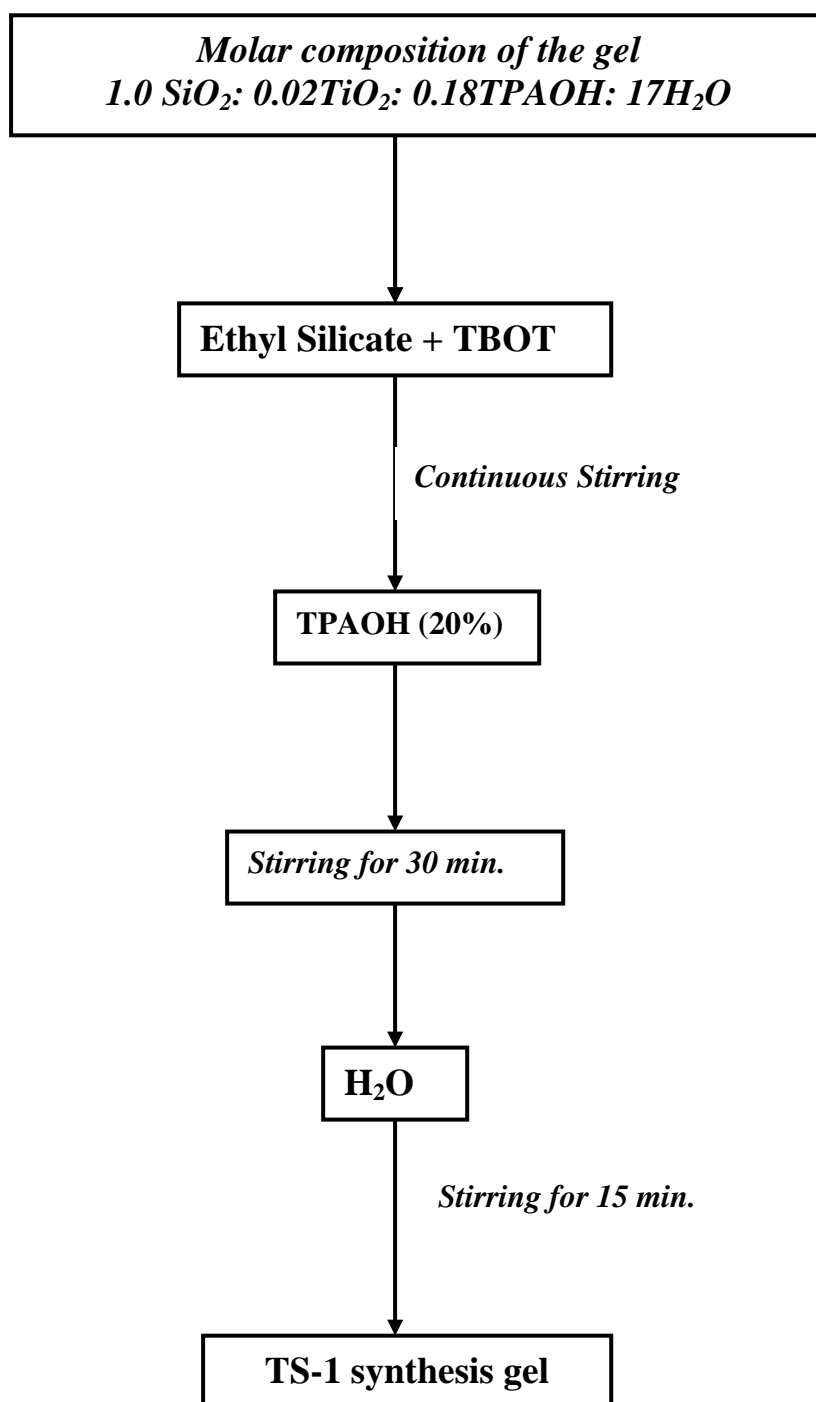


Fig. 2.2 Outline of the procedure used for synthesis gel preparation of TS-1 (Si/Ti=50).

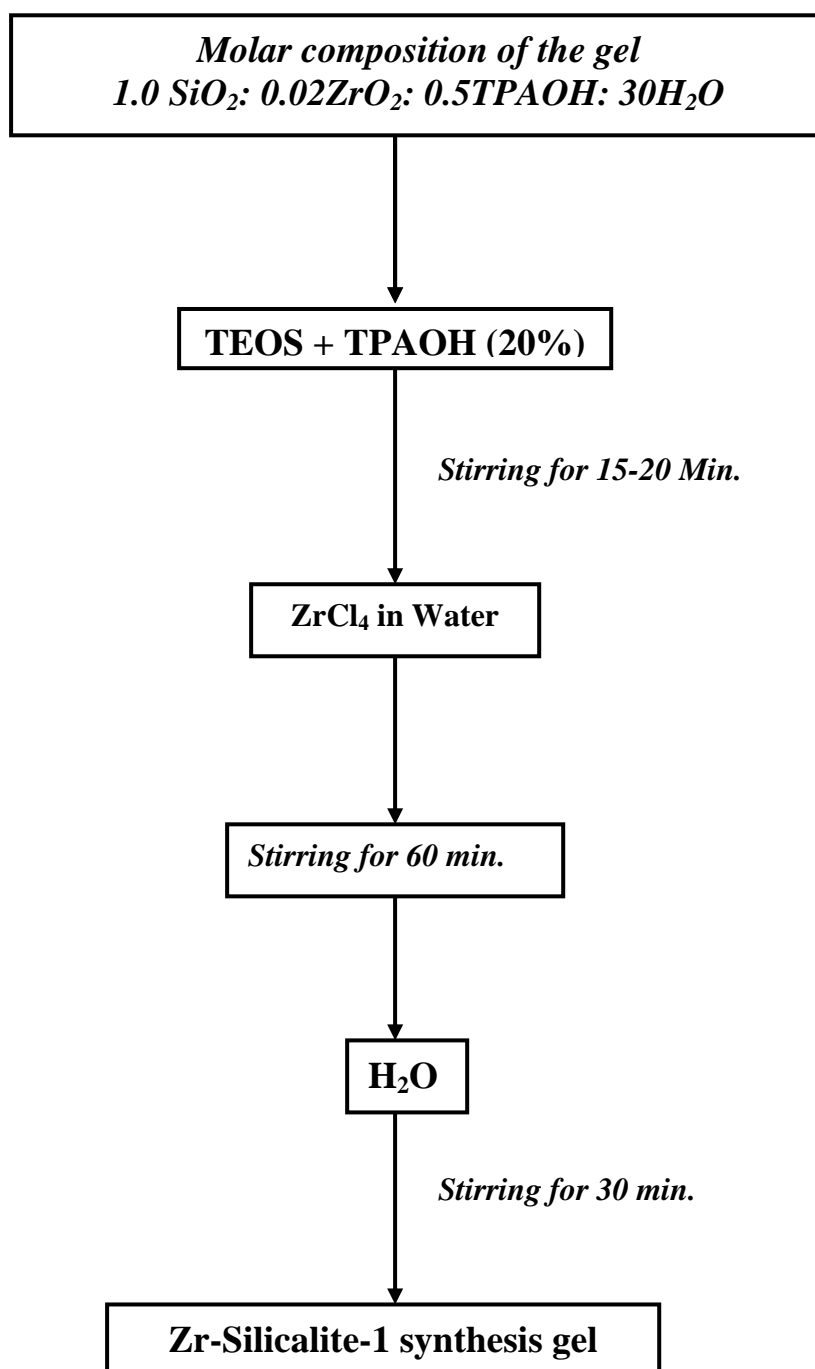


Fig. 2.3 Outline of the procedure used for synthesis gel preparation of Zr-silicalite-1 (Si/Zr=50).

2.3 Characterization

The calcined samples were characterized by powder X-ray diffraction; scanning electron microscopy, diffuse reflectance UV-visible spectroscopy, FTIR and NMR spectroscopic methods.

2.3.1 Powder X-ray diffraction

Powder XRD patterns of the as synthesized and calcined samples were obtained on a Philips diffractometer (PW 3071), using Ni filtered CuK α radiation ($\lambda = 1.5406 \text{ \AA}$) and X'Celerator as detector. The patterns were recorded in the 2θ range of 5- 55° at a scan step of 0.0167° and scan speed 20s/step. Silicon was used as an external standard. All 2θ values were corrected with respect to 2θ value of the (111) reflection of silicon as standard ($2\theta = 28.45^\circ$). The phase purity of all the samples was checked by comparing the X-ray data available in the literature for silica polymorph with MFI topology [4]. The degree of crystallinity of the calcined samples was determined with reference to a highly crystalline silicalite-1 sample (Si/M = ∞ prepared under similar conditions) as follows [5]:

$$\% \text{ Crystallinity} = \frac{\text{Area under all reflections in the whole XRD profile}}{(\text{Area under all reflections in the whole XRD profile} + \text{Background area})} \times 100$$

The unit cell parameters were calculated from the corrected d values and refined by using least squares fitting (X'Pert plus and GSAS [6] softwares). In order to determine the extent of isomorphous substitution in the metallosilicate samples, the calculated values of unit cell volume (UCV) were compared to those of theoretical values using the following equation [7]:

$$V_x = V_{\text{Si}} - V_{\text{Si}} (1 - d_{\text{M}}^3 / d_{\text{Si}}^3) x$$

where, V_{Si} is the unit cell volume of pure silicalite-1, d_{M} and d_{Si} are the tetrahedral T-O bond distances for the substituted tri or tetravalent metal and silicon atoms respectively and $x = \text{M}/(\text{Si}+\text{M})$ the atomic ratio in the product determined by elemental analysis of the metal to total concentration.

2.3.2 Rietveld refinement

Powder XRD patterns collected for all the samples were refined using the Rietveld method [8]. The unit cell parameters of each sample were refined with the Rietveld method using the GSAS [6] package and the EXPGUI graphical interface [9], which allows proper treatment of the instrumental aberration parameters, such as the goniometer shift and the sample displacement parameters. The goniometer zero correction was corrected against the nominal Si cell parameter, and then it was kept fixed for the refinement of all the XRD patterns. The initial structural coordinates for orthorhombic and monoclinic structure were taken from the literature [10, 11]. A constant 2θ range approximately from $5-16^\circ$ was excluded in each refinement, because of the asymmetry of the peaks. The pseudo-Voigt peak profile function, with up to 17 refinable parameters, was chosen and the peaks were truncated at 0.01% of the peak maxima. Background intensity was modeled by a Chebyshev type I polynomial function with 16 background parameters. An overall scale factor, the cell parameters, and the sample displacement parameter were simultaneously refined. Structural parameters were (atomic coordinates, isotropic thermal factors and site-occupancy multipliers) kept fixed during the refinement procedure. The R-weighted pattern (R_{wp}) factor was used as the criterion to follow the refinement process. The value of this factor varied between 4 and 7 % in all the fitted patterns.

2.3.3 Diffuse reflectance UV-visible spectroscopy

Diffuse reflectance (DR) UV-visible spectra of fine powder samples (about 0.5-0.7 g) were recorded on a Perkin-Elmer Lambda-650 UV-vis spectrometer (model UV-Vis 2101 PC). BaSO₄ was used as an external standard to correct the baseline in the spectra. All the samples were recorded in the range of 200-800 nm, though only charge transfer transitions in the UV region (200-400 nm) are of interest. No absorptions were found in the visible region.

2.3.4 Fourier transform infra-red spectroscopy

The framework IR spectra were recorded in the region of $400 - 4000 \text{ cm}^{-1}$ using a 60 SXB Nicolet FTIR spectrophotometer. The samples were prepared by KBr pellet (1:300 mg) technique. All spectra were run at a resolution 4 cm^{-1} .

2.3.5 Scanning electron microscopy (SEM) and Energy Dispersive Analysis of X-rays (EDAX)

The morphology and particle size were determined using a Leica Stereoscan-440 SEM equipped with a Phoenix EDAX attachment. The fine powder of the samples was loaded on a metallic sample holder, after dispersing it in ethyl alcohol. It was then coated with a thin layer of silver paste (conductivity paint) to prevent surface charging and to protect any thermal damage due to the electron beam. EDAX was employed for the elemental mapping of the Si, Fe, Ti, Zr and O.

2.3.6 Thermal analysis

In order to determine the decomposition temperature of occluded template within the channels of the zeolite and also to check the thermal stability of the sample at elevated temperatures, thermogravimetry (TG) and differential thermal analysis (DTA) were carried out using a Setaram TG/DTA instrument. The dried as-synthesized sample (~30 mg) was placed in a platinum crucible and α -alumina was used as a reference. The measurements were performed with a heating rate of 10 K min⁻¹ in the temperature range of 298 – 1273 K, under air-flow.

2.3.7 ²⁹Si MAS NMR spectroscopy

The solid state ²⁹Si MAS NMR spectra of the samples were obtained at room temperature on a 7 T Wide Bore Bruker NMR spectrometer (1 H Larmor frequency 300 MHz) using a 4 mm probe and a Magic Angle Spinning (MAS) rate of 14 KHz. The chemical shifts (in ppm) were recorded with respect to tetramethylsilane (TMS) in an external magnetic field of 7.0 Tesla.

2.3.8 Fe Mössbauer Spectroscopy

In-situ Mössbauer spectra were recorded in a versatile measuring cell [12]. Various treatments were applied to study the coordination of iron, i.e. evacuation and hydrogen reductions. Spectra were collected in constant acceleration mode, by using ⁵⁷Co/Rh (1 GBq) source. Spectra were decomposed to Lorentzian line shape components. The isomer shift values are relative to metallic alpha-iron. The accuracy of positional data is ca. ± 0.03 mm/s. Spectra were recorded subsequently, *i.e.* without changing the sample several treatments were performed on the same single sample.

2.4 Results and discussions

2.4.1 Powder X-ray diffraction

All of the as synthesized materials were white powders, exhibiting the typical X-ray diffraction patterns of zeolite with the MFI topology. No typical diffraction peaks due to metal oxide aggregates were found. Powder XRD patterns of both as synthesized as well as calcined FeS-1 samples are shown in Figure 2.4 and Figure 2.5 respectively.

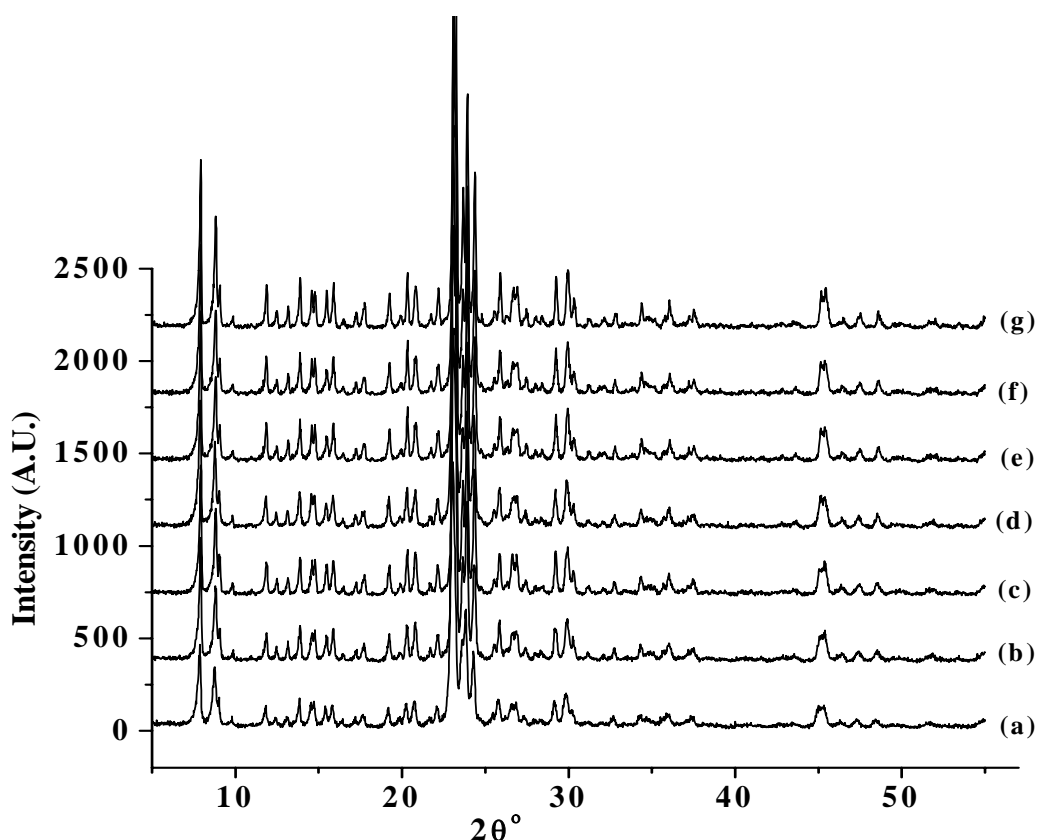


Fig. 2.4 Powder XRD patterns of the as synthesized Fe-silicalite-1 samples: (a) SFS- ∞ , (b) SFS-100, (c) SFS-75, (d) SFS-72, (e) SFS-50, (f) SFS-36 and (g) SFS-24.

Figure 2.4 shows XRD profiles of the as synthesized SFS- ∞ (curve a) and samples SFS-100, SFS-75, SFS-72, SFS-50, SFS-36 and SFS-72 (curves b to g, respectively). All FeS-1 samples exhibit a high crystallinity, without any impurity phase. The XRD profiles of Fe containing samples are found to be similar to that of silicalite-1 sample.

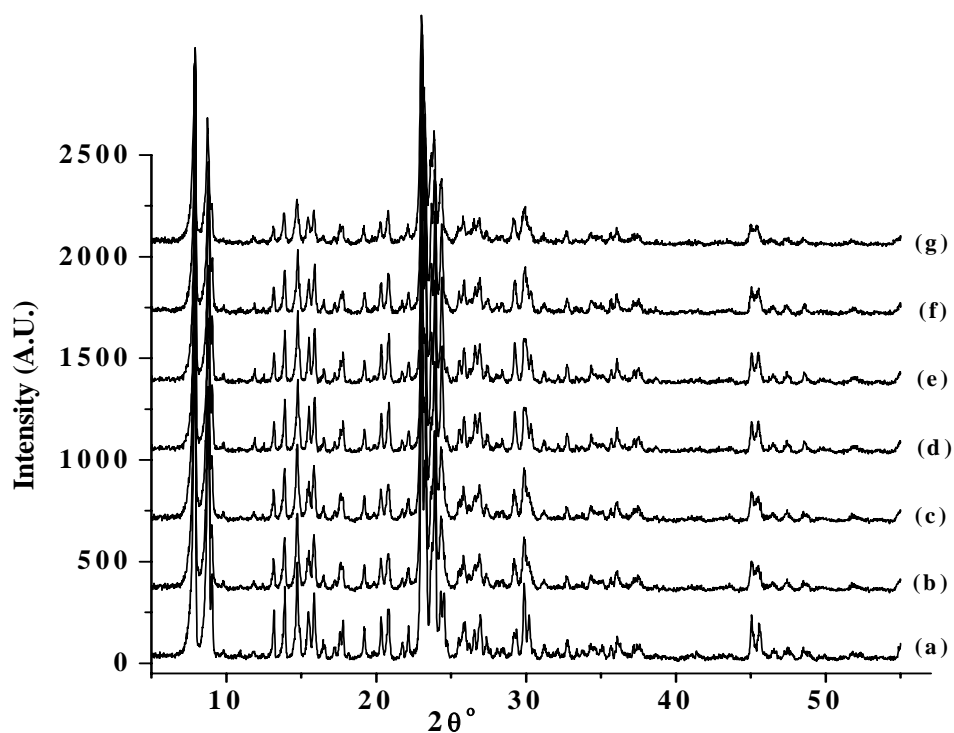


Fig. 2.5 Powder XRD patterns of the calcined Fe-silicalite samples: (a) CFS- ∞ , (b) CFS-100, (c) CFS-75, (d) CFS-72, (e) CFS-50, (f) CFS-36 and (g) CFS-24.

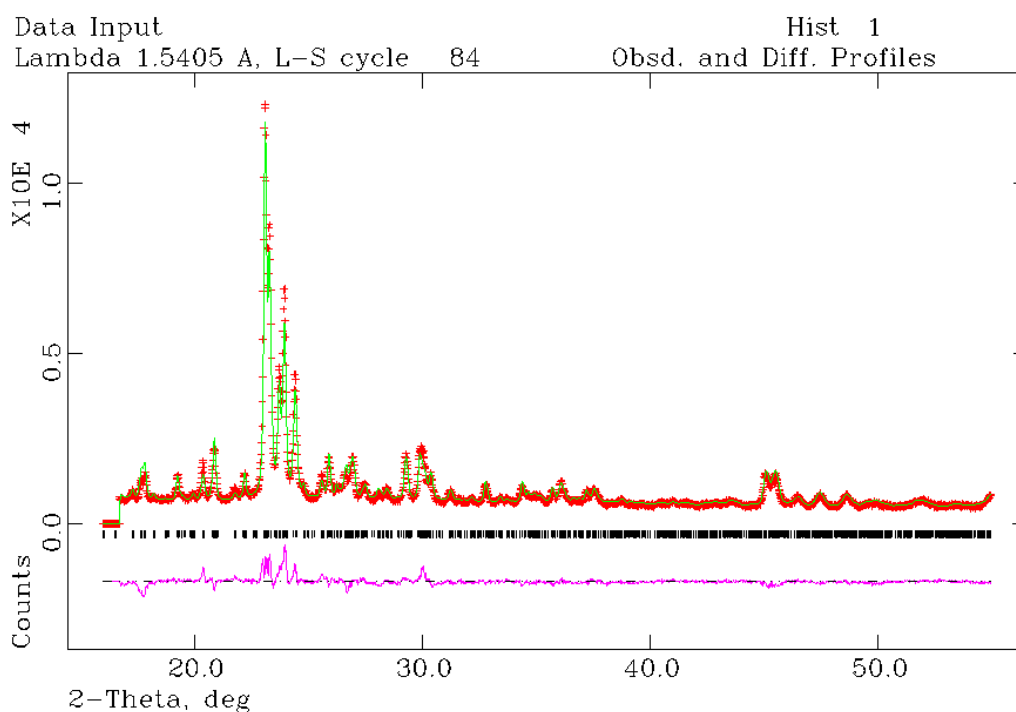


Fig. 2.6 Rietveld refinement plot of a typical XRD pattern of CFS-50 sample: a) red-observed b) green- calculated and c) at the bottom difference plot.

XRD profiles of the calcined samples are shown in Figure 2.5 and are found to be similar and in orthorhombic symmetry except CFS- ∞ , which undergo symmetry change (orthorhombic to monoclinic), on calcination in air at 773 K. The information regarding unit cell parameters was obtained by Rietveld refinement of the powder XRD patterns of calcined samples. A typical Rietveld plot for the powder XRD pattern of CFS-50 sample is shown in Figure 2.6 and there is fairly good match between calculated and experimental patterns. The interplanar d spacing of silicalite-1 shift to higher values due to the incorporation of the larger iron ions in the lattice (Shannon ionic radii: $\text{Si}^{4+} = 0.26 \text{ \AA}$ and $\text{Fe}^{3+} = 0.49 \text{ \AA}$) [13]. There is an increase in the unit cell volume (UCV) from 5348 to 5422 \AA^3 with decrease in Si/Fe molar ratio (Table 2.1). It is reasonable to consider that this expansion in UCV corresponds to isomorphous substitution of iron in the silicalite framework.

Table 2.1: Unit cell parameters of FeS-1 samples.

Sample	Si/Fe mole ratio		% Cryst.	Unit cell parameters (\AA)			UCV (\AA^3)
	XRD	EDAX		a	b	c	
CFS- ∞^a	-	-	100	20.120	19.880	13.371	5348
CFS-100	102	101	97	20.118	19.914	13.403	5370
CFS-75	88	80	95	20.120	19.912	13.410	5373
CFS-72	82	76	95	20.130	19.914	13.407	5374
CFS-50	55	52	93	20.083	19.976	13.428	5387
CFS-36	39	38	90	20.143	20.004	13.410	5403
CFS-24	30	28	88	20.162	20.036	13.421	5422

^aThis material possesses monoclinic symmetry and angle $\beta=90.23^\circ$.

Figure 2.7 shows the comparison of the experimental UCV with that calculated assuming the substitution of Si^{4+} by Fe^{3+} in tetrahedral positions. The unit cell volume calculated for various FeS-1 samples is plotted versus their iron content. A linear increase in the unit cell volume, V with the increase in the mole fraction of Fe ($x=\text{Fe}/(\text{Si}+\text{Fe})$) suggests the presence of Fe in the framework. Framework Si/Fe ratios were determined by XRD results and are given in Table 2.1. The framework Si/Fe ratio was equal to 30, 39, 55, 82, 88 and 102 for the samples CFS-24, CFS-36, CFS-50, CFS-72, CFS-75 and CFS-100 respectively. It is reported that the powder X-ray

diffraction profile of silicalite-1 (all silica polymorph where $\text{Si}/\text{M} = \infty$) prepared by various research workers, during their preparation of molecular sieves by isomorphously substituting the T element by titanium, tin, zirconium, vanadium, chromium, molybdenum, differ in their crystallinity and their unit cell volumes. Hence whenever a metal ion is being substituted, metal free all silica polymorph should also prepared for deciphering the unit cell expansion of the substituted samples. Increase or decrease in the unit cell volume of the substituted structures with respect to the corresponding silica polymorph is a clear indication of the presence of metal atom in the framework. Table 2.1 shows the % crystallinity of the FeS-1 samples, determined using the ratio of integral intensities of X-ray peaks in the whole pattern. In this case the sample of pure silicalite was chosen as standard, *i.e.* its crystallinity taken as 100%. This way of estimating the relative crystallinity of samples of different chemical composition is reliable.

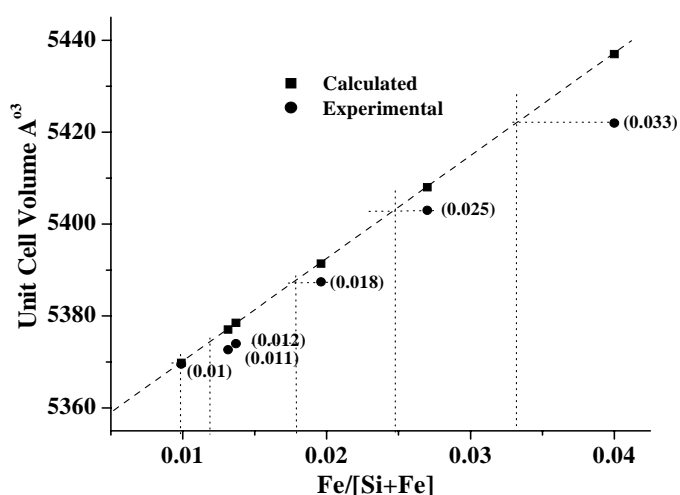


Fig. 2.7 Variation of unit cell volume with the Fe concentration in calcined FeS-1 molecular sieves (values in the parentheses are the real concentration of Fe in the framework).

The powder XRD patterns of as-synthesized and calcined TS-1 samples are shown in Figure 2.8 and Figure 2.9 respectively. The Figure 2.10 compares the experimental UCV with that calculated for various TS-1 samples plotted against their titanium content assuming replacement of Si^{4+} by Ti^{4+} in tetrahedral positions. A linear increase in the unit cell volume, V with the increase in the mole fraction of Ti ($x = \text{Ti}/(\text{Si} + \text{Ti})$) suggests the presence of Ti in the framework. A very good agreement

between the two up to a metal concentration (x) of 0.025 ($\text{Si}/\text{Ti} = 38$, output) is observed. Framework Si/Ti ratios obtained from XRD results are given in Table 2.2. The framework Si/Ti ratio was equal to 38, 65, 72, 95, 99 and 157 for the samples CTS-30, CTS-50, CTS-60, CTS-75, CTS-80 and CTS-100 respectively.

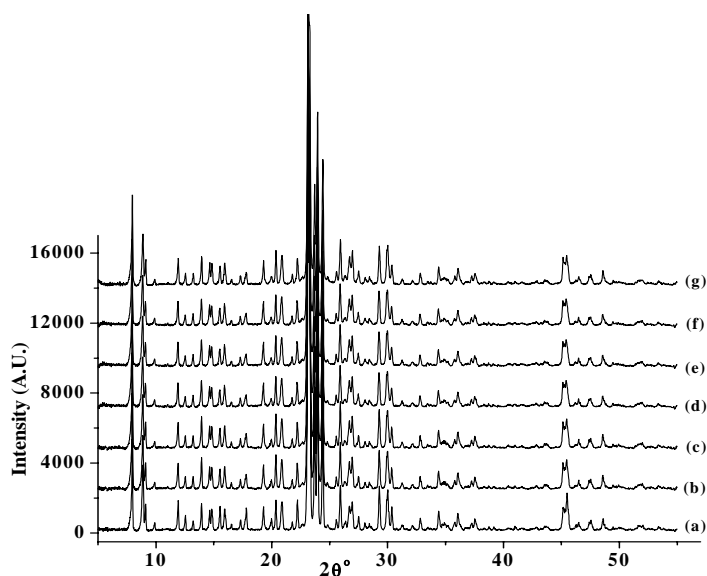


Fig. 2.8 Powder XRD patterns of the as-synthesized titanium silicalite (TS-1) samples: (a) STS- ∞ , (b) STS-100, (c) STS-80, (d) STS-75, (e) STS-60, (f) STS-50 and (g) STS-30.

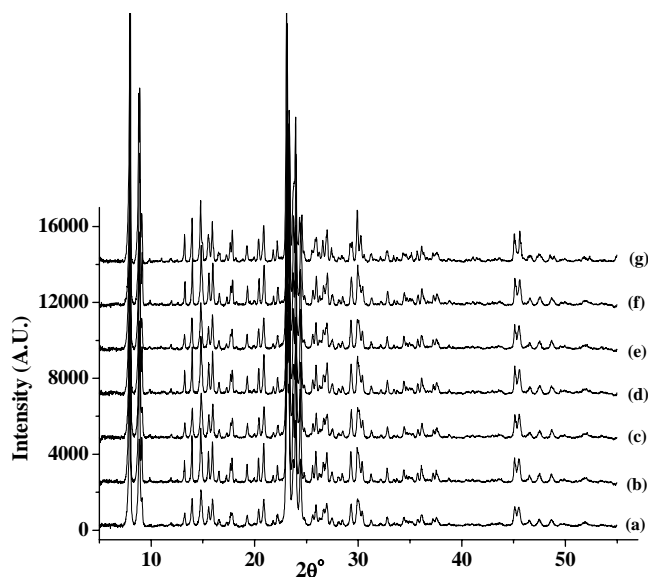


Fig. 2.9 Powder XRD patterns of the calcined titanium silicalite (TS-1) samples: (a) CTS- ∞ , (b) CTS-100, (c) CTS-80, (d) CTS-75, (e) CTS-60, (f) CTS-50 and (g) CTS-30.

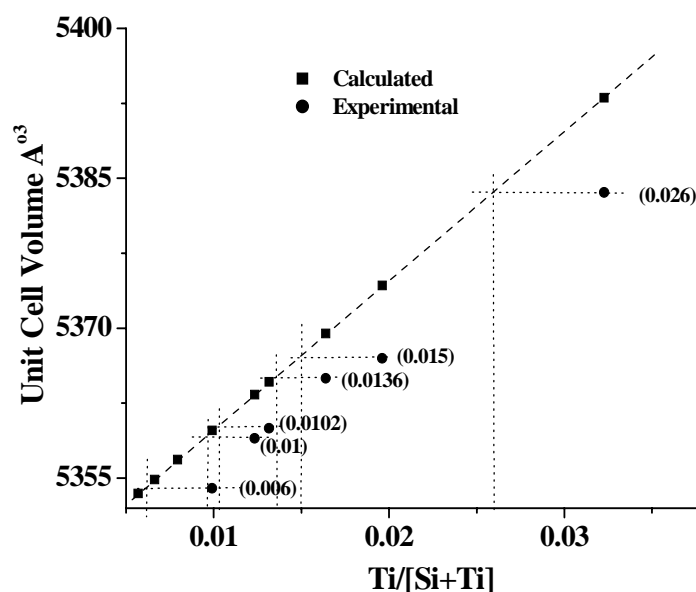


Fig. 2.10 Variation of unit cell volume with the Ti concentration in calcined TS-1 molecular sieves (values in the parentheses are the real concentration of Ti in the framework).

Table 2.2: Unit cell parameters of TS-1 samples

Sample	Si/Ti		% Cryst.	Unit cell parameters (Å)			UCV (Å ³)
	XRD	EDAX		a	b	c	
CTS-∞ ^a	-	-	100	20.103	19.878	13.375	5345
CTS-100	157	115	99	20.088	19.901	13.409	5354
CTS-80	99	86	97	20.094	19.910	13.395	5359
CTS-75	95	76	96	20.094	19.910	13.396	5360
CTS-60	72	67	95	20.099	19.912	13.405	5365
CTS-50	65	55	93	20.102	19.912	13.409	5367
CTS-30	38	35	90	20.124	19.940	13.417	5384

^a monoclinic symmetry and angle $\beta=90.35^\circ$.

The powder XRD patterns of as-synthesized and calcined ZrS-1 samples are shown in Figure 2.11 and Figure 2.12 respectively. Figure 2.13 show the comparison of the experimental unit cell volume with that calculated assuming the substitution of Si⁴⁺ by Zr⁴⁺ in tetrahedral positions. The comparison of the unit cell volume calculated for

various ZrS-1 samples is plotted against their Zr content. A linear increase in the unit cell volume, V with the increase in the mole fraction of Zr ($x = \text{Zr}/(\text{Si} + \text{Zr})$) suggests the presence of Zr in the framework.

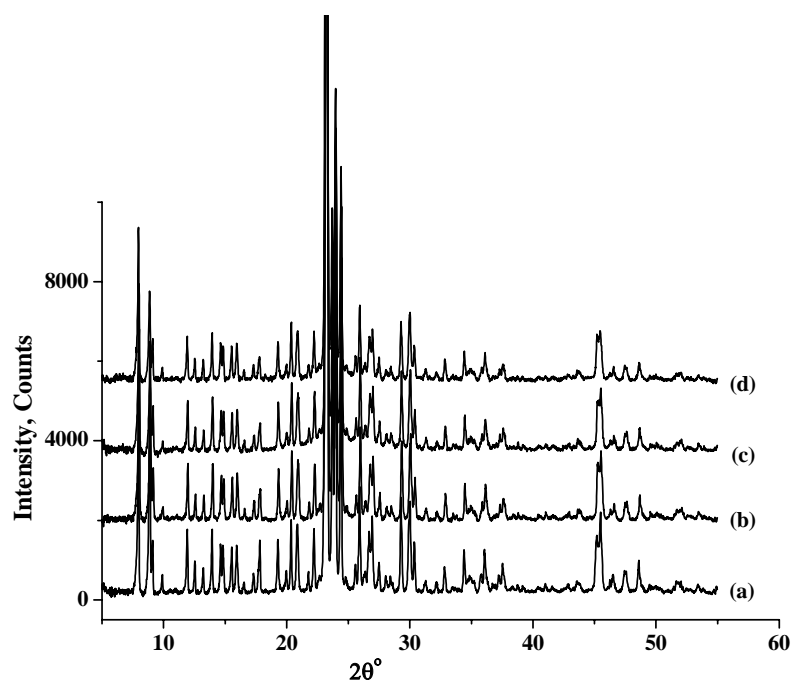


Fig. 2.11 Powder XRD patterns of as the synthesized zirconium silicalite (ZrS-1) samples: (a) SZS-∞, (b) SZS-100, (c) SZS-75 and (d) SZS-50.

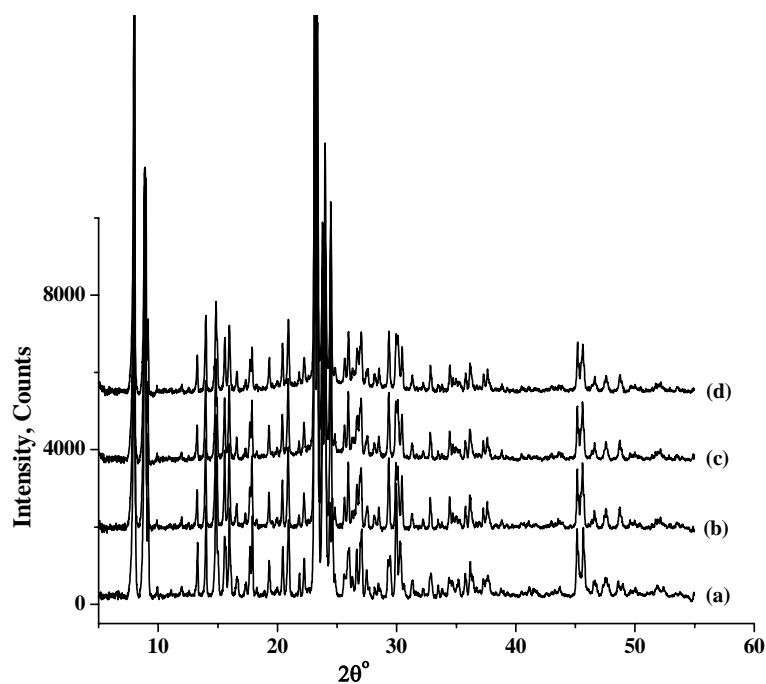


Fig. 2.12 Powder XRD patterns of the calcined zirconium silicalite (ZrS-1) samples: (a) CZS-∞, (b) CZS-100, (c) CZS-75 and (d) CZS-50.

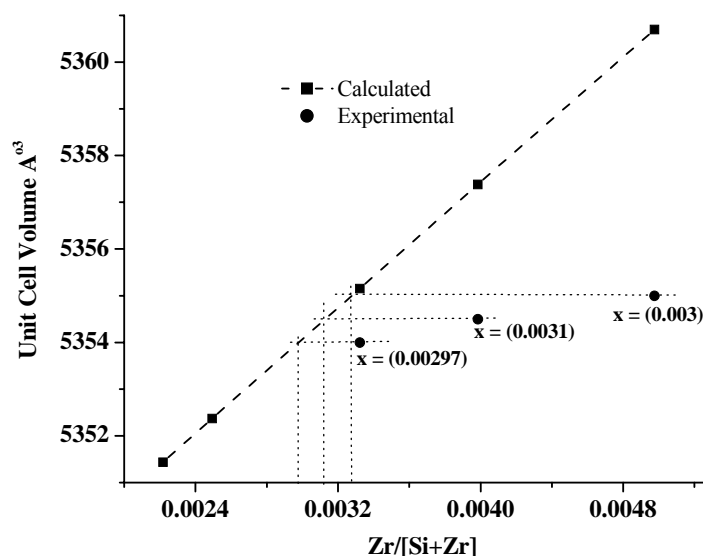


Fig. 2.13 Variation of unit cell volume with the Zr concentration in calcined ZrS-1 molecular sieves (values in the parentheses are the real concentration of Zr in the framework).

However, the deviation in the sample is quite significant indicating that not all the Zr in the sample is present in the framework. Framework Si/Zr ratios obtained from XRD results is given in Table 2.3. The framework Si/Zr ratio was equal to 302, 322 and 336 for the samples CZS-50, CZS-75 and CZS-100 respectively. It is observed that only a small amount of zirconium (0.3 atom/uc) is incorporated with a uniform distribution within the MFI framework due to its larger size.

Table 2.3: Unit cell parameters of ZrS-1 samples

Sample	Si/Zr		% Cryst.	Unit cell parameters (Å)			UCV (Å ³)
	XRD	EDAX		a	b	c	
CZS-∞ ^a	-	-	100	20.100	19.878	13.376	5344
CZS-50	302	54	76	20.094	19.897	13.394	5355
CZS-75	322	104	83	20.084	19.906	13.393	5354.5
CZS-100	336	129	76	20.082	19.908	13.393	5354

^a monoclinic symmetry and angle $\beta=90.20^\circ$.

2.4.2 Diffuse reflectance UV-visible spectroscopy

The coordination state and extent of aggregation of Fe^{3+} in the iron-containing zeolites were investigated by UV-vis spectroscopy [14-16]. The comparison of the UV-visible diffuse reflectance (DRUV-vis) spectra of the FeS-1 series of molecular sieves is shown in the Figure 2.14. The overall spectrum derives from the overlapping of several contributions of different iron species, as discussed in literature.

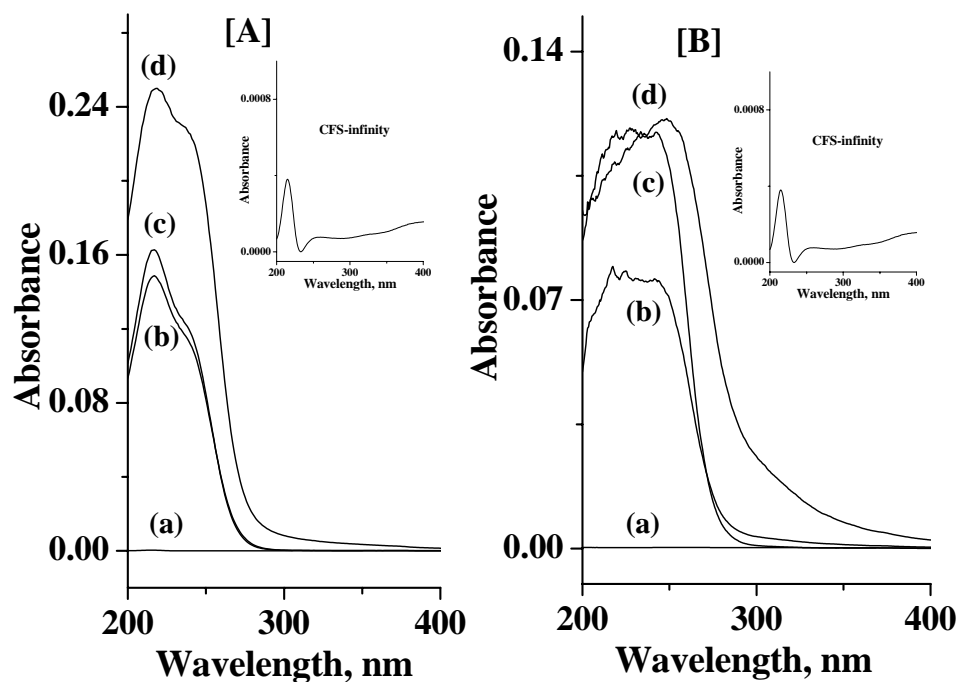


Fig. 2.14 Diffuse reflectance UV-visible spectra of FeS-1 samples [A] a) CFS- ∞ , b) CFS-100, c) CFS-75 and d) CFS-50; [B] a) CFS- ∞ , b) CFS-72, c) CFS-36 and d) CFS-24 (CFS- ∞ spectrum is shown inset).

For isolated Fe^{3+} sites, two charge transfer ($\text{Fe}^{3+} \leftarrow \text{O}^{2-}$) bands associated to $t_1 \rightarrow t_2$ and $t_1 \rightarrow e$ transitions are expected at about 215 and 240 nm respectively, for tetrahedral coordination. Bands at higher wavelength are generally attributed to charge transfer transitions of Fe^{3+} ions in small oligonuclear clusters ($\text{Fe}_x^{3+}\text{O}_y$) (broad bands between 300 and 450 nm) and larger Fe_2O_3 particles (above 450 nm). Based on the above assignments, it is possible to conclude that the two intense bands at about 217 and 245 nm, which are prominent in FeS-1 samples, are due to tetrahedral Fe^{3+} sites in the framework. The bands below 300 nm are typical LMCT bands of isolated

Fe^{3+} species either tetrahedrally or octahedrally coordinated. Obviously these peaks are absent in the spectrum of the silicalite-1 sample ($\text{CFS}=\infty$). In the UV spectra of the FeS-1 samples with higher Fe loading the broad band at 285 and 350 nm, can be assigned to the presence of some of the octahedral isolated iron species and oxo bridges between two iron ions respectively (octahedral Fe^{3+} in oligomeric clusters). These bands are absent in the case of CFS-72, CFS-75 and CFS-100 samples. From these observations we can conclude that the Fe^{3+} is present mainly as tetrahedral coordination. The spectrum of silicalite-1 is shown in the inset for clarity. The present UV-vis spectra indicate that the calcined materials contain a distribution of iron species ranging from isolated ions to bulky iron oxide agglomerates. Clearly, more extensive clustering takes place with increasing Fe loading.

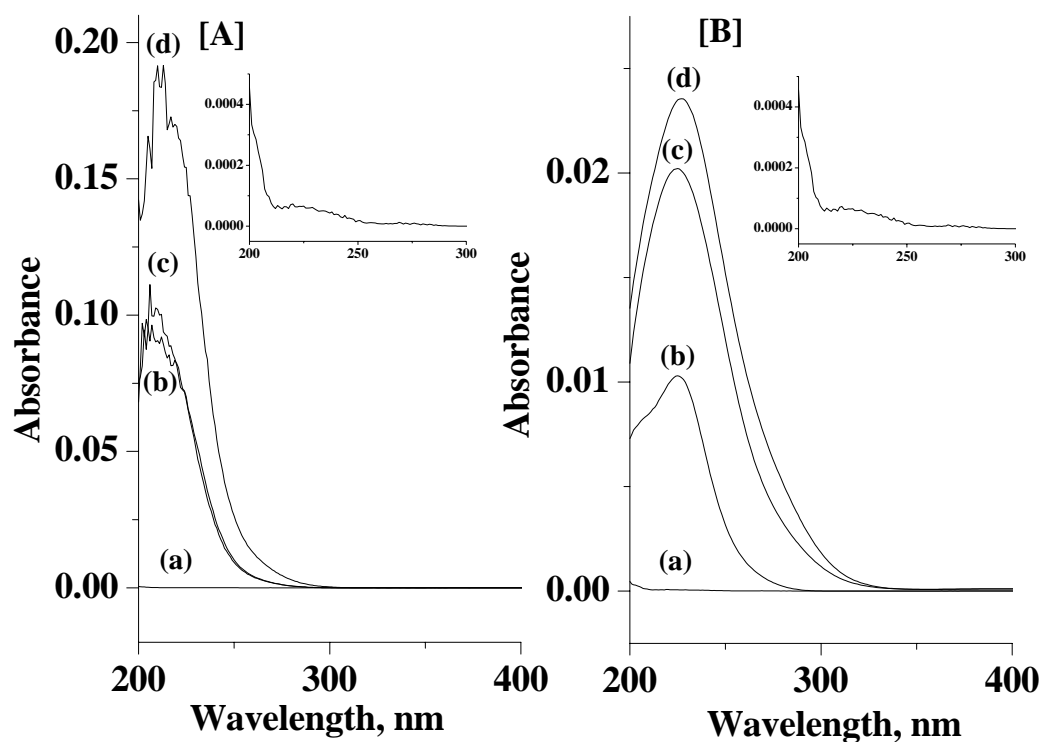


Fig. 2.15 Diffuse reflectance UV-visible spectra of TS-1 samples [A] a) CTS- ∞ , b) CTS-100, c) CTS-75 and d) CTS-50; [B] a) CTS- ∞ , b) CTS-80, c) CTS-60 and d) CTS-30 (CTS- ∞ spectrum is shown inset).

DRUV spectra of TS-1 have absorption at about 210-220 nm as shown in Figure 2.15. It is well established that charge transfer bands around 210–220 nm characterize isolated, tetrahedrally coordinated Ti species corresponding to the tetrahedral Ti in the silicalite framework [17]. The spectrum for TS-1 shows the strong absorption band at 210 nm and absence of absorption band at 330 nm due to TiO_2 in anatase form. Therefore, DRUV–vis spectra clearly indicates that a significant proportion of Ti sites in TS-1 materials probably possess a tetrahedral coordination. Shoulders around 230–240 nm are generally assigned to isolated Ti species in either 5- or 6-fold coordination [18-20].

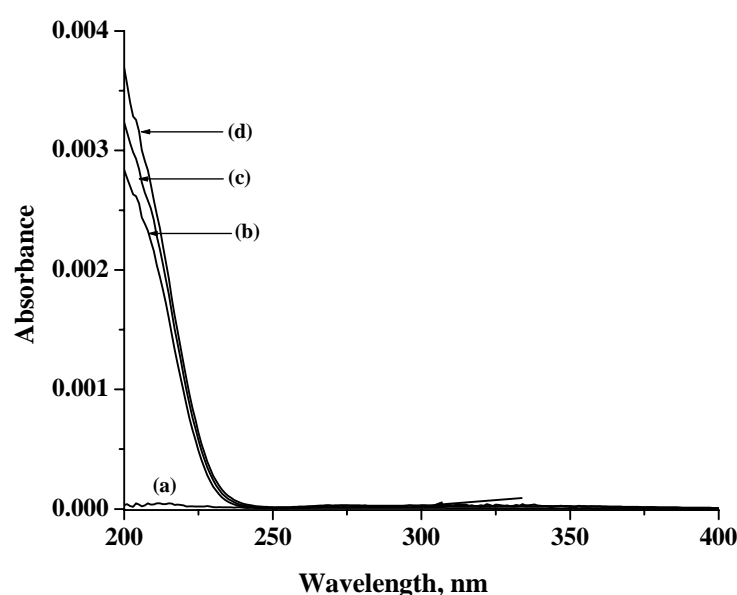


Fig. 2.16 Diffuse reflectance UV-visible spectra of ZrS-1 samples a) CZS- ∞ , b) CZS-100, c) CZS-75 and d) CZS-50.

Diffuse reflectance UV-visible spectra of ZrS-1 samples are shown in Figure 2.16. Curve b to d shows the presence of a characteristic absorption at about 212 nm attributable to charge transfer transitions involving the Zr(IV) (tetrahedral configuration) sites [21]. The spectra of CZS-50, CZS-75 and CZS-100 samples clearly indicate that major portion of zirconium form Si-O-Zr linkages. Absorption at 230 nm which may be due to Zr(IV) in other co-ordinations. These electronic transitions are clearly distinguishable from those in pure ZrO_2 (monoclinic symmetry), which shows absorption at about 240 and 310 nm. It confirms the atomic dispersion of Zr(IV) species in the form of Si-O-Zr linkages and not in the formation of Zr-O-Zr species.

2.4.3 FTIR spectroscopy

FTIR spectra of FeS-1 samples are shown in Figure 2.17. IR spectroscopy may be used to support the XRD data that the Fe is in the silicalite lattice. An additional broadening appears at 960 cm^{-1} for tetrahedral groups, $\text{Fe}(\text{OSi})_4$ in the spectra of FeS-1 samples which is absent in silicalite-1. Though one can hardly prove it spectroscopically since the intensive IR absorption due to the Fe, presence at $950\text{--}1000\text{ cm}^{-1}$ masks the peak at 960 cm^{-1} and the broadening in that region indicates the substitution of hetero metal atom in the silicalite lattice framework [23].

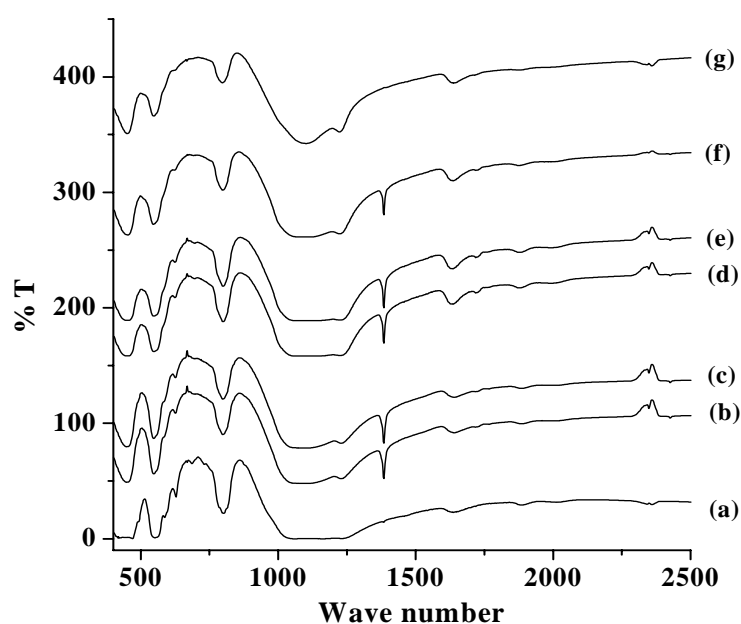


Fig. 2.17 FT-IR spectra of FeS-1 samples a) CFS- ∞ b) CFS-100, c) CFS-75, d) CFS-72, e) CFS-50, f) CFS-36 and g) CFS-24.

Figure 2.18 displays the FT-IR spectra of TS-1 samples. An absorption peak was found at 960 cm^{-1} in all TS-1 samples except silicalite-1, which is considered to be a collective vibration of the Si–O–Ti bond or Si–O bond perturbed by the presence of Ti atom in the framework of TS-1 [23, 24]. Since an absorption at 960 cm^{-1} could not be detected in the FT-IR spectrum of silicalite-1 (CTS- ∞), this absorption was taken as an evidence of the presence of a tetrahedrally coordinated Ti^{4+} framework incorporated into the skeleton of silicalite-1 [25]. Therefore, FT-IR results suggested that Ti is incorporated into the framework. Figure 4 illustrates the framework IR spectra of calcined silicalite-1 and TS-1 samples. An absorption band at 960 cm^{-1} has been observed in the case of all TS-1 samples. The relative intensity of these bands also increases with Ti content, similar observations have also been reported by others.

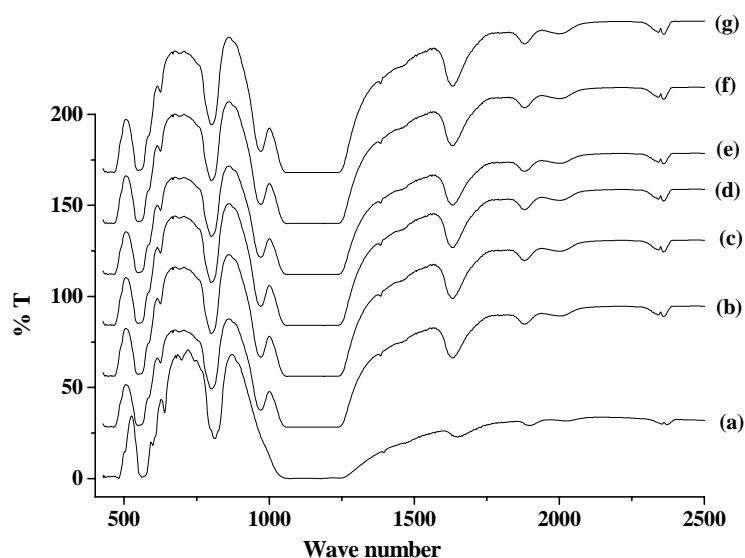


Fig. 2.18 FT-IR spectra of TS-1 samples a) CTS-∞ b) CTS-100, c) CTS-80, d) CTS-75, e) CTS-60, f) CTS-50 and g) CTS-30.

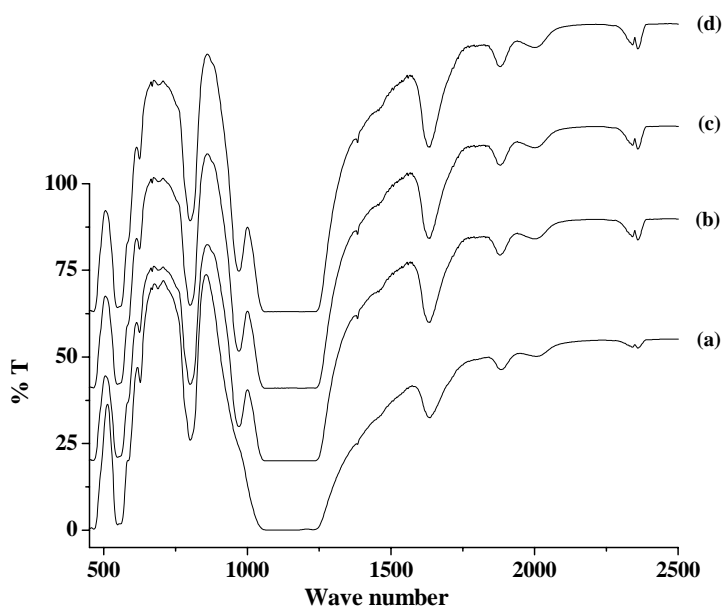


Fig. 2.19 FT-IR spectra of ZrS-1 samples a) CZS-∞ b) CZS-100, c) CZS-75 and d) CZS-50.

The 960 cm^{-1} was not observed in the IR spectra of calcined silicalite-1 synthesized in the absence of titanium under otherwise identical conditions. Boccuti *et al.* [24] have demonstrated that IR band around 960 cm^{-1} exhibited by zeolites can also be attributed to a stretching mode of a $[\text{SiO}_4]$ unit bonded to Ti^{4+} ion (O_3SiOTi).

Taramasso *et al.* [2] and others [18] have attributed this $950\text{-}970\text{ cm}^{-1}$ band to Ti incorporation in the zeolite framework. Figure 2.19 shows the FT-IR spectra of ZrS-1 samples. The framework FTIR spectra shows a shoulder at about 965 cm^{-1} which may be attributed to Si-O-Zr asymmetric stretching vibrations, on substitution of Zr^{4+} in the Si-O-Si linkages [26]. However, no such absorption was observed in silicalite-1 (CZS- ∞) sample. A similar band near 960 cm^{-1} has been reported for the $\text{SiO}_2/\text{TiO}_2$ and titanium silicates (TS-1 and TS-2) typically representing the asymmetric stretching vibrations of Si-O-Ti linkages [27-29]. Additionally, a band at 877 cm^{-1} was observed probably due to stretching vibrations of Zr=O species for higher Zr content [19, 20]. The band at 550 cm^{-1} is the characteristic of MFI structure, intensity of which increases with metal content of the zeolite.

2.4.4 Scanning electron microscopy (SEM)

Figure 2.20 shows the SEM of silicalite-1 and three typical (ratio Si/M=50) samples of FeS-1, TS-1 and ZrS-1, which was magnified 10^4 times. It shows that the particles of silicalite-1 (CFS- ∞) were prismatic and not aggregated (Figure 2.20 a).

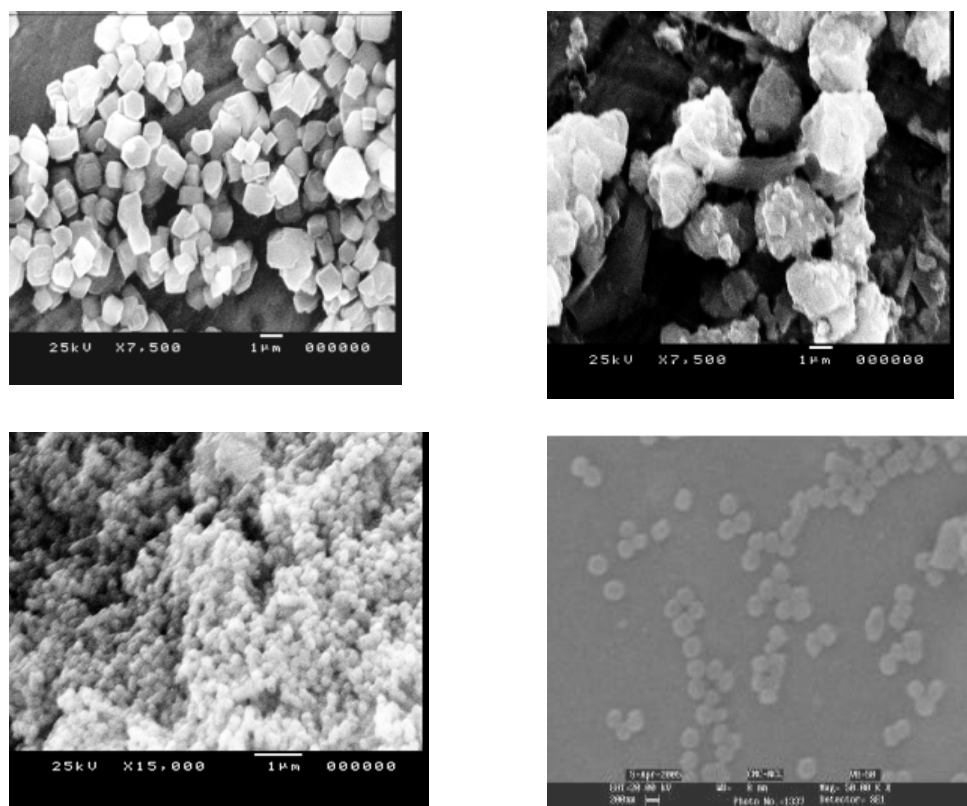


Fig. 2.20 Scanning electron micrographs of a) CFS- ∞ , b) CFS-50, c) CTS-50 and d) CZS-50.

The scanning electron micrographs of silicalite-1 are similar to the typical particles of ZSM-5. The size of the silicalite-1 crystals ($\sim 1\mu\text{m}$) differed from the other samples. The CFS-50 and CTS-50 particles were prismatic and aggregated (Figure 2.20 b and c respectively). This result was similar to that of the particle sizes of TS-1 reported in the literature, where hydrothermally synthesized TS-1 always exhibited 200–300 nm cuboid shaped crystallites [30, 31]. The CZS-50 particles were spherical, well dispersed and were not aggregated unlike CFS-50 and CTS-50 as shown in Figure 2.20 (d). Particle size of the metallosilicate molecular sieve is $<1\mu\text{m}$. The energy dispersive absorption of X-rays (EDAX) analysis was carried out for elemental mapping of the molecular sieves samples.

2.4.5 Thermal analysis

All as-synthesized FeS-1 samples were scanned in the range of 373 –1173 K for their TG analysis (Figure 2.21). The template decomposition temperature is shifted to a higher value from 680 K to 710 K for SFS- ∞ and SFS-50 samples respectively. This is due to the fact that in the case of silicalite-1 template plays a role of structure directing agent. While in the case of Fe substituted molecular sieves, the template plays a dual role as structure directing agent and as a counter cation to balance the framework negative charge.

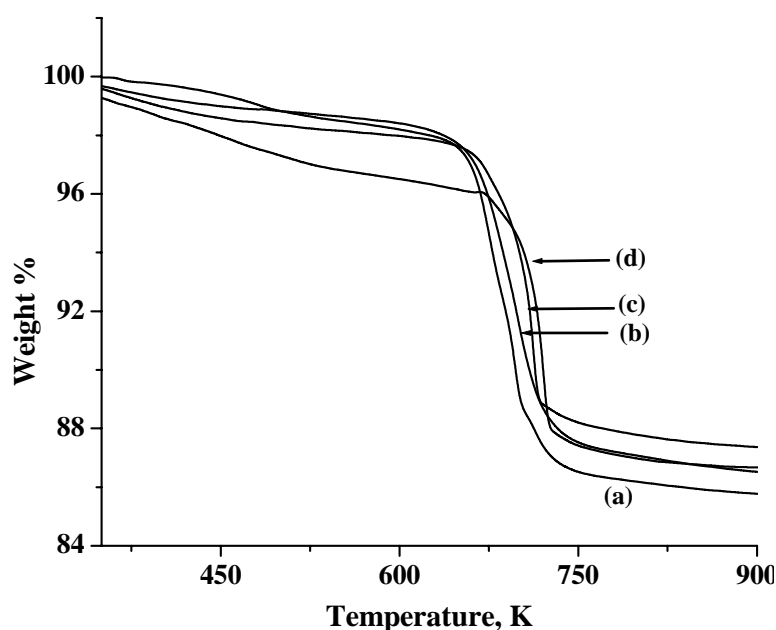


Fig. 2.21 TG plots of as synthesized FeS-1 samples: a) SFS- ∞ b) SFS-100, c) SFS-75 and d) SFS-50.

Negative charge on framework depends upon the Si/Fe ratio in the framework. As this ratio increases, the negative charge on the framework decreases. As the template decomposition temperature increases in the order $\text{Si/Fe}=\infty < \text{Si/Fe}=100 < \text{Si/Fe}=75 < \text{Si/Fe}=50$, there should be some interaction of the template molecule with framework *viz.*, the charge compensation in addition to the role as structure directing agent. Millini *et al.* have reported by studying the in situ HTXRD studies on template containing TS-1 and FeS-1 of various ratios, that template decomposition temperature was shifted to higher temperature in the case of metal substituted MFI as compared to the silica polymorph [32]. Thermogravimetric (TG) analysis showed a sharp weight loss in the range of 600 – 750 K, which is due to the decomposition of the occluded template within the channels of the zeolite structure. The total weight loss due to removal of the occluded template is about 12 wt. % for all samples and is in good agreement with the reports in literature [33]. The template decomposition process is shifted to higher temperatures than that for pure silicalite-1. This increase in the temperature of template decomposition may be attributed to the lattice distortion, as a result of the presence of heteroatoms in the framework and also due to the stronger interaction of template with metal ions in the framework.

2.4.6 ^{29}Si MAS NMR spectroscopy

^{29}Si MAS NMR is a useful method to elucidate structural variations concerning silicon in the zeolite [34]. The ^{29}Si chemical shifts of silicates are sensitive to local environment of the T –atoms connected with a given SiO_4 tetrahedron. ^{29}Si MAS-NMR spectrum of silicalite-1 sample was shown in Figure 2.19. The higher Q_4/Q_3 ratio in silicalite-1 sample shows that there is an increased condensation between silanol groups during the formation of silicalite-1. The resonance at –104 ppm in the ^{29}Si MAS NMR spectra can be assigned to silanols, in which the terminal hydroxyl groups are connected directly to the Si atoms in SiO_4 tetrahedral (Q_3 [$\text{Si}(\text{OSi})_3\text{OH}$]) species [34]. ^{29}Si MAS-NMR spectrum of TS-1 (with Si/Ti= 100, 75 and 50) samples are shown in Figure 2.20 respectively. All the TS-1 samples show two well resolved lines with chemical shifts at –104 and –114.9 ppm respectively, which have been attributed to the formation of Q_3 and Q_4 species. It can also be seen that the Q_3 amount does not change but the peak shifts from –114.9 to slightly up field with increasing the Ti species content in the TS-1 samples. It is therefore, likely due

to incorporation of part of Ti into the lattice of silicalite-1. Moreover, the lifetime of the ^{29}Si signal (T2) strongly decreases ($906\text{ms} > 732\text{ms} > 435\text{ms}$) with the Ti amount, thereby confirming this hypothesis. The peak at -114.9 ppm is normally assigned to resonance from Q_4 , $[\text{Si}(\text{OSi})_4]$ species. ^{29}Si MAS NMR spectra of TS-1 also exhibited a broad peak around -116.9 ppm, which has been attributed to the distorted Si—O—Si bonds resulting from the presence of Ti atoms in silicalite network [35]. The intensity of the (-116.9 ppm) peak increases with an increase in the titanium content.

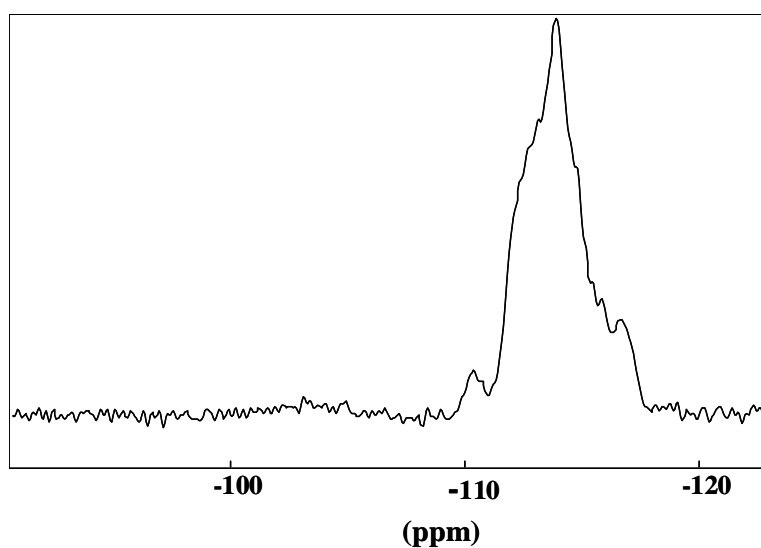


Fig. 2.19 ^{29}Si MAS NMR spectrum of silicalite-1 (CFS-∞).

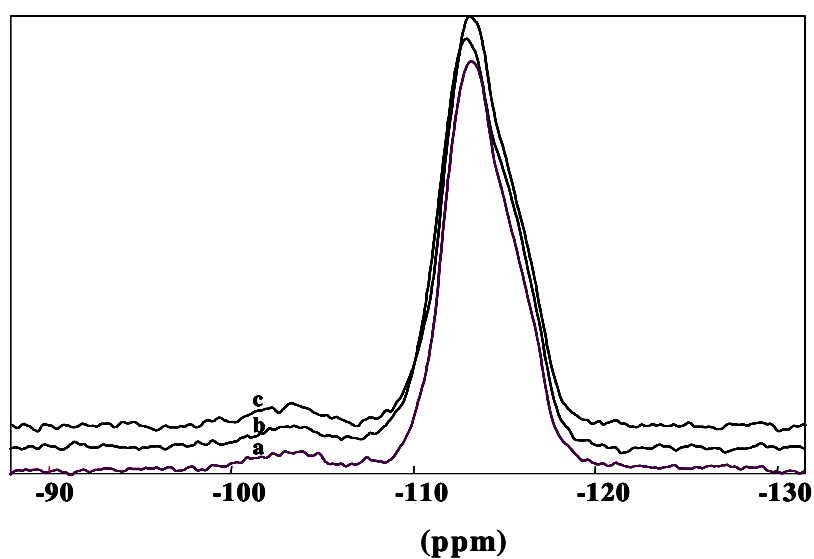


Fig. 2.20 ^{29}Si MAS NMR spectrum of (a) CTS-100, (b) CTS-75 and (c) CTS-100.

Tuel et al. have noted/attributed the presence of a shoulder at -116.9 ppm to the Q^4 line characteristic of the substituted MFI-type zeolites having an orthorhombic symmetry [36]. Only a few reports on solid-state ^{91}Zr NMR spectroscopy are available in the literature, which depicts the various phases of zirconia by their distinctive nuclear quadrupolar patterns [37]. However, it is difficult to record ^{91}Zr NMR signals for the samples with a lower Zr content. Since Zr^{4+} is a quadrupolar nuclei, it was not possible to get information on the local coordination of Zr^{4+} by MAS NMR experiments. ^{29}Si MAS NMR analysis of samples exhibited predominately an intense and broad signal at -113.8 ppm which was assigned to $Q_4[\text{Si}(\text{OSi})_4]$ species. The broadening of this resonance line was observed with an increase in Zr content.

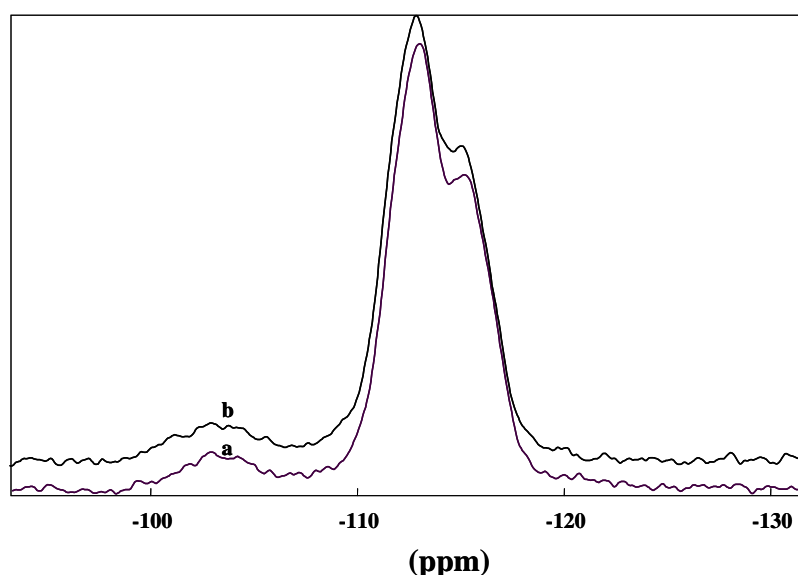


Fig. 2.21 ^{29}Si MAS NMR spectrum of (a) CZS-100 and (b) CZS-75.

This strong signal was flanked by a shoulder at -116 ppm, which was assigned to the distorted Si environment due to Si-O-Si or Si-O-Zr linkages. These results indicated that Zr^{4+} ions are probably linked to the defect silanol groups in tetrahedral coordination. Broadening of all signals in the spectra has been attributed to the large distribution of the T-O-T angles. The number of Q_3 species increases from 6.7 to 9.3 % (with very similar spectra) with increasing Zr content from Si/Zr = 100 to 50, which is essentially due to presence of Zr in the silica matrix. The only spectrum, which is not shown here, is CZS-50, because the Signal/Noise ratio was worse than the two others (lower ^{29}Si amount) and it does not really change.

2.4.7 Mössbauer Spectroscopy

Mössbauer spectroscopy is a devoted tool for characterizing the close neighborhood of iron, both as for coordination and oxidation states. There exist good compilations of data as for interdependence of Mössbauer parameters (isomer shift (IS) and quadrupole splitting (QS)) with the coordination and the structure, *e.g.* for silicate minerals [38]. In short, increasing symmetry results in decrease of QS for high-spin Fe^{3+} and the connection is opposite for Fe^{2+} . In correspondence, the method has successfully been applied since the early paper of Meagher *et al.* [39]. It was demonstrated that distinction between the framework (FW) and extraframework (EFW) positions is also possible, *e.g.* by comparing the reducibility of Fe^{3+} . Namely, FW iron is hardly reducible, whereas reduction of EFW iron is possible (*e.g.* in H_2 at 600 K). Further, symmetry of charge compensating cation has also influence on the charge distribution at the framework-substituted ion (reflected in the QS), *e.g.* Brönsted acidic H^+ in the vicinity of substituted iron results in high distortion (QS – 1.7-1.9 mm/s), whereas other cations of larger diameter result in less asymmetry (QS – 1.2-1.4 mm/s) [40]. A Mössbauer spectrum of the CFS-50 sample is shown in Figure 2.22. The results for the Mössbauer spectroscopy of CFS-50 sample are given in Table 2.4.

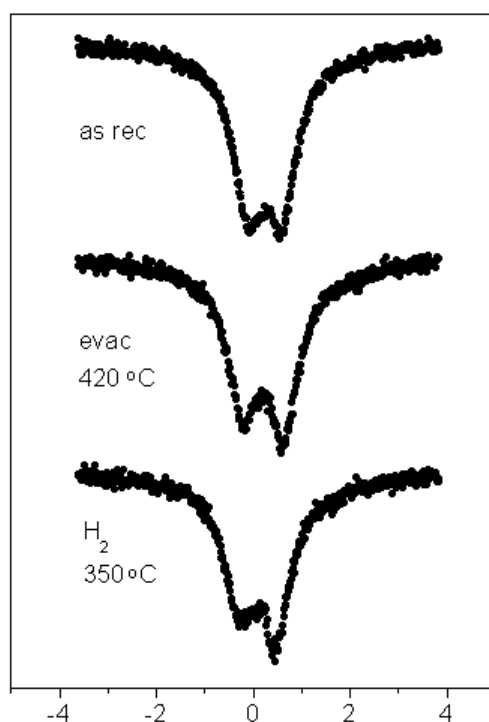


Fig. 2.22 Mössbauer spectra of CFS-24 sample.

Preliminary interpretation of the Mössbauer spectra is made as:

As received (calcined): The parameters of the Fe^{3+} doublet (1) correspond to the framework-substituted iron, since the isomers shift is below 0.3 mm/s. The same holds good for the singlet. Hence we can conclude that in the calcined state, iron might be coordinated with adsorbed water, etc. thus the obtained data have a limited relevance. (Usually the data on the evacuated sample are more informative.) Hence the sample is evacuated at 420°C for 2h, and measured at ambient temperature: The evacuation usually results in two features in the spectra:

1) (mostly at the NH_4^+ form) the Fe^{3+} doublet exhibits a larger quadrupole splitting ($1.8 < \text{QS} < 2.0$ mm/s), due to the removal of adsorbed water and formation of Brönsted acidic sites. Samples with Na^+ counteractions also exhibit the larger QS (> 1.4 mm/s).

2) Auto-reduction ($\text{Fe}^{3+} \Rightarrow \text{Fe}^{2+}$) may also take place to a limited extent, indicating the partial removal of the framework iron to extra-framework sites. None of these features is found in the spectrum.

Treatment in hydrogen at 350 °C: A treatment in hydrogen results in the appearance of Fe^{2+} in noticeable amounts (9 %) present in the sample, which is certainly a small amount (Table 2.4). Since Fe^{3+} in the framework positions is more stable and do not reduce against as compared to the extra-framework positions, the appearance of Fe^{2+} indicates that major concentration of Fe is substituted in the framework.

Table 2.4 The Mössbauer parameters extracted from the spectra of CFS-24 sample.

Treatment	Component	IS	QS	FWHM	RI
As received	Fe^{3+} doubl (1)	0.27	0.76	0.60	49
	Fe^{3+} singl	0.29	-	1.42	51
Evac. 420 °C (Meas: 20 °C)	Fe^{3+} doubl (1)	0.23	0.87	0.63	54
	Fe^{3+} singl	0.42	-	1.86	46
H_2 , 350 °C (Meas: 220 °C)	Fe^{3+} doubl (1)	0.12	0.80	0.76	86
	Fe^{3+} doubl	0.25	0.35	0.22	4
	Fe^{2+} doubl	1.16	1.01	0.83	9

(IS: isomer shift, mm/s, related to metallic α -iron; QS: quadrupole splitting, mm/s; FWHM: line width (full width at half maximum), mm/s; RI: relative percentage of the given components in the spectrum, %).

2.4 Conclusions

Silicalite-1 and metallosilicate molecular sieves with different Si/M (M=Fe, Ti and Zr) ratio have been synthesized by hydrothermal synthesis method and characterized in detail by X-ray diffraction, TG-DTA, FTIR, SEM-EDAX, DR UV-vis, ^{29}Si MAS NMR and Mössbauer spectroscopic techniques. A linear increase in the unit cell volume, V with the increase in the mole fraction of metal atom, M ($x=\text{M}/\text{Si}+\text{M}$) suggests the presence of metal atom in the framework. Isomorphous substitution of Si^{4+} by metal atoms (T = Fe, Ti and Zr) reflected in an increase of the interplanar d -spacing and in the presence of an IR band at 960 cm^{-1} in the calcined sample, the intensity of which increases with increase in metal content of the material. Expansion of the unit cell volume calculated from Rietveld refinement of powder XRD patterns and absence of a separate oxide phase clearly indicate incorporation of metal atoms in the MFI lattice. Diffuse UV-vis reflectance and NMR spectral data support the general conclusions on the location and environment of metal ions. ^{29}Si MAS NMR spectra of TS-1 and ZrS-1 exhibited a broad peak around -116.9 ppm , which has been attributed to the distorted Si—O—Si bonds resulting from the presence of metal atoms in silicalite network and the intensity of the which increases with increase in the metal content. Fe-Mössbauer spectroscopic studies reveal that appearance of Fe^{2+} species in noticeable amounts (9 %) form upon reductive treatments. Since Fe^{3+} in the framework positions is more stable and do not reduce against as compared to the extra-framework positions, the appearance of Fe^{2+} indicates that major concentration of Fe is substituted in the framework. TG analysis shows that template decomposition temperature was shifted to higher temperature in the case of metal substituted MFI as compared to the silica polymorph.

2.5 References

1. R. Szostak, V. Nair, T.L. Thomas, *J. Chem. Soc., Faraday Trans.* 83 (1987) 487.
2. M. Taramaso, G. Perego, B. Notari, *US Pat.*, 4410501, 1983.
3. B. Rakshe, Veda Ramaswamy, S.G. Hegde, R. Vetrivel, A.V. Ramaswamy, *Catal. Letters*, 45 (1997) 41.
4. R. von Ballmoos, J. B. Higgins, *Collection of simulated XRD powder patterns for zeolites*, Second Revised Edition (Princeton, 1990).

5. Veda Ramaswamy, *Catalysis; Principles and Applications*, (2002) Ed., B. Viswanathan, S. Sivasanker, A.V. Ramaswamy, Narosa Publishing house, New Delhi.
6. A.C. Larson, R.B. Von Dreele, "General Structure Analysis System (GSAS)", Los Alamos National Laboratory Report LAUR 86-748 (2000).
7. B. Notari, *Catal. Today*, 18 (1993) 163.
8. H.M. Rietveld, *Acta. Crystallogr.* 22 (1967) 151.
9. A.C. Larson, R.B. von Dreele, GSAS Generalized structure analysis system, Laur 86-748, Los Alamos National Laboratory, Los Alamos, New Mexico, 1994.
10. H. van Koningsveld, H. van Bekkum, J.C. Jansen, *Acta Crystallogr.*, B43, (1987) 127.
11. H. van Koningsveld, J.C. Jansen and H. van Bekkum, *Zeolites*, 10 (1990) 235.
12. J. A. Melero, G. Calleja, F. Martínez, R. Molina, K. Lázár, *Micropor. Mesopor. Mater.*, 74 (2004) 11.
13. R.D. Shannon, *Acta. Cryst. A*, 32 (1976) 751.
14. S. Bordiga, R. Buzzoni, F. Geobaldo, C. Lamberti, E. Giamello, A. Zecchina, G. Leofanti, G. Petrini, G. Tozzola, G. Vlaic, *J. Catal.*, 158 (1996) 486.
15. Y. Han, X. Meng, H. Guan, Y. Yu, L. Zhao, X. Xu, X. Yang, S. Wu, N. Li, F. Xiao, *Micropor. Mesopor. Mater.*, 57 (2003) 191.
16. G. Berlier, G. Spoto, P. Fiescaro, S. Bordiga, A. Zecchina, E. Giamello, C. Lamberti, *Microchem. J.*, 71 (2002) 101.
17. M. Sasidharan, R. Kumar, *J. Catal.*, 220 (2003) 326.
18. A. Thangaraj, S. Sivasanker, P. Ratnasamy. *J. Catal.*, 131 (1991) 394.
19. M.R. Boccuti, K.M. Rao, A. Zecchina, *Stud. Surf. Sci. Catal.*, 48 (1988) 133.
20. T. Blasco, M.A. Cambor, A. Corma, *J. Am. Chem. Soc.*, 115 (1993) 1806.
21. G. R. Wang, X. Q. Wang, X. S. Wang, S. X. Yu, *Stud. Surf. Sci. Catal.*, 83 (1994) 67.
22. R. Szostak, T. L. Thomas, *J. Catal.*, 100 (1986) 555.
23. S. Bordiga, A. Damin, F. Bonino, C. Lamberti, *Top. Organomet. Chem.*, 16 (2005) 37.
24. M.R. Boccuti, K.M. Rao, A. Zecchina, G. Leofanti, G. Petrini, *Stud. Surf. Sci. Catal.*, 48 (1989) 133.

25. G. Richiardi, A. Damin, S. Bordiga, C. Lamberti, G. Spano, F. Rivetti, A. Zecchina, *J. Am. Chem. Soc.*, 123 (2001) 11409.
26. R. Szostak, *Molecular Sieves: Principles of Synthesis and Identification* (van Nostrand Reinhold, New York, 1989) p. 317.
27. P.J. Dirken, M.E. Smith, H.J. Whitfield, *J. Phys. Chem.*, 99 (1995) 395.
28. D. Scarano, A. Zecchina, S. Bordiga, F. Geobaldo, G. Spoto, G. Petrini, G. Leofanti, M. Padovan, G. Tozzola, *J. Phys. Chem.*, 89 (1993) 4123.
29. Z. Liu, R. L. Davis, *J. Phys. Chem.*, 98 (1994) 1253.
30. D.P. Serrano, M.A. Uguina, G. Ovejero, R. Van Grieken, M. Camacho, *Micropor. Mater.*, 4 (1995) 273.
31. A.J.H.P. van der Pol, A.J. Verduyn, J.H.C. van Hooff, *Appl. Catal., A* 92 (1992) 113.
32. M. Milanese, G. Artioli, A.F. Gualtieri, L. Palin, C. Lamberti, *J. Am. Chem. Soc.*, 125 (2004) 14549.
33. R. Millini, G. Perego, D. Berti, W. O. Parker Jr., A. Carati, G. Bellussi, *Micropor. Mesopor. Mater.*, 35-36 (2000) 387.
34. D.H. Brouwer, R.J. Darton, R.E. Morris and M.H. Levitt, *J. Am. Chem. Soc.*, 2005, 127, 10365.
35. G. Perego, G. Bellussi, C. Corno, M. Taramasso, F. Buonomo, A. Esposito. *Stud. Surf. Sci. Catal.*, 28 (1986) 129.
36. A. Tuel, Y.B. Taarit, *J. Chem. Soc. Chem. Commun.*, (1992) 1578.
37. a) T.J. Bastow, M.E. Smith, S.N. Stuart, *Chem. Phys. Lett.*, 191 (1992) 125.
b) J.S. Hartman, F.P. Koffyberg, J.A. Ripmeester, *Journal of Magnetic Resonance* 91 (1991) 400.
38. R. Burns, *Hyperfine Interactions* 91 (1994) 739.
39. A. Meagher, V. Nair, R. Szostak, *Zeolites*, 8 (1988) 3.
40. K. Lazar, G. Borbely, H. Beyer, *Zeolites*, 11 (1991) 214.

Chapter **3**

Thermal Expansion Behavior Of Silicalite And Metallosilicate Molecular Sieves

3.1 Introduction

Zeolites and metallosilicate molecular sieves have opened a new class of compounds, which shows specific catalytic properties in alkylation, isomerisation, oxidation and hydroxylation reactions. Many of such reactions are carried out at a temperature greater than 623 K using catalysts, which are calcined more than 773 K. During activation of the catalysts one may need to heat these materials at a temperature of 1023 K. Hence zeolites and molecular sieves used as catalysts need to have the appropriate thermal and hydrothermal stability to withstand the extreme conditions frequently involved in their use and regeneration. Thus, the information regarding the stability of these materials is necessary. Zeolites and molecular sieves are metastable materials. Their stability is different in different environments *viz.*, acidic or alkaline. They are stable to ionizing radiation and can be used to adsorb radioactive cations. There are very few reports in literature for the thermal stability studies of zeolites and molecular sieves, carried out by using *in-situ* high temperature X-ray diffraction (HTXRD) technique *e.g.*, manganese silicalite-1 (MnS-1) [1] aluminophosphate-17 (AlPO₄-17) [2], and ZrS-1 [3] molecular sieves. Apart from the thermal stability, the understanding of the zeolites and molecular sieves behavior upon heating is of great importance, since only in the dehydrated or calcined state and under operating conditions (high temperature), the sorptive and catalytic properties and molecular sieve effects are observed. Upon heating, zeolites undergo different kinds of structural changes including: i) cell volume contraction due to the removal of water and/or templating organic molecules (dehydration and calcination); ii) displacive or reconstructive phase transformation(s) to more or less metastable phase(s); iii) structural collapse; iv) structural breakdown (*i.e.* complete amorphization); v) negative thermal expansion (NTE).

High temperature XRD technique has been used to study the zeolites and molecular sieves *viz.*, pure silica zeolites ITQ-1, ITQ-3, and SSZ-23 [4], ITQ-4 [5], faujasite [6], ZSM-5 [7-9], and AlPO-5 [7] and AlPO-17 [2], and these materials are reported to exhibit strong negative thermal expansion on heating. P. Lightfoot *et al.* [10] reported that ITQ-5, ITQ-7, ITQ-9 and MAPO-17 molecular sieve materials shows NTE while CIT-5 and AlPO-31 have shown positive thermal expansion (PTE) upon heating. Computational studies [11-13] have predicted the probable new materials that show contraction of the lattice on heating. The negative thermal expansion properties of these materials are reported to be dependant totally on the

framework structures and chemical content of the framework. In connection with this, the PTE reported for CIT-5 and AIPO-31 in literature is attributed to their one-dimensional channel systems and high framework density. It is reported that MAPO-17 molecular sieve has shown less NTE than AIPO-17, which is attributed to the dependence of thermal behavior on chemical content of the framework. Strength of NTE in the MFI type molecular sieve material is reported to be affected by isomorphous substitution of Si by heteroatom [14], *i.e.* the thermal expansion coefficients depend on the chemical composition of the framework. The adsorbed and absorbed water species also affect the thermal behavior of ZSM-5 zeolites and make this behavior complex at high temperature when water is removed from the framework [9]. This dependence of NTE on the chemical composition has opened the wide area for the researchers to study the NTE in the similar framework materials with different chemical composition.

Different types of mechanisms have been reported that are responsible for the contraction of these materials when heated. One route to observe NTE is based on increasing the symmetry of polyhedra with increasing temperature [15]. A second mechanism for NTE is actually caused by the normal PTE of certain M-O bonds [16]. A third mechanism for negative thermal expansion is based on interstitial cations within a network changing sites as a function of temperature [17]. A fourth mechanism for NTE is based on the transverse thermal motion of oxygen in M-O-M linkages [18, 19]. Requirements for negative thermal expansion by the transverse thermal motion of oxygen include an open framework structure with oxygen in two-fold coordination. The transverse thermal vibrations of Si-O-Si linkages in zeolites and metallosilicate molecular sieves are reported to be responsible for NTE exhibited by these materials [20]. The reason for the NTE observed over large temperature region in the zeolites and molecular sieves is still unclear and insufficiently understood in the case of zeolites and molecular sieves.

Research interest is increasing day by day on the materials exhibiting NTE. Materials that display NTE are being investigated both because of their technological interest and scientific curiosity. No metallosilicate molecular sieve materials are studied for their high temperature behavior till to date. So we have studied the thermal stability of silicalite-1 and metallosilicate molecular sieves such as Fe-silicalite-1, TS-1 and ZrS-1 from the data obtained on the stability studies, we have selected the temperature range for NTE experiments. We have also studied the NTE

in CFS- ∞ molecular sieve in the range 373-673K with detailed structural analysis. Full Rietveld analysis has been carried out to look in to the changes taking place in the bond distances and bond angles of the framework as a function of temperature, to explain the NTE behavior in this type of material. There are no reports on the thermal behavior of metal substituted MFI type materials with variable Si/M ratios. So we made an attempt to study the thermal expansion behavior of metal substituted MFI type structures with different Si/M ratios (M=Fe³⁺, Ti⁴⁺ and Zr⁴⁺). The HTXRD studies have been carried out in the temperature range 373-773 K. Rietveld analyses have been carried out to look in to the changes taking place in the cell parameters as a function of temperature. The effect of isomorphous substitution of Si⁴⁺ by heteroatom and compositional dependence of the thermal behavior is studied.

3.2 Experimental

3.2.1 Collection of XRD patterns for thermal stability studies

Calcined samples CFS- ∞ , CFS-50, CTS-50 and CZS-50 (Chapter 2, Section 2.2) were subjected to *in-situ* HTXRD experiments to observe the structural stability of the sample as a function of temperature. The HTXRD data were recorded on a Philips X'Pert Pro 3040/60 XRD unit equipped with Anton Paar HTK 1600 attachment. Alumina was used as the standard for calibration of the high temperature stage. A small amount of sample was mounted on a platinum strip, which serves as the sample stage as well as the heating element. A Pt/Rh-13% thermocouple spot-welded to the bottom of the stage was used for measuring the temperature. The HTXRD patterns were scanned in the 2θ range 5–55° with a step size of 0.02° and a rate of 1° min⁻¹ for two typical samples CFS- ∞ and CZS-50 using Ni-filtered Cu-K α radiations ($\lambda=1.54187\text{\AA}$). While the HTXRD patterns were scanned for CTS-50 and CFS-50 samples, in the 2θ range 5–60° with a step size of 0.02° and a rate of 1° min⁻¹ using Fe-filtered Co-K α ($\lambda=1.7903\text{\AA}$) radiation. Scintillation counter was the detector employed for the data collection of all the samples. The patterns were scanned between 298 K (room temperature) and 1623 K in static air. The powder patterns were recorded at temperature intervals of 150 K from 423 to 1623 K. A heating rate of 10 K min⁻¹ and a soaking time of 10 min were employed. The XRD profiles were refined using X'Pert plus refining package provided by Philips to obtain information on the lattice parameters and the phase composition.

3.2.2 Data collection for negative thermal expansion studies

The data collection is done for various samples using different radiation targets (Cu and Co), temperature ranges, and temperature intervals for different purposes. The details of the same are given in Table 3.1. For detailed structural analysis, the HTXRD patterns of CFS- ∞ sample in the temperature range 373–673K were collected. The 2θ region of 10–60° was scanned in the continuous mode with a step size of 0.0167 and a time 20 s/step using Ni filtered Cu K α radiation ($\lambda = 1.5406\text{\AA}$) and X'celerator as detector. A small amount of silicon (NIST, USA, $a = 5.4311\text{\AA}$) as an internal standard was added to the sample. The sample thickness was ~0.5mm which was mounted on a platinum strip (cavity), which serves as the sample stage as well as the heating element. Diffraction patterns were collected at every 50 K interval. A heating rate of 10 K min⁻¹ and a soak time of 10 min were applied. Bragg–Brentano geometry was employed. The optics used in the incident beam (primary) were 0.04 radian sollar slit, ½° divergence slit and 10 mm mask, and 0.02 radian sollar slit in the secondary beam path. The X-ray data reported here pertains to only the orthorhombic phase, which exists in the temperature range 373 - 673 K, since this is the structure that is most relevant to catalysis.

The HTXRD patterns for the metallosilicate molecular sieves FeS-1, TS-1 and ZrS-1 with different Si/M ratio (Si/M = 50, 75, 100 and ∞ , where M = Fe, Ti and Zr) were collected in the temperature range 373-773 K. Data was collected for the 2θ region 5-60° in the continuous mode with a step size of 0.0167°, time per step was 20 seconds, using Ni filtered Cu K α radiation ($\lambda = 1.5406\text{\AA}$) and X'celerator as detector. Diffraction patterns were collected at every 50 K interval from 373 to 773 K. Bragg–Brentano geometry was employed. The same strategy was applied for the data collection of all the samples. The XRD profiles were refined to obtain information about the variations in the cell parameters as a function of temperature. The linear coefficient of thermal expansion (CTE) ' α ' is calculated by following equation:

$$\alpha = \frac{L - L_0}{L_0(T - T_0)} \quad (3.1)$$

where L_0 and L are the values of the lattice constant at temperatures T_0 (initial temperature) and T , respectively. The volume coefficient of thermal expansion α_v is calculated by following equation:

$$\alpha_v = \frac{V - V_o}{V_o(T - T_o)} \quad (3.2)$$

where V is the volume and T the temperature.

Table 3.1 List of different conditions for the data collection on the various metallosilicate molecular sieves in the different temperature ranges and different 2θ ranges.

Sample	Target	Temp. Range	Temp. Interval	2θ range	Purpose
CFS- ∞ & CZS-50	Cu	298-1623 K	150 K	5-55°	Thermal Stability
CFS-50 & CTS-50	Co	298-1623 K	150 K	5-60°	Thermal Stability
CFS- ∞	Cu	373-673 K	50 K	10-60°	NTE studies
FeS-1 (Si/Fe = 50, 75, 100 and ∞)	Cu	373-773 K	50 K	5-60°	NTE studies
TS-1 (Si/Ti = 50, 75, 100 and ∞)	Cu	373-773 K	50 K	5-60°	NTE studies
ZrS-1 (Si/Zr = 50, 75, 100 and ∞)	Cu	373-773 K	50 K	5-60°	NTE studies

3.2.3 Rietveld refinement

The HTXRD patterns collected were refined using the Rietveld method [21]. The unit cell parameters at each temperature were refined with the Rietveld method using the GSAS [22] package and the EXPGUI graphical interface [23], which allows proper treatment of the instrumental aberration parameters, such as the goniometer shift and the sample displacement parameters. The goniometer zero correction was applied with respect to Si as standard, and the sample displacement as a function of temperature was determined manually from the Si reflection (111) at different temperatures. The starting atomic coordinates and thermal parameters for the

silicalite-1 phase in the orthorhombic symmetry (space group $Pnma$ (62)) were taken from the X-ray crystal structure of H-ZSM-5 determined by van Koningsveld [24]. It was decided to exclude the reflections from Pt and Si rather than model them as additional phases in the diffraction patterns. The pseudo-Voigt peak profile function, with up to 17 refinable parameters, was chosen and the peaks were truncated at 0.01% of the peak maxima. Background intensity was modeled by a Chebyshev type I polynomial function with 16 background parameters. An overall scale factor, the cell parameters, and the sample displacement parameter were simultaneously refined. Because of the complexity of the structure, soft restraints were applied to Si–O bond distances ($1.59 \pm 0.05 \text{ \AA}$) with a suitable weighting factor, which was gradually reduced as the refinement proceeded. Framework atoms of the same element type were constrained to have the same isotropic thermal displacement parameters. The Rietveld refinement of PXRD pattern of metallosilicate molecular sieves collected at various temperatures was carried out in the similar way.

For FeS-1, TS-1 and ZrS-1 samples Fe, Ti and Zr respectively, were not included in the original models. Atomic coordinates, isotropic thermal parameters and site occupancy factors were kept constant throughout the refinement of the HTXRD data of metallosilicate molecular sieves.

3.3 Results and discussion

3.3.1 Thermal stability analysis

Multiple plot of the *in-situ* HTXRD patterns of CFS- ∞ sample in air at various temperatures from 298-1323 K are shown in Figure 3.1. Appearance of α -cristobalite phase is seen in the HTXRD profile at 1023 K and the structure of silicalite-1 collapses completely at 1173 K. Figure 3.2 shows the HTXRD profiles of CFS-50 from 298 K to 1323 K and after cooling to room temperature. Appearance of α -cristobalite phase was observed at 1173 K and the MFI structure decomposed to α -cristobalite (SiO_2) at 1323 K. In the case of tetravalent metallosilicate analogues, CTS-50 and CZS-50, the material is even stable up to 1623 K. The *in-situ* HTXRD patterns of calcined CTS-50 and CZS-50 samples from 298 to 1623 K are shown in Figure 3.3 and 3.4, respectively. There is marked decrease in intensity of all reflections in CTS-50 and CZS-50 samples decreases in the XRD pattern collected at temperature 1473 and 1623 K, which may be due to the partial amorphization of

zeolitic phase at such a high temperature. The CFS- ∞ and CFS-50 samples show a lower thermal stability as compared to CTS-50 and CZS-50 samples. The siliceous end member of the TS-1 and ZrS-1 family *i.e.* CTS- ∞ and CZS- ∞ are stable upto 1023 K (not shown) and there is absence of α -cristobalite phase and the results are discussed in later portion of this chapter (*vide section 3.3.3*).

One of the reasons behind this is likely due to, the source of Si used for synthesis of these materials. CFS- ∞ and CFS-50 samples were synthesized using sodium silicate as a silicon source and hence Na⁺ ion is present in the channels of both the materials. It is reported that the thermal stability of sodium zeolites of the MFI family differs from one sample to another according to the method of preparation; it increases regularly as the Na content of the crystals is reduced [25]. Our results are in well agreement with these results where Na containing molecular sieves *viz.*, CFS- ∞ and CFS-50 were decomposed at 1023 K and 1173 K respectively where as CTS-50 and CZS-50 were found to be stable upto 1623 K. The thermal stability of the exchanged zeolites/molecular sieves depends strongly on the identity of the exchanged cation, the structure of the zeolite host, and the ion-exchange conditions chosen for the experiment [26]. Structures of the zeolites get damaged due to the interaction of the zeolite framework with acidic species formed within the micropores. The temperature of framework collapse depends mainly on the silicon content of the zeolite and the framework damage caused by the ion exchange. The formation of α -cristobalite does not seem to result from direct conversion of MFI \rightarrow α -cristobalite; it commences only after the zeolite phase has become wholly, or largely, amorphous. After the heat-induced collapse of the framework structure, an amorphous phase is formed from the zeolite precursors, followed by the crystallization of dense silicate phase.

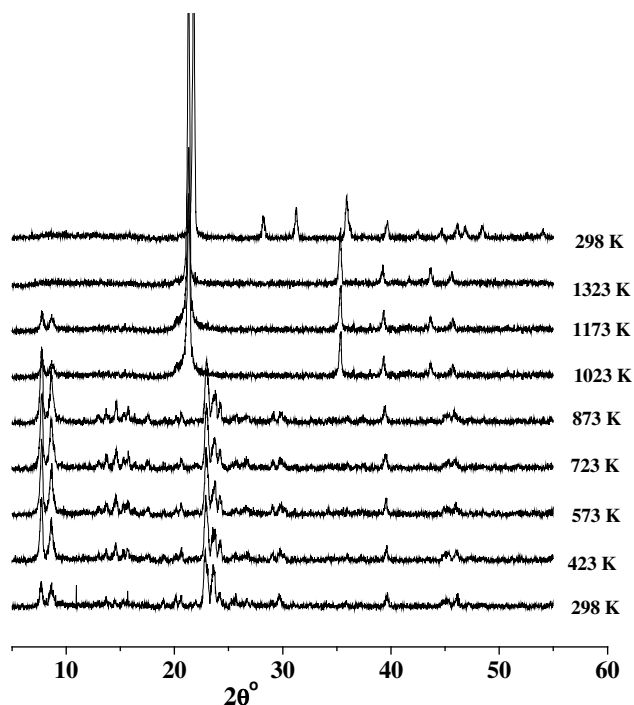


Fig. 3.1 The multiple plots of powder XRD patterns of the calcined the silicalite-1 sample scanned in air at various temperatures at 298 K and from 423 K to 1323 K at 150 K intervals and again at 298 K after cooling.

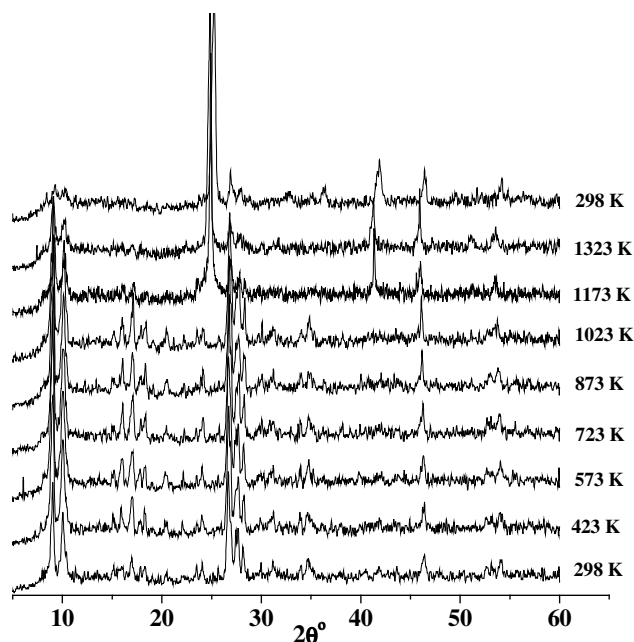


Fig. 3.2 The multiple plots of powder XRD patterns of the CFS-50 sample scanned in air at various temperatures at 298 K and from 423 K to 1323 K at 150 K intervals and again at 298 K after cooling.

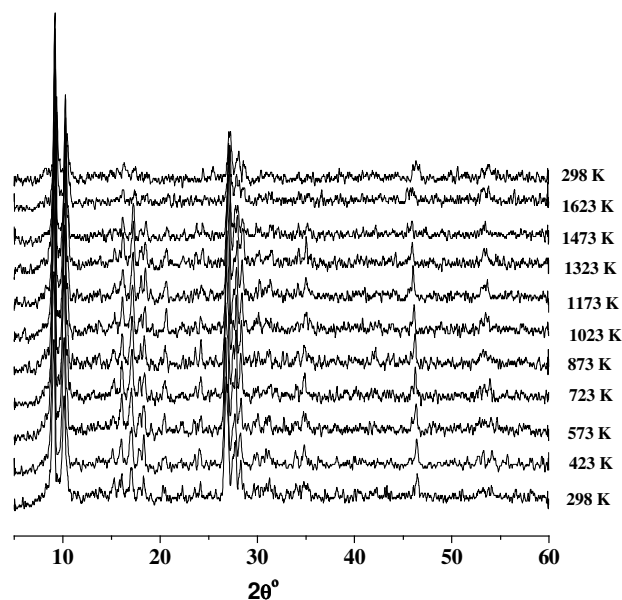


Fig. 3.3 The multiple plots of powder XRD patterns of the CTS-50 sample scanned in air at various temperatures at 298 K and from 423 K to 1623 K at 150 K intervals and at 298 K after cooling.

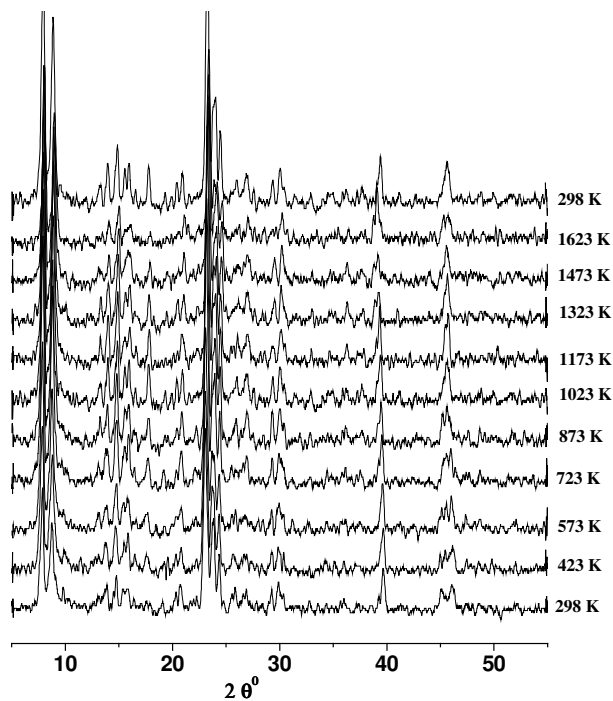


Fig. 3.4: The multiple plots of powder XRD patterns of the CZS-50 sample scanned in air at various temperatures at 298 K and from 423 K to 1623 K at 150 K intervals and at 298 K after cooling.

Siliceous zeolites have higher thermal stability provided that they have no defects in the framework structure [27]. Petrovic *et al.* [28] have carried out detailed thermochemical studies regarding the stability of frameworks in high silica zeolites ZSM-5, ZSM-11, ZSM-12, SSZ-24 and faujasite to correlate the crystal structure with stability. They have reported that decrease in Si-O-Si angle below 140° is the major destabilizing factor in these materials. K. de Boer *et al.* [29] have also shown a linear relationship between the destabilization and the percentages of angles smaller than or equal to 140° in the structures. The Si-O-Si bond angle below 140° does not exist for a large number of structures. Since we could not do the refinement of the HTXRD profiles (which are scanned fast and the counting statistics are not good), we could not calculate the bond angles in CFS-∞ and CFS-50 to correlate the Si-O-Si bond angles with the destabilization from the present data. The thermal contraction in the framework structure is likely due to the decrease in T-O-T angles with increase of temperature. The destabilizing factor for the thermally weaker CFS-∞ at 1023 K is likely due to the defects in the framework and also due to the distortion of the tetrahedra in its flexible framework and its anharmonic vibrations resulting in decrease of the Si-O-Si bond angles. CFS-∞ and CFS-50 decomposes to α -cristobalite which is the stable phase having 6 membered rings in its framework. In the case of CFS-50, the lower charge of Fe³⁺ requires charge compensation thereby producing lattice strain sufficient to promote decomposition of that material at 1173 K. The main reason for the lower thermal stability of CFS-∞ and CFS-50 was the presence of extraframework cations in the channels. On the other hand, in the case of CTS-50 and CZS-50, the flexibility of the framework for the isomorphous substitution of Si⁴⁺ by the larger cation Ti⁴⁺ and Zr⁴⁺ is depending on the composition of the cations and the framework density.

Table 3.2: Framework density and thermal expansion coefficients of CFS-∞, CFS-50, CTS-50 and CZS-50 in temperature range 298-1023 K.

Sample	FD/1000 (\AA^3)	α_a	α_b	α_c	α_V	α
CFS-∞	17.95	-5.76	-0.49	-0.62	-6.75	-2.25
CFS-50	17.82	-2.76	-4.72	-5.54	-12.91	-4.30
CTS-50	17.88	-7.33	-3.74	-5.04	-16.02	-5.34
CZS-50	17.93	-8.24	-4.50	-5.25	-17.92	-5.97

Flexibility of zeolite framework is to some extent, revealed by the possible variation in the framework density of the structure, which depends on the composition and pore volume. The framework density calculated using the unit cell volume (from XRD data) of the four samples is given in Table 3.2. The data in Table 3.2 reveal that the flexibility of CFS-50 is less than the corresponding Ti and Zr analogues (reflected in framework density value). Subtle difference in electrostatic and covalent bond interactions in CFS-50 lowers the thermal stability as compared to the covalent interactions in CTS-50 and CZS-50. Van Santen and co workers have extensively studied the lattice relaxation of silica [30] and AlPO_4 polymorphs [31] and have reported the relative importance of the electrostatic vs. covalent interactions in structural stability. Comparison of volume thermal expansion coefficients and framework density of CFS-50, CTS-50 and CZS-50 (Figure 3.5) with respect to temperature shows that the strength of contraction increases with the increase in framework density. Lower the framework density higher is the NTE. Higher the framework density of the metallosilicate molecular sieves having MFI structure higher is the stability. The effect of ‘T’ atoms (T= Fe, Ti and Zr) on the thermal stability can thus be correlated to the framework density determined experimentally.

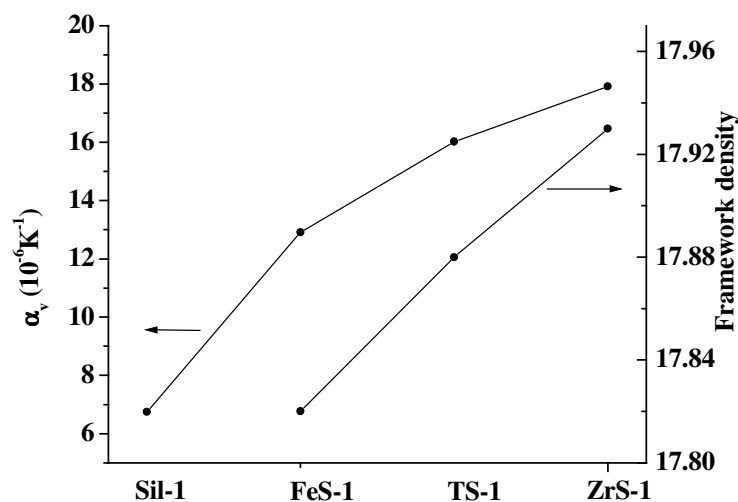


Fig.3.5 Comparison of the variation of framework density and volume thermal expansion coefficient in CFS-∞, CFS-50, CTS-50 and CZS-50 samples.

According to Woodcock *et al.* [32], transverse vibrations of Si-O-Si/M bridging oxygen are responsible for negative thermal expansion (NTE) in zeolite

systems. Transverse vibrations of these bonds give rise to negative thermal expansion of materials. Table 3.2 gives the lattice/volume thermal expansion coefficient (TEC) of CFS- ∞ , CFS-50, CTS-50 and CZS-50 samples. Lattice or volume thermal expansion coefficient was calculated using the formula, $\alpha_v = \Delta V / (T - RT) V_{RT}$ where T and RT are the typical temperature of the scan and room temperature respectively, ΔV is the difference in the unit cell volume of the material at T and RT. All the materials show the negative thermal expansion coefficients in the studied temperature range and called as negative thermal expansion (NTE). NTE is anisotropic in all the materials, it is more along 'a' and 'c' axes than 'b' axes in CTS-50 and CZS-50 and it is more along 'b' and 'c' than 'a' axes in CFS-50. Lattice thermal expansion coefficients (α_v) in temperature range 298-1023 K were $-6.75 \times 10^{-6} \text{ K}^{-1}$ for CFS- ∞ , $-12.91 \times 10^{-6} \text{ K}^{-1}$ for CFS-50, $-16.02 \times 10^{-6} \text{ K}^{-1}$ for CTS-50 and $-17.92 \times 10^{-6} \text{ K}^{-1}$ for CZS-50. Isomorphous substitution of Si^{4+} by Fe^{3+} , Ti^{4+} and Zr^{4+} in the framework has increased the thermal stability of the material with respect to CFS- ∞ and the strength of NTE is increased to 2 to 3 times (Table 3.2). The highest lattice thermal expansion coefficient (α_v) was $-11.53 \times 10^{-6} \text{ K}^{-1}$ for CFS-50 in the temperature range 298-1173 K, $-20.86 \times 10^{-6} \text{ K}^{-1}$ for CTS-50 and $-25.54 \times 10^{-6} \text{ K}^{-1}$ for CZS-50 respectively, in the temperature range 298-1623 K. The difference in the magnitude of NTE is likely due to the composition and nature of heteroatom present in the lattice. The strength of negative thermal expansion increases in this order, CZS-50 > CTS-50 > CFS-50 > CFS- ∞ .

The very strong NTE coefficients observed is likely due to the transverse vibration of the bridging oxygen in 2 fold co-ordination between two polyhedrons causing a shortening of Si-Si non-bonding distance [33, 16]. Due to the low torsional and bending frequencies of the T-O-T bond, the zeolite lattice is highly flexible. When the topology of the zeolite framework requires the adaptation of bond lengths and bond angles, T-O-T angle and bond length changes are more preferred over deformation of the tetrahedra [31]. The transition metal substituted zeolites are used for different applications. Whatever application is planned, the zeolite, the exchange conditions, and the thermal conditions have to be chosen with care. From the results of these studies we have planned our rest of the experiments below the temperature 773 K.

3.3.2 Detailed structural analysis of silicalite-1 for negative thermal expansion (NTE) studies

Temperature resolved PXRD patterns collected over the temperature range 373-673 K in 50 K intervals are shown Figure 3.7. It is clear from the Figure 3.7 that silicalite-1 material under examination shows orthorhombic phase in the temperature range studied corroborating with the literature data. The data quality of the scan is comparatively good due to the X'celerator detector, which uses the RTMS (real time multiple strip) technology enhancing both the resolution and intensity of the reflections. We do not observe any phase transition in the temperature range 373-673 K.

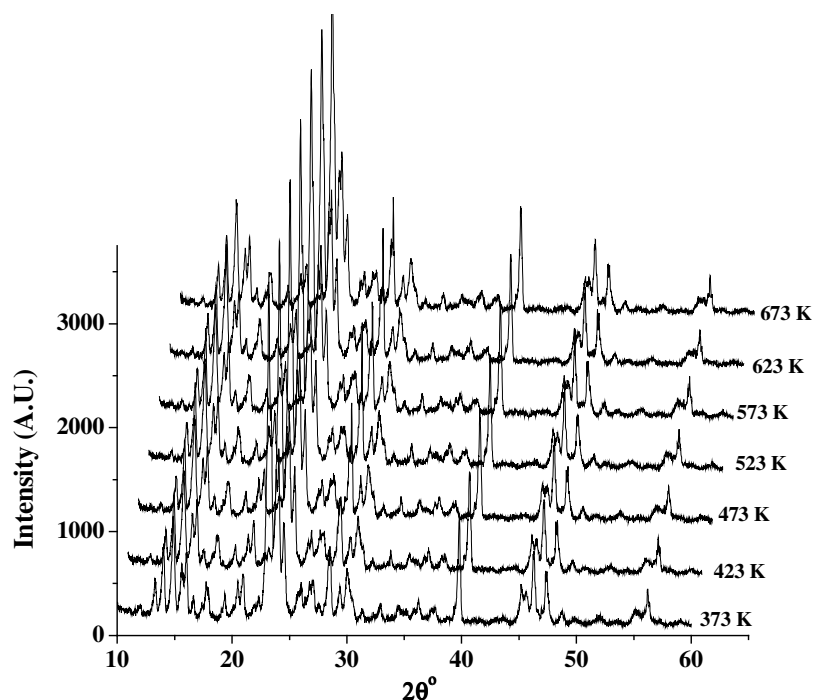


Fig.3.7 Multiple plot of powder XRD patterns of silicalite-1 as function of temperature scanned in air from 373 to 673 K at 50 K intervals.

Information regarding unit cell parameters as a function of temperature is extracted from Rietveld refinement technique. Quality of the Rietveld refinement is monitored through R_{wp} -values from the fit. The agreement between the experimental and the simulated diffraction patterns after Rietveld refinement of the powder XRD pattern collected at 373 K is shown in Figure 3.8.

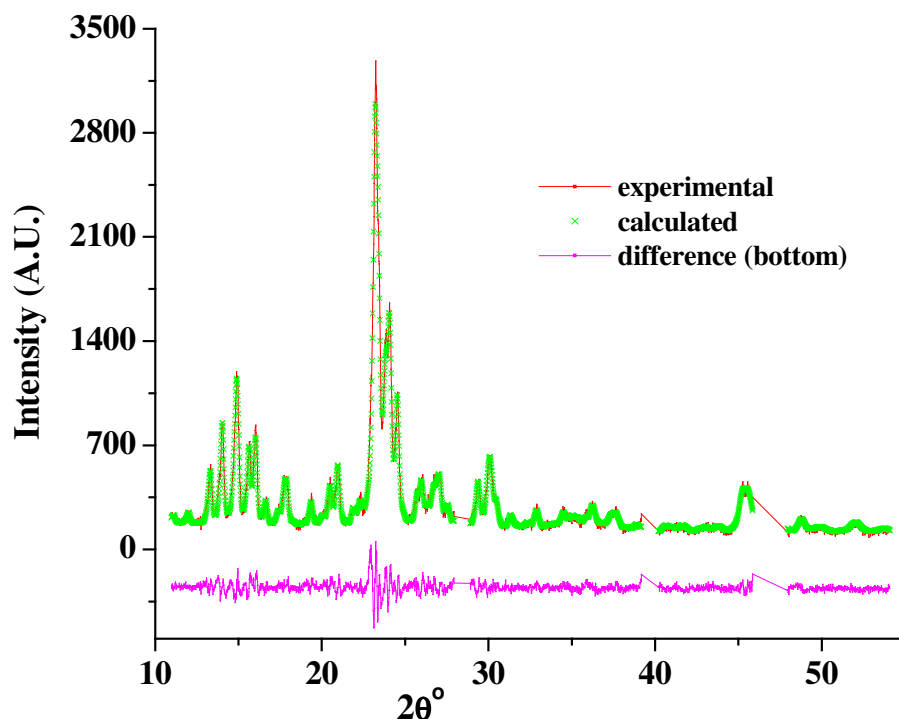


Fig.3.8 Rietveld refinement of the powder XRD pattern collected at 373 K, showing the experimental, calculated and difference plots. (The 2θ region 27.9-28.9 and 39.2-40.2 and 45.9-47.9 shows the gap for excluded reflections of Si and Pt respectively.)

All the details of the Rietveld refinement at 373 K are listed in Table 3.3. R_{wp} values for all the fits were below 10.0 %. Unit cell parameters obtained from Rietveld refinement technique have been plotted as a function of temperature, which is shown in Figure 3.9. The error bars shown are according to estimated standard deviation from the Rietveld refinement. These values at different temperatures were used in further calculations of the thermal expansion coefficient values. Although, there is no appreciable change in the unit cell volume in the temperature range 373-423K, yet there is contraction along a axis, expansion along b axis and no change in the c direction. In the temperature range 473-673K, the thermal contraction is anisotropic along the three crystallographic axes. The extent of thermal contraction along a (0.026 Å) axis is comparatively more than along b (0.005 Å) and c (0.010 Å) axes. Unit cell volume in the overall temperature range 373-673 K decreased from 5342.80 to 5330.64 Å³. There is overall negative thermal expansion in the temperature range 373-673 K.

Table 3.3: Crystallographic data and experimental conditions for the Rietveld refinement of silicalite-1 (scan at 373K scan).

Sample	Silicalite-1
Formula	Si ₉₆ O ₁₉₂
Crystal system	Orthorhombic
Space group	<i>Pnma</i>
<i>a</i> (Å)	20.087(2)
<i>b</i> (Å)	19.875(2)
<i>c</i> (Å)	13.383(2)
<i>V</i> (Å ³)	5342.82(9)
λ (Å)	1.5406
2θ range (°)	10–60
Step size (° 2θ)	0.0167
No. of data points	2342
R_p (%)	7.52
R_{wp} (%)	9.52
Red. χ^2	2.72
Background function	Shifted Chebyshev 16-coefficients
Profile function	Pseudo-Voigt

The thermal expansion coefficient calculated according to the Equation 3.1 along *a* axis (α_a) is $-4.314 \times 10^{-6} \text{ K}^{-1}$ in the temperature range 373-673 K. The thermal expansion along *b* axis is marginal as compared to *a* axis. The thermal expansion coefficients along *b* axis and along *c* axis (α_b) are $-0.838 \times 10^{-6} \text{ K}^{-1}$ and (α_c) = $-2.490 \times 10^{-6} \text{ K}^{-1}$ respectively, in the temperature range 373-673 K. Lattice thermal expansion coefficient (α_v) in the overall temperature range 373-673K is $-7.586 \times 10^{-6} \text{ K}^{-1}$. Figure 3.10 shows the plot of 2θ shift due to sample displacement with respect to temperature, which shows a systematic increase in sample displacement as the temperature increases. This sample displacement was determined from the refinement of the reflections of the ‘Si’ material used as internal standard. These values for sample displacement were used for the correction in the HTXRD patterns.

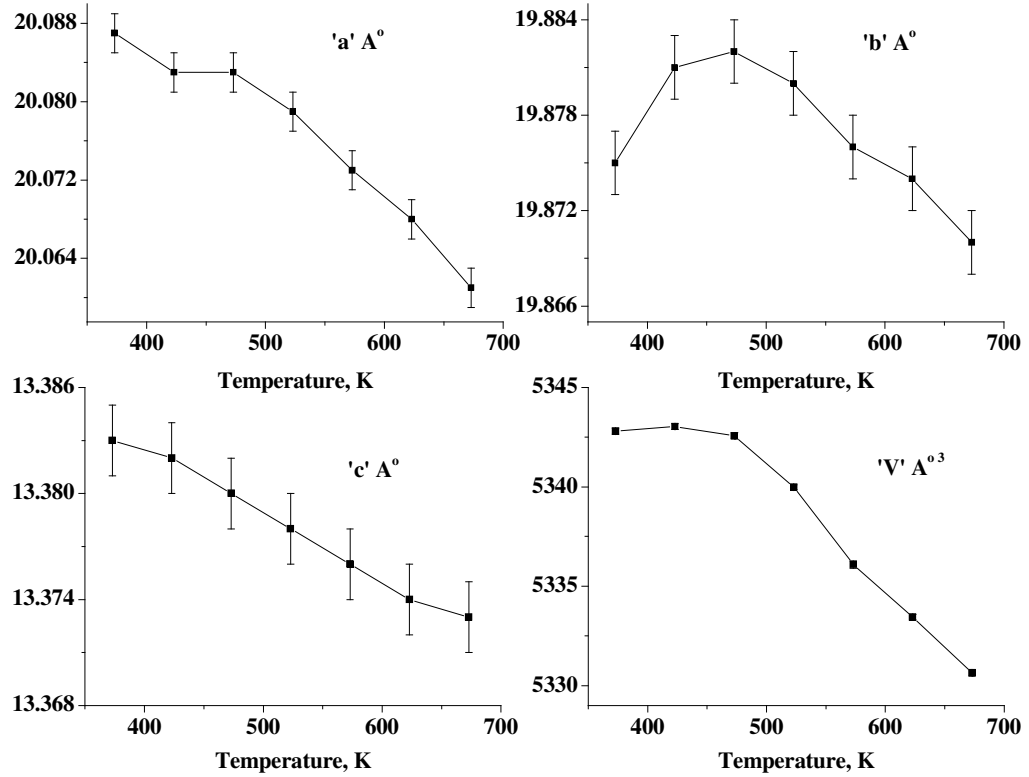


Fig. 3.9 Variation of unit cell parameters a (Å), b (Å), c (Å) and V (Å³) with temperature for silicalite-1 (373-673 K).

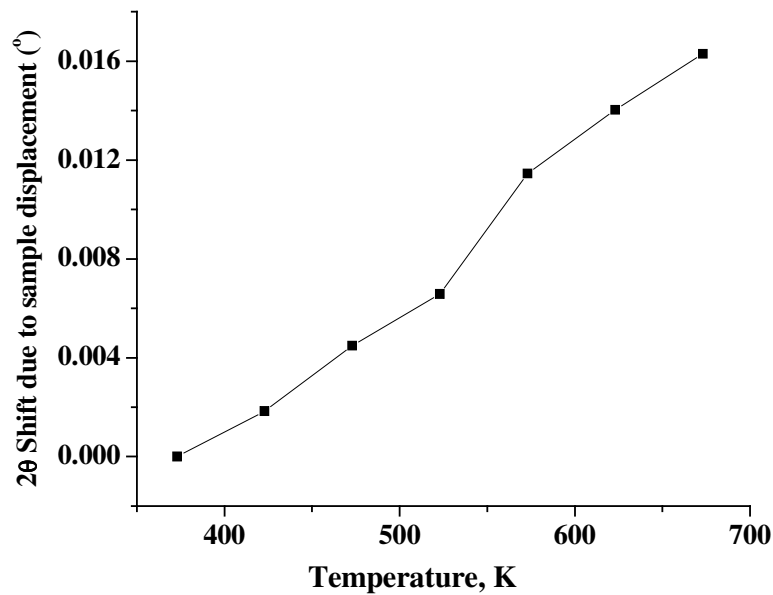


Fig. 3.10 2θ shift due to sample displacement as a function of temperature.

Refinement of the fractional coordinates of the constituent atoms has been carried out to observe the changes in the structure as a function of temperature. The results from the Rietveld refinement of the XRD patterns at seven temperatures between 373 and 673 K in steps of 50 K enabled us to gain more insight into the structural changes responsible for the negative thermal expansion in silicalite-1. MFI framework in the *Pnma* space group has twenty-six Si-O-Si bonds present in the unit cell. The bond angles and bond distances were calculated from the final refinement data to look for any change with respect to increase in temperature. Figure 3.11 shows changes in Si₁-O distances as a function of temperature. There is no appreciable change in the Si₁-O bond distances as a function of temperature. These changes in Si-O distances are nearly equal to the estimated standard deviation (0.002Å) of the Rietveld refinement.

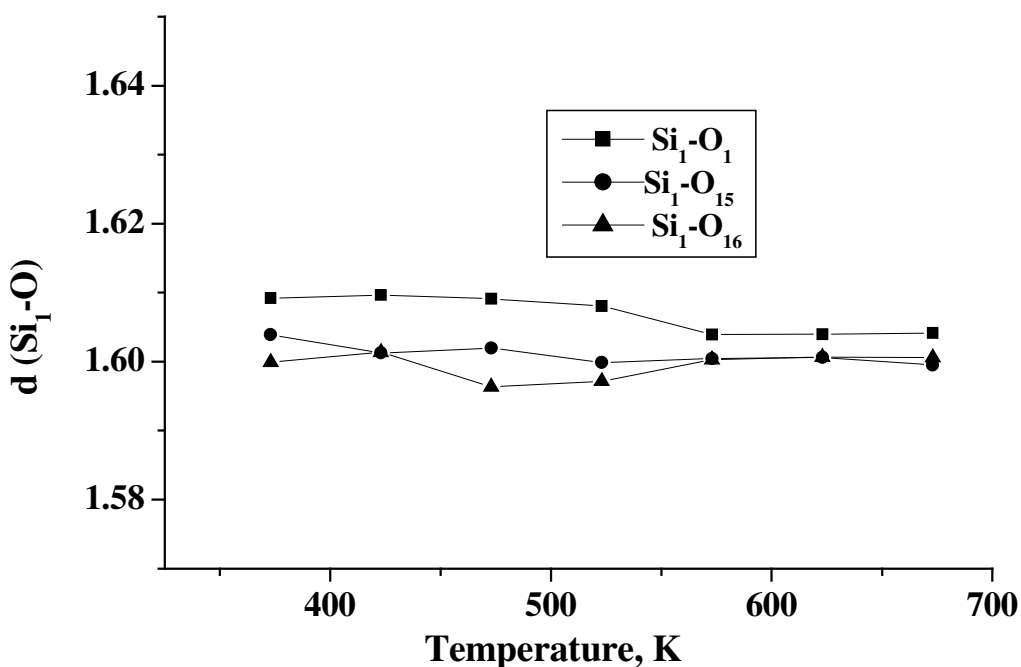


Fig. 3.11 Variation of different Si₁-O bond distances as a function of temperature.

The changes in the average Si₁-O bond distances and averaged Si-O-Si bond angle as a function temperature are plotted in Figure 3.12. Since there was no regular trend in the change in Si-O-Si bond angles, we have averaged them, which decreases from 153° to 149°. The average Si₁-O distance remains approximately constant as a function of temperature. All other Si_n-O (where n= 2 to 12) bonds show fairly same

trend in their behavior. Hence, changes in Si-O bond distances do not seem to be responsible for the contraction of the framework.

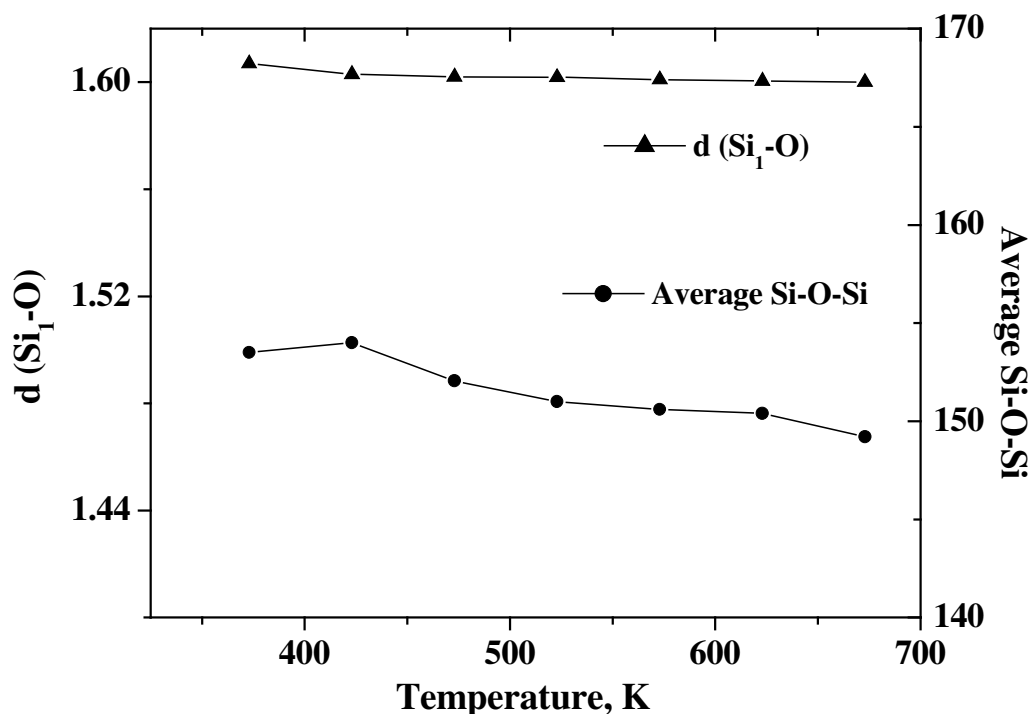


Fig. 3.12 Average changes in $d(\text{Si}_1\text{-O})$ and Si-O-Si bond angles with temperature.

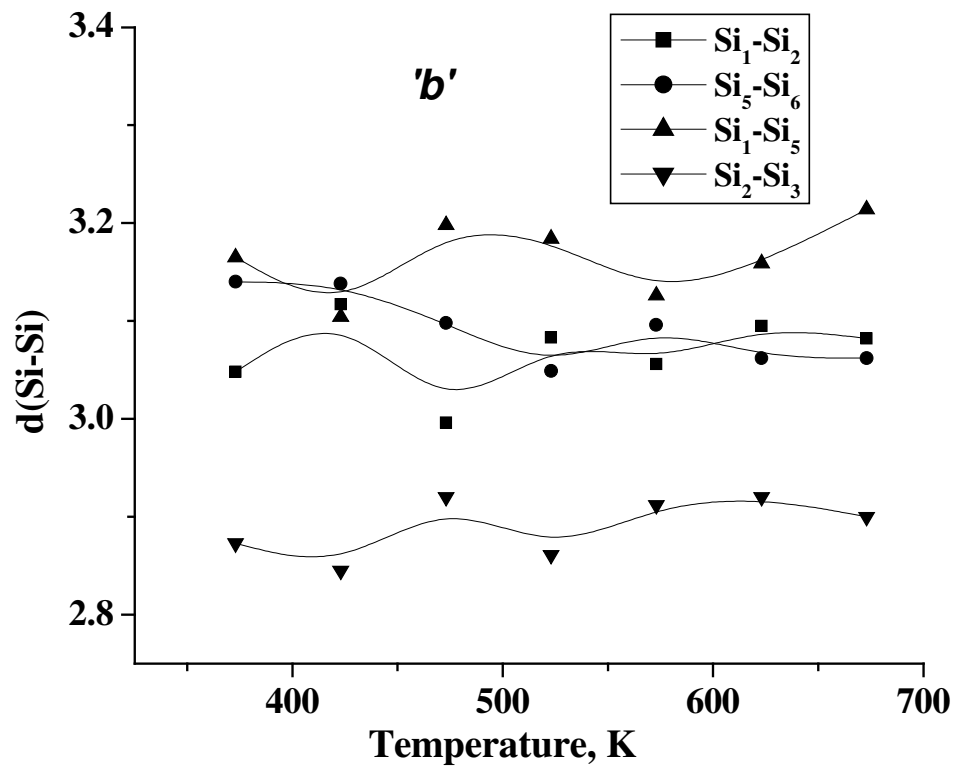
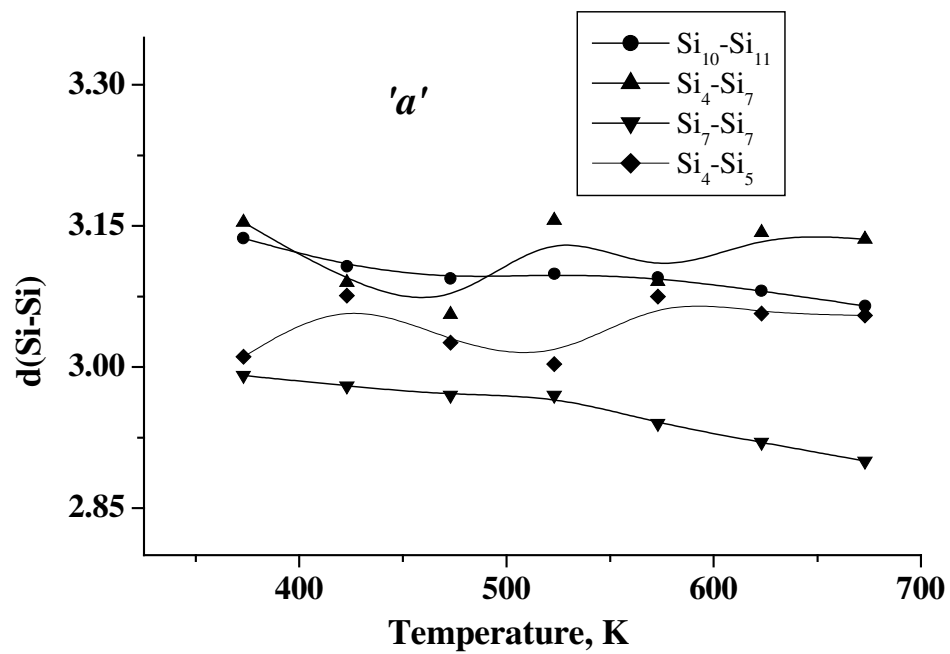
Changes in Si-Si non-bonding distances as a function of temperature may affect the three crystallographic axes and the change is more predominant when its inter atomic vector has its major component parallel. Orientation of the Si-Si vectors with the crystallographic axis is calculated by taking the cosine function of the angle made by Si-O-Si bond with that axis. A change in a particular Si-O-Si bond angle can be said to have strongly contributed to a change in that axis, if $\cos\theta$ is greater than ~ 0.7 (*i.e.*, $\theta < \sim 45^\circ$) as suggested by Bull *et al.* [34]. Angle made between each of Si-O-Si vectors and three crystallographic axes in silicalite-1 in *Pnma* space group are listed in Table 3.4 along with the calculated $\cos\theta$ values. Along the crystallographic axis *a*, there are eight Si-Si distances ($\cos\theta > 0.7$), for which the inter atomic vectors are having their major components parallel to *a* axis. The bond distances Si₃-Si₁₂, Si₄-Si₅, Si₄-Si₇, Si₇-Si₇, Si₉-Si₉, Si₁₀-Si₁₀, Si₁₀-Si₁₁ and Si₁₂-Si₁₂ are the distances for which major components of the Si(O)Si interatomic vectors are parallel to *a* axis. There is

decrease in d (Si-Si) for the Si₃-Si₁₂, Si₄-Si₇, Si₇-Si₇, Si₁₀-Si₁₁ and Si₁₂-Si₁₂ and the major decrease in d (Si-Si) is for Si₇-Si₇ (0.14 Å) and Si₁₂-Si₁₂ (0.086Å).

Table 3.4: Angles θ and $\cos \theta$ made between each of the Si(O)Si vectors and the three crystallographic axes.

Bonds	θ_a	θ_b	θ_c	$\cos\theta_a$	$\cos\theta_b$	$\cos\theta_c$
Si ₁ -O ₁ -Si ₂	59.18	39.50	67.85	0.512	0.772	0.377
Si ₂ -O ₂ -Si ₃	49.45	45.17	73.55	0.650	0.705	0.283
Si ₃ -O ₃ -Si ₄	88.89	89.31	1.30	0.019	0.012	0.999
Si ₄ -O ₄ -Si ₅	19.20	84.66	71.62	0.944	0.093	0.315
Si ₅ -O ₅ -Si ₆	79.13	32.68	59.60	0.188	0.842	0.506
Si ₂ -O ₆ -Si ₆	54.04	55.09	55.08	0.587	0.572	0.572
Si ₇ -O ₇ -Si ₈	67.00	23.34	86.22	0.391	0.918	0.066
Si ₈ -O ₈ -Si ₉	81.23	20.14	72.02	0.152	0.939	0.309
Si ₉ -O ₉ -Si ₁₀	89.67	86.40	3.61	0.006	0.063	0.998
Si ₁₀ -O ₁₀ -Si ₁₁	32.40	69.42	66.14	0.844	0.352	0.404
Si ₁₁ -O ₁₁ -Si ₁₂	89.76	25.19	64.81	0.004	0.905	0.426
Si ₈ -O ₁₂ -Si ₁₂	53.78	50.16	60.63	0.591	0.641	0.490
Si ₂ -O ₁₃ -Si ₈	79.13	89.04	10.91	0.189	0.017	0.982
Si ₅ -O ₁₄ -Si ₁₁	52.40	89.13	37.62	0.610	0.015	0.792
Si ₁ -O ₁₅ -Si ₁₀	48.89	72.93	46.06	0.657	0.293	0.694
Si ₁ -O ₁₆ -Si ₄	58.79	50.49	55.14	0.518	0.636	0.572
Si ₄ -O ₁₇ -Si ₇	17.72	74.04	82.50	0.952	0.275	0.130
Si ₆ -O ₁₈ -Si ₉	48.12	70.71	48.14	0.666	0.330	0.667
Si ₃ -O ₁₉ -Si ₆	58.86	51.95	53.57	0.517	0.616	0.594
Si ₃ -O ₂₀ -Si ₁₂	27.33	64.83	80.04	0.888	0.425	0.173
Si ₁ -O ₂₁ -Si ₅	77.77	23.47	70.29	0.212	0.917	0.337
Si ₇ -O ₂₂ -Si ₁₁	74.08	16.27	86.75	0.274	0.960	0.057
Si ₇ -O ₂₃ -Si ₇	10.89	90.00	79.11	0.982	0	0.188
Si ₁₂ -O ₂₄ -Si ₁₂	3.33	90.00	86.67	0.998	0	0.058
Si ₉ -O ₂₅ -Si ₉	35.45	90.00	54.55	0.815	0	0.580
Si ₁₀ -O ₂₆ -Si ₁₀	29.99	90.00	60.01	0.866	0	0.499

The changes in some of these Si-Si non-bonding distances are given in Figure 3.13 (a), which show a major change in $d(\text{Si-Si})$ as a function of temperature.



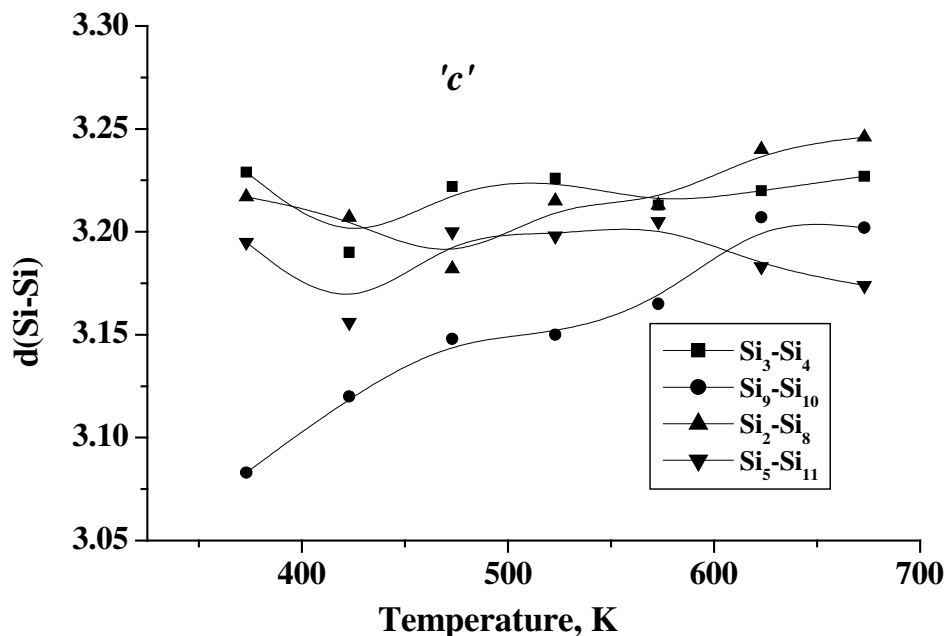


Fig. 3.13 Variation in the Si-Si non-bonding distances as a function of temperature. The three graphs (a-c) show those vectors, which are having their largest components parallel to the three crystallographic axes *a*, *b* and *c* respectively.

Along *b* axis there are also eight Si-Si non-bonding distances, for which the inter atomic vectors have their major components parallel to *b* axis and these distances are Si₁-Si₂, Si₁-Si₅, Si₂-Si₃, Si₅-Si₆ (Figure 3.13 b), Si₇-Si₈, Si₇-Si₁₁, Si₈-Si₉ and Si₁₁-Si₁₂ (not shown). There is an expansion in the lattice along *b* axis as a function of temperature from 373 to 423 K. The non-bonding distances of Si₁-Si₅, Si₂-Si₃ and Si₁₁-Si₁₂ whose vector components are parallel to *b* axis increase as a function of temperature. The major changes are seen only in the distances of the Si₇-Si₈ (0.039 Å) and Si₁₁-Si₁₂ (0.116 Å), which are increasing, and Si₅-Si₆ (0.078 Å) and Si₈-Si₉ (0.095 Å), which are decreasing, as a function of temperature in the range 373-673 K. Along the *c* axis there are only four Si-Si distances, for which the inter atomic vectors have their major components oriented parallel to the *c* axis. The non-bonding distance of the Si₃-Si₄ and Si₉-Si₁₀ increases as a function of temperature, while there is a decrease in the non-bonding distances of the Si₂-Si₈ and Si₅-Si₁₁ (Figure 3.13 c), which may cause the contraction along the *c* axis.

One of the reasons for the anisotropy in the negative thermal expansion behavior in silicalite-1 along three crystallographic axes is likely due to the layered

structure of the MFI material. In MFI type of material there is stacking of the two dimensional layer along a axis (Figure 3.14 a). This two dimensional layer is in bc plane (Figure 3.14 b and c). This stacking makes silicon atoms to be more denser along b and c directions as compared to a direction.

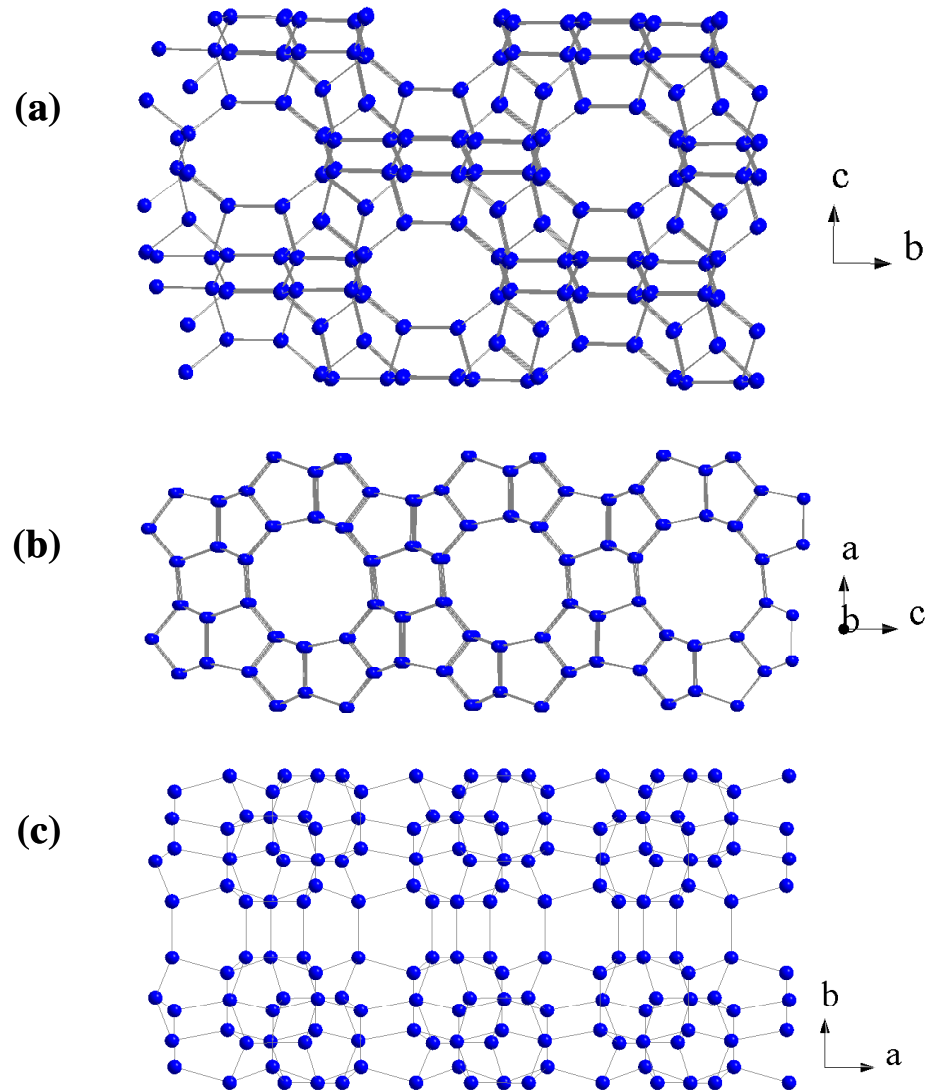


Fig. 3.14 Framework topology of silicalite-1 having MFI structure. The silicon atoms are shown in blue and oxygen atoms are not shown for sake of clarity. (a) Shows the view along 100 axis (b) Shows the view along 010 axis (c) Shows the view along 001 axis.

These dense Si portions may be acting as condensed matter and resisting to contract. While there is greater porous portion along a axis and hence Si framework may be getting easily contracted. Hence, there may be more reduction along the axis in which there is stacking of these layers in the bc plane. The thermal behavior of the ferrierite material studied so far in the literature [34] can also be explained in the same way. Ferrierite material has a layered structure. These layers are in the ab direction and are stacked along c axis and a large contraction in the c axis in that material as compared to a and b axes is reported. Sleight *et al.* [35] also described anisotropic thermal expansion in cordierite and β -eucryptite in the same way. In both cordierite and β -eucryptite, there are layers of polyhedra, which expands horizontally (ab direction) and as the layers undergo thermal expansion, they are pulled together in the other directions; as a result there is contraction along c direction.

The bond angles and bond distances in SiO_4 remain unchanged in the temperature range studied indicating the rigid tetrahedral nature of SiO_4 units. From these results, one can conclude that the negative thermal expansion of silicalite-1 is related to the transverse vibrations of the two-coordinate bridging oxygen atoms, a mode of lattice vibration, which can easily get excited with low energy input. This can induce a coupled rotation of the essentially rigid SiO_4 tetrahedra. There are no systematic changes in refined atomic coordinates and bond angles calculated in the present study. The Si-Si distances decreases due to the transverse vibration of two corner sharing oxygen atoms, and the constituent Si-O bond distance remain approximately constant. These vibrations can take place in a correlated fashion as phonon modes that do not change Si-O bond length but do excite transverse Si-O-Si vibrations, which are called rigid unit modes (RUM) [36]. This confirms that presence of rigid unit modes are responsible for the NTE observed in silicalite-1. To correlate the changes in individual Si-O-Si angles with the associated Si-O bond lengths as a function of temperature, a typical plot is shown in Figure 3.15 for a set of two bond lengths $\text{Si}_1\text{-O}_1$ and $\text{Si}_2\text{-O}_1$ along with the $\text{Si}_1\text{-O}_1\text{-Si}_2$ bond angle. It shows that the bond length is approximately constant while the bond angles decreases, supporting the presence of rigid unit modes.

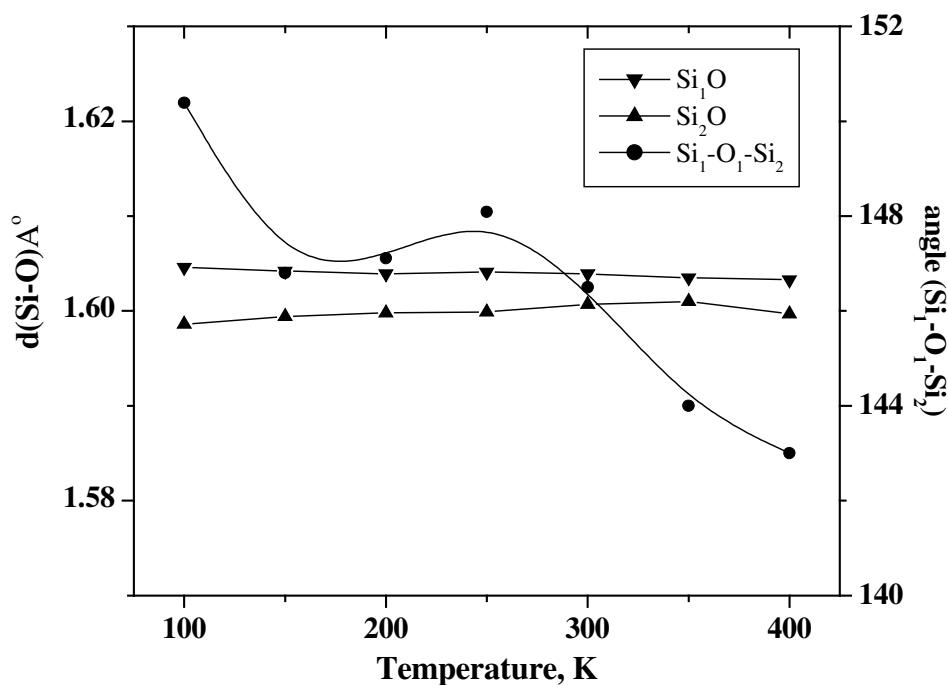


Fig. 3.15 The changes in individual $\text{Si}_1\text{-O}_1\text{-Si}_2$ angles with the associated Si-O_1 bond lengths as a function of temperature.

The variation in the trend seen in temperature range 473-573 K could probably be due to the displacive phase transformation within the same space group or any other mechanism. From the Figure 3.13 (a-c), one can conclude that the Si-Si non-bonding distances decreases as a function of temperature. This decrease in the Si-Si non-bonding distances is a result of the transverse vibrations of bridging oxygen atoms (two fold coordination) between two rigid polyhedrons, which is responsible for the NTE observed. This is also discussed as intrinsic mechanism of negative thermal expansion in the literature [9]. The high temperature thermal behavior of the material of this type is also explained by molecular dynamic simulation studies, which also infers that the bending of Si-O-Si linkages and rotation of SiO_4 tetrahedra play an important role in NTE [38]. After refinement of powder patterns collected at 373 K and 673 K, we have measured the distance between $\text{O}_5\text{-O}_{11}$ and $\text{O}_{21}\text{-O}_{22}$ atoms in the rings using Diamond 2.1c software.

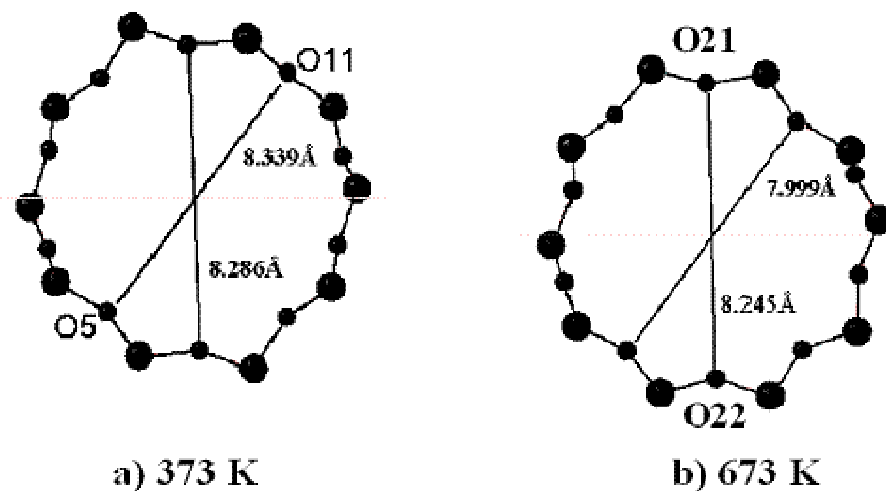


Fig.3.16 Pictorial representation of how the rings and cavities change dimension with temperature (straight channel) are shown for the sample scanned at a) 373 K and b) 673 K.

The dimensions of the straight channel showed a decrease with increase in temperature, which is pictorially illustrated in Figure 3.16. The distance between the O_5 - O_{11} and O_{21} - O_{22} decreases as a function of temperature from 8.339Å and 8.286Å at 373 K to 7.999Å and 8.245Å at 673 K, respectively.

3.3.3 NTE behavior of metal incorporated molecular sieves

The thermal-expansion properties [38] of substances are very important in materials design; for example, cracks may generate when materials expand or contract by different amounts, on heating. The most famous example of a substance that contracts when heated is ice: it transforms into water, which has a higher density than ice. Negative thermal expansion (NTE) in solids is relatively rare, although examples have been found in zeolites [39]. Negative thermal expansion (NTE) behavior is an exotic material property with attractive potential applications, most notably in moderating the predominantly positive thermal expansion (PTE) behavior of materials, particularly those in high precision applications where instability associated with temperature fluctuation often reduces performance. It is assumed that NTE is usually caused by transverse thermal motion of oxygen or a cation. The basic rule is that the oxygen (or a cation) coordination should not exceed two. Other important factors are the density of the structure and the size of the cations.

Negative thermal expansion was recently discovered in a large family of zeolites and molecular sieves with the open framework structure. For this behavior of these materials, transverse vibrations of Si-O-Si linkages present in the structure are held responsible. The structure of zeolites made up of tetrahedral arrangement of SiO₄ units in three dimensions. The SiO₄ tetrahedra share corners to form a network structure where every oxygen atom is bound to two silicon atoms. The negative thermal expansion is attributed to transverse thermal motion of oxygen in the Si-O-Si linkages. These motions of the oxygen atoms may be correlated by considering them to be based on rocking motions of the connected polyhedra. In this type of structure, these rocking motions can only occur, if the tetrahedra undergo slight change in the shape during the rocking. Therefore, rigid tetrahedra inhibit the rocking motion and inhibit negative thermal expansion. A major factor enhancing the rigidity in polyhedra is anion-anion repulsion. In case of transition metal incorporated metallosilicate molecular sieves the MO₄ tetrahedra become larger due to larger cation size, the oxygen-oxygen distances within the tetrahedra increase and oxygen-oxygen repulsions are diminished. Thus, we can expect transition metal cations with larger ionic radii incorporated into the molecular sieves to give enhanced negative thermal expansion. To test this hypothesis, we have measured the thermal expansion of various metallosilicate molecular sieves *viz.*, FeS-1, TS-1 and ZrS-1.

Materials that exhibit negative thermal expansion (NTE) behavior are of particular interest for their ability to compensate for the positive thermal expansion (PTE) observed in other materials. Applied in this way, NTE/PTE composites can be tuned to exhibit a preferred intermediate (*e.g.*, zero) thermal expansion behavior. Once considered rare, NTE has been reported in an increasingly wide range of materials, including members of the oxides, zeolite, cyanides, and Prussian blue structural families. The mechanism responsible for NTE behavior in these materials is generally well understood: on an elementary level, thermally induced transverse vibrational motion of bridging oxide has the effect of drawing their metal-atom “anchors” closer together. Indeed, both expansion and contraction upon sorption of guests have been observed in various zeolites. However, the effect of Si/M ratio on thermal expansion behavior within zeolite materials remains unclear. Given that NTE properties are dependent on lattice dynamic effects in siliceous zeolites, which may be perturbed by the isomorphous substitution of hetero elements, an exploration of the dependence of NTE on heteroatom substitution of such systems is of fundamental interest. Here in this section, we have studied the dependence of NTE on Si/M ratio for FeS-1, TS-1 and ZrS-1 metallosilicate molecular sieves.

To study the effect of different Si/M ratios on the negative thermal expansion behavior of the MFI framework, we have carried out HTXRD studies on the calcined analogue of FeS-1, TS-1 and ZrS-1 materials (having Si/M ratio 50, 75, 100 and ∞) in the temperature range 373–773 K. The multiple plot of XRD patterns collected at different temperatures for CFS-50 sample is shown in Figure 3.17. The information regarding unit cell parameters is obtained from Rietveld refinement of the powder XRD patterns as a function of temperature. The variations in the unit cell dimensions and volume for the FeS-1 samples CFS- ∞ , CFS-100, CFS-75 and CFS-50 with different Si:M ratios over a temperature range of 373–773 K are given in Table 3.5, Table 3.6, Table 3.7 and Table 3.8, respectively. Thermal expansion coefficients are calculated for the temperature range 373–773 K. Figure 3.18 shows the variation of thermal expansion coefficients in the temperature range 373–773 K for CFS- ∞ , CFS-100, CFS-75 and CFS-50 samples *i.e.* with increasing Fe concentration. The magnitude of the thermal expansion coefficient shows an increasing trend from the sample CFS- ∞ to CFS-50 sample and there is linear relationship between the thermal expansion coefficients of the framework and the Fe concentration in the framework.

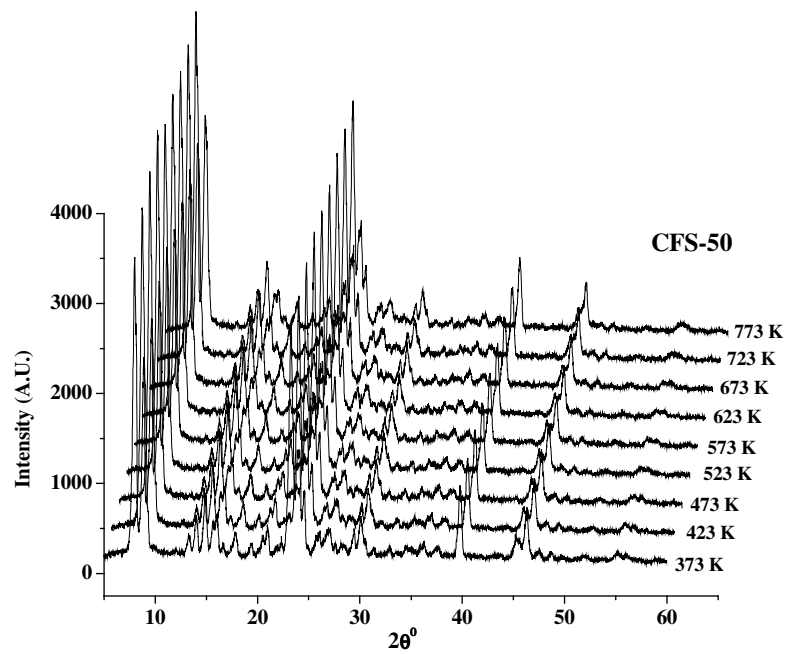


Fig. 3.17 Evolution of CFS-50 diffraction patterns in the temperature range 373-773 K.

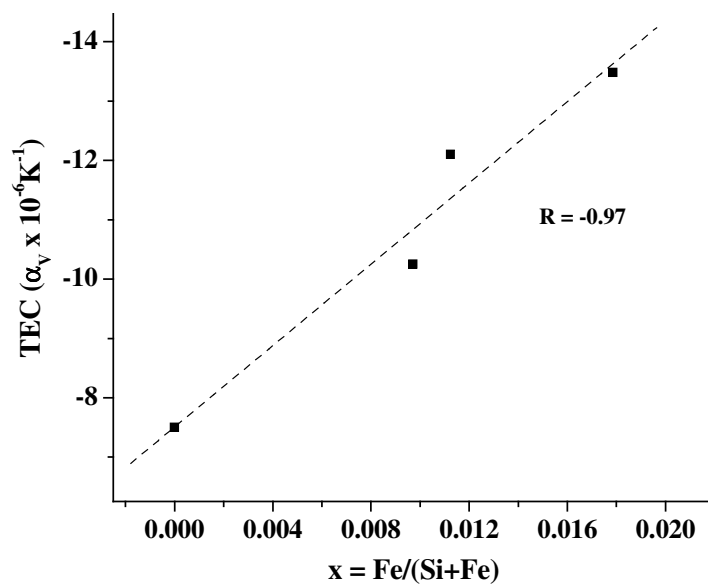


Fig. 3.18 Volume thermal expansion coefficients versus concentration of Fe in the framework 'x' ($\text{Fe}/(\text{Si}+\text{Fe})$) in the temperature range 373-773 K.

Table 3.5: Variation of cell parameters and unit cell volume with temperature obtained from HTXRD analysis of CFS-∞.

T, K	'a' Å	'b' Å	'c' Å	'V' Å ³	$\alpha_V \times 10^{-6} \text{K}^{-1}$
373	20.087	19.875	13.383	5343	--
423	20.083	19.881	13.382	5343	0
473	20.083	19.882	13.38	5342	-1.87
523	20.079	19.88	13.378	5340	-3.74
573	20.073	19.876	13.376	5336	-6.55
623	20.068	19.874	13.374	5333	-7.49
673	20.061	19.87	13.373	5331	-7.49
723	20.058	19.868	13.371	5329	-7.49
773	20.056	19.867	13.368	5327	-7.49

Table 3.6: Variation of cell parameters and unit cell volume with temperature obtained from HTXRD analysis of CFS-100.

T, K	'a'	'b'	'c'	'V'	$\alpha_V \times 10^{-6} \text{K}^{-1}$
373	20.118	19.913	13.399	5367	----
423	20.114	19.912	13.396	5364	-11.18
473	20.112	19.912	13.395	5364	-5.59
523	20.105	19.908	13.392	5361	-7.45
573	20.099	19.903	13.39	5357	-9.32
623	20.097	19.901	13.388	5355	-8.94
673	20.094	19.889	13.386	5350	-10.56
723	20.092	19.887	13.385	5348	-10.11
773	20.087	19.884	13.383	5345	-10.25

Table 3.7: Variation of cell parameters and unit cell volume with temperature obtained from HTXRD analysis of CFS-75.

T, K	'a'	'b'	'c'	'V'	$\alpha_V \times 10^{-6} \text{K}^{-1}$
373	20.121	19.911	13.405	5371	----
423	20.116	19.91	13.402	5368	-11.17
473	20.114	19.91	13.399	5366	-9.31
523	20.108	19.905	13.397	5362	-11.17
573	20.105	19.903	13.395	5360	-10.24
623	20.1	19.897	13.395	5357	-10.42
673	20.094	19.893	13.393	5354	-10.55
723	20.09	19.887	13.39	5350	-11.17
773	20.084	19.878	13.389	5345	-12.10

Table 3.8: Variation of cell parameters and unit cell volume with temperature obtained from HTXRD analysis of CFS-50.

T, K	'a'	'b'	'c'	'V'	$\alpha_V \times 10^{-6} \text{K}^{-1}$
373	20.114	19.928	13.416	5378	-----
423	20.112	19.928	13.416	5377	-3.72
473	20.104	19.927	13.418	5375.5	-4.65
523	20.101	19.923	13.414	5372	-7.44
573	20.096	19.92	13.409	5368	-9.29
623	20.087	19.916	13.407	5364	-10.41
673	20.08	19.908	13.403	5358	-12.39
723	20.072	19.905	13.4	5354	-12.75
773	20.067	19.9	13.395	5349	-13.48

Negative thermal expansion of CFS-50 is very high ($\alpha_V = -13.48 \times 10^{-6} \text{K}^{-1}$) for the 373–773 K temperature range. CFS-50 shows negative thermal expansion along all three unit-cell axes as is expected for large cation present in framework structure. The origin of high NTE is likely due to the polyhedral flexibility of MFI

structure and the large ionic size of Fe^{3+} . The mechanism of NTE in zeolite family is the rocking motion, back and forth of semi-rigid polyhedra due to the correlated transverse thermal vibrations of two-fold coordinated oxygens. In zeolites, this mechanism cannot function without further distortions of building tetrahedra with the increasing temperature. These distortions occur more easily in large polyhedra, where oxygen-oxygen repulsive interactions are minimized.

Similarly, we have studied the variations in unit cell parameters as a function of temperature in the case of TS-1 and ZrS-1 having different Si/M (M = Ti and Zr) ratio. The information regarding unit cell parameters is obtained from Rietveld refinement of the powder XRD patterns collected as a function of temperature. The multiple plots of XRD patterns collected at different temperatures for CTS-50 sample are shown in Figure 3.19. The variation of cell parameters and unit cell volume of CTS- ∞ , CTS-100, CTS-75 and CTS-50 materials as a function of temperature are given in Table 3.9, Table 3.10, Table 3.11 and Table 3.12, respectively. Thermal expansion coefficients are calculated in the temperature range 373-773 K. Figure 3.20 shows the comparison of thermal expansion coefficients in the temperature range 373-773 K for CTS- ∞ , CTS-100, CTS-75 and CTS-50. The negative value of thermal expansion coefficients was enhanced for the CTS-50 sample to $-14.4 \times 10^{-6} \text{ K}^{-1}$ than that for the CTS- ∞ sample where it was $-9.83 \times 10^{-6} \text{ K}^{-1}$. The volume thermal expansion coefficients for CTS-75 and CTS-100 samples in the temperature range 373-773 K were $-12.59 \times 10^{-6} \text{ K}^{-1}$ and $-11.21 \times 10^{-6} \text{ K}^{-1}$, respectively.

The multiple plots of XRD patterns collected at different temperatures for CZS-50 sample are shown in Figure 3.21. The variation of cell parameters and unit cell volume of CZS- ∞ , CZS-100, CZS-75 and CZS-50 samples as a function of temperature are given in Table 3.13, Table 3.14, Table 3.15 and Table 3.16, respectively. Thermal expansion coefficients are calculated for the temperature range 373-773 K. The volume thermal expansion coefficients of these materials are compared for the temperature range 373-773 K. Figure 3.22 shows the comparison of thermal expansion coefficients in the temperature range 373-773 K for CZS-50, CZS-75, CZS-100 and CZS- ∞ . The magnitude of thermal expansion coefficient was increased by some amount for the CZS-50 sample to $-11.67 \times 10^{-6} \text{ K}^{-1}$ than that for the CZS- ∞ sample where it was $-10.76 \times 10^{-6} \text{ K}^{-1}$. The volume thermal expansion coefficients for CZS-75 and CZS-100 samples in the temperature range 373-773 K were nearly same ($-11.20 \times 10^{-6} \text{ K}^{-1}$).

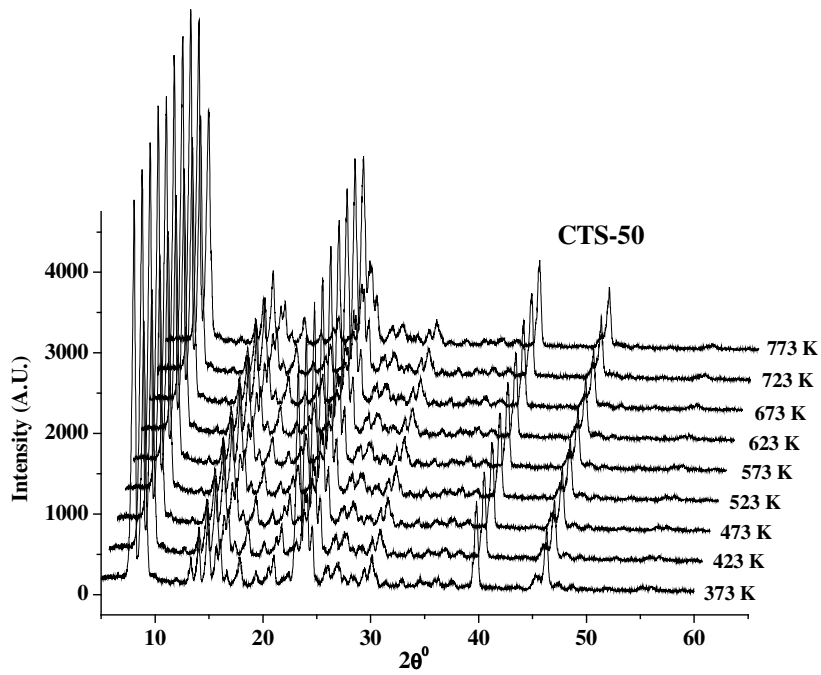


Fig. 3.19 Evolution of CTS-50 diffraction patterns in the temperature range 373-773 K.

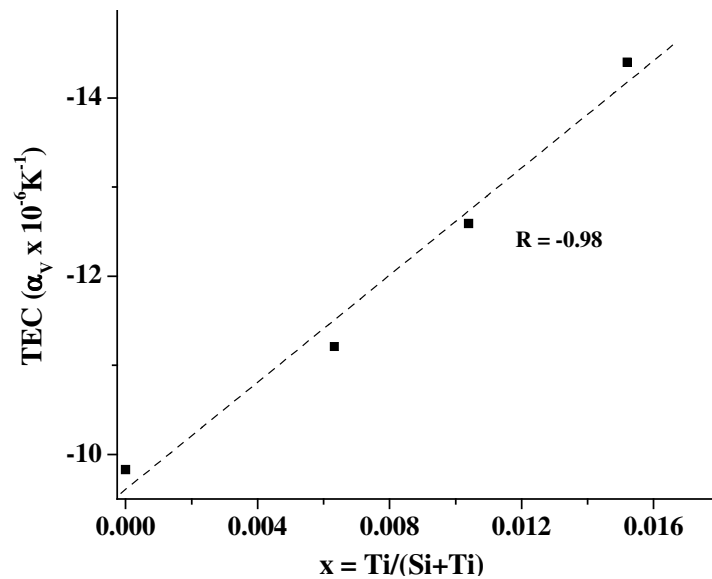


Fig. 3.20 Volume thermal expansion coefficients versus concentration of Ti in the framework 'x' ($\text{Ti}/(\text{Si}+\text{Ti})$) in the temperature range 373-773 K.

Table 3.9: Variation of cell parameters and unit cell volume with temperature obtained from HTXRD analysis of CTS-∞.

T, K	'a' Å	'b' Å	'c' Å	'V' Å ³	$\alpha_V \times 10^{-6} \text{K}^{-1}$
373	20.058	19.874	13.392	5338	----
423	20.056	19.872	13.391	5337	-3.75
473	20.045	19.872	13.389	5333	-9.36
523	20.043	19.87	13.389	5332	-7.49
573	20.04	19.869	13.378	5327	-10.30
623	20.03	19.868	13.377	5323	-11.24
673	20.027	19.863	13.375	5321	-10.61
723	20.025	19.858	13.374	5318	-10.70
773	20.022	19.856	13.374	5317	-9.83

Table 3.10: Variation of cell parameters and unit cell volume with temperature obtained from HTXRD analysis of CTS-100.

T, K	'a'	'b'	'c'	'V'	$\alpha_V \times 10^{-6} \text{K}^{-1}$
373	20.091	19.901	13.391	5354	----
423	20.092	19.9	13.39	5354	0
473	20.087	19.9	13.389	5352	-3.73
523	20.08	19.897	13.388	5349	-6.22
573	20.075	19.892	13.382	5344	-9.34
623	20.066	19.887	13.378	5339	-11.21
673	20.062	19.883	13.376	5336	-11.21
723	20.059	19.88	13.373	5333	-11.21
773	20.055	19.877	13.37	5330	-11.21

Table 3.11: Variation of cell parameters and unit cell volume with temperature obtained from HTXRD analysis of CTS-75.

T, K	'a'	'b'	'c'	'V'	$\alpha_V \times 10^{-6} \text{K}^{-1}$
373	20.115	19.898	13.393	5360	----
423	20.109	19.895	13.394	5359	-3.73
473	20.109	19.892	13.392	5357	-5.60
523	20.106	19.883	13.391	5353	-8.71
573	20.101	19.875	13.388	5348	-11.19
623	20.09	19.867	13.385	5342	-13.43
673	20.083	19.856	13.383	5337	-14.30
723	20.082	19.852	13.382	5336	-12.79
773	20.079	19.85	13.381	5333	-12.59

Table 3.12: Variation of cell parameters and unit cell volume with temperature obtained from HTXRD analysis of CTS-50.

T, K	'a'	'b'	'c'	'V'	$\alpha_V \times 10^{-6} \text{K}^{-1}$
373	20.119	19.934	13.417	5381	----
423	20.119	19.931	13.421	5382	3.71
473	20.113	19.926	13.417	5377	-7.43
523	20.11	19.923	13.413	5374	-8.67
573	20.105	19.919	13.41	5371	-9.29
623	20.1	19.914	13.405	5366	-11.50
673	20.089	19.909	13.401	5360	-13.01
723	20.085	19.905	13.399	5357	-12.74
773	20.076	19.898	13.393	5350	-14.40

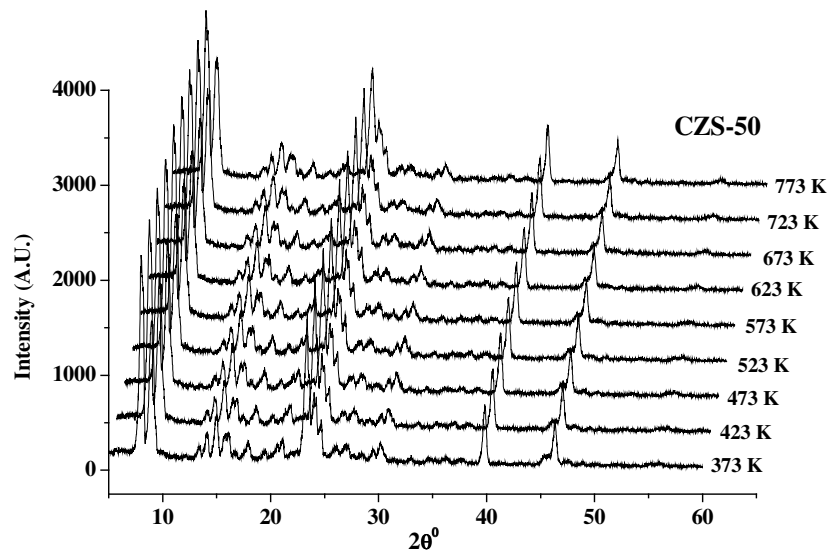


Fig. 3.21 Evolution of CZS-50 diffraction patterns in the temperature range 373-773 K.

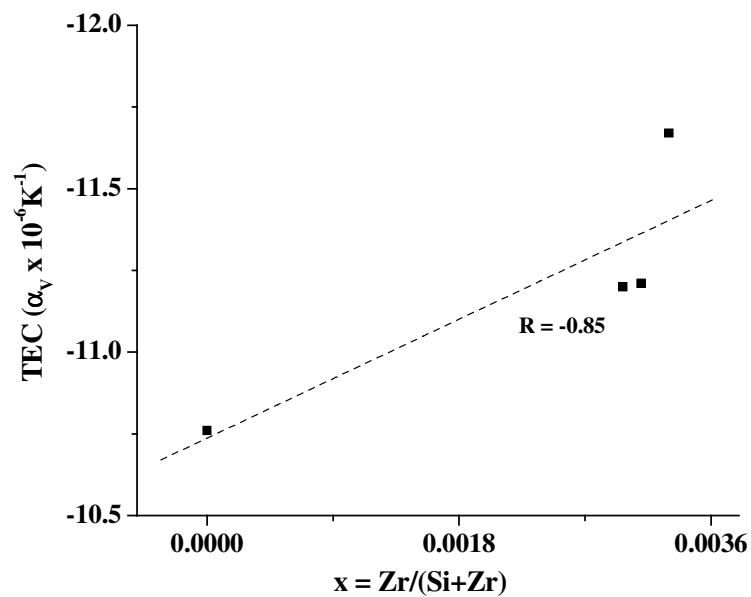


Fig. 3.22 Volume thermal expansion coefficients versus concentration of Zr in the framework 'x' ($\text{Zr}/(\text{Si}+\text{Zr})$) in the temperature range 373-773 K.

Table 3.13: Variation of cell parameters and unit cell volume with temperature obtained from HTXRD analysis of CZS-∞.

T, K	'a' Å	'b' Å	'c' Å	'V' Å ³	$\alpha_V \times 10^{-6} \text{K}^{-1}$
373	20.093	19.882	13.381	5346	----
423	20.09	19.882	13.38	5344	-7.48
473	20.084	19.88	13.379	5342	-7.48
523	20.081	19.878	13.375	5339	-8.73
573	20.079	19.873	13.37	5335	-10.29
623	20.074	19.866	13.366	5330	-11.97
673	20.069	19.864	13.364	5328	-11.22
723	20.066	19.861	13.362	5325	-11.22
773	20.064	19.859	13.36	5323	-10.76

Table 3.14: Variation of cell parameters and unit cell volume with temperature obtained from HTXRD analysis of CZS-100.

T, K	'a'	'b'	'c'	'V'	$\alpha_V \times 10^{-6} \text{K}^{-1}$
373	20.097	19.896	13.39	5354	----
423	20.092	19.895	13.387	5351	-11.20
473	20.089	19.895	13.387	5350	-7.47
523	20.087	19.895	13.385	5349	-6.22
573	20.082	19.89	13.382	5345	-8.40
623	20.075	19.887	13.378	5341	-9.71
673	20.069	19.882	13.375	5337	-10.58
723	20.063	19.878	13.374	5334	-10.67
773	20.059	19.87	13.369	5329	-11.20

Table 3.15: Variation of cell parameters and unit cell volume with temperature obtained from HTXRD analysis of CZS-75.

T, K	'a'	'b'	'c'	'V'	$\alpha_V \times 10^{-6} \text{K}^{-1}$
373	20.100	19.891	13.393	5354	----
423	20.099	19.89	13.397	5355	3.74
473	20.094	19.893	13.396	5355	1.87
523	20.090	19.888	13.392	5351	-3.73
573	20.087	19.885	13.388	5348	-5.60
623	20.079	19.884	13.386	5344	-7.47
673	20.071	19.877	13.382	5339	-9.34
723	20.066	19.869	13.378	5334	-10.67
773	20.06	19.866	13.376	5330	-11.21

Table 3.16: Variation of cell parameters and unit cell volume with temperature obtained from HTXRD analysis of CZS-50.

T, K	'a'	'b'	'c'	'V'	$\alpha_V \times 10^{-6} \text{K}^{-1}$
373	20.092	19.906	13.393	5357	----
423	20.091	19.91	13.396	5358	3.73
473	20.088	19.911	13.395	5358	1.87
523	20.082	19.909	13.393	5355	-2.49
573	20.073	19.906	13.388	5350	-6.53
623	20.065	19.902	13.384	5349	-5.97
673	20.059	19.898	13.38	5341	-9.96
723	20.051	19.894	13.377	5336	-11.20
773	20.044	19.889	13.374	5332	-11.67

From the data represented in Table 3.12, 3.15 and 3.16 it is clear that the sample CTS-100 shows positive thermal expansion in the temperature region 373-423 K while CZS-75 and CZS-50, respectively, shows the positive thermal expansion in

the temperature range 373-473 K. This behavior can be explained on the basis that the polyhedral frameworks of these molecular sieves are getting unfolded and after saturation of the unfolding they starts to show negative thermal expansion property, which is intrinsic property of the framework of such materials [37].

3.4 Conclusions

In-situ HTXRD studies were carried out in order to study the thermal stabilities of the metallosilicate molecular sieves in the temperature range 298-1623 K. Appearance of α -cristobalite phase was seen at 1023 and 1173 K in CFS- ∞ and CFS-50 samples while CTS-50 and CZS-50 samples remain thermally stable upto 1623 K. This transformation was irreversible. Lattice thermal expansion coefficients (α_v) in the temperature range 298-1023 K were $-6.75 \times 10^{-6} \text{K}^{-1}$ for CFS- ∞ , $-12.91 \times 10^{-6} \text{K}^{-1}$ for CFS-50, $-16.02 \times 10^{-6} \text{K}^{-1}$ for CTS-50 and $-17.92 \times 10^{-6} \text{K}^{-1}$ for CZS-50. The highest lattice thermal expansion coefficients (α_v) obtained were $-11.53 \times 10^{-6} \text{K}^{-1}$ for CFS-50 in temperature range 298–1173 K, $-20.86 \times 10^{-6} \text{K}^{-1}$ for CTS-50 and $-25.54 \times 10^{-6} \text{K}^{-1}$ for CZS-50, respectively, in the temperature range 298–1623 K.

In-situ HTXRD studies were carried out in the temperature range 373-673 K to study the structural changes as a function of temperature on the CFS- ∞ sample. From the Rietveld refinement data we have calculated the changes in the Si-O bond distances, Si-O-Si bond angles and Si-Si non-bonding distances as a function of temperatures. The Si-O bond distances seem to play no role in the NTE, as there is no change in their distances as a function of temperature. The transverse vibrations of the Si-O-Si bridging oxygen atoms decreases the Si-Si non-bonding distances which causes the contraction in the material as a function of temperature. The observed decrease in Si-Si non-bonding distances with the constituent Si-O bond distances remaining constant, supports that the transverse vibrations of the bridging oxygen atoms in the structure are responsible for the NTE in this material. The HTXRD studies carried out on the metallosilicate molecular sieves TS-1, FeS-1 and ZrS-1 of different Si/M ratio (Si/M=50, 75 and 100). All the samples exhibit negative thermal expansion on heating in the temperature range 373-773 K and the strength of NTE increases with decreasing Si/M ratio.

3.5 References

1. N. N. Tusar, N. Z. Logar, I. Arcon, F. Thibault-Starzyk, A. Ristic, N. Rajic, V. Kaucic, *Chem. Mater.*, 15 (2003) 4745.
2. M. P. Attfield, A. W. Sleight, *Chem. Mater.*, 1 (1998) 2013.
3. D. S. Bhange, Veda Ramaswamy, *Mater. Res. Bull.*, 41 (2006) 1392.
4. D. A. Woodcock, P. Lightfoot, P. A. Wright, L.A. Villaescusa, M. J. Diaz-Cabanas, M. A. Cambor, *J. Mater. Chem.*, 9 (1999) 349.
5. D. A. Woodcock, P. Lightfoot, L. A. Villaescusa, M. J. Diaz-Cabanas, M. A. Cambor, D. Engberg, *Chem. Mater.* 11 (1999) 2508.
6. M. P. Attfield, A. W. Sleight, *J. C. S. Chem. Commun.*, 5 (1998) 601.
7. S. H. Park, R. W. Grosse Kunstleve, H. Graetsch, H. Gies, *Stud. Surf. Sci. Catal.*, 105 (1997) 1989.
8. B. A. Marinkovic, P. M. Jardim, A. Saavedra, L. Y. Lau, C. Baetz, R. R. de Avillez, F. Rizzo, *Micropor. Mesopor. Mater.*, 71 (2004) 117.
9. P. M. Jardim, B. A. Marinkovic, A. Saavedra, L. Y. Lau, C. Baetz, F. Rizzo, *Micropor. Mesopor. Mater.*, 76 (2004) 23.
10. P. Lightfoot, D.A. Woodcock, M.J. Marple, L.A. Villescusa and P.A. Wright, *J. Mater. Chem.* 1 (2001) 212.
11. P. Tschaufeser, S. C. Parker, *J. Phys. Chem.*, 99 (1995) 10609.
12. J. W. Couvest, R. H. Jones, S. C. Parker, P. Tschaufeser, C. R. A. Catlow, *J. Phys. Condens. Matter.*, 5 (1993) L329.
13. J. D. Gale, *J. Phys. Chem. B*, 102 (1998) 5423.
14. D. S. Bhange, Veda Ramaswamy, *Mater. Res. Bull.*, 42 (2007) 851.
15. I. D. Brown, R. D. Shannon, *Acta Crystallogr.*, A 29 (1973)266.
16. A. W. Sleight, *Endeavor*, 19 (1995) 64.
17. A. W. Sleight, *Current Opinion in Solid State & Materials Science* 3 (1998) 128.
18. G. K. White, *Contemp. Phys.*, 34 (1993) 193.
19. J. S. O. Evans, T. A. Mary, A. W. Sleight, *J. Solid State Chem.*, 133 (1997) 580.
20. B. A. Marinkovic, P. M. Jardim, F. Rizzo, A. Saavedra, L.Y. Lau, E. Suard, *Micropor. Mesopor. Mater.* Article in press, (2008).
21. H. M. Rietveld, *Acta. Crystallogr.*, 22 (1967) 151.

22. A. C. Larson, R. B. von Dreele, *GSAS Generalized structure analysis system*, Laur 86-748, Los Alamos National Laboratory, Los Alamos, New Mexico, 1994.
23. B. Toby, *J. Appl. Cryst.*, 34 (2001) 210.
24. H. van Koningsveld, H. van Bekkum, J. C. Jansen, *Acta Crystallogr.*, B43, (1987) 127.
25. S. P. Zhdanov, N. N. Feoktistova, N. I. Kozlova, I. G. Polyakova, *Russian Chemical Bulletin*, 34 (1985) 2463.
26. C. Weidenthaler, W. Schmidt, *Chem. Mater.*, 12 (2000) 3811.
27. G. Niu, Y. Huang, X. Chen, J. He, Y. Liu, A. He, *Appl. Catal. B: Environ.*, 21 (1999) 63.
28. I. Petrovic, A. Navrotsky, M. E. Davis, S. I. Zones, *Chem. Mater.*, 5 (1993) 1805.
29. K. de Boer, A. P. J. Jansen, R. A. van Santen, *Phys. Rev.*, 52 (1995) 12579.
30. G. J. Kramer, B. W. H. van Beest, R.A. van Santen, *Nature*, 351 (1991) 636.
31. R. A. van Santen, A. J. M. de Man, W. P. J. H. Jacobs, E. H. Teunissen, G. J. Kramer, *Catal. Lett.*, 9 (1991) 273.
32. D. A. Woodcock, P. Lightfoot, L. A. Villaescusa, M. J. Diaz Cabanas, M. A. Cambor, *Chem. Mater.*, 11 (1999) 2508.
33. V. Korthuis, N. Khosrovani, A. W. Sleight, N. Roberts, R. Dupree, W. W. Warren, *Chem. Mater.*, 7 (1995) 412.
34. I. Bull, P. Lightfoot, L. A. Villaescusa, L. M. Bull, R. K. B. Gover, J. S. O. Evans, R. E. Morris, *J. Am. Chem. Soc.*, 125 (2003) 4342.
35. A.W. Sleight, *Inorg. Chem.*, 37 (1998) 2854.
36. A. Bieniok, K. D. Hammonds, *Micropor. Mesopor. Mater.*, 25 (1998) 193.
37. S. Sen, R. R. Wusirika, R. E. Youngman, *Micropor. Mesopor. Mater.*, 87 (2006) 217.
38. R. Roy, D. K. Agrawal, H. A. McKinstry, *Annu. ReV. Mater. Sci.*, 19 (1989) 59.
39. T. A. Mary, J. S. O. Evans, A. W. Sleight, *Science*, 272 (1996) 90.

Chapter **4**

**Non-isothermal Kinetic Studies Of The Template
Decomposition From The Silicalite-1 Framework**

4.1 Introduction

4.1.1 Kinetics of reactions

The study of the kinetics of the processes provides rate equations, which are needed for the design of pilot or full-scale production plants and parameters such as the activation energy, which allow different processes or different reaction conditions to be compared. This can help in the optimization of existing processes and the development of new processes and synthesis routes. Time resolved powder X-ray diffraction (TR-PXRD) and differential scanning calorimetry (DSC) are the two techniques that are most frequently used to study the kinetics of solid-state phase transitions and chemical reactions that involve solid components. For both TR-PXRD and DSC, two methods of data collection are commonly used: the isothermal method and the non-isothermal method.

The isothermal method involves heating or cooling the system under study, to a temperature beyond the reaction onset temperature and then monitoring the reaction at that fixed temperature. This approach has the advantage of the well-established methods of data analysis [1], but suffers from the following disadvantages. Multiple measurements are required, knowledge of the reaction onset temperature is necessary before measurements are made and it is not always possible to heat the sample to the required reaction temperature before the reaction has commenced.

The non-isothermal method involves heating or cooling of the sample to a temperature well beyond the reaction temperature at a constant rate, while monitoring the reaction. This avoids the experimental problems associated with the isothermal method. In some cases one non-isothermal measurement can give as much information as a series of isothermal measurements and therefore offers a much more efficient data collection route. For this reason many methods for the analysis of non-isothermal data have been proposed and the results of a large number of kinetic studies using the non-isothermal method have been reported [2-7]. Until the report of Kennedy and Clark [8], the existing methods for the analysis of data collected under non-isothermal conditions were inappropriate for the majority of reactions and transformations, which made the comparison of reported values, determined using different methods, impossible. A general method for the analysis of non-isothermal kinetic data is reported by Kennedy and Clark [8], which is free from any assumptions, can be used with any rate equation and to analyze the data, collected using both TR-PXRD and DSC.

4.1.2 Theoretical background

Integrated rate equations can be written generically in the form:

$$f(\alpha) = kt \quad (1)$$

where α is the degree of reaction, k is the reaction rate, t is the elapsed time since the start of the reaction and f is a function that relates the degree of reaction to the product kt . Some commonly used expressions are listed in Table 4.1.

Table 4.1 Common forms of integrated rate equation [1].

Acceleratory rate equations	
Power law	$f(\alpha) = \alpha^{1/m}$
Exponential law	$f(\alpha) = \ln \alpha$
Sigmoid rate equations	
Avrami	$f(\alpha) = [-\ln(1 - \alpha)]^{1/n}$
Prout-Tomkins	$f(\alpha) = \ln[\alpha/(1 - \alpha)]$
Deceleratory rate equations	
One-dimensional diffusion	$f(\alpha) = \alpha^2$
Two-dimensional diffusion	$f(\alpha) = (1 - \alpha) \ln(1 - \alpha) + \alpha$
Three-dimensional diffusion	$f(\alpha) = [1 - (1 - \alpha)^{1/3}]^2$
Geometric models	
Contracting area	$f(\alpha) = 1 - (1 - \alpha)^{1/2}$
Contracting volume	$f(\alpha) = 1 - (1 - \alpha)^{1/3}$

The reaction rate is temperature dependant and can usually be calculated from the Arrhenius equation [9]:

$$k = A \exp(-E / RT) \quad (2)$$

Here, T is the absolute temperature, R is the molar gas constant, E is the overall effective activation energy of the reaction and A is a constant known as the pre-exponential factor, which defines the maximum possible value of k .

Non-isothermal experiments take place under conditions of constantly ramping temperature. If we define T_0 as the temperature at the start of the reaction and b as the heating rate ($^{\circ}\text{C}/\text{min}$), then the temperature at time t is given by:

$$T = bt + T_o \quad (3)$$

Equations (1) and (3) can be combined in a number of ways to give expressions relating the degree of reaction to the activation energy. Such expressions form the basis of the current methods of non-isothermal data analysis. The most commonly used methods are those proposed by Kissinger [2], Augis and Bennett [3], Takhor [4], Coats and Redfem [5], Sestak [6] and Satava [7]. All of these methods were developed by simplifying the equations using some assumptions. But these methods have their limitations in their applicability, *viz.*,

1. Two of these methods, Kissinger and Auger were derived specifically in terms of the Avrami equation [10-14] and are not applicable to a general rate equation.
2. The methods of Kissinger, Augis and Bennett, Coats and Redfem, Sestak, Satava except Takhor assume that T_o is negligibly small compared with T . This assumption introduces a substantial error for reactions that take place well above absolute zero.
3. All of the methods except that of Augis and Bennett ignore the temperature dependence of k during differentiation of the Avrami equation.
4. The scope of application of the methods of Sestak, Satava, Coats and Redfem, Augis and Bennett is limited by assumptions concerning the size of the activation energy and associated quantities.

4.1.3 New method of analysis

To overcome the limitations of the above said methods, a new method of analysis using non-isothermal conditions is reported by Kennedy and Clark [9]. Kennedy and Clark have combined integrated rate equation and Arrhenius equation to give an expression that is generally applicable. Equation (1) can be rearranged as,

$$k = \frac{f(\alpha)}{t} \quad (4)$$

Then equating with equation (2) gives

$$\frac{f(\alpha)}{t} = Ae^{(-E/RT)} \quad (5)$$

And then equation (3) can be used to substitute temperature for time dependence, which gives:

$$\frac{bf(\alpha)}{(T - T_o)} = Ae^{(-E/RT)} \quad (6)$$

Taking logarithm on both sides of this equation, we get:

$$\ln\left[\frac{bf(\alpha)}{T - T_o}\right] = \ln(A) - \frac{E}{RT} \quad (7)$$

Plotting the left-hand side of this equation against $1/T$ should give a straight line of gradient $-E/R$ and intercept $\ln(A)$. This is the non-isothermal equivalent to the Arrhenius equation (1) and will be referred as $\ln\text{-}\ln$ plot. This equation can be incorporated in any rate equation and is free from any of the assumptions used to derive previous expressions, but surprisingly was proposed first time as a basis for the analysis of non-isothermal kinetic data by Kennedy and Clark. Kennedy and Clark further modified this equation as follows:

$$\ln[g(\alpha)] = \frac{1}{p}\left[\ln(A) - \frac{E}{RT}\right] + \frac{1}{p}\ln\left(\frac{(T - T_o)}{b}\right) \quad (8)$$

Where $g(\alpha)$ is the integral of the kinetic model function $f(\alpha)$ and p is the unknown constant for the power law equations. Since the quantity $[\ln(A) - E/RT]/p$ is constant for any particular value of T , a plot of $\ln[g(\alpha)]$ versus $\ln[(T - T_o)/b]$ will have gradient $1/p$. For example, for the Avrami equation, putting $g(\alpha) = \ln[-(\ln(1 - \alpha))]$ will yield a plot with gradient ' n ' and for a power law rate equation, a plot with gradient ' m ' will result from making $g(\alpha) = \ln(\alpha)$. So any extra parameters can be found by making a series of measurements at different heating rates and then selecting the value of the fraction transformed corresponding to a chosen temperature from each of the measurements made. The temperatures at which the values of the fraction transformed are selected are most sensibly chosen so that each value is non-zero. Values of the fraction transformed can be selected at more than one temperature; this gives a number of estimates of the parameter p . For the case of the Avrami equation this method is equivalent to the method proposed by Ozawa [15] for determining ' n ' but without the assumption that T_o is independent of heating rate since T_o is explicitly included in equation (8). For powder diffraction studies, the degree of reaction can be obtained directly from normalized TR-PXRD peak intensities.

4.1.4 Template decomposition in as synthesized MFI type molecular sieves

The synthesis of the MFI type molecular sieves is assisted with the help of structure directing organic molecules. The tetrapropylammonium cation (TPA^+), in the hydroxide or in the salt form, is the most commonly used template, although the use of other organic compound is reported [16-18]. The pictorial diagram of TPA^+ occluded in silicalite-1 is shown in Figure 4.1. During the synthesis, these template molecules get occluded within pores of the MFI framework. To make these molecular sieves accessible for guest molecules of interests and use as catalysts for chemical reactions, it is important to remove the occluded template molecules, and hence calcination/decomposition of template is required. Generally calcination is carried out in the air from 298-823 K. Thermogravimetric analysis has been used extensively in the past to study the decomposition of the template cation, TPA^+ [19-21]. The weight loss of the sample as a function of temperature is recorded using thermogravimetric analysis. Over the temperature range from 573 to 823 K, the decomposition of template molecules takes place. The loss in weight corresponds exactly to the TPA^+ content of the zeolite, for e.g. four template molecules per unit cell (12% weight loss).

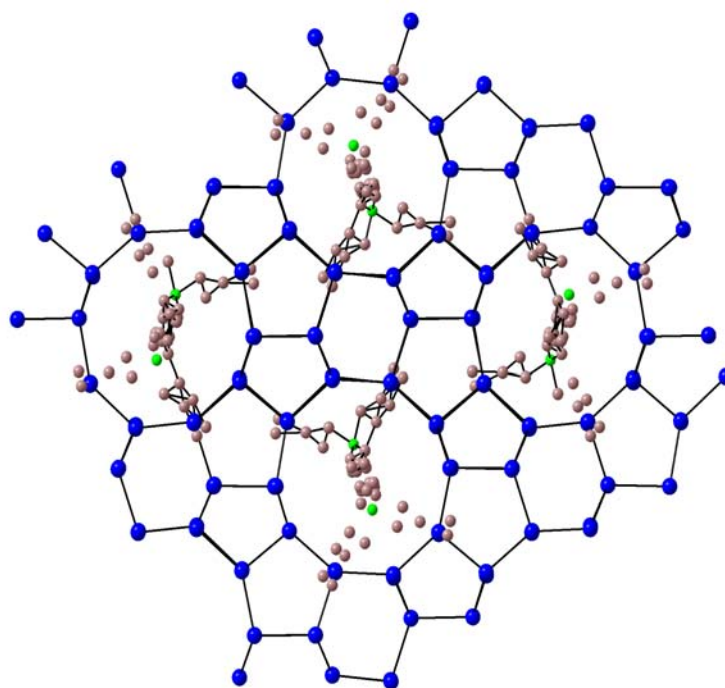


Fig. 4.1 TPA^+ occluded in silicalite-1, viewed along 010 directions. ‘Si’ atoms are shown in blue. The ‘O’ atoms are not shown; ‘N’ is shown in green and ‘C’ in brown color.

Activation energy and reaction rate constant were determined from thermogravimetric analysis by assuming the reaction as first order [20]. High temperature powder X-ray diffraction (HTXRD) studies reported recently have shown that this decomposition is a half order reaction and a diffusion limited one [22, 23]. In these studies template occupancy was determined by Rietveld refinement, which directly gives composition of TPA⁺. Variation in the intensities of reflections 101/011 and 200/020 as a function of temperature is reported as a measure of template present in the silicalite-1 framework at the respective temperature.

In the present work, we have carried out HTXRD studies on as synthesized silicalite-1, FeS-1, TS-1 and ZrS-1 molecular sieves. Apparent activation energy of template decomposition has been measured without any prior knowledge of the reaction mechanism using Kissinger and Flynn-Wall-Ozawa methods [24-26]. Reaction order of template decomposition was carried out according to the method proposed by Kennedy and Clark [8]. Structural changes in the framework of silicalite-1 as a function of template removal are also studied. For comparison purposes, we have carried out TG studies on a typical sample of silicalite-1 and the non-isothermal reaction kinetics of the template decomposition is compared with HTXRD data.

4.2 Experimental

4.2.1 Data collection for kinetic analysis using HTXRD and TG

HTXRD data were collected on as synthesized silicalite-1 using the three heating rates (1, 3 and 5°C/min). A Philips X-ray diffractometer (Cu K α radiation), equipped with an Anton Paar HTK 16 heating chamber and X'Celerator as detector was used to collect the data at different heating rates (1, 3 and 5°C/min). In these experiments, the data acquisition time for each experimental point was 3 min. In each series, the time to reach maximum temperature was determined not only by the heating rate but also by the data acquisition time and number of investigated data points. All experiments were performed in static air. The 2θ region 5–50° was investigated. Data were collected from 298 K to 823 K with an interval of 25 K. Similar strategies were applied for the data collection on the series of samples of FeS-1, TS-1 and ZrS-1. The unit cell parameters of the sample scanned at various temperatures were extracted by carrying out the Rietveld refinement using General Structure Analysis System (GSAS) package [27, 28]. The initial atomic co-ordinates

for as synthesized silicalite-1 (with TPA⁺) and calcined silicalite-1 were taken from the literature [29]. Reflections from the Platinum strip sample holder have been used as internal standard. This helps in determining the sample height-displacement error. These sample displacements at each temperature have been fixed for the refinement of parameters in the MFI phase. In order to follow the template decomposition, a quantitative phase analysis was performed in which the orthorhombic MFI with full occupancy (as-synthesized form) and zero occupancy (calcined form) of the atoms in the template molecules, respectively, was refined as two separate phases. This gives the direct value of the template decomposition (conversion). In these refinements, the cell parameters for both structure models were kept fixed at the previously obtained values. Hence, only the background was corrected manually and the scale factors were refined. Thermogravimetric analysis was done on the as synthesized silicalite-1 at 10, 15 and 20°C/min heating rates using Perkin Elmer diamond TG analyzer in the temperature range 308 - 873 K.

4.2.2 Kinetic studies

The kinetic analysis of the data obtained from HTXRD experiments were carried out using the plot of conversion factor (α) versus temperature and the conversion factor is calculated as:

$$\alpha = \left[\frac{I_c^T - I_c^{T=25^\circ C}}{I_c^{Max} - I_c^{T=25^\circ C}} \right] \quad (9)$$

where I_c^T is the sum of the peak areas under the reflection peaks 101/011 and 200/020 divided by two and I_c^{max} corresponds to maximum value of I_c . The kinetic analysis based on a conversion factor α calculated from the intensity change of the low-angle peaks during template removal was previously used as basis for a kinetic analysis of the template removal reaction in silicalite-1 [23]. The weight fractions of the template containing as well as calcined forms of the silicalite-1 were obtained by Rietveld refinement procedure. We have then compared the values of conversion factors obtained from intensity changes and weight fractions obtained from Rietveld refinement. The comparison of the Kissinger method [24] and the isoconversional method of Flynn-Wall-Ozawa [25, 26] were employed for obtaining the apparent activation energy of the template decomposition. The above two methods can give

activation energy Ea for template decomposition in silicalite-1 without any prior knowledge of the reaction mechanism. According to the Kissinger method, the slope of the plot of $\ln(\beta/T_p^2)$ versus $1/T_p$ is proportional to Ea , according to the following equation:

$$\ln\left(\frac{\beta}{T_p^2}\right) = -\frac{Ea}{RT_p} + k \quad (10)$$

In this equation β is the heating rate, T_p is the temperature at which the reaction rate is maximum, R is the molar gas constant and k is the rate constant. The alternative method developed by Flynn-Wall-Ozawa (where the slope of the plot of $\ln\beta$ versus $1/T$ is proportional to Ea) is also used to calculate the activation energy using the following equation:

$$\ln \beta = \ln \frac{AEa}{R} - 1.052 \frac{Ea}{RT} - 5.33 - \ln g(\alpha) \quad (11)$$

where A is the frequency factor and $g(\alpha)$ is the integral of the kinetic model function $f(\alpha)$ (here it is assumed that the kinetic model function is invariant for all the heating rates). The reaction order for the Avrami equation was determined according to the following equation proposed by Kennedy and Clark:

$$\ln[g(\alpha)] = n \ln \left[\ln(A) - \frac{Ea}{RT} \right] + n \ln \left[\left(\frac{T - T_0}{\beta} \right) \right] \quad (12)$$

where $g(\alpha)$ is $[-\ln(1-\alpha)]$ and n is the reaction order. In the above equation, the term $n[\ln(A) - E/RT]$ is constant for any value of T and hence the slope of the plot of $\ln g(\alpha)$ versus $\ln [(T-T_0)/\beta]$ will give the value of n . Apparent energy of activation as well as reaction order was calculated from the HTXRD data using above equations. Apparent activation energies of isomorphously substituted FeS-1, TS-1 and ZrS-1 (with Si/M = 50, 75 and 100) were calculated from the HTXRD experiments for comparison with silicalite-1.

The kinetic analyses of the data obtained from the TG data were carried out only on as synthesized silicalite-1 sample for comparison with HTXRD data. The conversion factor (α) is calculated as:

$$\alpha = \left[\frac{L^T - L^{423K}}{L^{823K} - L^{423K}} \right] \quad (13)$$

where L^T = % weight loss at temperature T , K, L^{423K} = % weight loss at 423 K, L^{823K} = % weight loss at 823 K. Here, the weight loss before 423 K is assumed to be due to

loss of water and hence this temperature (423 K) is taken as the initial temperature for the actual weight loss calculation and there is no more weight loss beyond 823 K, which generally is the calcination temperature employed for the use as a catalyst. It is observed that there is maximum weight loss upto the temperature 823 K.

4.3 Results and Discussion

4.3.1 Kinetic studies using HTXRD technique

In the present work, the kinetic analysis was based on a conversion factor α calculated from the intensity changes of the reflections (101/011 and 200/020) using HTXRD data. Figure 4.2 shows the multiple XRD plot collected during heating the as synthesized silicalite-1 sample from 298 K to 823 K at a heating rate of 1°C/min. The patterns of silicalite-1 collected for heating rate 3 and 5°C/min were similar and are not shown here. Although there is a variation in the intensities of some reflections, the patterns collected for all heating rates are nearly similar. Decomposition of the template molecule inside the silicalite-1 enhances the intensities of some reflections, which are sensitive to template occupancy, but there are more significant changes in the intensities of the reflections 101/011 and 200/020 as template moves out from the framework. Calculation method for conversion factor (α) is given in Table 4.2 for HTXRD data.

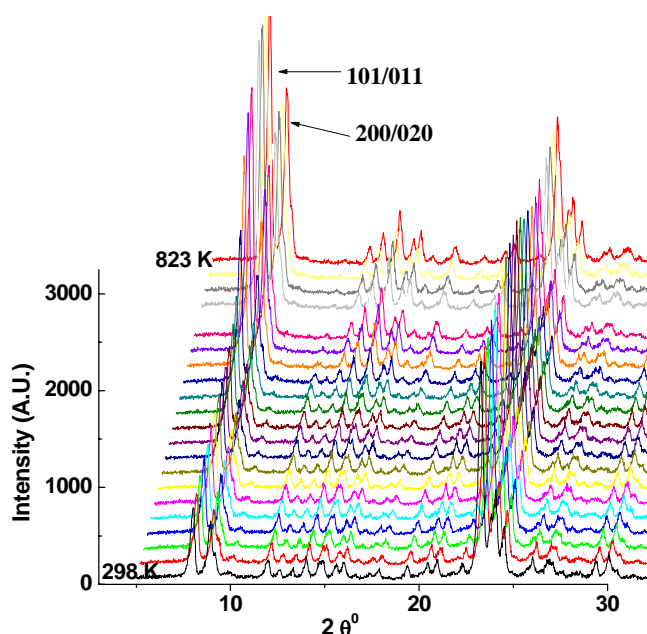


Fig. 4.2 Multiple plot of powder XRD patterns of template containing silicalite-1 during heating (heating rate $\beta=1^\circ\text{C}/\text{min}$) scanned in air from 298 to 823 K at 25 K intervals.

Table 4.2 The peak area under the reflections 101/011 and 200/020 for heating rate 1°C/min and conversion factors (α) at respective temperatures.

Sr.No.	Temp °C	Peak Area	Peak area/2 (I_c^T)	α
1.	25	434	217	0.000
2.	50	441	220.5	0.005
3.	75	472	236	0.033
4.	100	478	239	0.038
5.	125	483	241.5	0.042
6.	150	492	246	0.051
7.	175	508	254	0.065
8.	200	513	256.5	0.068
9.	225	518	259	0.074
10.	250	521	260.5	0.075
11.	275	535	267.5	0.088
12.	300	574	287	0.123
13.	325	647	323.5	0.187
14.	350	950	475	0.455
15.	375	1242	621	0.713
16.	400	1410	705	0.861
17.	425	1474	737	0.917
18.	450	1549	774.5	0.982
19.	475	1562	781	0.994
20.	500	1568	784	1.000
21.	525	1568	784	1.000
22.	550	1568	$I_c^{\max} = 784$	1.000

I_c^T = Sum of the peak areas under the 101/011 and 200/020 reflections at T, K.

I_c^{\max} = Maximum value of I_c .

α at 400 K can be calculated as: $\alpha = (705-217)/(784-217) = 488/567 = 0.861$.

The area under peak is calculated from the software X'Pert Graphics provided by Philips. All the patterns were processed in similar way to avoid the errors. Same 2θ region was used to find the area under peak. The HTXRD data were used to determine the activation energy of template burning process for the TS-1 and FeS-1 samples having different Si/M (M = Fe, Ti or Zr) ratio (*vide section 2.2*). Figure 4.3 shows the conversion factor α calculated from the intensity data and the refined weight fraction of the calcined MFI structure determined by Rietveld refinement as a function of temperature for heating rate of $1^\circ\text{C}/\text{min}$. The agreement between the curves is very good indicating a connection between these separate observations.

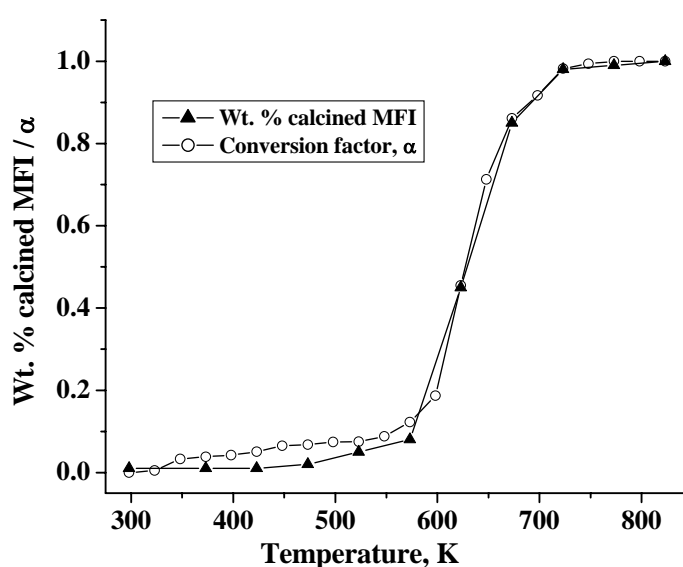


Fig. 4.3 The weight % of calcined MFI from the Rietveld refinement and the conversion factor α calculated from the intensity data as a function of temperature for heating rate of $1^\circ\text{C}/\text{min}$.

Figure 4.4 shows the effect of heating rate on the conversion factor (α) as a function of temperature. From the conversion (α) data we have calculated the ' T_p ' the temperature at which reaction rate is maximum. The derivative plots of the curves in Figure 4.4 were fitted for Gaussian peak fit. The derivative plot for heating rates $1^\circ\text{C}/\text{min}$, $3^\circ\text{C}/\text{min}$ and $5^\circ\text{C}/\text{min}$ are given in inset of Figure 4.4. The values of the temperature at which reaction rates are maximum for three heating rates are given in Table 4.3. These values of T_p are used for the plots of Kissinger method to calculate

apparent activation energy (E_a). According to Kissinger method (equation 10), the plot of $\ln(\beta/T_p^2)$ versus $1/T_p$ is proportional to the E_a .

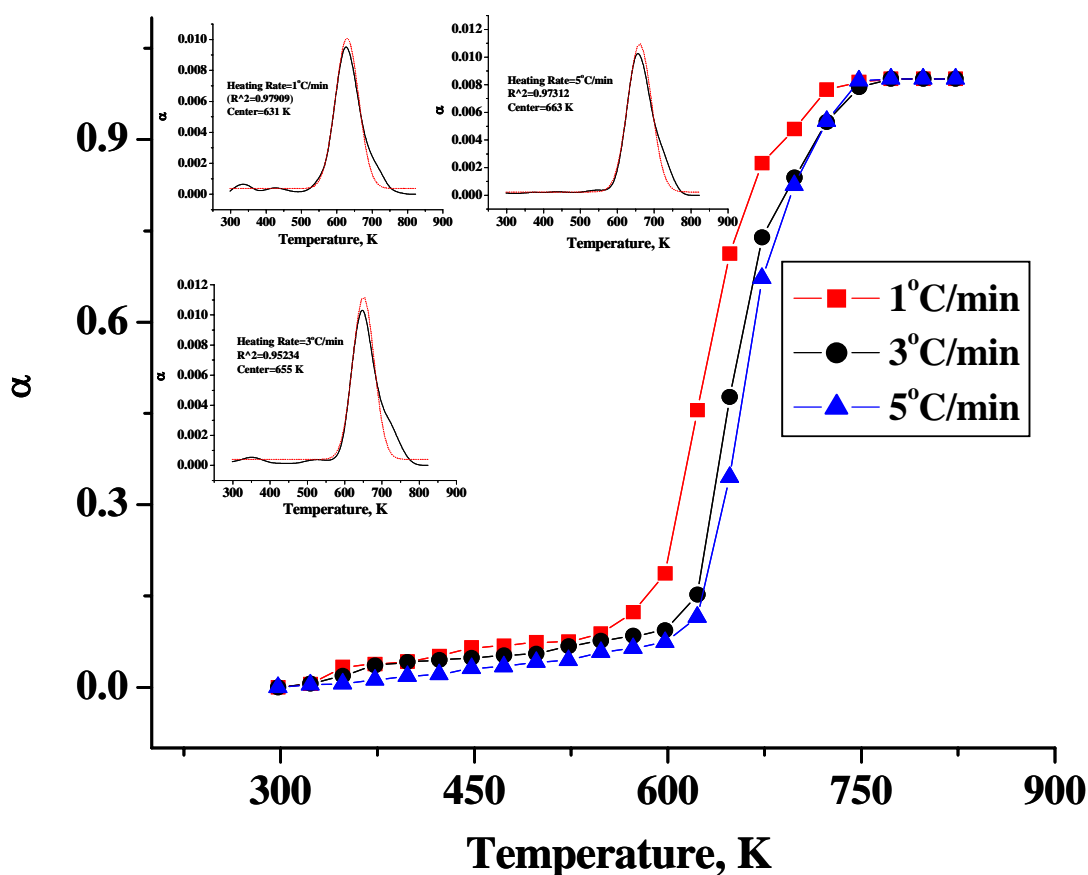


Fig. 4.4 The conversion factor α (obtained from HTXRD data) as function of temperature for heating rates 1°C/min (■), 3°C/min (●) and 5°C/min (▲). The conversion factor is calculated on the basis change in intensities of low angle reflections (101/011 and 200/020) from 298 to 823 K and derivative plots (inset) fitted with Gaussian fit for heating rates 1°C/min, 3°C/min and 5°C/min.

Table: 4.3 The values of T_p obtained from derivative plot of the curves in Figure 4.3.

Heating Rate °C/min.	T_p	1000/ T_p
1	631	1.5847
3	655	1.5267
5	663	1.5082

A plot of $\ln(\beta/T_p^2)$ versus $1/T_p$ for the data obtained from studies is shown in Figure 4.5. Apparent activation energy (E_a) calculated from this plot is 125 kJ mol^{-1} . The values obtained from our studies are in good agreement with the values reported in the literature [22, 23].

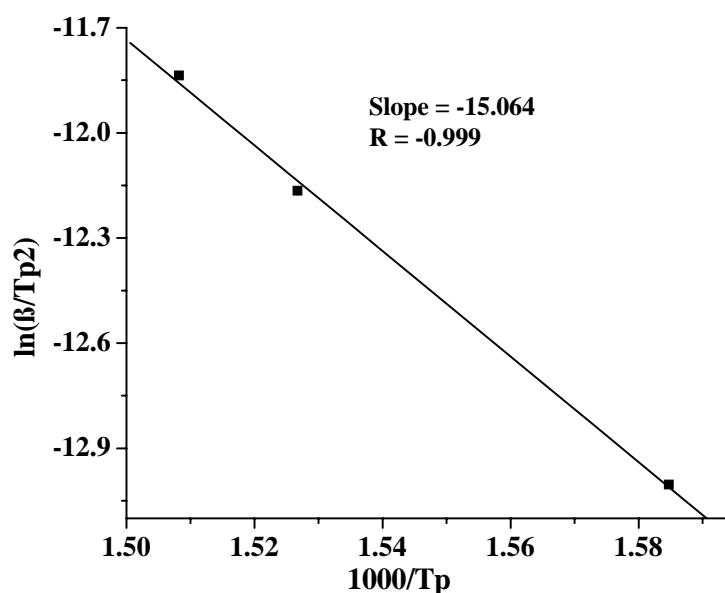


Fig. 4.5 A plot of $\ln(\beta/T_p^2)$ versus $1000/T_p$ for the data obtained from HTXRD. According to the Kissinger method, the slope is proportional to E_a .

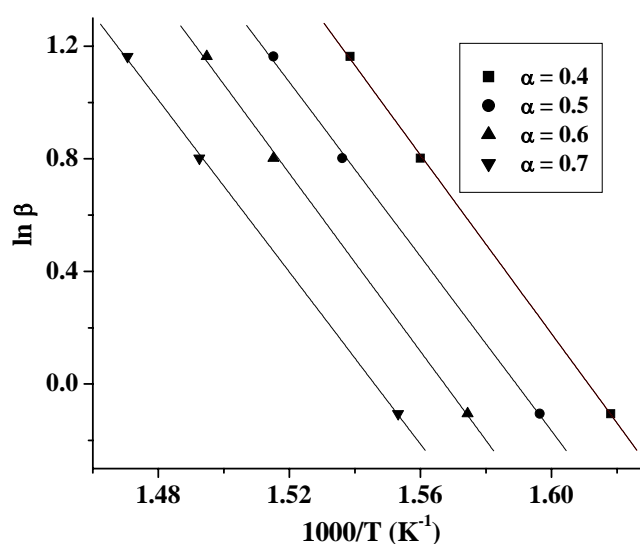


Fig. 4.6 Plot of $\ln \beta$ versus $1000/T$ for different values of conversion (α). The slope of each curve is proportional to E_a (slope $\times 8.314/1.052$) according to the method of Flynn, Wall and Ozawa using HTXRD data.

Figure 4.6 shows the plot of $\ln\beta$ versus $1/T$ for different α values from the data obtained by HTXRD studies. Apparent activation energy is proportional to the slope of each curve according to Flynn-Wall-Ozawa method (equation 11). Apparent activation energy (E_a) values for each α have been calculated from these graphs and are given in the Table 4.4 from the HTXRD data. The averaged value is approximately equal to the value obtained by Kissinger method and the values reported in literature. Parallel curves in the plots indicate only one rate-limiting step.

Table 4.4 The apparent activation energy, calculated from Figure 4.6 according to equation 11 from the HTXRD data.

α	Slope	E_a , KJ/Mole	R^2
0.4	15.87	125	0.998
0.5	15.48	122	0.999
0.6	15.79	125	0.999
0.7	15.27	121	0.996
Mean	---	124	---

The R^2 (regression factor) value for each linear fit of the curves in Figure 4.6 is also reported.

Avrami equation is successfully used in the literature to fit the kinetic data. Under the assumption that the Avrami equation is valid for the silicalite-1 powder studied here, the reaction order is determined using the equation 12 proposed by Kennedy and Clark. The plot of $\ln[-\ln(1-\alpha)]$ versus $\ln[(T-T_0)/\beta]$ is shown in Figure 4.7. The value obtained from the slope is nearly equal to 2.0 for the data from the heating rate 5°C/min. The values obtained for other heating rates are given in Table 4.5. The value for reaction order is nearly equal to two for all the heating rates. These results are in contrast with the results reported previously where the reaction order was half [22, 23]. This half order reaction was explained on the basis of diffusion limitation of mass transfer through the sinusoidal channels of MFI. But Lee *et al.* [20] reported that activation energy was independent of sample weight and crystal size, which indicates that macropore mass transfer limitations and micropore mass transfer limitations are insignificant. Jirka *et al.* [30] also reported with the help of *in-situ* X-

ray photoelectron spectroscopic studies of the template decomposition from the silicalite-1 that intracrystalline diffusion of the template degradation products is not the rate-limiting step in the kinetics of the template removal. The second order reaction determined from our data can be explained on the basis of interactions of template molecule with the silicalite-1 framework.

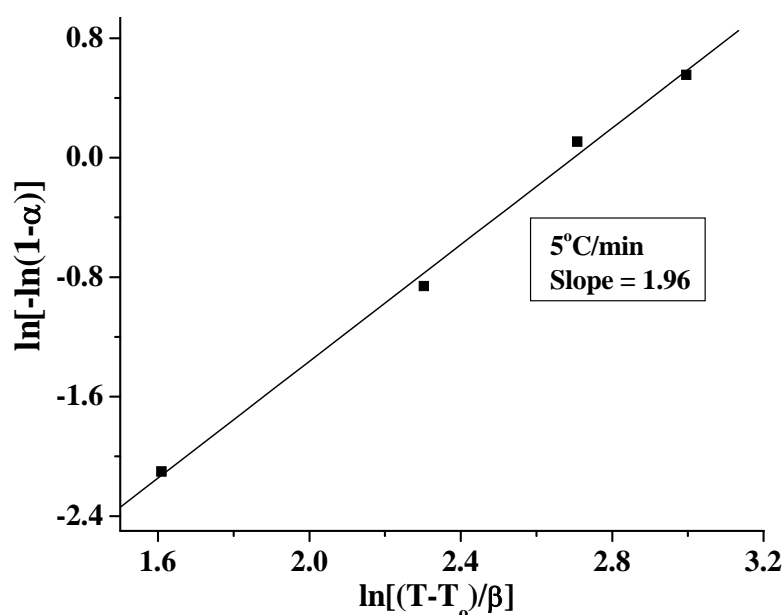


Fig. 4.7 Plot of $\ln[-\ln(1-\alpha)]$ versus $\ln[(T-T_0)/\beta]$ for $\beta=5^\circ\text{C}/\text{min}$ (HTXRD). According to Avrami equation slope of this plot is equal to the order of reaction (n).

Table 4.5 The order of reaction determined from HTXRD data for different heating rates according to equation 12.

Heating rate $^\circ\text{C}/\text{min}$.	Order of reaction
1	2
3	2
5	2

In literature the decomposition of another template tetra-propylammonium bromide (TPABr) alone (in the absence of the silicalite-1) is shown to be an endothermic process and the decomposition of a physical mixture of TPABr and silicalite-1 also shows the same mechanism [31]. On the other hand the mechanism for decomposition of template when occluded in the silicalite-1 is exothermic and is

significantly different. Hence, the hypothesis that the silicalite framework catalyses the decomposition of template can be discarded. After calcination (or removal of template) there are some structural changes in the MFI framework indicated by the longer T-O as compared to that of as synthesized form [32]. There is a contraction in the unit cell volume after the removal of the template [22, 23, 32, 33]. From all these evidences, we can say that the decomposition of TPA^+ is not a simple decomposition and its mechanism is different than ordinary decomposition. The reaction is second order and hence there are no diffusion limitations as reported in the literature [23].

The second order of template decomposition can be attributed to the fact that TPA^+ is positioned in two different orientations inside the silicalite-1 framework; the so called TPA_1 and TPA_2 having an occupancy of 0.6 and 0.4, respectively [34] as shown in Figure 4.8. Price *et al.* [35] have also reported that the template ions at the intersection of the straight and sinusoidal channel are oriented in two different conformations. Part of the TPA^+ ion in the sinusoidal channel is in the folded conformation while extended conformation is present in the straight channel. Hence there may be different mechanism present for template decomposition in these two physically different environments of the template molecule.

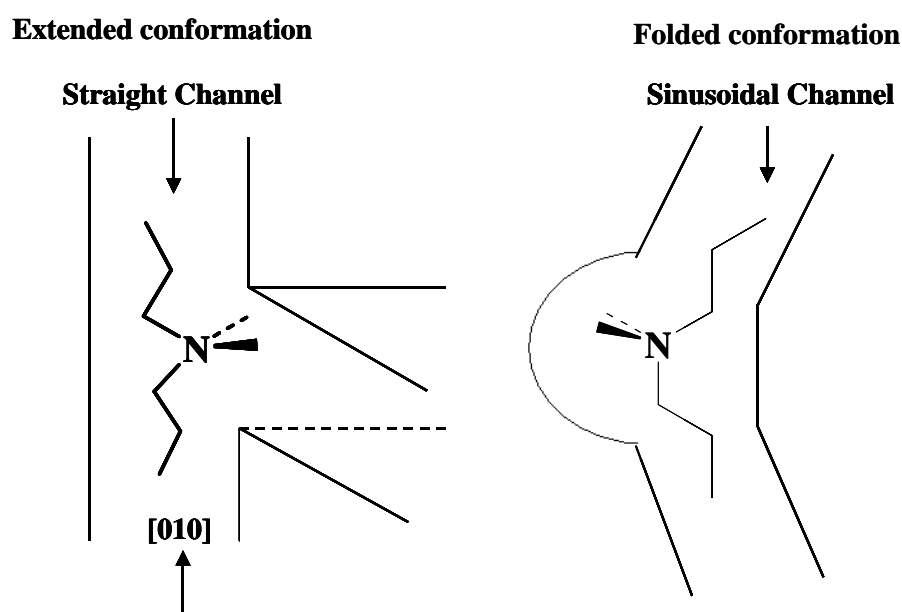


Fig. 4.8 Two types of orientation of TPA molecule in the MFI channels.

4.3.2 Kinetic studies using thermogravimetric (TG) analysis

Thermogravimetric analysis method is used to compare the results obtained from the HTXRD technique. Kinetic analysis is based on a conversion factor α calculated from the % weight loss. Figure 4.9 shows the thermograms recorded at different heating rates 10, 15 and 20 °C/min. The heating rate was found to correlate directly with the rate of weight loss and the temperature at the maximum weight loss rate. The temperature of decomposition increases by a few K as the heating rate increases. The nature of the thermograms is same for all the three different heating rates. Onset temperature for decomposition reaction is recorded from these thermograms. It is also clear that after 823 K the weight loss is constant. The % weight loss upto 500 K is due to the removal of adsorbed water species and the decomposition of the TPA ion located outside the crystal [31]. The weight loss in the temperature range 500–700 K is attributed to the decomposition of TPA ions occluded in the zeolitic pores; this decomposition is also termed as the Si–O–TPA⁺ ion pair decomposition [31]. The weight loss after 700 K can be attributed to the water lost during dehydroxylation of Si–OH.

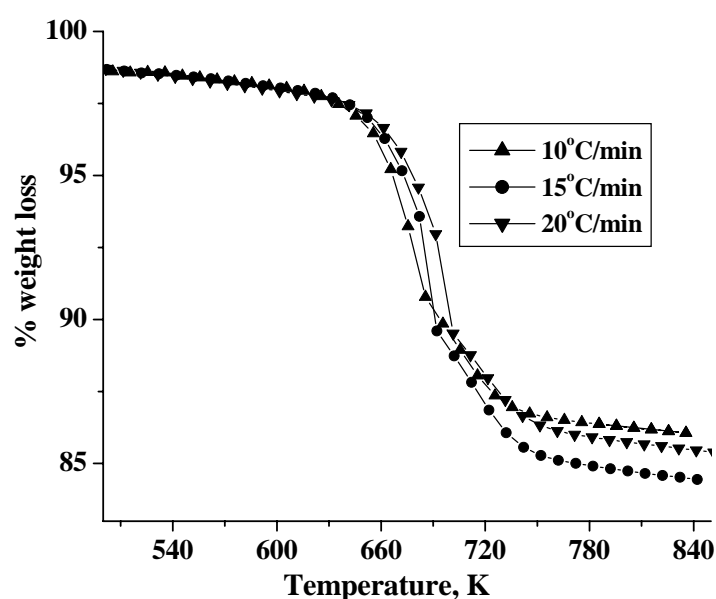


Fig. 4.9 Thermograms (TG) collected during the template decomposition from silicalite-1 framework at different heating rates (▲ 10 °C/min, ● 15 °C/min and ▼ 20 °C/min.)

Conversion factor α was calculated using equation 13 from the data obtained from TG and are normalized to unity. Figure 4.10 shows the conversion of template

molecule as a function of temperature obtained from TG data. Since the curves in this graph show similar trend like HTXRD (Figure 4.3), kinetic studies can be carried out by both TG and HTXRD techniques.

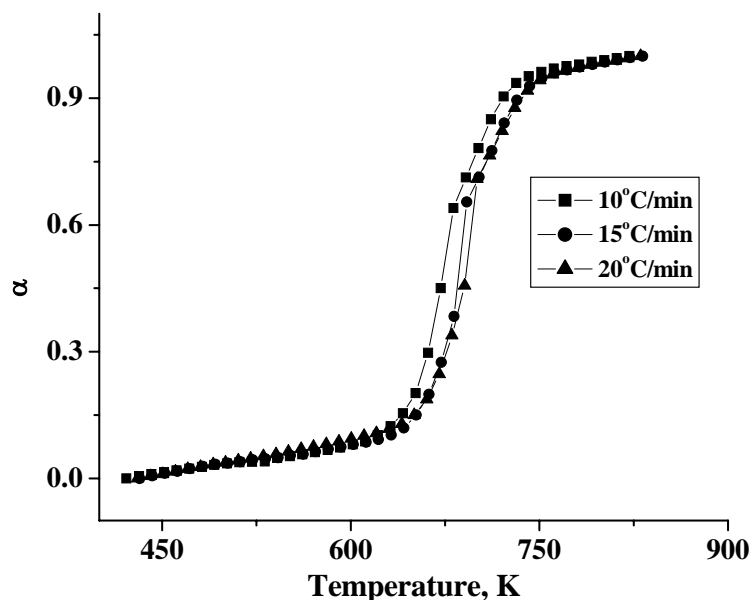


Fig. 4.10 The conversion factor α - obtained from TGA data ($\beta=10$ °C/min (■), 15 °C/min (●) and 20 °C/min (▲).

Figure 4.11 shows the plot of $\ln(\beta/T_p^2)$ versus $1/T_p$ for data obtained from thermogravimetric studies. Slope of this plot is proportional to apparent activation energy (E_a) and E_a is 129 kJ mol^{-1} according to equation 10 (Kissinger method). The values obtained from both the studies are nearly the same and agree with the values reported in the literature [22, 23]. Figure 4.12 shows the plot of $\ln\beta$ versus $1/T$ for different α values from the data obtained by TG studies. Apparent activation energy is proportional to the slope of each curve according to equation 12 (Flynn-Wall-Ozawa method). Apparent activation energy (E_a) values for each α have been calculated from this graph, are given in the Table 4.6. The averaged value is nearly similar to that obtained by HTXRD studies and approximately equal to the values reported in literature. Parallel curves in the plot indicate only one rate-limiting step. Avrami equation was successfully used to fit the kinetic data in the literature. Under the assumption that the Avrami equation is valid for the silicalite-1 powder studied here, the reaction order is determined using the equation 12. The plot of $\ln[-\ln(1-\alpha)]$ versus $\ln[(T-T_0)/\beta]$ from the data obtained by TG is shown in Figure 4.13. The value

obtained from the slope is nearly equal to 2.0 for heating rate 10 °C/ min. The values obtained for other heating rates are given in Table 4.7. The value for reaction order is nearly equal to two for all the heating rates.

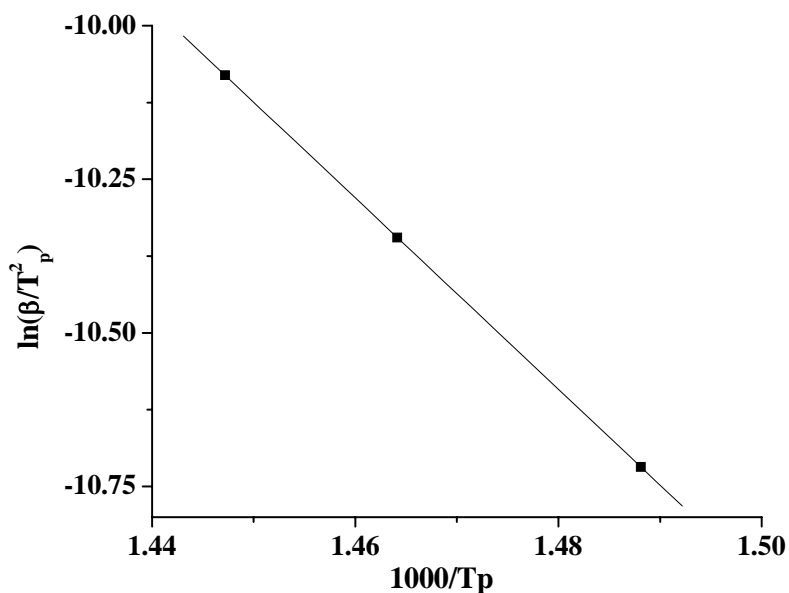


Fig. 4.11 A plot of $\ln(\beta/T_p^2)$ versus $1000/T_p$ obtained from TGA data.

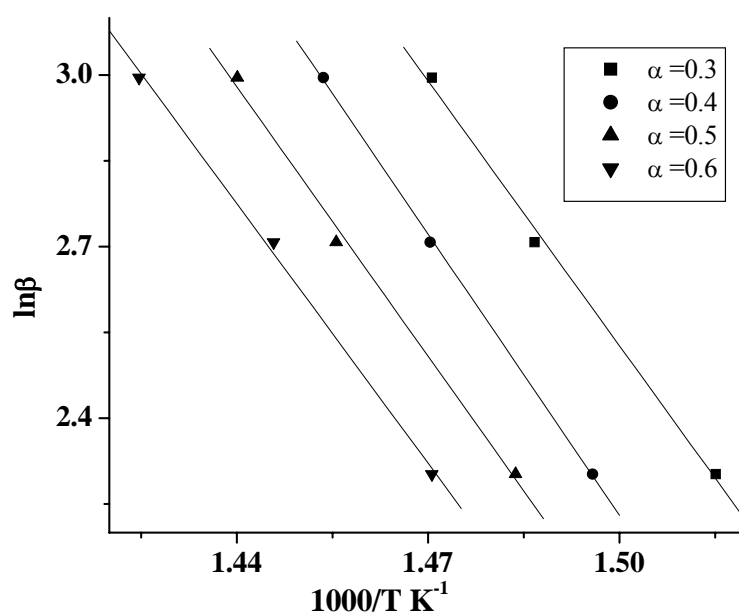


Fig. 4.12 Plot of $\ln\beta$ versus $1000/T$ for different values of conversion (α). The slope of each curve is proportional to Ea (slope $\times 8.314/1.052$) according to the method of Flynn, Wall and Ozawa using TG data.

Table 4.6 The apparent activation energy, calculated from Figure 4.12 according to equation 11.

α	Slope	E_a , KJ/Mole	R^2
0.3	15.43	122	0.998
0.4	16.38	129	0.999
0.5	15.72	124	0.997
0.6	15.14	120	0.998
Mean	---	123	---

The R^2 value for each linear fit of the curves in Figure 4.12 is also reported.

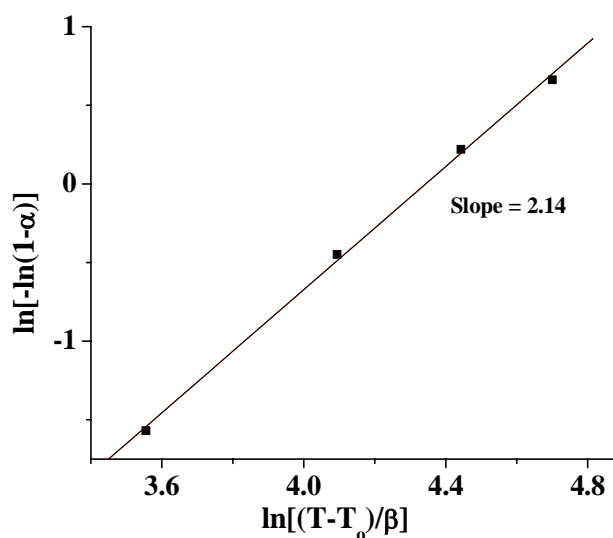


Fig. 4.13 Plot of $\ln[-\ln(1-\alpha)]$ versus $\ln [(T-T_0)/\beta]$ for $\beta=10^\circ\text{C}/\text{min}$ (TG data). According to Avrami equation slope of this plot is equal to the order of reaction (n).

Table 4.7 The order of reaction determined from TG data for different heating rates according to equation 12.

Heating rate $^\circ\text{C}/\text{min}$.	Order of reaction
10	2
15	2
20	2

The activation energy (E_a) for FeS-1, TS-1 and ZrS-1 samples obtained from the HTXRD data collected using different heating rates is given in Table 4.8. It is clear from the Table 4.8 that the values of activation energies of the template decomposition process depends on the chemical nature as well as chemical composition of the framework in which the template is occluded. The activation energy of the template decomposition process increases with increase in the ionic radii of the heteroatom substituted and also with increase in the concentration of metal ion in the framework of silicalite-1. In the case of FeS-1 samples the activation energy is increased more as compared to TS-1 and the ZrS-1 samples of the same Si/M ratio in the synthesis gel. This large increase in the activation energy value in the FeS-1 samples can be correlated with the fact that the template is playing dual role of structure directing and counteraction to compensate the framework charge, unlike in the other two heteroatoms (Ti and Zr) where charge compensation effect is not necessary.

Table 4.6 The apparent activation energy, calculated by Kissinger method and from the HTXRD data obtained for FeS-1, TS-1 and ZrS-1 samples.

Si/M ratio (in synthesis gel)	Activation energy (E_a) KJ/Mole		
	FeS-1	TS-1	ZrS-1
100	149	138	129
75	159	144	136
50	171	154	140

4.3.3 Structural changes in the silicalite-1 as function of template removal

Structural changes in the template-containing silicalite-1 framework during heating are extracted from the Rietveld refinement of the powder XRD patterns collected at different temperatures. Figure 4.14 (a-d) shows the changes in unit cell parameters during template removal for heating rate of 1, 3 and 5 °C/min. There is a large contraction in the unit cell volume as the template is removed from the framework. All the heating rates applied show similar behavior in the contraction of the unit cell. Irrespective of the heating rates applied, the magnitude of the contraction

of unit cell parameters at any particular temperature *viz.*, at 823 K or at room temperature on cooling, remained the same.

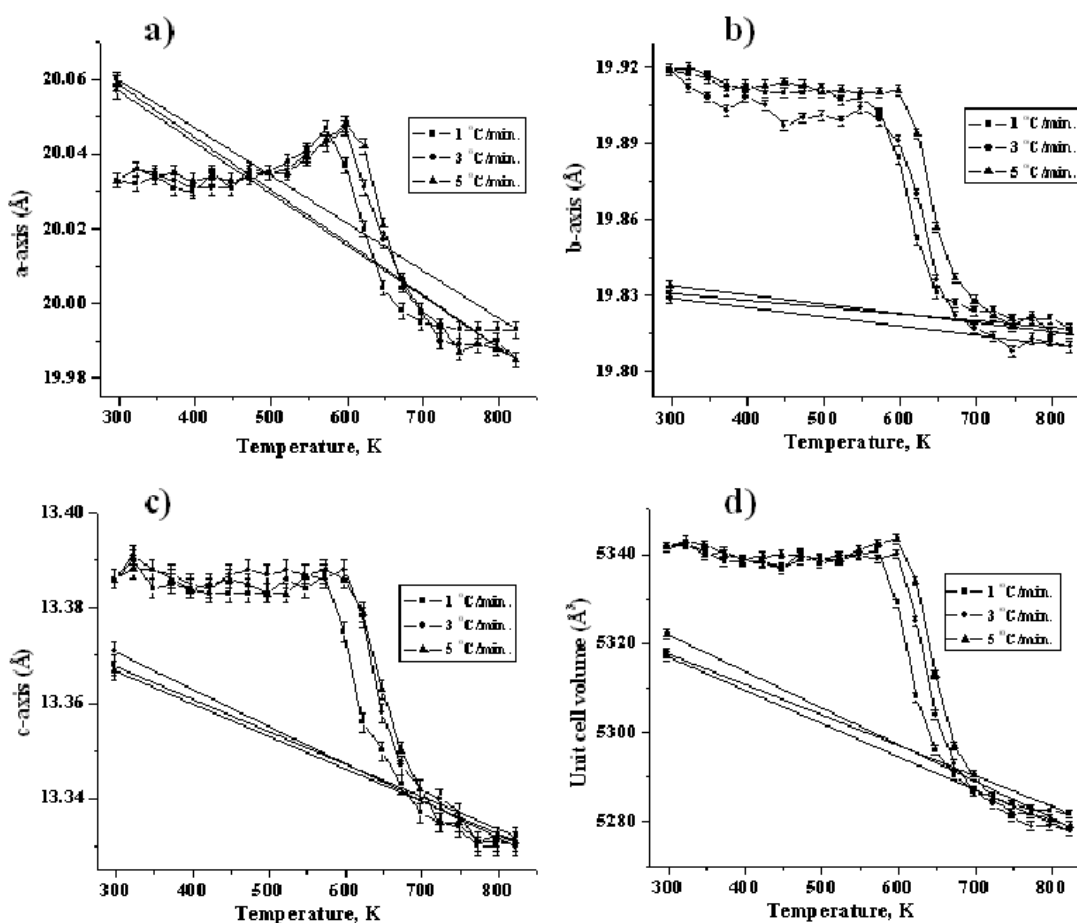


Fig. 4.14 The variation of the unit cell axes and volume during heating up to 823 K of TPA-MFI powder using three different heating rates 1 °C/min (squares), 3 °C/min (circles), and 5 °C/min (triangles). The RT data after calcination for each series is indicated. Legend: (a) a-axis, (b) b-axis, (c) c-axis and (d) unit cell volume.

Volume contraction is attributed to the transverse vibrations of Si-O-Si bridging oxygens as a function of temperature. It is now very well documented that MFI type zeolite framework normally contract on heating [36, 37]. Gualtieri *et al.* [23] also reported the same behavior of the silicalite-1 framework in their in situ studies and the results are used to correlate the thermal cracking in silicalite-1 membranes. The increase in unit cell parameters after template removal along crystallographic ‘*a*’ direction may be due to the unfolding of tetrahedras along that direction.

4.4 Conclusions

Non-isothermal reaction kinetics of the template decomposition of the tetrapropylammonium cations (TPA⁺) intercalated in silicalite-1 framework has been carried out using HTXRD technique thermogravimetric (TG) analysis. Conversion factor for template decomposition is calculated using two methods *viz.*, changes in the intensities of the Bragg reflections 101/011 and 200/020 in the HTXRD patterns scanned at different temperatures (range 298-823 K) and % weight loss from the thermogravimetric analysis. The calculated apparent activation energy for template decomposition in air was 125 and 129 kJ mol⁻¹ respectively, for the two techniques HTXRD and TG, calculated using the Kissinger method. By Flynn–Wall–Ozawa approach of isoconversion, apparent activation energy for template decomposition in air was 124 and 123 kJ mol⁻¹ respectively, for HTXRD and TG data. The reaction order was determined using the method of Kennedy and Clark and it is ~2 by both the techniques. The second order of template decomposition can be attributed to the fact that TPA⁺ is positioned in two different orientations inside the silicalite-1 framework.

4.5 References

1. C. H. Bamford, C. E. H. Tipper (Eds.), *Comprehensive Chemical Kinetics*, Vol. 22, Elsevier, New York, 1980, Ch. 3.
2. H. E. Kissinger, *J. Res. NBS*, 57 (1956) 217.
3. J. A. Augis, J. E. Bennett, *J. Thermal Anal.*, 13 (1978) 283.
4. R. L. Takhor, *Advances in nucleation and crystallization of glasses*, Am. Ceram. Soc., Columbus, 1972, p. 166.
5. A. W. Coats, J. P. Redfem, *Nature*, 201 (1964) 68.
6. J. Sestak, *Thermochim. Acta.*, 3 (1971) 150.
7. V. Satava, *Thermochim. Acta.*, 2 (1971) 423.
8. J. A. Kennedy, S.M. Clark, *Thermochim. Acta.*, 307 (1997) 27.
9. S. Arrhenius, *Zeitschrift fur Physicalische Chemie* 226 (1889) 226.
10. M. Avrami, *J. Chem. Phys.*, 7 (1939) 1103.
11. M. Avrami, *J. Chem. Phys.*, 8 (1940) 212.
12. M. Avrami, *J. Chem. Phys.*, 9 (1941) 177.
13. W. A. Johnson, K. E. Mehl, *Trans. AIME*, 135 (1939) 416.
14. B. V. Erofeev, N. L. Mitskevich, *Reactivity of Solids*, Elsevier, Amsterdam,

- 1961, p. 273.
15. T. Ozawa, *Polymer*, 12 (1971) 150.
 16. Z. B. Gabelica, J. Nagy, P. Bodart, N. Devalle, A. Nastro, *Zeolites*, 7 (1987) 67.
 17. B. M. Lok, T. R. Cannan, C. A. Messina, *Zeolites* 3 (1983) 282.
 18. H. Hagiwara, Y. Kiyozumi, M. Kurita, T. Sato, H. Shimada, K. Suzuki, S. Shin, A. Nishijima, N. Todo, *Chem. Lett.*, 10 (1981) 1653.
 19. M. Soulard, S. Bilger, H. Kessler, J. L. Guth, *Zeolites*, 7 (1987) 463.
 20. J. C. Lee, D. T. Hayhurst, *Chem. Eng. Comm.*, 77 (1989) 15.
 21. O. Pachtová, M. Kocirik, A. Zikánová, B. Bernauer, S. Miachon, J. -A. Dalmon, *Micropor. Mesopor. Mater.*, 55 (2002) 285.
 22. M. Milanese, G. Artioli, A. F. Gualtieri, L. Palin, C. Lamberti, *J. Am. Chem. Soc.*, 125 (2004) 14549.
 23. M. L. Gualtieri, A. F. Gualtieri, J. Hedlund, *Micropor. Mesopor. Mater.*, 89 (2006) 1.
 24. H. E. Kissinger, *Anal. Chem.*, 29 (1957) 1702.
 25. J. H. Flynn, L. A. Wall, *J. Polym. Sci. Part B*, 4 (1966) 323.
 26. T. Ozawa, *Bull. Chem. Soc. Jpn.*, 38 (1965) 1881.
 27. H. M. Rietveld, *Acta. Crystallogr.*, 22 (1967) 15; *J. Appl. Crystallogr.*, 2 (1969) 65.
 28. A. C. Larson, R. B. von Dreele, *GSAS Generalized structure analysis system*, Laur 86-748, Los Alamos National Laboratory, Los Alamos, New Mexico, 1994.
 29. H. van Koningsveld, H. van Bekkum, J. C. Jansen, *Acta. Crystallogr.*, B43 (1987) 127.
 30. I. Jirka, O. Pachtova, P. Novak and M. Kocirik, *Langmuir*, 18 (2002), 1702.
 31. K. H. Gilbert, R. M. Baldwin, J. Douglas Way, *Ind. Eng. Chem. Res.*, 40 (2001), 4844.
 32. R. Millini, G. Perego, D. Berti, W. O. Parker Jr., A. Carati, G. Bellussi, *Micropor. Mesopor. Mater.*, 35-36 (2000) 387.
 33. J. Dong, Y. S. Lin, M. Z. C. Hu, R. A. Peascoe, E. A. Payzant, *Micropor. Mesopor. Mater.*, 34 (2000) 241.
 34. L. Palin, C. Lamberti, A. Kvick, F. Testa, R. Aiello, M. Milanese, D.

-
- Viterbo, *J. Phys. Chem. B*, 107 (2003) 4034.
35. G. D. Price, J. J. Pluth, J. V. Smith, J. M. Bennett, R. L. Patton, *J. Am. Chem. Soc.*, 104 (1982) 5971.
36. D. S. Bhange, Veda Ramaswamy, *Micropor. Mesopor. Mater.*, 103 (2007) 235.
37. B. A. Marinkovic, P.M. Jardim, A. Saavedra, L.Y. Lau, C. Baehtz, R.R. de Avillez, F. Rizzo, *Micropor. Mesopor. Mater.*, 71 (2004) 117.

Chapter **5**

Low Temperature XRD (LTXRD) Studies

5.1 Introduction

The MFI framework [1] shows a two-dimensional pore system consisting of two intersecting sets of tubular channels [2,3], a linear one parallel to the [010] direction, with an opening of approximately 5.4-5.6 Å, and a sinusoidal one parallel to the [100] direction, with an opening of 5.1-5.5 Å. Both channels are defined by 10 member rings of SiO₄ tetrahedra. MFI-type zeolites (zeotype) materials are among the most important microporous solids for their large use in the field of catalysis and fine chemicals. The mostly used MFI material is ZSM-5 zeolite, first synthesized in the Mobil laboratories in the late 1970s [2]. The isomorphous substitution of Si by other tetrahedrally coordinated heteroatoms (different from Al³⁺) such as Ti⁴⁺ or Fe³⁺ in small amounts (up to 2-3% in weight) provides new materials, named as titanium silicalite-1 [4] and iron silicalite-1 [5], respectively (more briefly TS-1 and FeS-1), showing specific catalytic properties in oxidation and hydroxylation reactions, related to the coordination state of the heteroatom [6]. The MFI framework can be synthesized also in the totally siliceous form, resulting in silicalite-1 material [7, 8].

In recent years, TS-1 and FeS-1 have attracted particular interest in the scientific community as partial oxidation catalysts. TS-1 is an active and selective catalyst in a number of low temperature oxidation reactions with aqueous H₂O₂ as the oxidant [9, 10]. For this reason, it has been one of the most studied materials in heterogeneous catalysis in the last two decades [11-15]. As for FeS-1, one-step oxidation of benzene to phenol using N₂O as oxidant [16] is worth noticing. Indeed, the selective addition of an oxygen atom into an aromatic ring to yield phenols and naphthols is a very promising tool for the chemical industry, because the commonly employed route *via* the three-step cumene process is of great technological complexity. Due to these important properties TS-1 and FeS-1 samples have been subjected to a number of investigations [17-22].

The precise structural role played by the Ti atoms in TS-1 was the subject of lively debate up until the middle of the nineties: titanyl groups, extraframework defect sites or TiO₂ nanoclusters, monomeric and dimeric Ti species, or Ti species incorporated in edge sharing units forming bridges across the zeolite channels, have all been documented in literature [11, 14, 23]. While the orthorhombic MFI type molecular sieve features 12 crystallographically distinct T sites, which we will refer to as T1 to T12, following the notation of van Koningsveld *et al.* [24], the monoclinic symmetry has 24 T sites in one asymmetric unit of MFI. So far, it is not clear whether

the Ti ions are distributed randomly among all 12 T sites or whether they preferentially occupy some of the 12 positions. The siting of ‘heteroatoms at different T sites’ and its influence on catalytic properties will provide valuable information for understanding the methods to tailor the zeolites/molecular sieves for meeting the needs of catalytic applications. The site where ‘T’ heteroatom is incorporated in the framework of MFI and its effect on the acidic property as well as the catalytic reactivity and selectivity can be probed once the location of ‘heteroatoms’ and their occupancy in the framework is determined. Attempts to use X-ray diffraction techniques, including high-resolution synchrotron, for determining the preferential siting of Ti in TS-1 by Rietveld refinement, have been hindered by the substitution of low concentration of Ti in the framework and the poor contrast between Si and Ti scattering coefficients. A low-temperature XRD study [25] indicated that likely about half of the total Ti content is located at sites T10 and T11, whereas the remaining half is probably spread among sites T1 to T3 and T5 to T9. Sites T4 and T12 were not substituted by Ti. The synchrotron radiations X-ray diffraction studies have revealed that Ti is homogeneously distributed in the MFI framework or may be slightly partitioned on different sites in different samples [26]. Direct evidence that Ti atoms are not equidistributed over the 12 crystallographically independent T sites of the MFI framework has been highlighted by neutron diffraction data collected using HRPD [27]. In particular, Lamberti *et al.* [27] found Ti atoms to occupy T6, T7, and T11 sites with highest probability. In a similar study, Hajar *et al.* [28] detected Ti substitution for Si at T3, T7, T8, T10, and T12 positions, whereas Henry *et al.* [29] reported T8, T10 and T3 sites as most preferred for incorporating Ti centers in the MFI lattice. We here summarized in the Table 5.1, the data from different experimental and computational studies, which provide different selections of preferred sites for Ti substitution in MFI. However, an issue important for understanding the stability and catalytic properties of these molecular sieves is still open, namely, the distribution of the heteroatoms over the structurally different, independent T sites of the MFI framework.

Theoretical studies of TS-1 employed both molecular mechanic energy minimization and structurally constrained quantum chemical approaches to predict the preferred location of Ti in the MFI framework. Sastre and Corma [30], minimizing a force-field-based classical energy expression (molecular mechanics, MM) of orthorhombic MFI, identified T8 as the favored site and gave an energy range of 16

kJ/mol for the different T sites. Using molecular dynamics (MD) simulations, Oumi *et al.* [31] studied the anisotropic lattice expansion of MFI upon substitution of titanium at different lattice positions; comparing to earlier experiments, they also proposed T8 as the favorable substitution site. In a similar study, Smirnov and van de Graaf [32] did not find a preferable site for Ti substitution. Njo *et al.* [33] used a combined MC/MM (Monte Carlo/MM) approach and identified T12 as the preferential site. Millini *et al.* [15] carried out density functional calculations on cluster models of fixed geometry and did not find any clear energetic preference for Ti substitution; the relative energies of the substitution sites spanned a range of about 12 kJ/mol. Sauer and co-workers [34] used an MM approach based on a force field that had been parametrized on quantum chemistry results; they calculated the maximum energy difference, 11 kJ/mol, between the lowest energy T7 and the highest-energy T9 positions. They also carried out more elaborate QM-potential method embedded-cluster calculations, but only for three selected crystallographic sites, where they found a different ordering of the site stabilities and twice-larger energy differences. The only comprehensive QM/MM study where all T sites have been investigated was based on a rather small QM model, TO_4 , containing only one T atom. This minimal QM model yielded rather small Ti-O-Si angles and Ti-O distances that were 5 picometer shorter than the experimental values.

From this overview of computational studies, one notes that the predictions of the most favorable sites for Ti substitution in TS-1 vary from one calculation to another. Apparently, just as the case in experimental studies, available theoretical approaches *failed* to provide a consistent picture of preferential siting of Ti in TS-1 zeolite. However, these theoretical methods are not free from obvious drawbacks and, therefore, their results cannot be considered as final. Earlier high-level quantum chemistry calculations on cluster models with constrained geometry neglected the elasticity and the polarizability of the system under consideration. However, even the more recent hybrid QM/MM (quantum mechanics/ MM) calculations employing the ONIOM23 or the QM-potential methods did not explicitly account at the QM level for the electrostatic interactions, which are included only at the classical level. Deka *et al.* [35] have accounted these drawbacks and used covalent elastic polarizable environment method and reported that T5, T7, T8 and T12 the probable sites for Ti location. In the present work, we have made an attempt to locate the Ti and Fe in the MFI framework of TS-1 and FeS-1 molecular sieves respectively. To the best of our

knowledge there are only two studies that have been carried out in literature to locate the Fe in MFI framework. Milanesio *et al.* [18] inferred the location of Fe³⁺ at T9 and T10 sites and Ott *et al.* [28] reported T8 as preferred site for Fe³⁺. We hope that our experimental data contribute in some way to this controversial and important debate.

Table 5.1: Preferential sites of Ti substitution in the MFI lattice from experimental and computational studies:

	Technique/method ^a	Occupied 'T' sites	Reference
Computational	LDA	T3, T10, T11, T12	15
	MD	T8	31
	MC/MM	T2, T7, T11, T12	33
	MM	T6, T7, T8, T9	29
	MM	T5, T7, T11, T12	34
	QM-POT (HF:MM)	T5, T7, T8	34
	ONIOM (B3LYP:B3LYP)	T1, T9, T10, T12	36
	CovEPE (BP:MM)	T5, T7, T8, T12	35
Experimental	XRPD	T4, T5, T11, T12	26
	XRD	T10, T11	25
	NPD	T6, T7, T11	27
	NPD	T3, T7, T8, T10, T12	28
	NPD	T3, T8, T10	29

[^a XRPD, X-ray powder diffraction; XRD, X-ray diffraction; NPD, neutron powder diffraction; LDA, local density approximation; MD, molecular dynamics; MC, Monte Carlo method; MM, molecular mechanics; ONIOM, N-layer integrated molecular orbitals and molecular mechanics method; QM-pot, hybrid quantum mechanics/potential function method; covEPE, covalent elastic polarizable environment method.]

MFI-type materials (TS-1, ZSM-5, silicalite-1) show two stable structures: a low temperature phase having the monoclinic symmetry and the high temperature phase having the orthorhombic symmetry [37-43]. Upon certain treatments, the apparent symmetry changes to monoclinic with small changes in lattice parameters.

By moving from the $Pnma$ space group of the orthorhombic phase to the $P12_1/n1$ space group of the monoclinic phase, an interchange of the a and b axes occurs. This in turn interchanges the x and y atomic co-ordinates and the interchange of Miller indices h and k . The straight channel running along b direction of orthorhombic phase (i.e. 010) gets aligned along a direction in the monoclinic phase. The β angle will increase more than 90° but will vary marginally. With this small change in unit cell shape, symmetry elements like mirror planes parallel to (010) bisecting the sinusoidal channels are removed. The view of orthorhombic phase along 010 direction and monoclinic phase along 100 direction is illustrated in the Figure 5.1.

The phase transition temperature mainly depends on the following parameters:-

- 1) The chemical composition of the framework.
- 2) The density of internal defects (Si vacancies generating).
- 3) The nature and equilibrium pressure of adsorbed organic molecules.
- 4) Presence/absence of the template.
- 5) As far as trivalent heteroatoms are concerned, the chemical nature of the counterions.

High resolution XRD data at room temperature indicated that the samples with very low content of Ti are monoclinic while the high Ti containing samples are orthorhombic. Marra *et al.* [25] have studied the structure modifications on cooling a high Ti loaded sample from RT to 80 K under anhydrous conditions using high resolution powder X-ray diffraction technique using synchrotron radiation.

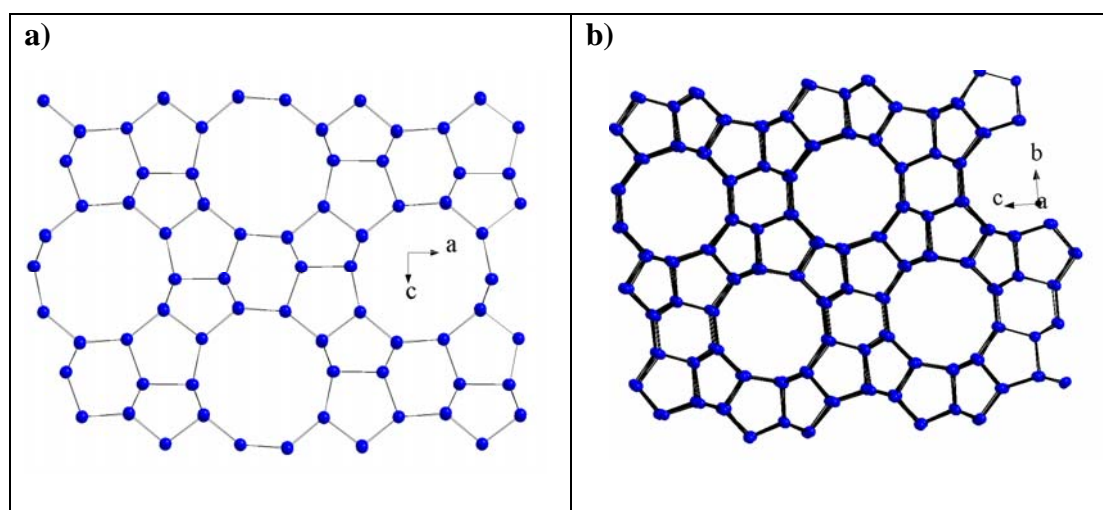


Fig. 5.1 View a) along 010 direction of orthorhombic phase in $Pnma$ space group and b) along 100 direction of monoclinic phase in $P12_1/n1$ space group.

5.2 Experimental

5.2.1 Data collection for LTXRD studies

Three TS-1 samples CTS-30, CTS-60 and CTS-80 (*vide section 2.2*) were taken for the structural studies using low temperature XRD. The samples were scanned on a Philips X-pert Pro diffractometer equipped with a proportional counter and Cu-K α radiation and an Anton Paar TTK 450 low temperature camera. The samples were mounted on a flat bed sample holder equipped with a Pt-Pt/Rh thermocouple attached to the bottom of the plate (Zapon lacquer was used to pack the sample in the sample holder). The sample holder was placed inside a sealed chamber cooled by liquid nitrogen. The measurements were carried out under vacuum of $\sim 10^{-6}$ torr using turbo molecular pump and Pirani gauge to measure the pressure. The powder X-ray diffraction patterns were recorded at various temperatures from 298 K to 80 K at regular intervals. A soak time of 10 min was employed at every step to ensure that the temperature felt throughout the sample was uniform. The scans in the 2θ range 22.5 to 25° were monitored for the phase transition from the splitting of 1 3 3 reflection of the orthorhombic symmetry into the $-3\ 1\ 3$ and $3\ 1\ 3$ reflections of the monoclinic symmetry. The samples were scanned at temperature below their individual phase transition temperatures (for monoclinic phase analysis) and at temperature above the phase transition temperature (for orthorhombic phase analysis) with speed of 0.025°/min. These slow scans were subjected to the Rietveld refinement procedure to obtain the structural information in depth. Three FeS-1 samples CFS-24, CFS-36 and CFS-72 (*vide section 2.2*) were taken for the structural studies using low temperature XRD. Similar strategy described for TS-1 was employed for the data collection on these samples.

5.2.2 Rietveld refinement

The XRD patterns collected were refined using the Rietveld method [44]. The unit cell parameters at each temperature were refined with the Rietveld method using the GSAS [45] package and the EXPGUI graphical interface [46], which allows proper treatment of the instrumental aberration parameters, such as the goniometer shift and the sample displacement parameters. The goniometer zero correction was applied with respect to Si standard scanned separately. The starting atomic coordinates and thermal parameters for the TS-1 phase in the orthorhombic symmetry

(space group $Pnma$) and monoclinic symmetry (space group $P_1 2_1/n_1$) were taken from the X-ray crystal structure of H-ZSM-5 determined by van Koningsveld [24, 37]. It was decided to exclude the reflections for 2θ region from $5-18^\circ$ in the diffraction patterns due to the fact that the low-angle reflections are most strongly affected by non-framework species. However, the intensities of high angle reflections are generally dominated by the positions of the framework atoms, so that these can be compared quite well. The pseudo-Voigt peak profile function, with up to 17 refinable parameters, was chosen and the peaks were truncated at 0.01% of the peak maxima. Background intensity was modeled by a Chebyshev type I polynomial function with 16 background parameters. An overall scale factor, the cell parameters and the sample displacement parameter were simultaneously refined. While refining the structural parameters, because of the complexity of the structure, soft restraints were applied to Si–O bond distances ($1.59 \pm 0.05 \text{ \AA}$) with a suitable weighting factor, which was gradually reduced as the refinement proceeded. Framework atoms of the same element type were constrained to have the same isotropic thermal displacement parameters.

5.3 Results and discussion

5.3.1 Phase transition in TS-1

Figure 5.2 shows the multiple plot of the LTXRD patterns for the TS-1 sample with Si/Ti = 30 in the 2θ range 22.5 to 25° . It can be seen that the orthorhombic phase is stable up to 180 K. At 170 K, the splitting of $1\ 3\ 3$ reflection of the TS-1 sample (orthorhombic symmetry) can be observed at $2\theta=24.5^\circ$. This indicates the lowering of the orthorhombic symmetry to the monoclinic crystal system. The $-3\ 1\ 3$ and $3\ 1\ 3$ reflections of the monoclinic symmetry are observed till temperature as low as 140 K. When the sample was heated back to the room temperature, it was observed that the split peaks disappear and the $1\ 3\ 3$ reflection of the orthorhombic symmetry is observed indicating the reversible phase transformation in the TS- 1 sample. The multiple plot of the LTXRD patterns of the TS-1 sample containing Si/Ti = 60 are shown in Figure 5.3. The powder patterns for this sample also show a similar splitting of the $1\ 3\ 3$ reflection for the orthorhombic unit cell. However it can be observed that the splitting of peaks is not distinct and the peaks overlap to a great extent. The orthorhombic to monoclinic transition occurs at 190 K. Figure 5.4 shows the LTXRD

patterns of the TS-1 sample with Si/ Ti = 80. It is seen that the 1 3 3 reflection at $2\theta=24.5^\circ$ split at 200 K. However the split is not very apparent and is masked by the broadening of the reflections.

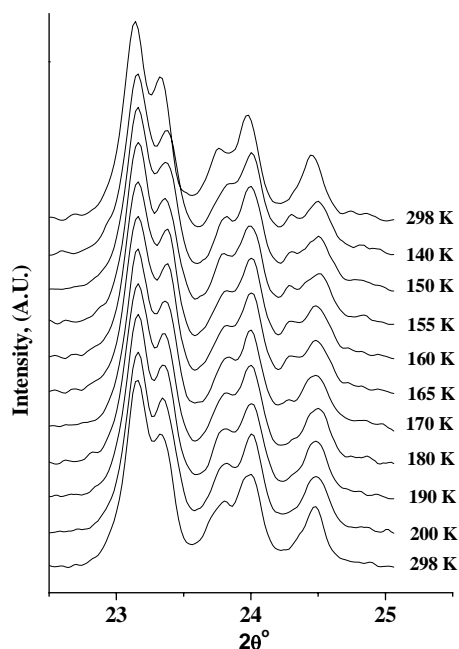


Fig. 5.2 The evolution of the XRD patterns in $22.5\text{-}25^\circ$ 2θ region as a function of the temperature collected for the sample CTS-30 ($T_{PT} = 170$ K).

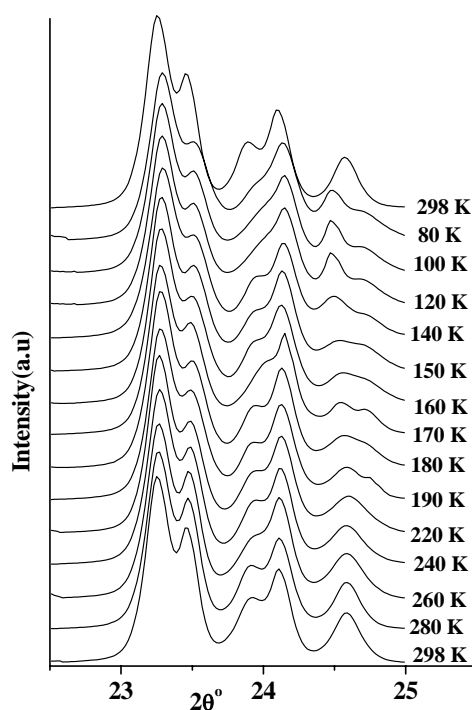


Fig. 5.3 The evolution of the XRD patterns in $22.5\text{-}25.5^\circ$ 2θ region as a function of the temperature collected for the sample CTS-30 ($T_{PT} = 190$ K).

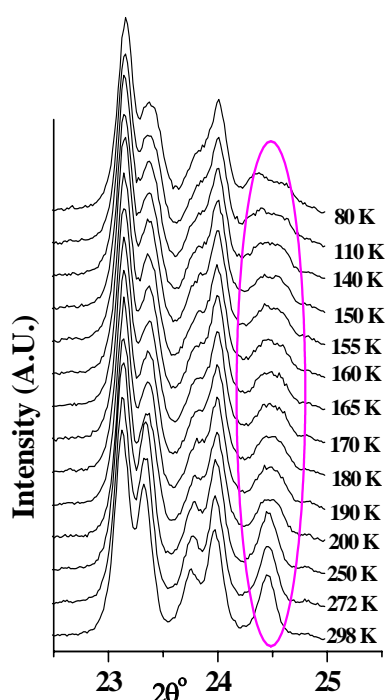


Fig. 5.4 The evolution of the XRD patterns in 22.5-25° 2θ region as a function of the temperature collected for the sample CTS-80 ($T_{PT} = 200$ K).

This indicates that the phase transition temperature (T_{PT}) for orthorhombic symmetry to monoclinic symmetry in TS-1 molecular sieves depends on the framework composition of the TS-1 samples under study. The phase transition temperature depends on the framework Si/Ti ratio and increases with the increase in Si/Ti ratio in the framework. In other words higher concentration of the Ti in the framework (*i.e.* lower Si/Ti ratio) will lower the phase transition temperature. The transition temperature is 170 K, 190 K and 200 K for CTS-30, CTS-60 and CTS-80 samples respectively. The temperature-dependent studies allowed us to set the best temperatures to collect the powder XRD patterns (slow scan) of the samples in the orthorhombic and monoclinic phases, under static conditions for structural studies (to identify the location of Ti in the framework) using Rietveld refinement procedure. The slow scan XRD data is collected for these samples at temperature below and above the phase transition temperature for the 2θ region from 5-55°. The temperature below the phase transition temperature for all the samples was 80 K where all the samples showed the monoclinic symmetry. While 180 K for CTS-30, 220 K for CTS-60 and 250 K for CTS-80 were the temperatures selected, for the data collection to generate structural data when these samples are in the orthorhombic symmetry.

The unit cell parameters of the orthorhombic phase of the three TS-1 samples are given in Table 5.2. Table 5.3 reports the atomic coordinates obtained after Rietveld refinement of the data collected on the sample CTS-80 at 250 K in *Pnma* space group and the Rietveld plot is shown in Figure 5.5.

Table 5.2 Lattice parameters and Rietveld refinement parameters of PXRD patterns of TS-1 samples scanned at low temperature above phase transition.

Sample	T, K	Lattice parameters			UCV, Å ³	<i>Rwp</i> %	<i>Rp</i> %	χ^2
		<i>a</i> , Å	<i>b</i> , Å	<i>c</i> , Å				
CTS-30	180	20.118	19.935	13.414	5380	9.66	7.53	2.84
CTS-60	220	20.095	19.910	13.403	5362	9.82	7.83	2.96
CTS-80	250	20.092	19.910	13.394	5358	9.52	7.52	2.71

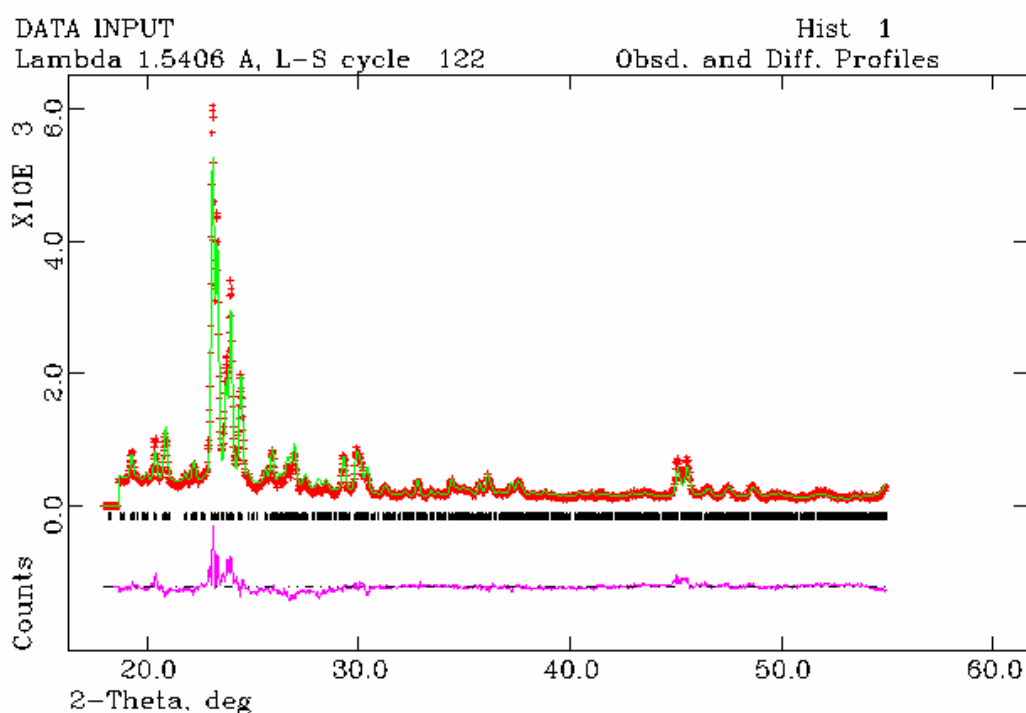


Fig. 5.5 Observed, calculated and difference profiles and reflections positions for the orthorhombic CTS-80 measured at 250 K.

Table 5.3 Atomic parameters resulting from the Rietveld refinement of the orthorhombic CTS-80 sample collected at 250 K.

Atom	<i>x</i>	<i>y</i>	<i>z</i>	Uiso (Å ²)
Si(1)	0.431(7)	0.055(9)	-0.284(6)	0.024
Si(2)	0.308(10)	0.024(7)	-0.153(5)	0.024
Si(3)	0.287(7)	0.098(6)	0.044(7)	0.024
Si(4)	0.115(8)	0.050(9)	0.002(6)	0.024
Si(5)	0.063(8)	0.044(8)	-0.210(6)	0.024
Si(6)	0.201(9)	0.073(7)	-0.361(7)	0.024
Si(7)	0.416(8)	-0.180(7)	-0.377(4)	0.024
Si(8)	0.315(6)	-0.150(9)	-0.178(8)	0.024
Si(9)	0.264(8)	-0.174(6)	0.062(6)	0.024
Si(10)	0.113(7)	-0.147(7)	0.024(3)	0.024
Si(11)	0.078(9)	-0.133(10)	-0.157(3)	0.024
Si(12)	0.180(10)	-0.182(6)	-0.272(6)	0.024
O(1)	0.326(4)	0.061(5)	-0.185(9)	0.048
O(2)	0.288(4)	0.080(5)	-0.038(4)	0.048
O(3)	0.193(8)	0.055(11)	0.005(9)	0.048
O(4)	0.061(9)	0.031(6)	-0.152(4)	0.048
O(5)	0.119(6)	0.042(4)	-0.272(3)	0.048
O(6)	0.220(4)	0.006(5)	-0.281(8)	0.048
O(7)	0.403(5)	-0.161(6)	-0.260(5)	0.048
O(8)	0.326(5)	-0.136(4)	-0.017(5)	0.048
O(9)	0.219(5)	-0.172(10)	0.050(2)	0.048
O(10)	0.102(5)	-0.193(5)	-0.029(9)	0.048
O(11)	0.122(7)	-0.154(2)	-0.254(6)	0.048
O(12)	0.264(7)	-0.180(8)	-0.229(4)	0.048
O(13)	0.307(6)	-0.064(2)	-0.144(10)	0.048
O(14)	0.064(8)	-0.031(3)	-0.211(4)	0.048
O(15)	0.423(5)	0.126(7)	-0.454(3)	0.048
O(16)	0.395(4)	0.012(2)	-0.334(5)	0.048
O(17)	0.409(3)	-0.086(5)	-0.501(8)	0.048
O(18)	0.166(6)	0.134(6)	-0.358(7)	0.048
O(19)	0.222(6)	-0.002(9)	-0.402(4)	0.048
O(20)	0.198(5)	-0.167(5)	-0.382(3)	0.048
O(21)	-0.036(5)	0.030(2)	-0.243(6)	0.048
O(22)	0.002(7)	-0.182(9)	-0.214(7)	0.048
O(23)	0.445(8)	-0.250(0)	-0.276(5)	0.048
O(24)	0.214(5)	-0.250(0)	-0.346(5)	0.048
O(25)	0.273(6)	-0.250(0)	0.003(5)	0.048
O(26)	0.134(6)	-0.250(0)	0.140(5)	0.048

The fit parameters are $R_{wp} = 9.52$, $R_p = 7.52$ and $\chi^2 = 2.71$.

The collected XRD patterns of the CTS-30, CTS-60 and CTS-80 samples at temperature 80 K were analyzed by Rietveld refinement procedure for their structural evolution. The unit cell parameters of the monoclinic phase of the three TS-1 samples are given in Table 5.4. Table 5.5 reports the atomic coordinates obtained after Rietveld refinement of the data collected on the sample CTS-80 at 80 K in $P 1 2_1/n 1$ space group and the Rietveld plot is shown in Figure 5.6.

Table 5.4 Lattice parameters and Rietveld refinement parameters of PXRD patterns of TS-1 samples scanned at low temperature 80 K.

Sample	Lattice parameters				UCV, \AA^3	R_{wp} %	R_p %	χ^2
	a , \AA	b , \AA	c , \AA	β°				
CTS-30	19.930	20.110	13.410	90.30	5375	6.96	5.2	4.06
CTS-60	19.911	20.089	13.402	90.35	5360	6.54	4.99	3.61
CTS-80	19.908	20.089	13.393	90.36	5356	7.02	5.34	4.20

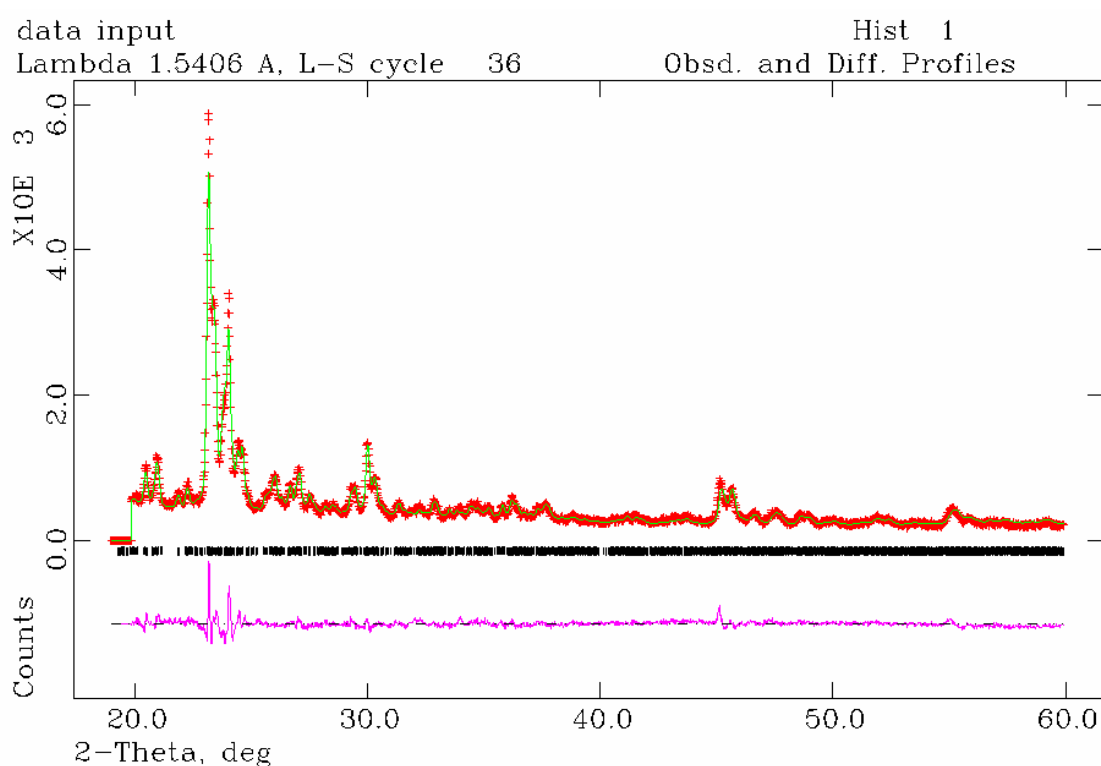


Fig. 5.6 Observed, calculated and difference profiles and reflections positions for the monoclinic CTS-80 measured at 80 K.

Table 5.5 Atomic parameters resulted from Rietveld refinement of the monoclinic CTS-80 sample collected at 80 K.

Atom	<i>x</i>	<i>y</i>	<i>z</i>	Uiso (Å ²)
Si(1)	0.077(6)	0.376(9)	-0.316(9)	0.020
Si(2)	0.010(6)	0.272(7)	-0.209(9)	0.020
Si(3)	0.058(8)	0.294(5)	-0.004(4)	0.020
Si(4)	0.144(8)	0.088(3)	0.088(5)	0.020
Si(5)	0.064(9)	0.070(5)	-0.161(9)	0.020
Si(6)	0.032(6)	0.279(3)	-0.318(2)	0.020
Si(7)	-0.187(4)	0.409(5)	-0.288(7)	0.020
Si(8)	-0.192(8)	0.311(6)	-0.121(2)	0.020
Si(9)	-0.208(5)	0.223(2)	0.063(2)	0.020
Si(10)	-0.171(9)	0.059(7)	0.026(6)	0.020
Si(11)	-0.076(7)	-0.000(5)	-0.196(2)	0.020
Si(12)	-0.207(5)	0.178(9)	-0.344(2)	0.020
Si(13)	0.452(4)	0.401(9)	-0.381(4)	0.020
Si(14)	0.42978	0.312(8)	-0.215(4)	0.020
Si(15)	0.35482	0.275(5)	0.054(5)	0.020
Si(16)	0.484(9)	0.172(10)	0.032(9)	0.020
Si(17)	0.535(9)	0.109(2)	-0.221(6)	0.020
Si(18)	0.413(9)	0.207(2)	-0.418(9)	0.020
Si(19)	0.620(2)	0.427(7)	-0.251(5)	0.020
Si(20)	0.576(3)	0.274(3)	-0.147(8)	0.020
Si(21)	0.680(5)	0.288(3)	0.095(2)	0.020
Si(22)	0.571(1)	0.107(8)	0.127(5)	0.020
Si(23)	0.695(2)	0.083(3)	-0.172(9)	0.020
Si(24)	0.726(2)	0.157(1)	-0.343(2)	0.020
O(1)	0.104(2)	0.162(8)	-0.137(6)	0.038
O(2)	0.053(5)	0.240(5)	-0.108(2)	0.038
O(3)	0.005(2)	0.157(6)	-0.016(9)	0.038
O(4)	0.012(2)	0.193(8)	-0.127(9)	0.038
O(5)	0.053(4)	0.225(9)	-0.370(2)	0.038
O(6)	0.017(4)	0.164(7)	-0.225(8)	0.038
O(7)	-0.091(5)	0.364(2)	-0.195(6)	0.038
O(8)	-0.179(5)	0.418(10)	-0.023(9)	0.038
O(9)	-0.104(2)	0.179(6)	-0.009(9)	0.038
O(10)	-0.197(2)	0.168(3)	-0.205(6)	0.038
O(11)	-0.245(4)	0.155(2)	-0.113(7)	0.038
O(12)	-0.034(2)	0.273(5)	-0.462(6)	0.038
O(13)	-0.131(8)	0.254(7)	-0.225(6)	0.038
O(14)	0.065(3)	0.169(6)	-0.149(4)	0.038
O(15)	0.100(2)	0.459(3)	-0.356(6)	0.038

O(16)	0.032(9)	0.366(3)	-0.439(2)	0.038
O(17)	-0.132(6)	0.423(3)	-0.272(2)	0.038
O(18)	0.089(8)	0.172(7)	-0.349(9)	0.038
O(19)	0.036(6)	0.208(10)	-0.500(3)	0.038
O(20)	-0.182(4)	0.196(2)	-0.482(2)	0.038
O(21)	0.099(3)	-0.166(3)	-0.232(6)	0.038
O(22)	-0.250(7)	-0.05(3)	-0.145(2)	0.038
O(23)	-0.267(2)	0.470(8)	-0.469(9)	0.038
O(24)	-0.224(2)	0.261(6)	-0.316(6)	0.038
O(25)	-0.228(8)	0.285(2)	0.113(8)	0.038
O(26)	-0.274(4)	0.164(3)	0.041(7)	0.038
O(27)	0.346(9)	0.518(2)	-0.110(4)	0.038
O(28)	0.426(9)	0.165(3)	-0.110(7)	0.038
O(29)	0.468(4)	0.181(7)	-0.055(7)	0.038
O(30)	0.527(4)	0.029(4)	-0.080(7)	0.038
O(31)	0.366(9)	0.147(3)	-0.207(4)	0.038
O(32)	0.546(2)	0.350(2)	-0.378(2)	0.038
O(33)	0.558(3)	0.406(2)	-0.037(2)	0.038
O(34)	0.679(9)	0.347(2)	-0.064(2)	0.038
O(35)	0.648(5)	0.317(6)	0.079(2)	0.038
O(36)	0.669(2)	0.119(5)	-0.099(5)	0.038
O(37)	0.577(5)	0.100(9)	-0.242(4)	0.038
O(38)	0.761(2)	0.159(6)	-0.363(2)	0.038
O(39)	0.547(6)	0.471(2)	-0.237(9)	0.038
O(40)	0.570(9)	0.020(3)	-0.288(2)	0.038
O(41)	0.407(7)	0.366(8)	-0.272(9)	0.038
O(42)	0.548(9)	0.416(3)	-0.586(7)	0.038
O(43)	0.709(7)	0.503(2)	-0.542(2)	0.038
O(44)	0.257(9)	0.210(2)	-0.551(5)	0.038
O(45)	0.578(9)	0.180(7)	-0.282(2)	0.038
O(46)	0.706(8)	0.249(6)	-0.268(5)	0.038
O(47)	0.445(2)	0.055(6)	-0.168(3)	0.038
O(48)	0.585(4)	0.048(2)	-0.159(2)	0.038

The fit parameter are Rwp=7.02%; Rp=5.34% and reduced $\chi^2 = 4.20$.

5.3.2 An attempt to locate Ti in the MFI framework by low temperature XRD

After the refinement of the atomic coordinates of the orthorhombic symmetry for each sample and taking them as starting point, we have made an attempt to refine the Ti occupancies over the 12 independent T sites of the MFI framework. The powder XRD patterns collected for the orthorhombic phases of the three TS-1 samples were analyzed by using Rietveld refinement procedure. The quality of the Rietveld refinement could not be improved significantly by introducing the Ti atoms

on tetrahedral sites and furthermore no significant density was detected in the difference Fourier maps. However, attempts were made to test the preference of Ti atoms for the different tetrahedral sites, employing different refinement strategies. The different approaches were first tested and critically compared on CTS-30 sample, as it is one of the samples showing the highest Ti content. Successively these strategies were applied to other samples of TS-1 (*i.e.*, CTS-60 and CTS-80).

The refinement strategies tested on the sample CTS-30 are as follows: (S1) simultaneous refinement of the Ti and Si proportion ($Ti+Si=1.0$) in all tetrahedral sites, with no limitation on overall Ti content and (S2) simultaneous refinement of the Ti and Si proportion ($Ti+Si=1.0$) in all tetrahedral sites, with the total Ti content of the sample constrained to the value measured by chemical analysis (*i.e.*, 2.6 Ti atoms per cell in CTS-30). The site occupancy factors resulting from the different refinements for sample CTS-30 are listed in the Table 5.6.

The tests performed on sample CTS-30 clearly indicate that the refinement strategy does not substantially influence the final results. The T sites containing significant amounts of Ti are independent of the refinement assumptions: sample CTS-30 always shows appreciable Ti occupancy only in sites T2, T4, T6 and T11, although the total absolute Ti content is slightly influenced by the overall chemical constraints. We have chosen to apply the two refinement strategies to all samples as follows: first the proportion of Ti and Si ($Ti+Si=1.0$) was allowed to vary simultaneously for each of the 12 tetrahedral sites, using a fixed unique isotropic displacement parameter which was refined earlier for silicon. In a second step, the Ti content was reset to 0 and fixed for all the T sites showing a negative Ti content. The Ti and Si fractional site occupancies were then allowed to vary again for the remaining sites, together with the displacement parameter.

All our attempts to refine part of the site scattering as Ti in sites T2 and T8 (indicated as preferential sites for Ti partitioning by Oumi *et al.* and Njo *et al.* [31, 33]) consistently resulted in full T2 and T6 sites occupied by Si atoms in CTS-30, T5 sites in CTS-60 sample and T8 in CTS-80 sample. The overall results indicate that in several samples there is no clear evidence of Ti partitioning, in agreement with the cited quantum mechanical calculations [15, 47]. In a few samples there might be a slight tendency for Ti partitioning, but the preferred T sites vary in different samples. We can conclude that there is no clear evidence of preferential substitution sites. Finally, it is worth emphasizing that this conclusion is in agreement with recent

microcalorimetric data on TS-1 [48], where the evolution of the heat of adsorption with coverage was found to be typical of heterogeneous surfaces. Similar results have been reported by Lamberti *et al.* [25]. This experimental evidence has been interpreted in terms of a distribution of Ti in several T sites, favoring the random distribution model. In fact, owing to the high dilution of the titanium centers in TS-1 we expect a homogeneous distribution of the Ti substitution sites only in the case of a strongly preferential T site [47]. The results of the Rietveld refinement analysis for the occupancies of Ti at the 12 different tetrahedral sites of MFI framework for the CTS-60 and CTS-80 samples are given in Table 5.7 and 5.8 respectively.

Table 5.6 Distribution of Ti sites as obtained by Rietveld refinement of the individual tetrahedral site occupancies in the orthorhombic CTS-30 sample measured at 180 K.

	T1	T2	T3	T4	T5	T6	T7	T8	T9	T10	T11	T12
S1	0	0.11	0	0.13	0.0	0.25	0	0	0	0	0.06	0
S2	0	0.11	0	0.16	0.0	0.26	0	0	0	0	0.09	0

Table 5.7 Distribution of Ti sites as obtained by Rietveld refinement of the individual tetrahedral site occupancies in the orthorhombic CTS-60 sample measured at 220 K.

	T1	T2	T3	T4	T5	T6	T7	T8	T9	T10	T11	T12
S1	0	0	0	0	0.27	0.06	0	0.01	0	0	0	0
S2	0	0	0	0	0.24	0.12	0	0.01	0	0	0	0

Table 5.8 Distribution of Ti sites as obtained by Rietveld refinement of the individual tetrahedral site occupancies in the orthorhombic CTS-80 sample measured at 250 K.

	T1	T2	T3	T4	T5	T6	T7	T8	T9	T10	T11	T12
S1	0	0	0	0	0	0	0	0.18	0	0	0	0.24
S2	Could not determine due to low concentration of Ti.											

Because of the relatively small contrast between the scattering coefficient of Ti and Si atoms in XRD, the results presented here should be considered as a weak evidence that titanium has a preferential tendency to occupy, *e.g.* in CTS-80 sample the T8 and T12 sites. In case of CTS-60 the occupied sites were T5, T6 and T8,

which suggests this occupancy is changing from sample to sample. In the case of CTS-30 sample, T2, T4, T6 and T11 are the occupied sites. The pictorial presentation of these occupied sites in MFI framework at 12 independent tetrahedral sites is shown using the software Diamond 2.1c. Figure 5.7 shows the location of Ti in MFI framework in the CTS-30, obtained after Rietveld refinement results using strategy 1.

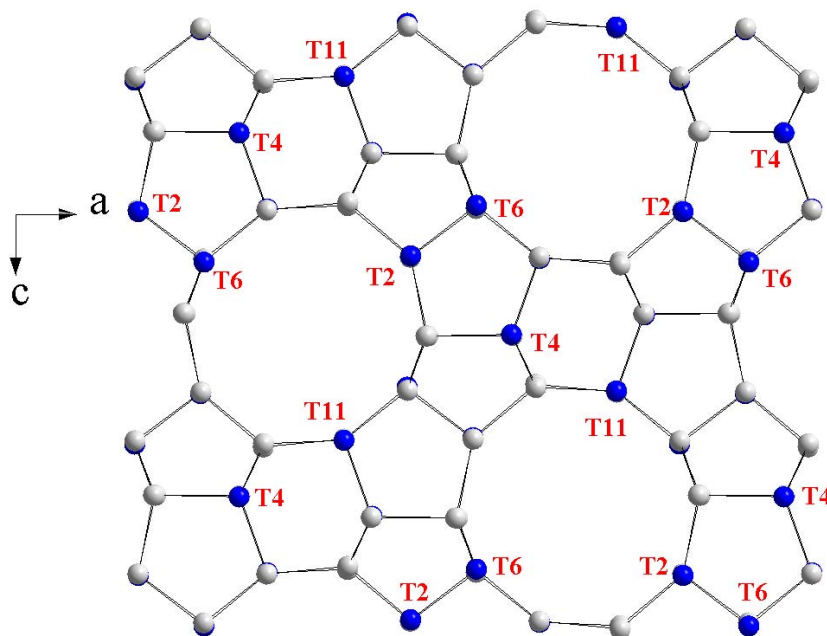


Fig. 5.7 Schematic representation of the preferential location of Ti atoms vacancies in the MFI framework (in orthorhombic symmetry) of CTS-30 sample. The gray atoms are Si and Blue are the possible sites for Ti, the oxygen atoms are not shown here for the clarity.

5.3.3 Phase transition in FeS-1

Figure 5.8 shows the multiple plot of the LTXRD patterns for the sample with Si/Fe = 24 in the 2θ range 22.5 to 25°. It can be seen that the orthorhombic phase is stable up to 143 K. At 133 K, the splitting of 1 3 3 reflection of the FeS-1 sample (orthorhombic symmetry) is observed at $2\theta = 24.5^\circ$. This indicates the lowering of the symmetry to the monoclinic crystal system. The $-3\ 1\ 3$ and $3\ 1\ 3$ reflections of the monoclinic symmetry are observed till temperature as low as 98 K. The multiple plot of the LTXRD patterns of the FeS-1 sample containing Si/Fe = 36 are shown in Figure 5.9. The powder patterns for this sample also show a similar splitting of the 1 3 3 reflection for the orthorhombic unit cell. The splitting of the 1 3 3 reflection of orthorhombic phase into the $-3\ 1\ 3$ and $3\ 1\ 3$ reflections of the monoclinic phase is not fully resolved and only a broadening of the $24.5^\circ\ 2\theta$ peak is visible. However the split is not evident and is masked by the broadening of the splitted peaks. It appears that the peaks get broaden at the temperature 190 K. This broadening can be explained on the basis of the small increase in the angle β (90.33°) suggesting that the monoclinic phase is not fully resolved. Figure 5.10 shows the evolution of FWHM of the peak centered at $24.5^\circ\ 2\theta$ for CFS-36 sample as a function of temperature. The reported FWHM is temperature independent in the 298-198 K interval. Starting from 198 K, a linear increase of the FWHM has been observed with decrease in the sample temperature and 173 K is assigned as temperature of phase transition from the changes in FWHM. Figure 5.11 shows the LTXRD patterns of the FeS-1 sample with Si/Fe = 72. It appears that the 1 3 3 reflection at $2\theta = 24.5^\circ$ seems to split at 223 K. When the samples were heated back to the room temperature, it was observed that the split peaks disappear and the 1 3 3 reflection of the orthorhombic symmetry is observed indicating the reversible phase transformation in the FeS-1 Multiple plot of such heating experiment is given in Figure 5.12 for the CFS-72 sample where it exhibits a reversible phase transition behavior. The temperature-dependent study allowed us to set the best temperatures to collect, the powder XRD patterns of the samples in the orthorhombic and monoclinic phases, under static conditions. The slow scan XRD data were collected for these samples at temperature below and above the phase transition temperature for the 2θ region from 5-55°. The data collections on the monoclinic phase of all the samples were carried out at 98 K. While 163 K, 223 K and 248 K were the temperatures selected for the data collection when these samples

showed the orthorhombic symmetry. When the samples did not show clear split in the XRD pattern, the temperature was identified by the FWHM vs. temperature plot.

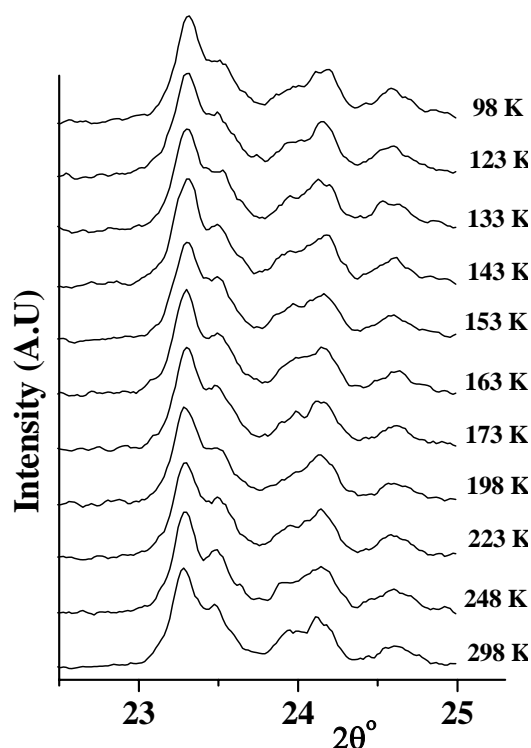


Fig. 5.8 The evolution of the XRD patterns in 22.5-25° 2θ region as a function of the temperature collected for the sample CFS-24 ($T_{PT} = 133$ K).

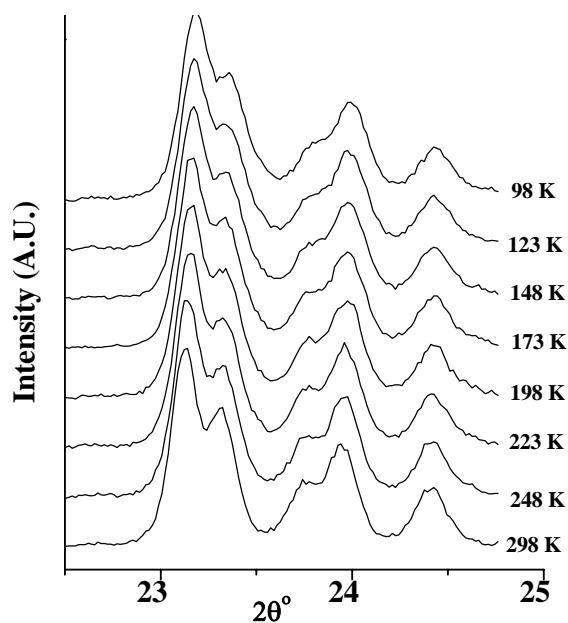


Fig. 5.9 The evolution of the XRD patterns in 22.5-25° 2θ region as a function of the temperature collected for the sample CFS-36 ($T_{PT} = 173$ K).

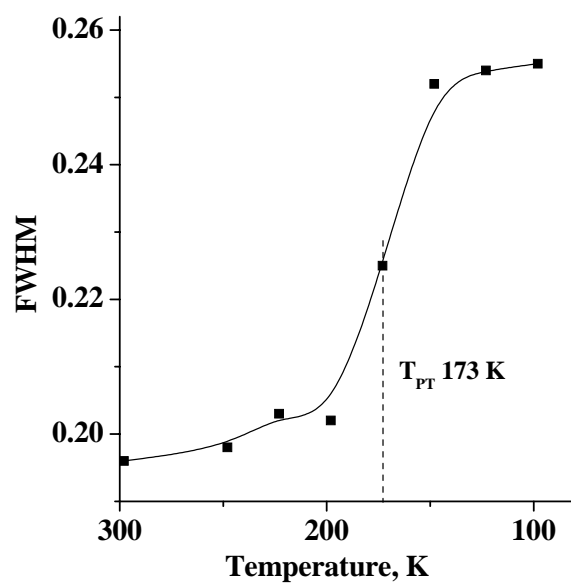


Fig. 5.10 FWHM of the 24.5° 2θ peak plotted as a function of temperature for the sample CFS-36.

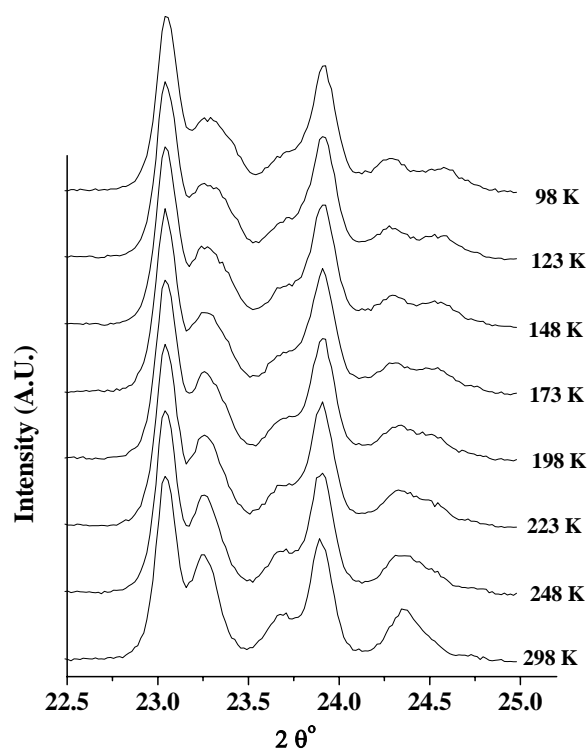


Fig. 5.11 The evolution of the XRD patterns in 22.5 - 25° 2θ region as a function of the temperature collected for the sample CFS-72 ($T_{PT} = 223$ K).

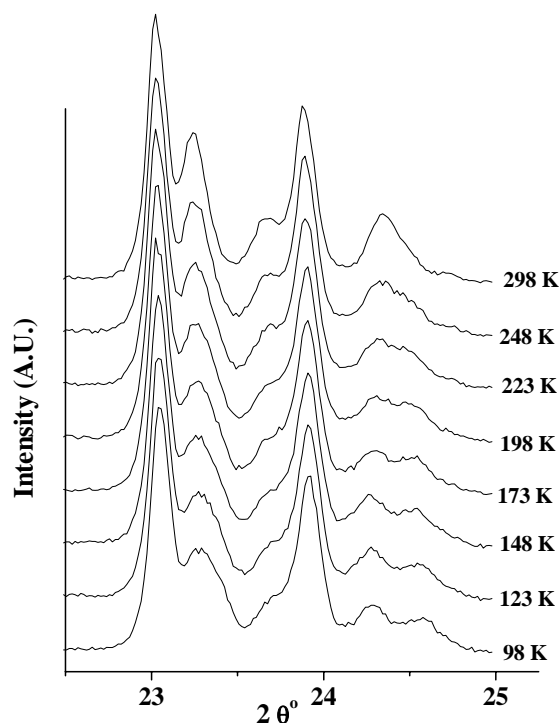


Fig. 5.12 The multiple plots of the XRD patterns as a function of the temperature heated from 98-298 K to check the reversibility of phase transition in CFS-72 sample.

The collected XRD patterns of the CFS-24, CFS-36 and CFS-72 samples at temperatures 163, 223 and 248 K respectively, were refined by Rietveld refinement procedure. The resultant information regarding unit cell parameters of the orthorhombic phase of the respective samples are given in Table 5.9. Table 5.10 Reports the atomic coordinates obtained after Rietveld refinement of the data collected on the sample CFS-72 at 248 K in *Pnma* space group and the Rietveld plot is shown in Figure 5.13.

Table 5.9 Lattice parameters and Rietveld refinement parameters of PXRD patterns of FeS-1 samples scanned at low temperature (T, K) above phase transition (T_{PT}).

Sample	T, K	Lattice parameters			UCV, \AA^3	R_{wp} %	R_p %	χ^2
		a , \AA	b , \AA	c , \AA				
CFS-24	163 (133)	20.191	19.940	13.460	5419	8.38	6.67	6.5
CFS-36	223 (173)	20.116	19.939	13.441	5391	7.9	6.22	3.42
CFS-72	248 (223)	20.120	19.914	13.408	5372	11.2	8.53	4.68

Values in parentheses show the phase transition temperature of respective sample.

Table 5.10 Atomic parameters resulting from the Rietveld refinement of the orthorhombic CFS-72 sample collected at 248 K.

Atom	<i>x</i>	<i>y</i>	<i>z</i>	Uiso (Å ²)
Si(1)	0.402 (7)	0.036 (11)	-0.320 (10)	0.027
Si(2)	0.297 (6)	0.024 (7)	-0.193 (9)	0.027
Si(3)	0.270 (6)	0.072 (9)	0.009 (6)	0.027
Si(4)	0.122 (7)	0.075 (9)	0.041 (8)	0.027
Si(5)	0.074 (8)	0.022 (8)	-0.152 (5)	0.027
Si(6)	0.192 (9)	0.080 (6)	-0.349 (7)	0.027
Si(7)	0.436 (7)	-0.158 (6)	-0.342 (3)	0.027
Si(8)	0.302 (5)	-0.133 (8)	-0.190 (4)	0.027
Si(9)	0.279 (7)	-0.162 (5)	0.032 (7)	0.027
Si(10)	0.115 (6)	-0.167 (6)	0.009 (6)	0.027
Si(11)	0.053 (9)	-0.117 (9)	-0.197 (6)	0.027
Si(12)	0.168 (6)	-0.167 (6)	-0.314 (8)	0.027
O(1)	0.299 (5)	0.082 (6)	-0.191 (8)	0.058
O(2)	0.293 (8)	0.093 (5)	-0.072 (6)	0.058
O(3)	0.210 (5)	0.060 (9)	0.004 (8)	0.058
O(4)	0.102 (9)	0.050 (5)	-0.090 (5)	0.058
O(5)	0.110 (7)	0.003 (8)	-0.263 (6)	0.058
O(6)	0.194 (6)	0.066 (6)	-0.258 (7)	0.058
O(7)	0.432 (5)	-0.171 (9)	-0.260 (8)	0.058
O(8)	0.328 (4)	-0.141 (7)	-0.119 (6)	0.058
O(9)	0.185 (7)	-0.156 (8)	0.047 (5)	0.058
O(10)	0.072 (10)	-0.155 (4)	-0.071 (7)	0.058
O(11)	0.094 (9)	-0.203 (8)	-0.277 (9)	0.058
O(12)	0.259 (6)	-0.118 (7)	-0.235 (9)	0.058
O(13)	0.304 (11)	-0.054 (8)	-0.172 (5)	0.058
O(14)	0.066 (8)	-0.063 (9)	-0.209 (4)	0.058
O(15)	0.397 (3)	0.129 (6)	-0.407 (7)	0.058
O(16)	0.419 (3)	-0.015 (8)	-0.392 (5)	0.058
O(17)	0.367 (8)	-0.124 (3)	-0.414 (7)	0.058
O(18)	0.197 (9)	0.155 (7)	-0.405 (9)	0.058
O(19)	0.161 (4)	-0.007 (9)	-0.383 (9)	0.058
O(20)	0.189 (9)	-0.146 (3)	-0.426 (7)	0.058
O(21)	-0.020 (4)	0.106 (8)	-0.194 (6)	0.058
O(22)	0.013 (6)	-0.132(7)	-0.251 (6)	0.058
O(23)	0.401 (5)	-0.25	-0.314 (8)	0.058
O(24)	0.259 (9)	-0.25	-0.315 (9)	0.058
O(25)	0.277 (6)	-0.25	0.016 (8)	0.058
O(26)	0.134 (9)	-0.25	0.106 (8)	0.058

The fit parameters are $Rwp = 11.2$, $Rp = 8.3$ and $\chi^2 = 4.68$.

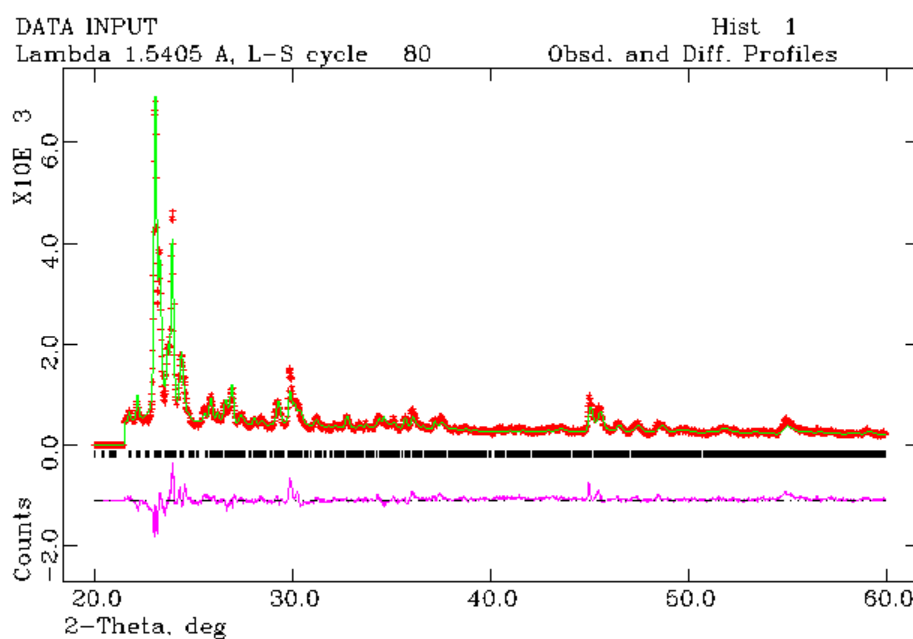


Fig. 5.13 Observed, calculated and difference profiles and reflections positions for the orthorhombic CFS-72 measured at 248 K.

The collected XRD patterns of the CFS-24, CFS-36 and CFS-72 samples at temperature 98 K were analyzed by Rietveld refinement procedure. The resultant information regarding unit cell parameters of the monoclinic phase of the respective samples are given in Table 5.11. Table 5.12 Reports the atomic coordinates obtained after Rietveld refinement of the data collected on the sample CFS-72 at 98 K in $P1$ $2_1/n1$ space group and the Rietveld plot is shown in Figure 5.14.

Table 5.11 Lattice parameters and Rietveld refinement parameters of PXRD patterns of FeS-1 samples scanned at low temperature 98 K.

Sample	Lattice parameters				UCV, \AA^3	R_{wp} %	R_p %	χ^2
	a , \AA	b , \AA	c , \AA	β°				
CFS-24	19.938	20.185	13.455	90.45	5414	10.31	8.30	3.28
CFS-36	19.939	20.167	13.385	90.36	5382	8.99	7.10	4.45
CFS-72	19.895	20.142	13.394	90.55	5367	7.84	6.22	2.91

Table 5.12 Atomic parameters resulted from Rietveld refinement of the monoclinic CFS-72 sample collected at 98 K.

Atom	<i>x</i>	<i>y</i>	<i>z</i>	Uiso (Å ²)
Si(1)	0.050(5)	0.417(6)	-0.306(4)	0.021
Si(2)	0.032(4)	0.251(9)	-0.195(9)	0.021
Si(3)	0.032(6)	0.228(6)	0.017(7)	0.021
Si(4)	0.067(6)	0.071(9)	0.013(7)	0.021
Si(5)	-0.013(7)	0.090(4)	-0.160(8)	0.021
Si(6)	0.077(6)	0.200(6)	-0.323(7)	0.021
Si(7)	-0.160(7)	0.459(7)	-0.300(5)	0.021
Si(8)	-0.102(8)	0.308(8)	-0.194(8)	0.021
Si(9)	-0.184(7)	0.282(5)	0.050(5)	0.021
Si(10)	-0.171(5)	0.139(6)	0.019(6)	0.021
Si(11)	-0.131(9)	0.080(6)	-0.153(5)	0.021
Si(12)	-0.171(6)	0.178(7)	-0.312(6)	0.021
Si(13)	0.436(5)	0.450(5)	-0.322(6)	0.021
Si(14)	0.471(5)	0.312(6)	-0.195(5)	0.021
Si(15)	0.473(5)	0.307(5)	0.016(8)	0.021
Si(16)	0.407(7)	0.149(8)	0.060(8)	0.021
Si(17)	0.461(7)	0.037(7)	-0.182(7)	0.021
Si(18)	0.477(6)	0.164(6)	-0.347(8)	0.021
Si(19)	0.676(5)	0.405(6)	-0.330(6)	0.021
Si(20)	0.631(6)	0.334(9)	-0.176(5)	0.021
Si(21)	0.669(7)	0.278(6)	0.038(3)	0.021
Si(22)	0.668(7)	0.123(8)	0.014(6)	0.021
Si(23)	0.652(7)	0.040(6)	-0.201(6)	0.021
Si(24)	0.645(6)	0.212(6)	-0.327(5)	0.021
O(1)	0.029(9)	0.358(9)	-0.24(4)	0.036
O(2)	0.082(9)	0.338(9)	-0.088(7)	0.036
O(3)	0.039(7)	0.12(4)	0.013(5)	0.036
O(4)	0.077(7)	0.081(6)	-0.10(4)	0.036
O(5)	0.066(9)	0.100(9)	-0.281(7)	0.036
O(6)	0.055(8)	0.154(8)	-0.232(9)	0.036
O(7)	-0.140(7)	0.392(9)	-0.184(9)	0.036
O(8)	-0.107(6)	0.273(8)	-0.119(8)	0.036
O(9)	-0.181(8)	0.24(4)	0.069(8)	0.036
O(10)	-0.170(7)	0.066(6)	-0.01(4)	0.036
O(11)	-0.143(8)	0.100(7)	-0.205(8)	0.036
O(12)	-0.164(6)	0.263(5)	-0.270(8)	0.036
O(13)	-0.069(5)	0.356(6)	-0.160(6)	0.036
O(14)	-0.09(8)	0.069(6)	-0.159(6)	0.036
O(15)	0.125(9)	0.415(7)	-0.35(4)	0.036

O(16)	-0.036(9)	0.420(7)	-0.419(8)	0.036
O(17)	-0.148(8)	0.456(6)	-0.39(4)	0.036
O(18)	0.168(7)	0.163(9)	-0.364(8)	0.036
O(19)	-0.022(8)	0.199(4)	-0.370(7)	0.036
O(20)	-0.152(9)	0.258(7)	-0.417(8)	0.036
O(21)	0.007(7)	0.07(4)	-0.237(6)	0.036
O(22)	-0.116(5)	-0.022(9)	-0.234(8)	0.036
O(23)	-0.237(9)	0.427(6)	-0.291(9)	0.036
O(24)	-0.263(8)	0.230(6)	-0.245(5)	0.036
O(25)	-0.27(4)	0.292(6)	0.020(4)	0.036
O(26)	-0.26(4)	0.093(4)	0.079(9)	0.036
O(27)	0.436(8)	0.302(9)	-0.22(4)	0.036
O(28)	0.397(8)	0.340(8)	-0.108(7)	0.036
O(29)	0.449(8)	0.270(9)	-0.036(7)	0.036
O(30)	0.439(7)	0.118(6)	-0.04(4)	0.036
O(31)	0.419(7)	0.170(9)	-0.21(4)	0.036
O(32)	0.395(8)	0.246(9)	-0.271(8)	0.036
O(33)	0.726(7)	0.400(7)	-0.200(4)	0.036
O(34)	0.635(6)	0.294(6)	-0.080(4)	0.036
O(35)	0.660(6)	0.18(4)	0.015(6)	0.036
O(36)	0.657(8)	0.076(5)	-0.080(4)	0.036
O(37)	0.700(6)	0.188(4)	-0.245(5)	0.036
O(38)	0.656(6)	0.292(8)	-0.150(4)	0.036
O(39)	0.573(7)	0.294(8)	-0.163(5)	0.036
O(40)	0.533(5)	0.129(4)	-0.211(6)	0.036
O(41)	0.381(9)	0.436(7)	-0.370(4)	0.036
O(42)	0.433(9)	0.400(6)	-0.378(9)	0.036
O(43)	0.614(7)	0.363(5)	-0.410(4)	0.036
O(44)	0.373(8)	0.278(8)	-0.360(4)	0.036
O(45)	0.568(7)	0.188(7)	-0.400(8)	0.036
O(46)	0.624(9)	0.152(7)	-0.401(7)	0.036
O(47)	0.459(7)	0.01(4)	-0.243(9)	0.036
O(48)	0.656(4)	0.031(3)	-0.289(7)	0.036

The fit parameter are Rwp=7.84%; Rp=6.22% and reduced $\chi^2 = 2.91$.

5.3.4 An attempt to locate Fe in the MFI framework by low temperature XRD

After the refinement of the atomic coordinates of the orthorhombic symmetry for each sample, and taking them as starting point we have made an attempt to refine the Fe occupancies over the 12 independent T sites of the MFI framework. Similar strategies like Ti were used to refine the occupancies of the Fe. As starting point of this analysis (*i.e.* 1.25 Fe atoms per unit cell for CFS-72 sample), a uniform distribution of Fe among the 12 T sites has been adopted: $x_{\text{Fe}(i)} = 0.013$ and $x_{\text{Si}} =$

0.987 ($i = 1$ to 12). Results of the Rietveld refinement by both the strategies for Fe occupancies are shown in Table 5.13, 5.14 and 5.15 for CFS-24, CFS-36 and CFS-72 samples respectively.

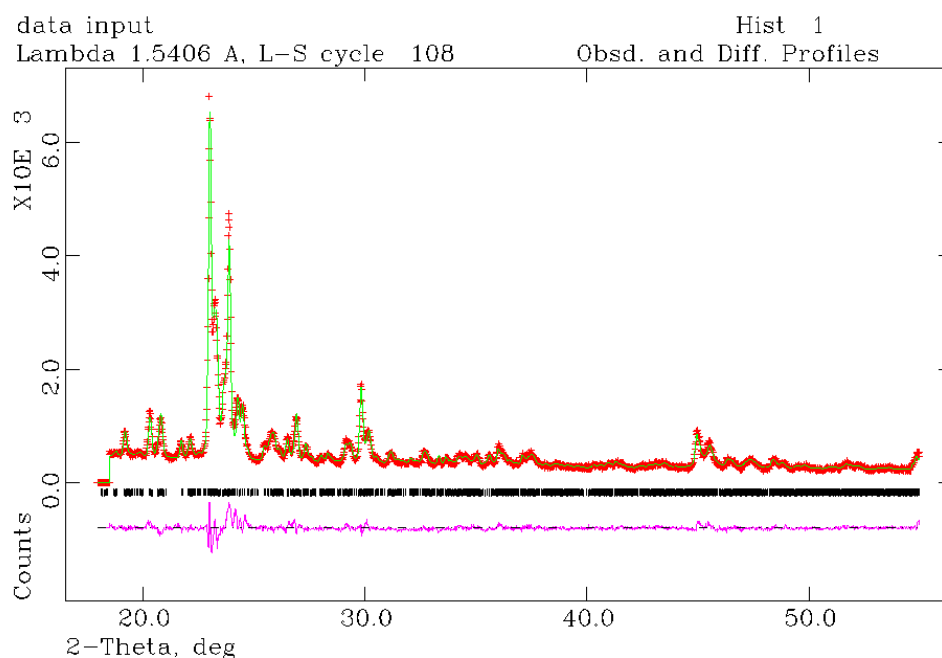


Fig. 5.14 Observed, calculated and difference profiles and reflections positions for the monoclinic CFS-72 measured at 98 K.

Table 5.13 Distribution of Fe sites as obtained by Rietveld refinement of the individual tetrahedral site occupancies in the orthorhombic CFS-24 sample measured at 163 K.

	T1	T2	T3	T4	T5	T6	T7	T8	T9	T10	T11	T12
S1	0	0.04	0	0	0.03	0.09	0	0	0	0.14	0	0
S2	0	0.01	0	0	0.02	0.23	0	0	0	0.22	0	0

Table 5.14 Distribution of Fe sites as obtained by Rietveld refinement of the individual tetrahedral site occupancies in the orthorhombic CFS-36 sample measured at 223 K.

	T1	T2	T3	T4	T5	T6	T7	T8	T9	T10	T11	T12
S1	0	0	0.05	0.18	0	0.04	0	0	0.05	0.17	0	0.49
S2	0	0	0	0.24	0	0.18	0.28	0	0.19	0	0	0.42

Table 5.15 Distribution of Fe sites as obtained by Rietveld refinement of the individual tetrahedral site occupancies in the orthorhombic CFS-72 sample measured at 250 K.

	T1	T2	T3	T4	T5	T6	T7	T8	T9	T10	T11	T12
S1	0.00	0.47	0.02	0.04	0.00	0.04	0.18	0.29	0	0	0.04	0.34
S2	0.00	0.36	0.02	0.04	0.02	0.04	0.37	0.52	0	0.04	0.08	0.21

We have provided first time the weak evidence that iron has a preferential tendency to occupy, *e.g.* in CFS-24 sample the T2, T5 and T10 sites. The pictorial presentation of these occupied sites in MFI framework at 12 independent tetrahedral sites is shown using the software Diamond 2.1c. Figure 5.15 show the location of Fe in MFI framework in the CFS-24 sample obtained after Rietveld refinement results using strategy 1.

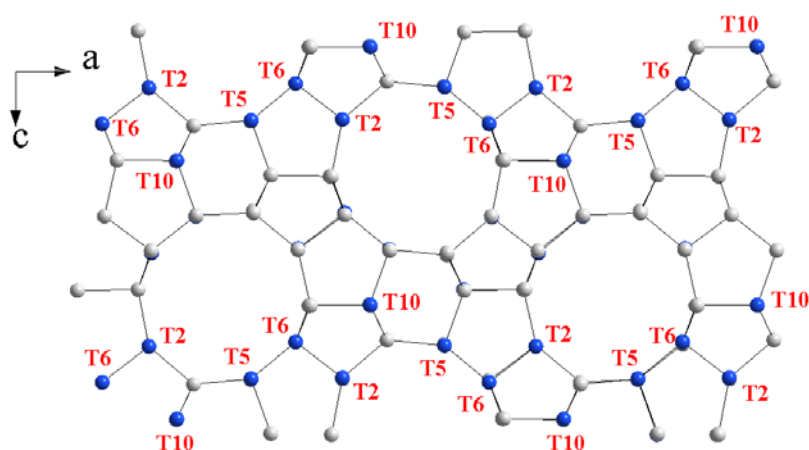


Fig. 5.15 Schematic representation of the preferential location of Fe atoms vacancies in the MFI framework (in orthorhombic symmetry) of CFS-24 sample. The gray atoms are Si and Blue are possible sites for Fe; the oxygen atoms are not shown here for the clarity.

Table 5.16 Comparison of the occupied ‘T’ sites by Ti and Fe in the various samples having different Si/M ratio.

T Sites	CTS-30 (38)	CTS-60 (72)	CTS-80 (99)	CFS-24 (30)	CFS-36 (39)	CFS-72 (82)
T1	---	---	---	---	---	---
T2	0.11	---	---	0.04	---	0.47
T3	---	---	---	---	0.05	0.02
T4	0.13	---	---	---	0.18	0.04
T5	---	0.27	---	0.03	---	---
T6	0.25	0.06	---	0.09	0.04	0.04
T7	---	---	---	---	---	0.18
T8	---	0.01	0.18	---	---	0.29
T9	---	---	---	---	0.05	---
T10	---	---	---	0.14	0.17	---
T11	0.06	---	---	---	---	0.04
T12	---	---	0.24	---	0.49	0.34

Values in parentheses are the Si/M framework ratio determined by XRD.

From the Table 5.16 it is clear that the T1 site remains unoccupied in both TS-1 as well as FeS-1 samples. The T6 site is occupied by ‘heteroatoms’ in both the cases except the CTS-80 sample. At low concentration of framework Ti gets preferentially substituted at T8 and T12 sites while Fe get randomly occupied. It is also observed that the even ‘T’ sites are more susceptible for substitution rather than the odd ‘T’ sites.

5.4 Conclusions

The investigation of the phase transition temperature for various TS-1 and FeS-1 samples (concentration of Ti and Fe vary) to determine the effect of Si/M ratio on the phase transition temperature is carried out using LTXRD technique. These metallosilicate molecular sieves show orthorhombic phase in *Pnma* space group at room temperature whereas at low temperature the structure is transformed to

monoclinic symmetry in space group $P2_1/n$. The scans in the 2θ range 22 to 26° were monitored for the phase transition from the splitting of 1 3 3 reflection of the orthorhombic symmetry into the $-3\ 1\ 3$ and $3\ 1\ 3$ reflections of the monoclinic symmetry. Attempts have been made to locate the heteroatoms in the silicalite framework for TS-1 and FeS-1 samples at low temperature (below the room temperature and above the temperature of phase transition) by using the Rietveld refinement technique. The experiment to locate the T atoms in the metallosilicate molecular sieves are extremely challenging due to the low concentration of T atoms. Contribution from the thermal atomic displacement parameters should be necessarily lower and hence XRD patterns at low temperature are collected to locate the 'T' atoms. The results of the location of heteroatoms are also discussed and compared with the results in literature.

5.5 References

1. W. M. Meier, D. H. Olson, Ch. Baerlocher, *Atlas of Zeolite Structure Types*; Elsevier: London, 1996.
2. G. T. Kokotailo, S. L. Lawton, G. T. Olson, W. M. Meier, *Nature*, 272 (1978) 437.
3. G. T. Olson, G. T. Kokotailo, S. L. Lawton, W. M. Meier, *J. Phys. Chem.*, 85 (1981) 2238.
4. M. Taramasso, G. Perego, B. Notari, *U.S. Patent No.* 4,410,501, 1983.
5. R. Szostak, T. L. Thomas, *J. Catal.*, 100 (1986) 555.
6. B. Sulikowski, *Heterog. Chem. Rev.*, 3 (1996) 203.
7. E. M. Flanigen, J. M. Bennett, R. W. Grose, J. P. Cohen, R. L. M. Patton, R. Kirchner, J. V. Smith, *Nature*, 272 (1978) 512.
8. G. Artioli, C. Lamberti, G. L. Marra, *Acta Crystallogr.*, B 56 (2000) 2.
9. B. Notari, *Adv. Catal.*, 41 (1996) 253.
10. G. M. Clerici, G. Bellussi, U. Romano, *J. Catal.*, 129 (1991) 159.
11. G. Tozzola, M. A. Mantegazza, G. Ranghino, G. Petrini, S. Bordiga, G. Ricchiardi, C. Lamberti, R. Zulian, A. Zecchina, *J. Catal.*, 179 (1998) 64.
12. G. Deo, A. M. Turek, I. E. Wachs, D. R. C. Huybrechts, P. A. Jacobs, *Zeolites*, 13 (1993) 365.
13. D. R. Huybrechts, P. L. Buskens, P. A. Jacobs, *J. Mol. Catal.*, 71 (1992) 129.

14. S. Bordiga, A. Damin, F. Bonino, G. Ricchiardi, C. Lamberti, A. Zecchina, *Angew. Chem., Int. Ed.*, 41 (2002) 4734.
15. R. Millini, G. Perego, K. Seiti, *Stud. Surf. Sci. Catal.*, 84 (1994) 2123.
16. A. S. Kharitonov, T. N. L. Alexandrova, A. Vostrikova, K. G. Ione, G. I. Panov, *Russ. Patent* 4,445,646, 1988.
17. V. I. Sobolev, G. I. Panov, A. S. Kharitonov, V. N. Romannikov, A. M. Volodin, K. G. Ione, *J. Catal.*, 139 (1993), 435.
18. M. Milanese, C. Lamberti, R. Aiello, F. Testa, M. Piana, D. J. Viterbo, *Phys. Chem. B*, 104 (2000) 9951.
19. G. Berlier, A. Zecchina, G. Spoto, G. Ricchiardi, S. Bordiga and C. Lamberti, *J. Catal.*, 215 (2003) 264.
20. G. Berlier, F. Bonino, A. Zecchina, S. Bordiga, C. Lamberti, *Chem. Phys. Chem.*, 4 (2003) 1073.
21. A. M. Ferretti, C. Oliva, L. Forni, G. Berlier, A. Zecchina, C. Lamberti, *J. Catal.*, 208 (2002) 83.
22. G. Berlier, G. Spoto, S. Bordiga, G. Ricchiardi, P. Fisicaro, A. Zecchina, I. Rossetti, E. Selli, L. Forni, E. Giamello, C. Lamberti, *J. Catal.*, 208 (2002) 64.
23. P. Ratnasamy, D. Srinivas, H. Knozinger, *Advances in catalysis*, 48 (2004) 1.
24. H. van Koningsveld, H. van Bekkum, J. C. Jansen, *Acta Crystallogr. B*, 43 (1987) 127.
25. G. L. Marra, G. Artioli, A. N. Fitch, M. Milanese, C. Lamberti, *Micropor. Mesopor. Mater.*, 40 (2000) 85.
26. C. Lamberti, S. bordiga, A. Zecchina, A. Carati, A. N. Fitch, G. Artioli, G. Petrini, M. Salvalaggio, G. L. Marra, *J. Catal.*, 183 (1999) 222.
27. C. Lamberti, S. Bordiga, A. Zecchina, G. Artioli, G. Marra, G. Spano, *J. Am. Chem. Soc.*, 123 (2001) 2204.
28. C. A. Hajar, R. M. Jacubinas, J. Eckert, N. J. Henson, P. J. Hay, K. C. Ott, *J. Phys. Chem. B*, 104 (2000) 12157.
29. P. F. Henry, M. T. Weller, C. C. Wilson, *J. Phys. Chem. B*, 105 (2001) 7452.
30. G. Sastre, A. Corma, *Chem. Phys. Lett.*, 302 (1999) 447.
31. Y. Oumi, K. Matsuba, M. Kubo, T. Inui, A. Miyamoto, *Microporous Mater.*, 4 (1995) 53.
32. K. S. Smirnov, B. van de Graaf, *Microporous Mater.*, 7 (1996) 133.

33. S. L. Njo, H. van Koningsveld, B. van de Graaf, *J. Phys. Chem. B*, 101 (1997) 10065.
34. G. Ricchiaridi, A. de Man, J. Sauer, *Phys. Chem. Chem. Phys.*, 2 (2000) 2195.
35. R. C. Deka, V. A. Nasluzov, E. A. Ivanova Shor, A. M. Shor, G.N. Vayssilov, N. Rosch, *J. Phys. Chem. B*, 109 (2005) 24304.
36. T. Atoguchi, S. Yao, *J. Mol. Catal. A*, 191 (2003) 281.
37. H. Van Koningsveld, J. C. Jansen, H. Van Bekkum, *Zeolites*, 10 (1990) 235.
38. H. Van Koningsveld, J. C. Jansen, H. Van Bekkum, *Zeolites*, 7 (1987) 564.
39. C. A. Fyfe, G. J. Kennedy, C. T. de Schutter, G. T. Kokotailo, *J. Chem. Soc. Chem. Commun.*, (1984) 541.
40. D. G. Hay, H. Jager, *J. Chem. Soc. Chem. Commun.*, (1984) 1433.
41. D. G. Hay, H. Jager, G. W. West, *J. Phys. Chem.* 89 (1985) 1070.
42. E. L. Wu, S. L. Lawton, G. T. Olson, A. C. Rohrman Jr., G. T. Kokotailo, *J. Phys. Chem.*, 83 (1979) 2777.
43. H. Nakamoto, H. Takahashi, *Chem. Lett.*, (1981) 1013.
44. H. M. Rietveld, *Acta. Crystallogr.*, 22 (1967) 151.
45. A. C. Larson, R. B. von Dreele, *GSAS Generalized structure analysis system*, Laur 86-748, Los Alamos National Laboratory, Los Alamos, New Mexico, 1994.
46. B. Toby, *J. Appl. Cryst.*, 34 (2001) 210.
47. A. Jentys, C. R. A. Catlow, *Catal. Lett.*, 22 (1993) 251.
48. V. Bolis, S. Bordiga, C. Lamberti, A. Zecchina, A. Carati, G. Petrini, F. Rivetti, G. Spano, *Langmuir*, 15 (1999) 5753.

Chapter **6**



Summary And Conclusions



The thesis describes the hydrothermal synthesis of silicalite-1 and metallosilicate molecular sieves, various physicochemical characterization and in particular, powder XRD studies at non-ambient conditions. The thermal stability of the metallosilicate molecular sieves is checked *in-situ* using HTXRD technique. Studies on the negative thermal expansion behavior of silicalite-1 and metallosilicate molecular sieves are investigated by *in-situ* HTXRD analysis. Kinetics of template decomposition from silicalite-1 framework is also studied with *in-situ* HTXRD technique and the results are correlated with results obtained from thermogravimetric analysis. Orthorhombic to monoclinic phase transition studies in metallosilicate molecular sieves are carried out using low temperature XRD technique and attempts have been made to locate the Fe and Ti atoms in respective silicalite samples. This chapter present a brief summary of the work described in previous chapters and general conclusions arrived from the work.

Chapter 1 provides a general introduction to the zeolites and MFI type molecular sieves. A brief discussion about the powder X-ray diffraction technique with different geometries and its application for various property studies such as determination of crystallinity, crystallite size, phase analysis qualitatively as well as quantitatively, determination of unit cell parameters and structure determination is given in this chapter. Rietveld refinement technique is outlined in this chapter with its principle and various parameters that can be monitored during the Rietveld analysis and information about GSAS (General Structure Analysis System) software used for Rietveld refinement is described briefly. This chapter also describes the applications of powder X-ray diffraction technique for the characterization of zeolite molecular sieves and summarizes the available literature on it. Different applications viz., isomorphous substitution of 'T' atoms by heteroatoms, location of 'T' atoms in the framework of zeolites and orientation of organic molecules inside the zeolite channels are outlined. The *in-situ* powder X-ray diffraction technique used at high temperature and low temperature conditions is discussed. The applications of high temperature powder X-ray diffraction in kinetics of solid-state phase transitions, determination of thermal expansion coefficients and reaction kinetics are described briefly. The applications of LTXRD for the study of materials, which are liquids or gases at room temperature, charge density analyses, phase transitions and thermal expansion coefficients, are outlined. It also elucidates the physical principles of other analytical

techniques used for the characterization of metallosilicate molecular sieves such as UV-vis and MAS-NMR spectroscopy. This Chapter is mainly a review of the literature on the above said topics.

Chapter 2 describes the procedure for the hydrothermal synthesis of metallosilicate molecular sieves with different Si/M (M=Fe, Ti and Zr) ratio in synthesis gel. The characterization of the metallosilicate molecular sieves by different techniques *viz.*, X-ray diffraction, TG-DTA, FTIR, SEM-EDAX, DRUV-vis spectroscopy, ^{29}Si MAS NMR etc. is described in this chapter. Theory and experimental procedure employed for each technique is discussed in this section. This chapter also describes the Rietveld refinement technique employed to extract the unit cell parameters from the powder XRD patterns collected at room temperature. The expansion in unit cell parameters as a result of isomorphous substitution of Si by Fe, Ti and Zr is discussed in this chapter. Determination of Si/M ratio in the framework, with the experimental and theoretical values of unit cell volume using powder XRD data is also discussed in this chapter. The data from the XRD supports the isomorphous substitutions of Si by Fe, Ti and Zr but some of the portion remain as extraframework or other than tetrahedral coordinated atoms, which is concluded by the results of other spectroscopic techniques.

Chapter 3 describes *in-situ* high temperature X-ray diffraction (HTXRD) studies on silicalite-1 and metallosilicate molecular sieves (FeS-1, TS-1 and ZrS-1) with MFI structure (Si/M = 50) to study the thermal stability and thermal expansion behavior as a function of temperature in the temperature range 298–1623 K. The structure of silicalite-1 and FeS-1 (monoclinic and orthorhombic phase of silicalite-1 and FeS-1) collapsed at 1173 and 1323 K and transformed to α -cristobalite phase. This transformation is irreversible. The structure of TS-1 and ZrS-1 are stable even upto 1623 K. The thermal behavior of trivalent and tetravalent cations in the MFI framework depends on the role of counter cation present in the former. The sharp negative thermal expansion seen in all the samples is anisotropic, with relative strength of contraction in 'a' axis is being greater than 'b' and 'c' axes in TS-1 and ZrS-1 while contraction is less along 'a' axis in FeS-1. Lattice thermal expansion coefficients (α_v) in the temperature range 298–1023 K are $-6.75 \times 10^{-6} \text{ K}^{-1}$ for silicalite-1, $-12.91 \times 10^{-6} \text{ K}^{-1}$ for FeS-1, $-16.02 \times 10^{-6} \text{ K}^{-1}$ for TS-1 and $-17.92 \times 10^{-6} \text{ K}^{-1}$ for ZrS-1.

The highest lattice thermal expansion coefficients (α_v) obtained are $-11.53 \times 10^{-6} \text{ K}^{-1}$ for FeS-1 in the temperature range 298–1173 K, $-20.86 \times 10^{-6} \text{ K}^{-1}$ for TS-1 and $-25.54 \times 10^{-6} \text{ K}^{-1}$ for ZrS-1, respectively, in the temperature range 298–1623 K. The strength of contraction increases with increase in framework density in the three metallosilicate molecular sieves studied. Tetravalent cation substituted metallosilicate molecular sieves show very high thermal stability, while trivalent cation substituted samples are structurally/thermally less stable. The results of the thermal stabilities are discussed and compared with the theoretical studies in literature.

Detailed study of the negative thermal expansion behavior of these materials is carried out using Rietveld refinement of HTXRD patterns collected in the temperature range 373-673 K for silicalite-1 sample. The bond angles and bond distances are determined from the Rietveld refinement data to look for any structural changes taking place as a function of temperature. The Si-O bond distances, Si-O-Si bond angles and Si-Si non-bonding distances are calculated from the Rietveld refinement results and proposed the intrinsic NTE mechanism. The Si-O bond distances seem to play no role in the NTE, as there is no change in their distances as a function of temperature. The transverse vibrations of the Si-O-Si bridging oxygen atoms decreases the Si-Si non-bonding distances which causes the contraction in the material as a function of temperature. The observed decrease in Si-Si non-bonding distances with the constituent Si-O bond distances remaining constant, supports the correlation that the transverse vibrations of the bridging oxygen atoms in the structure are responsible for the NTE in this material. The chapter also describes the HTXRD studies carried out on the metallosilicate molecular sieves TS-1, FeS-1 and ZrS-1 of different Si/M ratio. All the samples exhibit negative thermal expansion on heating in the temperature range 373-773 K and the strength of NTE increases with decreasing Si/M ratio

Chapter 4 describes the non-isothermal reaction kinetics of the template decomposition from the as synthesized silicalite-1 framework which has been carried out using thermogravimetric analysis (TGA) and high temperature powder X-ray diffraction (HTXRD) techniques and are compared for the first time in literature. Template burning (or calcinations) of the as-synthesized material is a key step in the activation of a zeolitic material for its application as a catalyst or as a membrane. HTXRD experiments are carried out at different heating rates such as 1, 3 and 5

°C/min, while TG were measured at 10, 15 and 20 °C/min. The kinetic analysis is carried out using the plots of conversion factors (α) versus temperature. Conversion factor for template decomposition is calculated using two methods *viz.*, % weight loss from the thermogravimetric analysis and changes in the intensities of the Bragg reflections 101/011 and 200/020 in the HTXRD patterns scanned at different temperatures (range 298-823 K). A kinetic analysis based on the % weight loss from the TG data and the intensity change of the low angle peaks in the HTXRD patterns is performed using Kissinger and Flynn–Wall–Ozawa methods. According to the Kissinger method, the slope of the plot of $(\ln(\beta/T_p^2))$ versus $1/T_p$ is proportional to E_a , according to the following equation: β is the heating rate, R is the molar gas constant and k is the reaction rate constant. The calculated apparent activation energy for template decomposition in air is 129 kJ mol⁻¹ (TG) and 125 kJ mol⁻¹ (HTXRD) using the Kissinger method. The alternative method by Flynn-Wall-Ozawa (where the slope of the plot of $\ln\beta$ vs. $1/T$ is proportional to E_a) is also used to calculate the activation energy using the equation. Apparent activation energy for template decomposition in air is 123 kJ mol⁻¹ (TG) and 124 kJ mol⁻¹ (HTXRD) by Flynn–Wall–Ozawa approach. An advantage of this method is that any changes in the mechanism of the reaction are immediately apparent as variations in the slope for different α . The reaction order is determined by Avrami equation using the method of Kennedy and Clark. Avrami equation is successfully used to fit the kinetic data. The value for reaction order is nearly equal to two for all the heating rates. The reaction order determined using the method of Kennedy and Clark, is close to 2 for both the experimental data (TG and HTXRD), which rule out the diffusion limitation. The apparent activation energy E_a is determined to be 125 kJ mol⁻¹, which is in good agreement with the results reported in the literature. The second order of template decomposition can be attributed to the fact that TPA⁺ is positioned in two different orientations inside the silicalite-1 framework. The second order of template decomposition can be attributed to the fact that TPA⁺ is positioned in two different orientations inside the silicalite-1 framework; the so called TPA₁ and TPA₂ having an occupancy of 0.6 and 0.4, respectively. Part of the TPA⁺ ion in the sinusoidal channel is in the folded conformation, while extended conformation is present in the straight channel. Hence, there may be different mechanism present for template decomposition in these two physically different environments of the template molecule.

Thermogravimetric analysis is used extensively in the past to study the decomposition of the template cation, TPA^+ . The weight loss of a sample as a function of temperature is recorded using thermogravimetric analysis. Over the temperature range from 573 to 823 K, the decomposition of template molecules takes place. The loss in weight corresponds exactly to the TPA^+ content of the zeolite, for e.g. four template molecules per unit cell (12% weight loss).

Rietveld analysis has been carried out to look in to the structural changes taking place in the framework as a function of temperature. Template removal occurs with a contraction in unit cell dimensions. There is a large contraction in the unit cell volume as the template is removed from the framework and it is attributed to the transverse vibrations of Si-O-Si bridging oxygens as a function of temperature. In addition, the unit cell dimensions approach the same values regardless of heating rate.

Chapter 5 describes the investigation of the phase transition temperature for various TS-1 and FeS-1 samples (concentration of Ti and Fe vary) to determine the effect of Si/M ratio on the phase transition temperature. These metallosilicate molecular sieves show orthorhombic phase in $Pnma$ space group at room temperature whereas at low temperature the structure is transformed to monoclinic symmetry in space group $P2_1/n$. The powder X-ray diffraction patterns were recorded at various temperatures from 298 K to 80 K at regular intervals. The scans in the 2θ range 22 to 26° were monitored for the phase transition from the splitting of 1 3 3 reflection of the orthorhombic symmetry into the -3 1 3 and 3 1 3 reflections of the monoclinic symmetry. Attempts have been made to locate the heteroatoms in the silicalite framework for TS-1 and FeS-1 samples at low temperature (below the room temperature and above the temperature of phase transition) by using the Rietveld refinement technique. The experiment to locate the T atoms in the metallosilicate molecular sieves are extremely challenging due to the low concentration of T atoms. Contribution from the thermal atomic displacement parameters should be necessarily lower and hence XRD patterns at low temperature are collected to locate the 'T' atoms. The results of the location of heteroatoms are also discussed and compared with the results in literature.

List of publications

1. Extractive spectrophotometric determination of micro amounts of ruthenium (III) using 1,3-bis (hydroxymethyl) benzimidazole-2-thione: Analysis of fissium alloy. S. H. Gaikwad, **D. S. Bhange** and M. A. Anuse, *Revue Roumaine de chimie* 49, 631-639 (2004).
2. Chemical synthesis and compositional analysis of $[\text{Mo}(\text{S}_{1-x}\text{Se}_x)_2]$ semiconductor thin films. B. D. Ajalkar, S. H. Burungale, **D.S. Bhange** and P. N. Bhosale, *Journal of Materials Science*, 39, 1659-1664 (2004).
3. Photocatalytic decomposition of methylene blue on nanocrystalline titania prepared by different routes.
Veda Ramaswamy, **D.S. Bhange**, Vijayanand and Neelam Jagtap
Proceedings of '*Indo-Italian Brain storming workshop on Technology Transfer for Industrial Application of novel methods for environmental problems*' during 5-6 Dec. 2005 at the department of chemical engineering, BVP Deemed University, College of Engineering, Pune
4. Thermal Expansion studies in silicalite-1: In situ HTXRD studies.
D. S. Bhange and Veda Ramaswamy
Proceedings of International Symposium on Materials Chemistry, Eds: S.R. Bharadwaj *et al*, Ebenezer Publishing house, 84-87, (2006).
5. Negative thermal expansion in zirconium silicalite having MFI structure.
D.S. Bhange and Veda Ramaswamy,
Materials Research Bulletin, 41, 1392-1402 (2006).
6. High temperature thermal expansion behavior of silicalite-1 molecular sieve: in situ HTXRD study.
D. S. Bhange and Veda Ramaswamy, *Microporous and Mesoporous Materials*, 103, 235-242 (2007).
7. Thermal stability of the MFI type metallosilicate molecular sieves – an in situ HTXRD study.
D. S. Bhange and Veda Ramaswamy, *Materials Research Bulletin*, 42, 851-860 (2007).
8. NCL-7, A Novel All Silica Analogue of Polymorph B rich Member of BEA Family: Synthesis and Characterization.
M. D. Kadgaonkar, M. W. Kasture, **Deu S. Bhange**, P. N. Joshi, Veda Ramaswamy and R. Kumar,
Microporous and Mesoporous Materials 101, 108-114 (2007).
9. Nanostructured Thin films of Anthracene by Liquid-Liquid Interface Recrystallization Technique.
R. R. Hawaldar, A.M. Funde, **D. Bhange**, V. Ramaswamy, S. R. Jadkar, S. D. Sathaye, U. P. Mulik & D. P. Amalnerkar,
Solid State Phenomena 119, 27-34 (2007).
10. Synthesis and Characterization of NCL-5, NCL-6 and NCL-7: New Zeolites Enriched With Polymorph B of BEA Family.
M. D. Kadgaonkar, M. W. Kasture, **Deu S. Bhange**, P. N. Joshi, Veda Ramaswamy, N. M. Gupta and R. Kumar,

Microporous and Mesoporous Materials, 105, 82-88 (2007).

11. Photocatalytic decomposition of methylene blue on nanocrystalline titania prepared by different methods.
Veda Ramaswamy, N. B. Jagtap, S. Vijayanand, **D. S. Bhange** and P. S. Awati
Materials Research Bulletin, 43, 1145-1152 (2008).
12. Non-isothermal kinetic studies of the template decomposition from silicalite-1 framework- HTXRD and thermo gravimetric analysis.
D. S. Bhange, N. A. Pandya, R. K. Jha and Veda Ramaswamy, *Microporous and Mesoporous Materials* (Article in press)
13. Location of hetero atoms and phase transition studies in titano and iron silicalite MFI type molecular sieves using Low temperature XRD technique
D.S. Bhange and Veda Ramaswamy
Microporous and Mesoporous Materials (To be Communicated)
14. Negative thermal expansion behaviour in metallosilicate molecular sieves: Effect of frame work metal concentration
D.S. Bhange and Veda Ramaswamy
Physical Chemistry and Chemical Physics (To be Communicated)